



---

---

# Properties of high-redshift galaxies in different environments

---

---

**Yohana Herrero Alonso**

Leibniz-Institut für Astrophysik Potsdam (AIP)

Dissertation  
zur Erlangung des akademischen Grades

Doctor rerum naturalium  
(Dr. rer. nat.)

in der Wissenschaftsdisziplin  
Astrophysik

Eingereicht an der  
Mathematisch-Naturwissenschaftlichen Fakultät  
der Universität Potsdam

August 2023

## **Gutachter und Hauptbetreuer**

**Prof. Dr. Lutz Wisotzki**

Leibniz-Institut für Astrophysik Potsdam (AIP)

## **Gutachter und Zweitbetreuer**

**Prof. Dr. Philipp Richter**

Universität Potsdam (UP)

## **Gutachterin**

**Prof. Dr. Alison Coil**

University of California San Diego (UCSD)

“Without mountains, we might find ourselves relieved that we can avoid the pain of the ascent, but we will forever miss the thrill of the summit. And in such a terribly scandalous trade-off, it is the absence of pain that becomes the thief of life.”

– Craig D. Lounsbrough



The Lyman- $\alpha$  ( $\text{Ly}\alpha$ ) line commonly assists in the detection of high-redshift galaxies, the so-called Lyman-alpha emitters (LAEs). LAEs are useful tools to study the baryonic matter distribution of the high-redshift universe. Exploring their spatial distribution not only reveals the large-scale structure of the universe at early epochs, but it also provides an insight into the early formation and evolution of the galaxies we observe today. Because dark matter halos (DMHs) serve as sites of galaxy formation, the LAE distribution also traces that of the underlying dark matter. However, the details of this relation and their co-evolution over time remain unclear. Moreover, theoretical studies predict that the spatial distribution of LAEs also impacts their own circumgalactic medium (CGM) by influencing their extended  $\text{Ly}\alpha$  gaseous halos (LAHs), whose origin is still under investigation. In this thesis, I make several contributions to improve the knowledge on these fields using samples of LAEs observed with the Multi Unit Spectroscopic Explorer (MUSE) at redshifts of  $3 < z < 6$ .

I first use the widest sample of LAEs to study their large-scale clustering properties at different epochs. I optimize the clustering method to efficiently constrain the spatial distribution of MUSE LAEs. I then follow the traditional approach and assume a power-law correlation function to infer the clustering strength of the sample and the typical mass of the host DMHs. I explore whether these quantities depend on galaxy properties by splitting our sample into disjoint subsets. I find no evidence for a strong dependence on UV absolute magnitude,  $\text{Ly}\alpha$  equivalent width, and redshift. I compare our results with those from a semi-analytical model of LAE formation and adopt a galaxy-conserving evolution model to predict in which present-day DMHs MUSE-Wide-like DMHs will typically evolve.

I next include the deeper MUSE surveys and connect the clustering properties of  $\approx L^*$  LAEs with those of much fainter ones ( $\approx 0.04L^*$ ). I then apply halo occupation distribution (HOD) modelling to investigate the co-evolution between LAEs and their host DMHs. I am able to constrain the occupation of the DMHs, the DMH masses needed to host central and satellite LAEs, and the satellite fractions of our datasets. Our results suggest that the most common scenario for LAEs is that in which DMHs typically host only one LAE. I also report a strong ( $8\sigma$ ) clustering dependence on  $\text{Ly}\alpha$  luminosity, where the most luminous LAEs cluster twice more strongly and reside in ten times more massive DMHs than the lowest luminosity ones. This has important implications on evolving  $\text{Ly}\alpha$  luminosity functions, halo mass-dependent  $\text{Ly}\alpha$  escape fractions, and incomplete reionization signatures, which I discuss.

Third, I connect the clustering of LAEs to the surrounding CGM. Simulation studies predict that the  $\text{Ly}\alpha$  emission of faint, individually undetected LAEs significantly contribute to the observed extended LAHs. For the first time, I address this problem from an observational angle. I combine the HOD-modelled LAE clustering properties with assumptions on the  $\text{Ly}\alpha$  luminosity function to estimate the background surface brightness (SB) due to undetected LAEs. I consider various clustering scenarios and luminosities for the faint sources. I infer  $\text{Ly}\alpha$  SB profiles in the range of  $(0.4 - 2) \times 10^{20} \text{ erg s}^{-1} \text{ cm}^{-2} \text{ arcsec}^{-2}$ , which decline very slowly with distance from the center of the LAE. This provides evidence that the outer regions of observed LAHs ( $R \gtrsim 50 \text{ pkpc}$ ) could indeed be dominated by external LAEs. The inner regions, on the other hand, are too bright to be significantly affected by clustering. Overall, our results are in agreement with the predicted radial profiles from a plethora of simulations.

I finally explore whether environment also influences the LAHs. I adopt various approaches to identify overdense regions of LAEs at different scales. I use their available LAH properties and find that the distributions of the LAH scale length and halo fraction of the total  $\text{Ly}\alpha$  flux of LAEs that reside inside and outside overdense regions are mathematically indistinguishable.



Die Lyman- $\alpha$  ( $Ly\alpha$ )-Linie erleichtert die Detektion von Galaxien bei hoher Rotverschiebung, sogenannten den Lyman-Alpha-Emittern (LAEs). Die Erforschung ihrer Verteilung enthüllt nicht nur die großräumige Struktur des Universums in frühen Epochen, sondern bietet auch einen Einblick in die Entstehung und Entwicklung der Galaxien, die wir heute beobachten. Da Halos aus Dunkler Materie (DMHs) als Orte der Galaxienentstehung dienen, spiegelt die LAE-Verteilung auch die der zugrunde liegenden Dunklen Materie wider. Darüber hinaus sagen theoretische Studien voraus, dass die Verteilung von LAEs auch Auswirkungen auf ihr eigenes zirkumgalaktisches Medium (CGM) hat, indem sie ihre ausgedehnten gasförmigen  $Ly\alpha$ -Halos (LAHs) beeinflusst. In dieser Dissertation leiste ich mehrere Beiträge zur Verbesserung des Wissens über diese Felder anhand von Stichproben von LAEs, die mit dem Multi Unit Spectroscopic Explorer (MUSE) bei Rotverschiebungen von  $3 < z < 6$  beobachtet wurden.

Ich verwende zunächst die breiteste Stichprobe von LAEs, um ihre Clustering-Eigenschaften in verschiedenen Epochen zu untersuchen. Ich optimiere die Clustering-Methode, um die Verteilung von MUSE LAEs effizient einzuschränken. Anschließend folge ich dem traditionellen Ansatz und gehen von einer Potenzgesetz-Korrelationsfunktion aus, um die Clustering-Stärke der Stichprobe und die typische Masse der Wirts-DMHs abzuleiten. Ich finde keine Hinweise auf eine starke Abhängigkeit von der absoluten UV-Helligkeit, der  $Ly\alpha$ -Äquivalentbreite und der Rotverschiebung. Ich vergleiche unsere Ergebnisse mit denen eines semianalytischen Modells der LAE-Entstehung und verwende ein galaxienerhaltendes Evolutionsmodell, um vorherzusagen, in welchen heutigen DMHs sich MUSE-Wide-ähnliche DMHs typischerweise entwickeln werden.

Als nächstes beziehe ich die tieferen MUSE-Stichproben ein und verbinden die Clustering-Eigenschaften von  $\approx L^*$  LAEs mit denen von viel schwächeren ( $\approx 0.04L^*$ ). Anschließend wende ich die Modellierung der Halo-Besetzungsverteilung (HOD) an, um die Koevolution zwischen LAEs und ihren Wirts-DMHs zu untersuchen. Ich kann die Besetzung von DMHs, die DMH-Massen, die benötigt werden, um zentralen LAE und Satelliten-LAE enthalten zu können, und die Satellitenanteile unserer Datensätze einschränken. Unsere Ergebnisse deuten darauf hin, dass das häufigste Szenario für LAEs darin besteht, dass DMHs typischerweise nur einen LAE hosten. Ich zeige auch über eine starke ( $8\sigma$ ) Clustering-Abhängigkeit von der  $Ly\alpha$ -Leuchtkraft, wobei die leuchtkräftigsten LAEs doppelt so stark clustern und sich in  $\times 10$  massereicheren DMHs befinden als die mit der niedrigsten Leuchtkraft. Ich diskutiere wichtigen Auswirkungen auf die Entwicklung von  $Ly\alpha$ -Leuchtkraftfunktionen, der Zusammenhang der Halomassen und der  $Ly\alpha$  Fluchtanteile und unvollständige Reionisierungssignaturen.

Drittens verbinde ich das Clustering von LAEs mit dem umgebenden CGM. Zum ersten Mal gehe ich dieses Problem aus einer Beobachtungsperspektive an. Ich kombiniere die HOD-modellierten LAE-Clustering-Eigenschaften mit Annahmen zur  $Ly\alpha$ -Leuchtkraftfunktion, um die Hintergrundoberflächenhelligkeit (SB) aufgrund unentdeckter LAEs abzuschätzen. Ich betrachte verschiedene Clustering-Szenarien und Leuchtstärken für die schwachen Galaxien. Ich leite  $Ly\alpha$  SB-Profile im Bereich von  $(0.4 - 2) \times 10^{20} \text{ erg s}^{-1} \text{ cm}^{-2} \text{ arcsec}^{-2}$  ab, die mit der Entfernung vom Zentrum des LAE sehr langsam abnehmen. Dies liefert Hinweise darauf, dass die äußeren Regionen der beobachteten LAHs ( $R \gtrsim 50 \text{ pkpc}$ ) tatsächlich von externen LAEs dominiert werden könnten. Insgesamt stimmen unsere Ergebnisse mit den vorhergesagten Radialprofilen aus einer Vielzahl von Simulationen überein.

Ich untersuche schließlich, ob die Umgebung auch die LAHs beeinflusst. Ich wende verschiedene Ansätze an, um überdichte Regionen von LAEs auf verschiedenen Skalen zu identifizieren. Ich nutze ihre verfügbaren LAH-Eigenschaften und stellen fest, dass die Verteilungen der LAH-Skalenlänge und des Halo-Anteils am gesamten  $Ly\alpha$ -Fluss von LAEs, die sich innerhalb und außerhalb überdichter Regionen befinden, mathematisch nicht unterscheidbar sind.





# Acknowledgements

---

I would like to dedicate this thesis to everybody that helped me arrive where I am today and thank each single person who made this thesis possible.

In the first place, I want to thank my supervisor Prof. Dr. Lutz Wisotzki, who gave me the opportunity, already as a master student, to join his group and work with him on some of his many brilliant ideas. Lutz, I am very grateful for your guidance, counselling, criticism and for the many spontaneous and fruitful discussions we had during the last years. I really enjoyed the time working with you and I am very glad I learnt how to "do science" from you. Not all was about science though, the many exchanges we had about hiking related stuff were also very fun.

In the second place, I would like to thank Dr. Takamitsu Miyaji and Dr. Mirko Krumpel for teaching me most things I know today about clustering and HOD modelling. Thanks for having patience with me, specially at the beginning of this journey, when I only had a bare idea of what I was working on. Thanks a lot Takamitsu for hosting me in IAUNAM-E, and Lutz for offering me the opportunity. Those two months were really amazing, I got to know awesome people, and learnt a lot from each of you.

Thanks Prof. Dr. Philipp Richter for the many suggestions you always gave during our PhD meetings and for reviewing this thesis. Special thanks to Prof. Dr. Alison Coil for sneaking me into the UCSD seminar schedule and agreeing to be the external reviewer of this thesis. Thanks Dr. Axel Schwöpe and Prof. Dr. Martin M. Roth for taking the time and being part of my PhD committee. I would also like to thank the Galaxies and Quasars group as a whole. Many times I had specific questions and, it did not matter who of you I approached, you always had time for a chat. Special thanks to Tanya, Peter, Josie, and João for proofreading.

Although in the last place I thank my family, they definitely were the most important pillar. Special thanks to my mum Marisol and boyfriend João. You have supported me every single time I was a bit down, felt like I was losing the motivation or complained about hours for whatever reason. Muito obrigado pollito por me aguentar todos esses anos, sem ti tudo teria sido muito mais difícil. Muchas gracias mamá, este viaje sin ti hubiese sido muchísimo más duro y quién sabe si lo hubiese conseguido. Estas tesis va en tu nombre.



# Contents

---

<b>Abstract</b>	<b>v</b>
<b>Zusammenfassung</b>	<b>vii</b>
<b>Acknowledgements</b>	<b>ix</b>
<b>1 Introduction</b>	<b>1</b>
1.1 Large-scale structure of the universe . . . . .	1
1.1.1 Structure formation . . . . .	1
1.1.2 Galaxy formation . . . . .	2
1.2 Galaxy clustering . . . . .	3
1.2.1 The two-point correlation function . . . . .	4
1.2.2 Real and redshift space clustering . . . . .	4
1.2.3 Clustering interpretation . . . . .	5
1.2.4 Clustering dependence on galaxy properties . . . . .	7
1.3 Lyman- $\alpha$ emitters . . . . .	8
1.3.1 The Lyman- $\alpha$ emission . . . . .	9
1.3.2 Lyman- $\alpha$ gaseous halos . . . . .	10
1.3.3 Large-scale structure traced by Lyman- $\alpha$ emitters . . . . .	11
1.4 This thesis . . . . .	12
<b>2 Clustering properties of Lyman-<math>\alpha</math> emitters</b>	<b>15</b>
2.1 Introduction . . . . .	16
2.2 Data . . . . .	17
2.2.1 The MUSE-Wide survey . . . . .	17
2.2.2 LAE sample . . . . .	18
2.2.3 LAE subsets . . . . .	19
2.3 Methods . . . . .	20
2.3.1 K-estimator . . . . .	20
2.3.2 Two-point correlation function . . . . .	23
2.3.3 Bias and typical Dark Matter Halo masses from power-law fits . . . . .	23
2.3.4 Halo occupation distribution modelling . . . . .	24
2.4 Results . . . . .	25
2.4.1 K-estimator . . . . .	25
2.4.2 Power law fits . . . . .	26
2.4.3 Halo occupation distribution fit . . . . .	27
2.5 Discussion . . . . .	28
2.5.1 Comparison to Diener et al. (2017) . . . . .	28
2.5.2 Comparison with the literature . . . . .	28
2.5.3 PL vs HOD fits . . . . .	30
2.5.4 Clustering dependence on physical properties . . . . .	31
2.5.5 Cosmological simulations . . . . .	34
2.5.6 The fate of LAEs over cosmic time . . . . .	36
2.6 Conclusions . . . . .	37
2.A Effect of the HUDF parallel fields on the K-estimator . . . . .	37
2.B Effect of Ly $\alpha$ derived redshifts on the K-estimator . . . . .	38
2.C Error estimates in the K-estimator . . . . .	39

2.D	Two-point correlation function analysis . . . . .	40
2.D.1	2pcf method . . . . .	40
2.D.2	Error estimates . . . . .	41
2.D.3	Results . . . . .	42
2.D.4	K-estimator vs 2pcf . . . . .	42
2.E	Effect of redshift space distortions on our measurements . . . . .	43
<b>3</b>	<b>Clustering dependence on Lyman-<math>\alpha</math> luminosity</b>	<b>47</b>
3.1	Introduction . . . . .	48
3.2	Data . . . . .	49
3.2.1	MUSE-Wide . . . . .	49
3.2.2	MUSE-Deep . . . . .	49
3.2.3	MUSE Extremely Deep . . . . .	50
3.2.4	LAE subsamples . . . . .	51
3.3	Methods . . . . .	52
3.3.1	K-estimator . . . . .	52
3.3.2	Error estimation . . . . .	53
3.3.3	Halo occupation distribution modelling . . . . .	54
3.4	Results from HOD modelling . . . . .	56
3.4.1	Fit results from the MUSE-Wide survey . . . . .	56
3.4.2	Fit results from MUSE-Deep . . . . .	56
3.4.3	Fit results from the MUSE Extremely Deep Field . . . . .	59
3.5	Discussion . . . . .	59
3.5.1	Clustering dependence on Ly $\alpha$ luminosity . . . . .	59
3.5.2	Comparison to Herrero Alonso et al. (2021) . . . . .	62
3.5.3	Comparison with the literature . . . . .	63
3.5.4	Satellite fraction . . . . .	63
3.5.5	Implications . . . . .	64
3.6	Conclusions . . . . .	65
3.A	Effect of different fields on the clustering measurements . . . . .	66
3.B	Covariance matrix . . . . .	68
3.C	Error estimation comparison . . . . .	68
3.D	Dependence of HOD parameters on the shape of the K-estimator . . . . .	69
<b>4</b>	<b>Faint Lyman-<math>\alpha</math> emitter clustering contribution to Lyman-<math>\alpha</math> gaseous halos</b>	<b>73</b>
4.1	Introduction . . . . .	73
4.2	Data . . . . .	75
4.2.1	The MUSE-Wide survey . . . . .	75
4.2.2	MUSE Deep fields . . . . .	76
4.3	Clustering framework . . . . .	76
4.4	Contribution of faint LAEs to extended Ly $\alpha$ halos . . . . .	77
4.4.1	Ly $\alpha$ luminosity function . . . . .	78
4.4.2	Clustering enhancement factor . . . . .	79
4.4.3	Ly $\alpha$ surface brightness profile from undetected LAEs . . . . .	81
4.4.4	Comparison with observed surface brightness profile . . . . .	82
4.4.5	Comparison with the simulations . . . . .	82
4.4.6	How to measure the faint LAE SB contribution . . . . .	84
4.5	Conclusions . . . . .	85
4.A	Clustering comparison from LAE subsets of the MUSE-Wide survey . . . . .	86
4.B	Clustering enhancement factor derivation . . . . .	86
4.C	Effect of the velocity bandwidth on the faint LAE contribution to the extended LAHs . . . . .	87

<b>5</b>	<b>Properties of Lyman-<math>\alpha</math> gaseous halos in different environments</b>	<b>91</b>
5.1	Introduction . . . . .	91
5.2	Data . . . . .	92
5.2.1	MUSE Deep fields . . . . .	92
5.2.2	MUSE ultra deep field . . . . .	93
5.2.3	Ly $\alpha$ halo sample . . . . .	93
5.3	Environment characterization . . . . .	94
5.3.1	Voronoi-Delaunay tessellation . . . . .	95
5.3.2	Kernel-density estimator . . . . .	95
5.4	Ly $\alpha$ halo properties in different environments . . . . .	95
5.4.1	Voronoi-Delaunay overdensities . . . . .	95
5.4.2	Kernel-density estimator overdensities . . . . .	97
5.5	Discussion . . . . .	98
5.5.1	Comparison with the literature . . . . .	98
5.5.2	Implications . . . . .	99
5.6	Conclusions . . . . .	100
<b>6</b>	<b>Conclusions and outlook</b>	<b>103</b>
6.1	Summary . . . . .	103
6.2	Future perspectives . . . . .	105
6.2.1	The dark-baryonic matter relation . . . . .	105
6.2.2	The origin of Lyman- $\alpha$ halos . . . . .	105
6.2.3	Future instrumentation . . . . .	107
<b>A</b>	<b>Finding HST counterparts for MUSE data: QtCounterpart</b>	<b>109</b>
A.1	General concept . . . . .	109
A.1.1	Input data . . . . .	109
A.1.2	Requirements . . . . .	112
A.2	Description of QtCounterpart . . . . .	112
A.2.1	Output data . . . . .	114



## 1.1 Large-scale structure of the universe

Matter in the universe is not randomly distributed. Although the universe appears to be homogeneous on large scales, there is inhomogeneity or clumpiness on scales larger than the galactic sizes. This is commonly referred as the large-scale structure of the universe (or cosmic web). In the following, I explain in simple terms how this structure formed, starting from the first density fluctuations in the universe.

### 1.1.1 Structure formation

Quantum processes that occurred in the first fraction of a second during the inflationary era<sup>1</sup> produced fluctuations in the density field of the universe. These can be expressed as:

$$\delta(x) = \frac{\rho(x) - \bar{\rho}}{\bar{\rho}}, \quad (1.1)$$

where  $\rho(x)$  is the local density at a given position  $x$  and  $\bar{\rho}$  is the mean density of the universe. These density fluctuations grow under the influence of gravity by attracting matter. Their growth rate depends on the scale factor  $a$ , which parametrizes the relative expansion of the universe, and on the density of the dominant component of the universe at a given epoch. Depending on the nature of this constituent i.e., matter (dark and baryonic), radiation or dark energy, fluctuations grow at different rates.

During the first 47000 years of the universe (or up to a redshift of  $z = 3600$ ), the dominant constituent of the universe was radiation. As radiation redshifted away, the mass energy exceeded radiation energy and matter dominated the universe between  $0.4 < z < 3600$  (from 47000 years to 9.8 billion years after the Big Bang). The dark-energy-dominated era is believed to be the last phase of the universe, which started when

the universe was about 9.8 billion years ( $z = 0.4$ ) and continues today. Hence, the universe was matter dominated during the majority of its existence, which allowed mass density fluctuations to grow and form new structure.

For small density fluctuations ( $\delta(x) \ll 1$ ), we can assume spherical symmetry and apply linear structure formation theory. Fluctuations can then be decomposed as a superposition of plane harmonic waves,  $\delta_k$ , with different amplitudes, wavelengths and phases. Within this framework, high density fluctuations (but still  $\delta(x) \ll 1$ ) are the result of long wave superpositions and tend to be found close together i.e., tend to cluster, which is paramount for how matter is distributed in the universe today. This approach is often applied to the early universe because of its homogeneity (and thus small density fluctuations).

The relation between density fluctuations and harmonic waves is described by a Fourier transform:

$$\delta(x) = \sum_k \delta_k \cdot \exp(-ik \cdot x), \quad (1.2)$$

where the wave number  $k$  is defined as  $k = \frac{2\pi}{\lambda}$ , with  $\lambda$  being the wavelength. The squared of the amplitude of this equation averaged over all waves is the matter power spectrum,  $P(k)$ :

$$P(k) = \langle |\delta_k|^2 \rangle_k, \quad (1.3)$$

which informs about the amount of structure on any Fourier scale  $k$ .

As fluctuations continue growing ( $\delta(x) > 1$ ), spherical symmetry and linear theory do no longer apply. In non-linear structure formation, fluctuations collapse along one direction, forming sheets of matter (Zel'dovich, 1970). These then collapse along the second direction and form filaments of matter, which will eventually collapse to form dark matter halos (DMHs).

<sup>1</sup>The inflationary era is the period of time in which the early universe expanded exponentially. This epoch is believed to have lasted from  $10^{-36}$  seconds to  $10^{-32.5}$  seconds after the Big Bang. After this, the universe expanded at a slower rate.

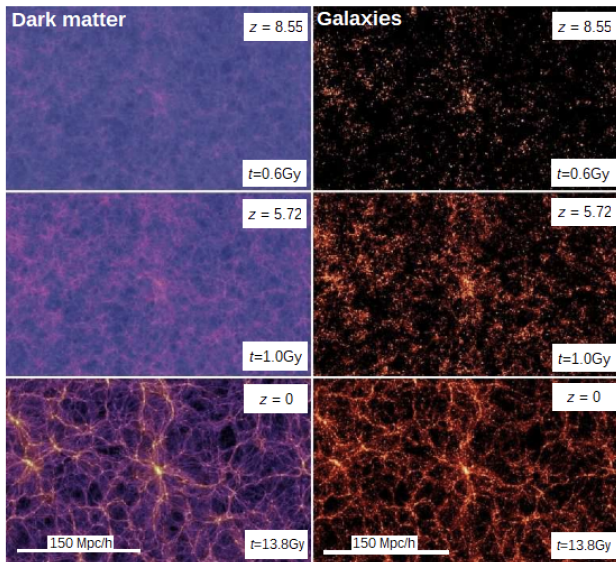


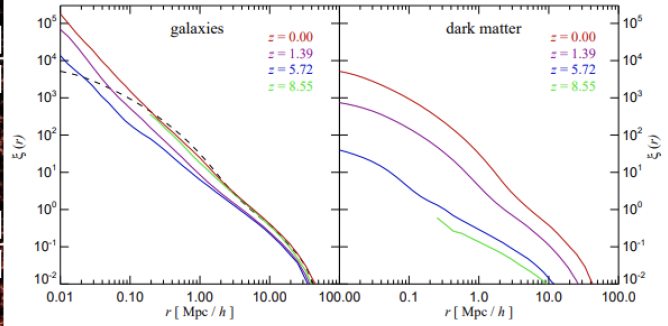
**Figure 1.1:** Dark matter and galaxy distribution. Left figure: Projected mass density illustrating the growth of structure from  $z = 8.55$  to  $z = 0$  (rows). The densest regions are the brightest. The density snapshots were projected over 15 comoving  $h^{-1}$  Mpc. The left and right columns show the dark matter and galaxy distributions, respectively. Right figure: The 2pcf of the same galaxies (left) and dark matter (right) as those in the left figure. Different colors represent the various redshifts considered in the left figure. For comparison, the  $z = 0$  2pcf of dark matter is shown as a dashed line in the galaxies panel. Image adapted from Springel et al. (2006).

As halos virialize, collapse halts and DMHs grow hierarchically by accretion and mergers with other halos (Sheth et al., 2001). This non-linear structure formation scenario is well described with a perturbative analytical approach. For instance, the well-known (extended) Press-Schechter formalism (Press & Schechter, 1974) provides expressions for the formation time of DMHs, the relative density at which the halo forms, its size, mass, etc.

Non-linear structure formation gives place to the cosmic web of dark matter filaments, where the most massive halos are found at the nodes and less massive halos are located throughout. These halos form the skeleton where stars and galaxies will be born.

### 1.1.2 Galaxy formation

The interaction between gravity, pressure and baryons produced acoustic density waves, which caused oscillations in the density field of the visible baryonic matter (rather than in the non-visible dark matter, as for DMH formation; see previous section). As understood by hierarchical structure formation, the first stars and galaxies formed from the collapse of these mass pertur-



bations, from small to larger mass scales. These oscillations can be seen today as wiggles in the matter power spectrum at around  $100 h^{-1}$  Mpc and are known as baryon acoustic oscillations (BAO)<sup>2</sup>.

Baryonic fluctuations did not collapse simultaneously with dark matter perturbations. During the matter-dominated era and before the recombination epoch<sup>3</sup>, photons were able to damp baryonic fluctuations by dragging baryons along, which impeded baryonic-matter fluctuations to grow. For dark matter perturbations, on the other hand, there was no obstacle that prevented their growth and only after these collapsed, baryonic-matter fluctuations did too.

After the collapse of baryonic perturbations, gas and dark matter were initially well mixed (plasma state). When gas was able to dissipate, it flowed into the potential well of DMHs (located in the highest density regions of the dark matter distribution). Gas settled into hydrostatic equilibrium and, once it became dense enough, it fragmented into the first stars by cooling and condensation (e.g., White & Rees, 1978; White & Frenk, 1991), following the already existing dark matter distribution. Galaxies then grew by gas accretion and merging, because their DMHs also

<sup>2</sup>BAO are considered a "standard ruler" for length scale. They represent the maximum distance the acoustic density waves could travel in the early universe before the first neutral atoms formed and halted the growth of the waves.

<sup>3</sup>The recombination epoch is the era in which electrons and protons combined to form neutral hydrogen atoms at  $z = 1100$ .



merged. The growth, properties and distribution of galaxies are therefore tightly connected to those of their host DMHs.

Because galaxies form in high density peaks of matter (see the two bottom panels of the left figure in Fig. 1.1), these are the only regions we observe when we look at the night sky. Galaxies are thus biased tracers of the matter distribution of the universe. This bias can be further strengthened or weakened due to baryonic processes such as gas cooling or feedback. While the former process increases the baryonic density and results in baryons forming more structure than dark matter, through the latter process we encounter the opposite scenario. Gas cooling can contract the DMH due to the galaxy formation in its center, which varies the amount of structure on small scales (Blumenthal et al., 2016). Feedback, on the other hand, can expand the DMH due to the large amounts of gas that galaxies may expel.

The left figure in Fig. 1.1 shows the dark matter (left panels) and galaxy (right panels) distributions at  $z = 8.55$ ,  $5.72$ ,  $0$ . While the dark matter distribution is extracted from the Millennium simulation (Springel et al., 2005), the galaxy distribution was derived from semi-analytic techniques that model galaxy formation. Although at  $z = 8.55$  (top row) structure was somewhat smooth, at  $z = 5.72$  (middle row) dark matter already displays an intermediate stage of the current cosmic web. Galaxies, visible as small clumps of stars, also formed (in the most massive DMHs). By  $z = 0$  (today, 13.8 billion years after the Big Bang; last row), the dark matter distribution is very pronounced and galaxies keep growing in the high density peaks of dark matter density. Today, about 27% of the mass of the universe is dark matter, whereas only 5% is baryonic matter (PlanckCollaboration, 2016).

To constrain the large-scale properties of the mass distribution of the universe and to interpret the dark matter-galaxy relation, it is crucial to understand the galaxy bias. Abundance matching studies (e.g., Behroozi et al. 2010), using galaxy clusters to aim at observationally finding individual DMHs (e.g., Yang et al. 2005a), weak gravitational lensing, satellite kinematics, galaxy voids, galaxy scaling relations, etc., offer information about the galaxy-halo relation (see Wechsler & Tinker 2018 for a review). One of the most common approaches to investigate this matter is by measuring how galaxies cluster.

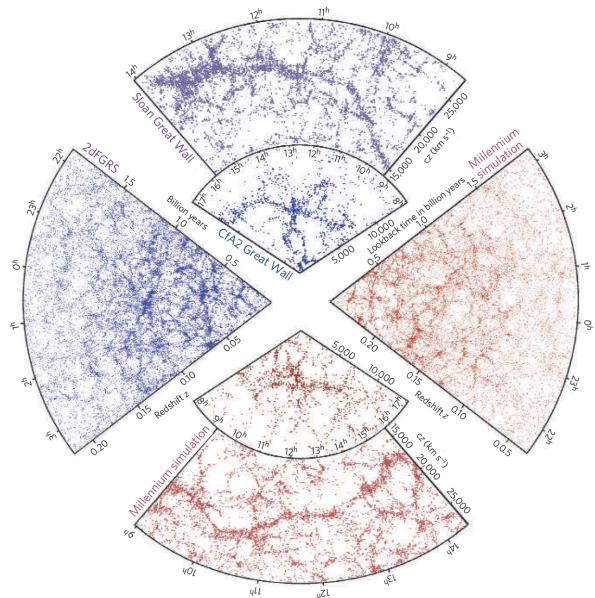


**Figure 1.2:** Large-scale structure of the universe traced by galaxies detected in spectroscopic redshift surveys (blue) and from mock catalogues built using semi-analytic modelling to simulate the formation and evolution of galaxies within the dark matter distribution of the Millennium cosmological simulation (red). Figure from Springel et al. (2006).

## 1.2 Galaxy clustering

The beginning of galaxy surveys allowed the first measurements of galaxy clustering (Baugh, 1996), although the "unevenness in the galaxy distribution" was already noted in the thirties (Shapley & Ames, 1932; Hubble, 1934). This field was revolutionized with the first large spectroscopic redshift surveys, such as the Center for Astrophysics redshift survey (CfA; Davis & Peebles, 1983), the Two-degree Field Galaxy Redshift Survey (2dFGRS; Colless et al., 2001), or the Sloan Digital Sky Survey (SDSS; Strauss et al., 2002).

These surveys are displayed on the left half of Fig. 1.2 (blue), where the underlying dark matter filaments and nodes are clearly traced by the surveyed galaxies. The right half of the figure shows mock galaxy samples (red) built using semi-analytic modelling of galaxy formation, coupled to the dark matter distribution of the Millennium simulations (Springel et al., 2005). This figure illustrates the excellent match between the predictions from the standard model of cosmology (i.e., Lambda Cold Dark Matter,  $\Lambda$ CDM) and large-scale observations.

Although complex and scale dependent, measuring the properties of this structure and inferring information about the bias between galaxy

and dark matter is regularly done with two-point correlation statistics (Mo & White, 1996; Coil et al., 2012).

### 1.2.1 The two-point correlation function

The clustering of galaxies is frequently measured with the two-point (auto) correlation function (2pcf or  $\xi(r)$ ). The 2pcf is defined as the excess probability  $dP$  over a random Poisson distribution of finding a galaxy  $i$  from another galaxy  $j$  at a given distance  $r$  in a volume  $dV$  with a number density  $n$  (Peebles, 1980):

$$dP = n \cdot [1 + \xi(r)] \cdot dV. \quad (1.4)$$

The 2pcf is the inverse fourier transform of the power spectrum (see Sect. 1.1.1) and similarly informs about the amount of structure on any scale  $r$ . While a clustered sample of galaxies would deliver  $\xi(r) > 0$  (i.e., there is structure being traced by the galaxy sample), in a randomly distributed dataset we would infer  $\xi(r) = 0$  (i.e., there is no structure imprinted in the dataset).

In practice, the 2pcf is estimated from the comparison between the observed number of galaxy pairs and the expectation for an unclustered sample (i.e., a set of randomly distributed galaxies, hereafter random sample). To perform that comparison, we create a random sample that covers the same area of the sky and presents a similar redshift distribution to the observed dataset. The random sample should be significantly larger (about hundred times) than the real dataset to avoid the inclusion of Poisson uncertainties in the measurements.

A widely used clustering estimator is the one proposed by Peebles & Hauser (1974):

$$\xi(r) = \frac{n_R}{n_D} \frac{DD(r)}{RR(r)} - 1, \quad (1.5)$$

where  $DD$  and  $RR$  are the pair counts of the real and random data, respectively. The corresponding mean number densities are  $n_D$  and  $n_R$  and account for the difference in the number of galaxies in the two samples. Another common estimator, based on the same concept but carrying smaller statistical uncertainties, is the one proposed by Landy & Szalay (1993). I apply this estimator in Chapter 2.

An example of 2pcf measurement is shown in the right figure of Fig. 1.1, which illustrates the 2pcf measured with galaxies (left panel) and dark matter (right panel) at various redshifts. These correspond to the same epochs as the simulations shown on the left figure. Both the galaxy and dark matter 2pcf present clustering signals ( $\xi(r) > 0$ ). The amplitude of the 2pcfs decreases with increasing redshift, although the galaxy 2pcf has a similar strength at  $z = 8.55$  and at  $z = 0$ . This clustering dependence on epoch (and on galaxy properties) will be covered in Sect. 1.2.4. Moreover, the shapes of the 2pcfs are clearly distinct. While the galaxy 2pcf can be approximated with a power law at large scales (see Sect. 1.2.3), that of the dark matter presents characteristic features.

### 1.2.2 Real and redshift space clustering

Clustering estimators rely on galaxy pair counts as a function of separation  $r$  to measure the clustering of a given dataset. Nevertheless, the distance between galaxy pairs cannot be measured directly. We instead employ the redshift information of the galaxies, assume a cosmological model, and calculate cosmological distances. We typically compute two distances: the transverse,  $r_p$ , and the line-of-sight separation between the galaxy pair,  $\pi$ . The redshifts are, however, affected by the peculiar velocity of the galaxies, which translates into distortions in the inferred cosmological distances. These are the so-called redshift space distortions (RSDs).

At small scales ( $< 1$  comoving  $h^{-1}\text{Mpc}$ ), the random velocities of galaxies create a Doppler shift that makes the distribution of galaxies in a redshift space look elongated along  $\pi$  towards the observer. This is known as the Finger-of-God (FoG) effect (see the stretching in the redshift-space galaxy distribution of the bottom panel of the left figure in Fig. 1.3). This distortion on the derived positions suppresses the correlation function along the line of sight and, when displayed on a two-dimensional representation of  $\pi$  versus  $r_p$ , the 2pcf contours also look elongated along the line of sight at small scales (see the bottom left panel of the right figure in Fig. 1.3). For comparison, note the circular symmetry of the real-space 2pcf in the top left panel of the same figure.

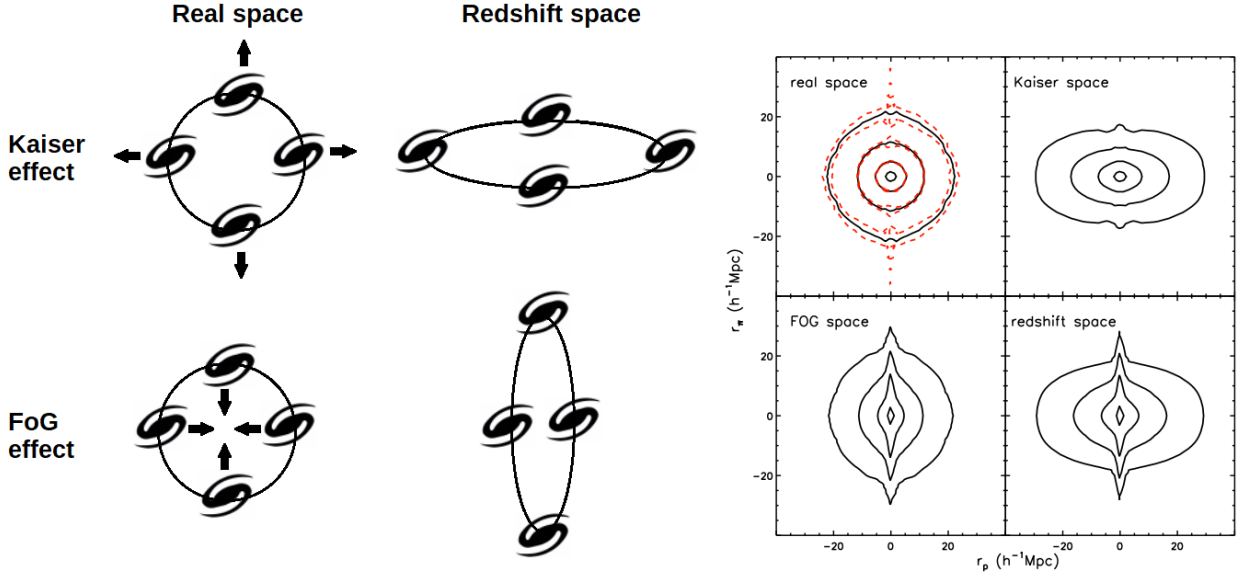


**Figure 1.3:** Redshift-space distortions. Left: real- and redshift-space distribution of four galaxies. At small scales, the redshift-space galaxy distribution is elongated along the line of sight towards the observer (FoG effect; bottom row). At large scales, the same distribution is squashed (Kaiser effect; top row). Note the circular symmetry of the real-space galaxy distribution. Right: Two-dimensional 2pcf contours (black) in line-of-sight,  $\pi$ , and transverse separation,  $r_p$ . The different spaces (panels) show the effect of the RSDs: Real space (top left), Kaiser space (top right), FoG space (bottom left) and redshift space (bottom right). The contour levels are  $\xi = 5, 1, 0.3, 0.1$ . The red dashed contours show  $1\sigma$  uncertainty. Contours from Shi et al. (2016).

At large scales ( $> 1$  comoving  $h^{-1}\text{Mpc}$ ), on the other hand, the coherent infall of galaxies onto larger structures i.e., galaxy groups or clusters, leads to the contraction of these structures, when presented in a redshift space. This is commonly referred as Kaiser infall (Kaiser 1987; see flattening in the top panel of the left figure in Fig. 1.3). The imprints of this effect are shown on the top right panel of the right figure, where the redshift-space 2pcf is suppressed at large scales (see real-space 2pcf in the top left panel of the same figure, for comparison). The last panel shows the combination of the FoG and Kaiser effects on the redshift-space 2pcf.

A somewhat novel RSD effect, tight to specific emission-line-selected galaxy populations, relates to radiative transfer processes (see Sect. 1.3.2). Redshift measurements derived from line shifts in the spectrum of a galaxy are often contaminated by the resonant scattering that some lines undergo. The inferred radial positions in redshift space are then also affected by this process. In fact, this offset in the galaxy positions also suppresses the clustering along the line of sight, which can be interpreted as an additional FoG effect (Zheng et al., 2011a; Wyithe & Dijkstra, 2011; Byrohl et al., 2019).

To minimize these effects, we first compute

the 2pcf in a 2D grid of  $r_p$  and  $\pi$  using one of the clustering estimators and then integrate  $\xi(r_p, \pi)$  over  $\pi$ . We thus obtain the projected 2pcf,  $\omega(r_p)$ :

$$\omega_p(r_p) \approx 2 \int_0^{\pi_{\max}} \xi(r_p, \pi) d\pi, \quad (1.6)$$

where  $\pi_{\max}$  is the maximum allowed  $\pi$  distance between two galaxies to be considered as a pair. Typically,  $\pi_{\max}$  is of the order of few tens of comoving  $h^{-1}\text{Mpc}$  and is chosen in such way that it accounts for most correlated pairs and the amplitude of  $\omega_p(r_p)$  is able to converge.

### 1.2.3 Clustering interpretation

Measuring the 2pcf in a galaxy sample only delivers a clustering signal (see right figure in Fig. 1.1), an excess probability of finding a galaxy pair at a given distance and an indication of structure in the dataset. In order to obtain clustering properties, we need to model that signal.

The traditional fit to the 2pcf has the shape of a power law (Peebles, 1980):

$$\xi(r) = \left(\frac{r}{r_0}\right)^{-\gamma}, \quad (1.7)$$

where  $\gamma$  and  $r_0$  are the correlation slope and cor-

relation length, respectively. The latter represents the characteristic scale at which the probability of finding a galaxy pair is the highest (i.e.,  $\xi(r_0) = 1$ ).

This approach treats scales in the linear ( $<1$  comoving Mpc) and non-linear ( $>1$  comoving Mpc) regime alike. The small scales of the 2pcf, however, do not follow a power law and, even in the linear regime, the correlation function may deviate from shape of a power law (Coil et al., 2008). A power law correlation function is thus an approximation and does not carry information about dark matter and galaxy formation. In fact, it does not distinguish between the different clustering contributions due to pairs of galaxies that belong to the same DMH (non-linear scales; one-halo term) and pairs that reside in distinct halos (linear scales; two-halo term). A more appropriate treatment is achieved through halo occupation distribution (HOD) modelling.

The HOD describes the probability that a halo of mass  $M_h$  contains  $N$  galaxies. It links, thus, galaxies with individual DMHs (Berlind & Weinberg, 2002). Cosmological N-body simulations typically provide the underlying dark matter distribution (Benson et al., 2000), which we then populate with HOD models by assuming that one galaxy is at the center of the DMH (the central galaxy), and the rest of the galaxies are satellites, which follow the Navarro-Frenk-White (NFW) profile (Navarro et al., 1997).

The mean occupation function for central galaxies,  $\langle N_c \rangle$ , can be approximated by a step function:

$$\langle N_c(M_h) \rangle = \frac{1}{2} \left[ 1 + \operatorname{erf} \left( \frac{\log M_h - \log M_{\min}}{\sigma_{\log M}} \right) \right], \quad (1.8)$$

while that of satellites galaxies,  $\langle N_s \rangle$ , is approximated by a power law (Zheng et al., 2007):

$$\langle N_s(M_h) \rangle = \langle N_c(M_h) \rangle \cdot \left( \frac{M_h - M_{\text{cut}}}{M_1} \right)^\alpha. \quad (1.9)$$

$\operatorname{Erf}(x)$  is the error function i.e.,  $\operatorname{erf}(x) = \frac{2}{\sqrt{\pi}} \int_0^x \exp(-t^2) dt$ ,  $M_{\min}$  is the threshold DMH mass to host a central galaxy,  $\sigma_{\log M}$  is the smoothing scale of the central halo occupation lower mass cutoff,  $M_1$  is the minimum DMH mass needed to host (on average) one satellite galaxy (besides the central one),  $\alpha$  is the slope of the number of satellites, and  $M_{\text{cut}}$  is the mass at which the satellite occupation becomes zero.

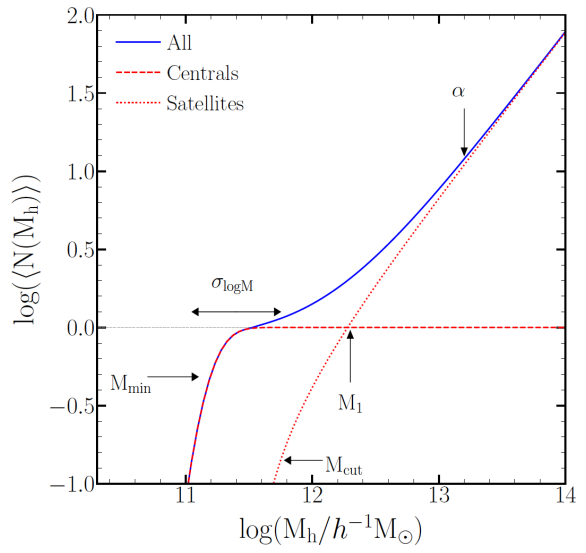


**Figure 1.4:** Mean number of galaxies per halo as a function of DMH mass for central (dashed red), satellite (dotted red) and total (solid blue) galaxies. The arrows show the HOD features that are sensitive to the five HOD parameters. The horizontal gray dotted line shows  $\langle N(M_h) \rangle = 1$ . Image from Contreras & Zehavi (2023).

The mean total occupation distribution,  $\langle N(M_h) \rangle$ , is then:

$$\langle N(M_h) \rangle = \langle N_c(M_h) \rangle + \langle N_s(M_h) \rangle. \quad (1.10)$$

This five-parameter HOD model is motivated and extensively described in Zheng et al. (2007).

With the DMHs populated by central and satellite galaxies, we then measure the 2pcf by combining the separate contributions from the one- (1h; i.e., galaxy pairs residing in the same DMH) and two-halo (2h; i.e., galaxy pairs residing in different DMHs) clustering terms:

$$\xi(r) = \xi_{1h}(r) + \xi_{2h}(r). \quad (1.11)$$

Figure 1.4 illustrates the effect of the HOD parameters on the shape of the occupation of the DMHs (see Appendix 3.D of Chapter 3 for the dependencies of the HOD parameters on the shape of the clustering statistic, using a simplified HOD model).  $M_{\min}$  and  $M_1$ , together with  $M_{\text{cut}}$ , shift to lower and higher halo masses the HOD of central and satellite galaxies, respectively.  $\alpha$  varies the slope of the number of satellite galaxies per halo and  $\sigma_{\log M}$  smooths the otherwise step function for central galaxies.

The power-law or HOD modelled correlation function is then scaled to match the measured clustering signal (see Sect. 1.2.1). The best-fit parameters are consecutively used to derive the

clustering strength of the galaxy sample, which relates the distribution of galaxies to that of the underlying dark matter,  $\xi(r)_{\text{DM}}$  (Kaiser, 1984). This is characterized by the large-scale bias factor,  $b$ :

$$b^2 = \frac{\xi(r)}{\xi(r)_{\text{DM}}}. \quad (1.12)$$

The bias factor illustrates the fact that the clustering of galaxies does not mirror the clustering of the bulk of matter (see Sect. 1.1.2 and right figure in Fig. 1.1). This bias increases with redshift, as the first galaxies collapsed in the most overdense regions of the universe (Fry, 1996). With time, galaxies become unbiased tracers of the mass distribution i.e.,  $b \rightarrow 1$  as  $t \rightarrow \infty$ . The bias factor also depends on scale (but becomes constant towards large scales) and galaxy properties (Wechsler & Tinker, 2018) and is typically used to derive the typical host DMH mass of the galaxy population (see Chapter 2). Note that while we measure  $\xi(r)$  from real data (see Sect. 1.2.1),  $\xi(r)_{\text{DM}}$  is the Fourier transform of the dark matter power spectrum.

### 1.2.4 Clustering dependence on galaxy properties

How galaxies trace the underlying mass distribution depends on how these were formed. Galaxies detected with different selection techniques are typically biased for and against certain galaxy properties. The clustering strength is known to depend on luminosity, mass, color, morphology, star formation rate, type, and redshift. The general trend is that more luminous, more (stellar) massive, redder, bulge-dominated, more star forming, early type, and higher redshift galaxies are clustered more strongly than fainter, less (stellar) massive, bluer, disk-dominated, less star forming, late type, and lower redshift ones.

At low redshift ( $z < 1$ ), large redshift surveys such as SDSS and 2dFGRS delivered most clustering trends known today. Zehavi et al. (2002), Zehavi et al. (2005), Zehavi et al. (2011) performed the first clustering studies of SDSS galaxies at  $z < 0.2$  and found that redder and brighter galaxies exhibit stronger and steeper correlation functions than bluer and fainter galaxies. At slightly lower redshifts ( $z < 0.03$ ), Li et al. (2006) showed that SDSS galaxies with higher stellar masses cluster more strongly than less massive ones. While some of these correlations were also found

by Norberg et al. (2001) using 2dFGRS data, Norberg et al. (2002) and Madgwick et al. (2003) further found a clustering dependence on spectral type.

Clustering analyses in DEEP2 (Newman et al., 2013) and the PRISM Multi-object Survey (PRIMUS; Coil et al. 2011) found similar correlations at intermediate redshifts ( $z \approx 1$ ). Coil et al. (2006), Coil et al. (2008) found that DEEP2 brighter galaxies reside in denser environments than fainter ones, with a stronger dependence than that found for lower redshift SDSS galaxies. The dependence on color was, however, of the same strength as that found for local galaxies. These findings were supported by Marulli et al. (2013) and Meneux et al. (2009), who showed a tight constraint for the dependence of clustering on luminosity and stellar mass from a sample of  $0.5 < z < 1.1$  galaxies from the VIMOS Public Extragalactic Redshift Survey (VIPERS; Guzzo et al. 2014) and from  $0.5 < z < 1$  zCOSMOS (Lilly et al., 2007) galaxies, respectively. Mosteck et al. (2013) also found a strong positive correlation between stellar mass and clustering amplitude, as well as a negative trend with specific star formation rate. This was confirmed by Coil et al. (2017) using PRIMUS and DEEP2 data.

At similar redshifts but using emission-line-selected galaxies, Sobral et al. (2010) studied the clustering properties of H $\alpha$ -selected galaxies at  $z \approx 0.9$  from the High- $z$  Emission Line Survey (HiZELS; Sobral et al. 2009). In line with previous studies, they found that galaxies with higher H $\alpha$  luminosities reside in denser regions than less luminous ones.

Clustering measurements at high redshifts ( $z > 1$ ) are more challenging. Gathering statistically relevant galaxy samples and simultaneously covering a representative volume of sky is not straightforward. There are, however, few studies that investigated clustering dependencies on physical properties. For instance, Adelberger et al. (2005) found a clustering strength increase with increasing luminosity from a sample of  $1.4 < z < 3.5$  galaxies selected photometrically. Using a sample of [OII] and H $\beta$ + [OIII] emission-line-selected galaxies at  $0.8 < z < 4.7$  from HiZELS, Khostovan et al. (2018) found a positive correlation between clustering strength, line luminosity, stellar mass, and redshift. Durkalec et al. (2018) also observed a correlation with stellar mass, together with a further dependence on UV luminosity, from  $2 < z < 5$  VIMOS Ultra Deep

Survey (VUDS; Tasca et al. 2017) galaxies. Similar results were obtained by Malkan et al. (2017) with SUBARU Deep Field (Furusawa et al., 2008) galaxies selected through the drop in the continuum bluewards of  $912 \text{ \AA}$  (Lyman-break galaxies, LBGs).

Although these correlations are significant at the redshifts mentioned above, they become somewhat unclear near the epoch of reionization ( $z \approx 6$ ). Accessing the very high-redshift universe is commonly achieved by targeting the Lyman- $\alpha$  ( $\text{Ly}\alpha$ ) emission line of young, star-forming galaxies, either with narrow-band (NB) filters or spectroscopy. Galaxies exhibiting strong  $\text{Ly}\alpha$  emission in their spectrum or selected through this emission are the so-called Lyman- $\alpha$  emitters (LAEs).<sup>4</sup>

### 1.3 Lyman- $\alpha$ emitters

Partridge & Peebles (1967) predicted that the  $\text{Ly}\alpha$  emission line could be used to detect high-redshift galaxies because most of the hydrogen ionising emission of a galaxy could be transformed into  $\text{Ly}\alpha$ , making it a prominent line that shifts into the optical at high redshifts. In fact, the  $\text{Ly}\alpha$  emission is nowadays a paramount cosmological feature for probing high-redshift galaxies. LAEs are young (20 – 500 Myr; e.g., Karman et al. 2017; Gawiser et al. 2007), probe the lower range of stellar masses ( $10^8 - 10^9 M_{\odot}$ ; e.g., Yuma et al. 2010), and copiously form stars (star formation rates of  $1 - 10 M_{\odot} \text{ yr}^{-1}$ ; e.g., Yuma et al. 2010). They are also compact and present low metallicities (subsolar; e.g., Acquaviva et al. 2011). However, many properties of these high-redshift galaxies are still under investigation, for instance the photon escape fraction, outflow rate, and dust content.

Partridge & Peebles (1967) estimated that 6 – 7% of the total radiation from a young galaxy is transformed into  $\text{Ly}\alpha$  emission (see next section for the physical explanation). This, however, turned out to be an overestimation of the observability of LAEs and it was not until the late nineties that the first LAEs were detected (Steidel et al., 1996; Cowie & M., 1998; Rhoads et al., 2000). Traditionally, broad-band filters were compared to NB filters to search for a flux excess in  $\text{Ly}\alpha$  and thus detect the LAE (Ouchi

et al., 2021). Later on, NB filters with widths (tens of  $\text{\AA}$ ) targeting the  $\text{Ly}\alpha$  wavelength at the redshift of interest were applied instead. Statistically substantial samples of LAEs, also covering large areas of the sky ( $> \text{deg}^2$ ), were obtained with this selection technique (Ouchi et al., 2003; Gawiser et al., 2007; Ouchi et al., 2017; Sobral et al., 2017).

NB detections, however, often require spectroscopic follow-up observations to confirm the redshift of the  $\text{Ly}\alpha$  emission. Besides, to avoid sample contamination by low-redshift interlopers and obtain precise redshift measurements, spectroscopic observations are preferred. Ideally, it would be optimal to perform spectroscopy of all existing galaxies over a large area of the sky, with a wide redshift coverage (not possible with NB filters). Although this is still beyond our current means, integral field units (IFUs) constitute a prominent leap forward to achieve this approach. IFUs combine imaging and spectroscopy to obtain spectra in each spatial pixel. In particular, the Multi Unit Spectroscopic Explorer (MUSE, Bacon et al., 2010) on the ESO-VLT has produced significant samples of LAEs over a wide range of redshifts with source densities of several tens or even hundreds of objects per  $\text{arcmin}^2$ , depending on the survey depth, (Inami et al., 2017; Urrutia et al., 2019), over modest sky coverages (tens of  $\text{arcmin}^2$ ).

MUSE observations aimed at building statistical samples of LAEs, targeting regions of the sky where additional radio, millimeter, far-, mid- and near-infrared, optical, ultraviolet, and X-ray data are available (e.g., GOODS fields). I refer to Appendix A for a self-developed Graphical User Interface (GUI) that assigns Hubble Space Telescope (HST) counterparts to MUSE detections (not only LAEs) by simultaneously inspecting MUSE pseudo-NB images and the corresponding HST cut-outs. The GUI, named `QtCounterpart`, also connects the spectroscopic data from MUSE to photometric properties from various photometric catalogues. Although `QtCounterpart` was optimized for MUSE and HST, it can also be applied to any other spectroscopic and photometric data.

The same fields that MUSE observed are currently being targeted by James Webb Space Telescope (JWST) Advanced Deep Extragalactic Survey (JADES; Eisenstein et al. 2023), which has

<sup>4</sup>Note that Quasi Stellar Objects (QSOs) also produce  $\text{Ly}\alpha$  emission from the interaction of black holes and their accretion disks. This thesis focuses on star-forming galaxies.

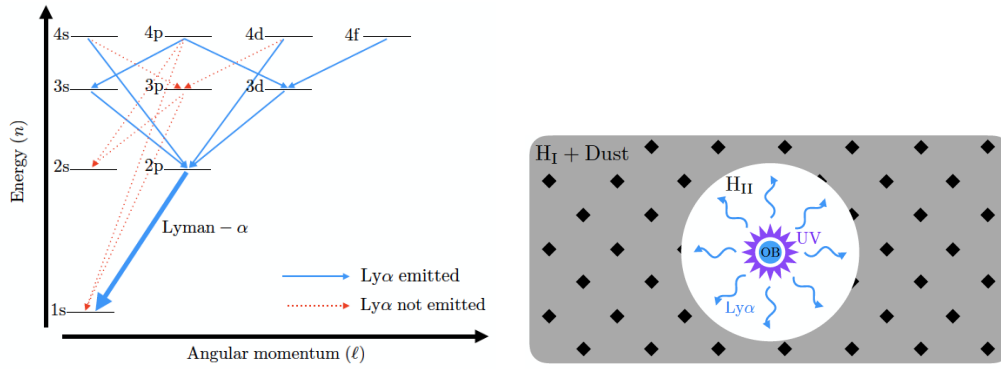


**Figure 1.5:** Ly $\alpha$  emission. Left panel: Energy levels of a hydrogen atom with increasing energy (quantum number  $n$ ) along the y-axis and angular momentum along the x-axis (quantum number  $l$ :  $s$ ,  $p$ ,  $d$  and  $f$ ). Thin blue lines show the cascades that end up emitting in Ly $\alpha$ . Cascades that do not produce a Ly $\alpha$  photon are shown in red. The transition that emits a Ly $\alpha$  photon ( $2p \rightarrow 1s$ ) is represented with a thick blue line. Figure adapted from Dijkstra (2014). Right panel: Artistic representation of the generation of Ly $\alpha$  photons. Young OB-type stars emit UV photons (violet), which ionize the surrounding neutral hydrogen (grey) and create an ionized bubble (white). When recombination takes place, Ly $\alpha$  photons are emitted (blue arrows). Image from Gurung-López (2019).

already confirmed some of the LAEs detected with MUSE. Much larger areas of the sky ( $\approx 540 \text{ deg}^2$ ) were sampled with the Hobby-Eberly Telescope Dark Energy Experiment (HETDEX; Gebhardt et al. 2021) spectroscopic survey, which targeted the north galactic cap.

### 1.3.1 The Lyman- $\alpha$ emission

The Ly $\alpha$  emission used to detect high-redshift galaxies is (intrinsically) the most luminous and most probable emission from a recombining hydrogen atom (68% probability assuming case B recombination; see below; Dijkstra 2014).

In quantum mechanics, the only stable state in the hydrogen atom is the fundamental level. Every electron in a higher energy state (with principal quantum number,  $n$ , and angular momentum quantum number,  $l$ ) will eventually migrate to lower energy levels, radiating photons and causing cascades. The photon emitted when an electron falls from the first excited state ( $n = 2$ ) to the fundamental one ( $n = 1$ ) is the Ly $\alpha$  photon (see left panel of Fig. 1.5). The energy difference between these levels is 10.2 eV, which dictates the energy of the photon. This transition has a wavelength of  $1215.67 \text{ \AA}$ , which falls in the ultraviolet (UV) part of the electromagnetic spectrum but is shifted into the optical at  $z \approx 3$ . This makes the Ly $\alpha$  line ideal to be detected with ground observations. Any other emission line produced from the migration of an electron from a higher

energy level ( $n > 2$ ) to the ground state also belongs to the Lyman series, named after their discoverer, Theodore Lyman in 1906.

Electrons that populate excited states of the hydrogen atom (responsible for the production of Ly $\alpha$  photons) are the result of an interaction with ionizing photons emitted by young and massive stars (O- and B-type stars) in star-forming regions of galaxies. A significant fraction of photons from these star-forming regions falls in the UV range of the electromagnetic spectrum and those with high energies<sup>5</sup> ( $\lambda < 912 \text{ \AA}$ ) ionize neutral hydrogen atoms in the interstellar medium of galaxies, forming HII regions (or star-forming regions). See the right panel of Fig. 1.5 for an artistic representation of this process.

Within the framework of quantum mechanics, there are two possibilities for an electron to populate an excited state in the hydrogen atom. The first possibility is the interaction between a free electron and the hydrogen atom (e.g., collision), where the free electron transfers part of its kinetic energy to a bounded electron and this shifts to a more energetic state, producing a cascade of photons (i.e., radiative cooling). The second possibility occurs when a proton captures a free electron and one photon is emitted (i.e., recombination). The latter is the main mechanism by which galaxies produce Ly $\alpha$  photons. There are two assumed scenarios for recombination (Baker & Menzel, 1938):

- Case A: The surrounding of the star for-

<sup>5</sup>The energy of the ionizing photons depends on the temperature of the star, which is determined by its mass. Because massive stars emit high-energy ionizing photons but have short lifetimes, they are mainly found in star-forming regions.

mation region is optically thin. The ionizing photons can thus escape the region. Free electrons can be captured in any level of a hydrogen atom, which emits another ionizing photon. The direct bind to the fundamental level is known as direct recombination to the ground state.

- Case B: The surrounding of the star formation region is optically thick. Ionizing photons are immediately absorbed (i.e., photoionization) by a nearby neutral hydrogen atom, which then emits an electron. This new free electron will eventually recombine with a proton, which can result in a cascade. Through this cascade, even the higher Lyman series photons will end up being transformed into Ly $\alpha$ .

Some of these Ly $\alpha$  photons escape the galaxy, others interact with dust grains and get absorbed and others interact with neutral hydrogen (HI). Each of these interactions can trigger a cascade and contribute to the diffuse Ly $\alpha$  emission observed around LAEs.

### 1.3.2 Lyman- $\alpha$ gaseous halos

The Ly $\alpha$  photons that are produced by the physical processes described above continue their journey through the interstellar, circumgalactic and intergalactic media (ISM, CGM, IGM). The long path that Ly $\alpha$  photons may travel increases the possibility that this emission gets either powered by physical processes (and eventually escapes the LAE; see below) or absorbed by dust grains (and therefore destroyed).

Due to the large scattering cross section of Ly $\alpha$  photons and neutral hydrogen, these undergo radiative transfer processes in which they constantly scatter. This cross section depends on the frequency but, close to the Ly $\alpha$  wavelength, can be as high as  $\approx 10^{-12} \text{ cm}^{-2}$ . The Ly $\alpha$  photon path is thus regulated by the distribution of hydrogen, which makes the observed Ly $\alpha$  luminosity a function of HI distribution, optical depth, dust content, etc.

During resonant scatterings, a hydrogen atom captures the Ly $\alpha$  photon, which excites the bounded electron to a higher energy level and subsequently migrates to the fundamental state, emitting another Ly $\alpha$  photon in a different direction. Besides modifying the photon direction, scattering can also propagate Ly $\alpha$  photons over

potentially large distances. This, among other factors, causes the Ly $\alpha$  emission to become diffuse (also the additional FoG effect described in Sect. 1.2.2), giving rise to the so-called extended Ly $\alpha$  halos (LAHs).

Local star formation regions are not only responsible for the emission of Ly $\alpha$  photons inside the LAE itself, but also for "in situ" recombinations. While Ly $\alpha$  photons produced within LAEs can scatter into the CGM (see a. in Fig. 5.2.3), "in situ" recombination refers to the ionizing photons that escape the galaxy and get converted into Ly $\alpha$  photons in the CGM. External processes such as fluorescence by the metagalactic UV background (see d. in Fig. 5.2.3) and gravitational cooling (see b. in Fig. 5.2.3) produce de-excitations to lower energy levels and collisional excitation from cooling gas accreted onto galaxies, respectively. All these physical processes can also power the Ly $\alpha$  emission, contributing thus to the extended LAHs.

Despite the complexity of these processes, there is a plethora of Ly $\alpha$  radiative transfer codes coupled to state-of-the-art simulations. Within this field, Ly $\alpha$  photons can be traced back to their origin, which is then used to assess the contribution from the various physical processes to the extended LAHs. Simulation studies (Shimizu & Umemura, 2010; Lake et al., 2015; Mas-Ribas & Dijkstra, 2016; Mas-Ribas et al., 2017; Mitchell et al., 2021; Byrohl et al., 2021) showed that there is another significant contribution to the LAHs: the Ly $\alpha$  emission originating in faint satellite galaxies (see c. in Fig. 5.2.3). This emission would be significant only by its collective effect, as most of these satellite LAEs are too faint to be detected individually at the sensitivity of current observations.

Although their origin is still under investigation and may also depend on environment, detections of LAHs are numerous. LAHs are commonly measured from a (pseudo-)NB image of the galaxy of interest. It is customary to place annuli of different radii around the center of the galaxy and quantify the surface brightness (SB) within them. We then obtain a SB profile (SB as a function of radius), which we compare to the expectations from a point source.

Narrowband imaging observations (Hayashino et al., 2004; Nilsson et al., 2009; Finkelstein et al., 2011) detected LAHs with SB levels of  $\sim 10^{-18} \text{ erg s}^{-1} \text{ cm}^{-2} \text{ arcsec}^{-2}$ . Stacks of the same type of observations



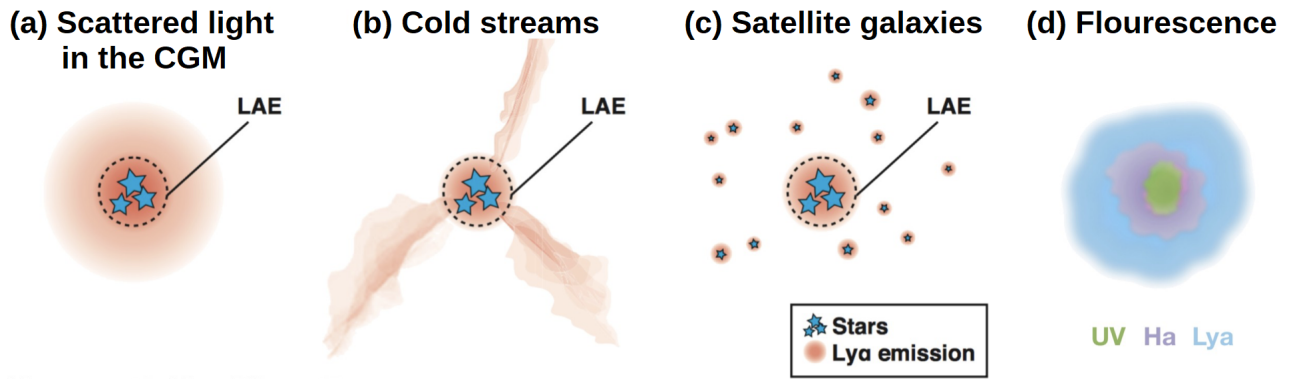


**Figure 1.6:** Illustration of four possible origins of the LAHs: a) resonant scattering into the CGM, b) gravitational cooling, c) faint satellite LAEs, and d) fluorescence represented by a more spatially extended  $H\alpha$  emission (violet) than continuum emission (green). Blue stars represent star-forming regions. Red shaded regions denote ISM and CGM gas. Dotted circles show the central regions of the LAE. The process of "in situ" recombination is not shown here. Image adapted from Momose et al. (2014b) and Mas-Ribas et al. (2017).

(Steidel et al., 2011; Matsuda et al., 2012; Momose et al., 2014a; Xue et al., 2017) extended that SB threshold by an order of magnitude,  $SB \sim 10^{-19} \text{ erg s}^{-1} \text{ cm}^{-2} \text{ arcsec}^{-2}$ . A major step forward in terms of sensitivity was achieved by employing spectroscopic instruments. MUSE evened the limiting SB of individual object-by-object measurements to the limits obtained by the stacking of NB data (Wisotzki et al., 2016; Leclercq et al., 2017; Kusakabe et al., 2018; Claeysens et al., 2022). Another breakthrough was the combination of stacking experiments and spectroscopic data, both with MUSE (Wisotzki et al., 2018) and HETDEX (Niemeyer et al., 2022).

LAHs detected with MUSE at  $3 < z < 6$  are ubiquitous and a factor 4 – 20 more extended than their corresponding UV galaxy sizes, presenting median scale lengths of few physical kpc (pkpc; Wisotzki et al. 2016; Leclercq et al. 2017; Claeysens et al. 2022; Kusakabe et al. 2022). While Wisotzki et al., 2018 measured extended LAHs with MUSE up to  $\approx 60$  pkpc at  $z = 3$ , recent works with HETDEX LAEs at  $1.9 < z < 3.5$  and Subaru LAEs at  $z = 2.2 - 2.3$  extended those scales to 160 pkpc and 200 pkpc, respectively (Niemeyer et al., 2022; Zhang et al., 2023).

### 1.3.3 Large-scale structure traced by Lyman- $\alpha$ emitters

Despite the complexity of the radiative transfer processes that the  $Ly\alpha$  emission undergoes, LAEs have been used to trace the large-scale structure of the high-redshift universe. Because of the sparseness of large spectroscopic samples

of LAEs, most studies investigated the clustering properties of LAEs with angular correlation functions (based on NB detections). Gawiser et al. (2007), Kovac et al. (2007), Shioya et al. (2009), and Ouchi et al. (2010) detected clustering signals from relatively small samples of LAEs at  $z \approx 3.1, 4.86, 6.6$ . They then fitted those signals with power law correlation functions to derive correlation lengths of  $r_0 \approx 2 - 5 h^{-1} \text{ Mpc}$  and large-scale bias factors of  $b = 3 - 6$ . Only one pilot study (Diener et al., 2017) investigated the clustering of spectroscopically detected MUSE LAEs at  $3 < z < 6$  and confirmed previous clustering signals and correlation lengths. Considerably larger samples of NB-selected LAEs found consistent results and derived typical DMH masses of  $M_h \approx 10^{11} h^{-1} M_\odot$  (Bielby et al., 2016).

Relying on angular correlations and power law fits, Ouchi et al. (2003) and Kusakabe et al. (2018) found a weak trend with  $Ly\alpha$  luminosity, where more luminous LAEs seemed to cluster more strongly than less luminous ones. Significant correlations were only reported by Khostovan et al. (2019), who observed a redshift-independent positive correlation between clustering strength and  $Ly\alpha$  luminosity, UV luminosity, and UV star formation rate in a sample of  $\sim 5000$  LAEs detected with various NB filters with discrete redshift slices within  $z \approx 2.5 - 6$ . They also found a clear clustering strength increase with increasing redshift.

There was only one study that modelled the clustering signal of a sample of NB-selected LAEs at  $z = 5.7, 6.6$  with HOD models. Ouchi et al., 2017 partially exploited the power of HOD modelling to infer the threshold DMH mass for cen-

tral galaxies ( $\log(M_{\min}/[M_{\odot}]) \approx 9.5$ ). Due to the limiting statistics, the rest of the HOD parameters were kept fixed based on assumptions.

## 1.4 This thesis

In this thesis I present results from four observational projects in the general framework of dark – baryonic matter relation, large-scale structure of the high-redshift universe traced by LAEs, its properties and their extended LAHs. Here, I provide an overview of the contents addressed in the individual chapters.

In Chapter 2, I optimize the method (the K-estimator from Adelberger et al. 2005) to study galaxy clustering in pencil-beam surveys (such as those yielded by MUSE) and study the clustering properties of a sample of LAEs from the MUSE-Wide survey (the largest MUSE dataset). I constrain correlation lengths and slopes, large-scale bias factors, and typical DMH masses. I support our results with the well-known 2pcf, measuring, for the first time, the spatial clustering of a spectroscopic sample of Ly $\alpha$ -selected galaxies. I then explore possible clustering dependencies on LAE properties and predict the fate of MUSE-Wide-like DMHs by  $z = 0$ . I also measure the clustering in a dark-matter-only cosmological simulation coupled to a semi-analytical model of LAEs and compare the outcome to our results.

In Chapter 3, I include the deeper MUSE surveys (MUSE-Deep and the MUSE Extremely Deep Field, MXDF) to connect the clustering properties of  $L^*$  LAEs with those of much fainter ones in the MXDF, now within the HOD modelling framework. I thus constrain the threshold DMH masses needed to host central and satellite LAEs, satellite fractions, and the HODs for LAEs of various Ly $\alpha$  luminosities ( $L_{\text{Ly}\alpha}$ ). I exploit the large dynamic range of  $L_{\text{Ly}\alpha}$  from the different surveys and investigate how the HOD parameters, large-scale bias factors and typical DMH masses vary with  $L_{\text{Ly}\alpha}$ . I discuss the implications of the clustering dependence on  $L_{\text{Ly}\alpha}$  in terms of evolving Ly $\alpha$  luminosity functions, detections of incomplete reionization at  $z \approx 6$ , and the relation between Ly $\alpha$  escape fraction and DMH mass.

In Chapter 4, I use the clustering dependence on  $L_{\text{Ly}\alpha}$  found in Chapter 3 to investigate the much debated relevance of undetected LAEs (fainter than those in the to-date deepest ever spectroscopic survey namely, the MXDF) for the

observed extended LAHs around LAEs. For the first time, I address this matter from an observational angle. I consider various clustering scenarios for the faint LAEs and make assumptions about the Ly $\alpha$  luminosity function. I then build expected Ly $\alpha$  SB profiles from clustered and individually undetected LAEs. I compare these profiles to those from stacked experiments of pseudo-NB images of MUSE LAEs and constrain the contribution of undetected LAEs to the total stacked Ly $\alpha$  SB profiles. I also compare our faint LAE radial profiles to those predicted from recent simulation studies. I outline possible future measurements to further constrain the impact of discrete undetected LAEs on observed LAHs.

In Chapter 5, I investigate whether the properties of LAHs are affected by environment. I apply different methods to consider distinct definitions of overdense region and compute the local overdensity of the LAEs in MUSE deep fields. I use their available LAH properties and study their possible variation with LAE overdensity.

The last chapter contains a final summary and discussion of the whole thesis and provides an outlook on future perspectives.

Chapters 2, 3, 4 are versions of publications that have recently appeared in *Astronomy & Astrophysics* (Herrero Alonso et al., 2021; Herrero Alonso et al., 2023a; Herrero Alonso et al., 2023b). Chapter 5 is a draft version of an upcoming publication. Each of these chapters includes a dedicated introduction that summarizes the state of research in the field and a separate conclusion, summing up the results of the individual chapter. For clarity, I also chose to give bibliographies at the end of each chapter.

## References

- Acquaviva, V., Gawiser, E., & Guaita, L., (2011), *ApJ*, 737, 47
- Adelberger, K. L., Steidel, C. C., Pettini, M., et al., (2005), *ApJ*, 558, A33
- Bacon, R., Accardo, M., Adjali, L., et al., (2010), *Proc. SPIE*, 7735, 773508
- Baker, J. G., & Menzel, D. H., (1938), *ApJ*, 88, 52
- Baugh, C., (1996), *MNRAS*, 280, 275
- Behroozi, P. S., Conroy, C., Wechsler, R. H., et al., (2010), *ApJ*, 717, 403
- Benson, A. J., Cole, S., Frenk, C. S., et al., (2000), *MNRAS*, 311, 793

- Berlind, A. A., & Weinberg, D. H., (2002), *ApJ*, 575, 587
- Bielby, R. M., Tummungpak, P., Shanks, T., et al., (2016), *MNRAS*, 456, 4061
- Blumenthal, G. R., Faber, S. M., Flores, R., et al., (2016), *ApJ*, 1986, 27
- Byrohl, C., Nelson, D., Behrens, C., et al., (2021), *MNRAS*, 506, 5129
- Byrohl, C., Saito, S., & Behrens, C., (2019), *MNRAS*, 489, 3472
- Claeysens, A., Richard, J., Blaizot, J., et al., (2022), *A&A*, 666, 22
- Coil, A. L., Blanton, M. R., Burles, S. M., et al., (2011), *ApJ*, 741, 8
- Coil, A. L., Georgakakis, A., Newman, J. A., et al., (2012), 6, *Planets, Stars and Stellar Systems* (Springer, Dordrecht)
- Coil, A. L., Mendez, A. J., Eisenstein, D. J., et al., (2017), *ApJ*, 838, 87
- Coil, A. L., Newman, J. A., Cooper, M. C., et al., (2006), *ApJ*, 644, 671
- Coil, A. L., Newman, J. A., Croton, D., et al., (2008), *ApJ*, 672, 153
- Colless, M., Dalton, G., Maddox, S., et al., (2001), *MNRAS*, 328, 1039
- Contreras, S., & Zehavi, I., (2023), *MNRAS*, arxiv, arxiv
- Cowie, L. L., & M., H. E., (1998), *ApJ*, 115, 1319
- Davis, M., & Peebles, P. J. E., (1983), *ApJ*, 267, 465
- Diener, C., Wisotzki, L., Schmidt, K. B., et al., (2017), *MNRAS*, 471, 3186
- Dijkstra, M., (2014), *PASA*, 31, e040
- Durkalec, A., Le Fèvre, O., Pollo, A., et al., (2018), *A&A*, 612, A42
- Eisenstein, D. J., Willott, C., Albers, S., et al., (2023), arXiv:2306.02465
- Finkelstein, S. L., Cohen, S. H., Windhorst, R. A., et al., (2011), *ApJ*, 735, 5
- Fry, J. N., (1996), *ApJ*, 461, L65
- Furusawa, H., Kosugi, G., Akiyama, M., et al., (2008), *ApJS*, 176, 1
- Gawiser, E., Francke, H., Lai, K., et al., (2007), *ApJ*, 671, 278
- Gebhardt, K., Cooper, E. M., Ciardullo, R., et al., (2021), *ApJ*, 923, 217
- Gurung-López, S., (2019), PhD thesis
- Guzzo, L., Scodreggio, M., Garilli, B., et al., (2014), *A&A*, 566, A108
- Hayashino, T., Matsuda, Y., Tamura, H., et al., (2004), *AJ*, 128, 2073
- Herrero Alonso, Y., Krumpel, M., Wisotzki, L., et al., (2021), *A&A*, 653, A136
- Herrero Alonso, Y., Miyaji, T., Wisotzki, L., et al., (2023a), *A&A*, 671, A5
- Herrero Alonso, Y., Wisotzki, L., Miyaji, T., et al., (2023b), *A&A*, arxiv:2308.05105
- Hubble, E., (1934), *ApJ*, 79, 8
- Inami, H., Bacon, R., Brinchmann, J., et al., (2017), *A&A*, 608, 26
- Kaiser, N., (1984), *ApJL*, 284, L9
- Kaiser, N., (1987), *MNRAS*, 227, 1
- Karman, W., Caputi, K. I., Caminha, G. B., et al., (2017), *A&A*, 599, A28
- Khostovan, A. A., Sobral, D., Mobasher, B., et al., (2018), *MNRAS*, 478, 2999
- Khostovan, A. A., Sobral, D., Mobasher, B., et al., (2019), *MNRAS*, 489, 555
- Kovac, K., Somerville, R. S., Rhoads, J. E., et al., (2007), *ApJ*, 668, 15
- Kusakabe, H., Shimasaku, K., Ouchi, M., et al., (2018), *PASJ*, 70, 4
- Kusakabe, H., Verhamme, A., Blaizot, J., et al., (2022), *A&A*, 660, A44
- Lake, E., Zheng, Z., Cen, R., et al., (2015), *ApJ*, 806, 46
- Landy, S. D., & Szalay, A. S., (1993), *ApJ*, 412, 64
- Leclercq, F., Bacon, R., Wisotzki, L., et al., (2017), *A&A*, 608, A8
- Li, C., Kauffmann, G., Jing, Y., et al., (2006), *MNRAS*, 368, 21
- Lilly, S. J., Le Fèvre, O., Renzini, A., et al., (2007), *ApJS*, 172, 70
- Madgwick, D. S., Hawkins, E., Lahav, O., et al., (2003), *MNRAS*, 344, 847
- Malkan, M. A., Cohen, D. P., Maruyama, M., et al., (2017), *ApJ*, 850, 5
- Marulli, F., Bolzonella, M., Branchini, E., et al., (2013), *A&A*, 557, A17
- Mas-Ribas, L., & Dijkstra, M., (2016), *ApJ*, 822, 84
- Mas-Ribas, L., Dijkstra, M., Hennawi, J. F., et al., (2017), *ApJ*, 841, 19
- Matsuda, Y., Yamada, T., Hayashino, T., et al., (2012), *MNRAS*, 425, 878
- Meneux, B., Guzzo, L., de la Torre, S., et al., (2009), *A&A*, 505, 463
- Mitchell, P., Blaizot, J., Cadiou, C., et al., (2021), *MNRAS*, 501, 5757
- Mo, H. J., & White, S. D. M., (1996), *MNRAS*, 282, 347
- Momose, R., Ouchi, M., Nakajima, K., et al., (2014a), *MNRAS*, 442, 110
- Momose, R., Ouchi, M., Nakajima, K., et al., (2014b), *MNRAS*, 457, 2318
- Mosteck, N., Coil, A. L., Michael, C. C., et al., (2013), *ApJ*, 767, 89

- Navarro, J. F., Frenk, C. S., & White, S. D. M., (1997), *ApJ*, 490, 493
- Newman, J. A., Cooper, M. C., Davis, M., et al., (2013), *ApJSS*, 208, 5
- Niemeyer, M. L., Komatsu, E., Byrohl, C., et al., (2022), *ApJ*, 929, 90
- Nilsson, K. K., Tapken, C., Moeller, P., et al., (2009), *A&A*, 498, 13
- Norberg, P., Baugh, C. M., Hawkins, E., et al., (2001), *MNRAS*, 328, 64
- Norberg, P., Baugh, C. M., Hawkins, E., et al., (2002), *MNRAS*, 332, 827
- Ouchi, M., Harikane, Y., Shibuya, T., et al., (2017), *PASJ*, 70, S13
- Ouchi, M., Ono, Y., & Shibuya, T., (2021), *ARAA*, 58, 617
- Ouchi, M., Shimasaku, K., Furusawa, H., et al., (2003), *ApJ*, 582, 60
- Ouchi, M., Shimasaku, K., Furusawa, H., et al., (2010), *ApJ*, 723, 869
- Partridge, R. B., & Peebles, P. J. E., (1967), *ApJ*, 147, 868
- Peebles, P. J. E., (1980), Princeton, N.J., Princeton Univ. Press
- Peebles, P. J. E., & Hauser, M. G., (1974), *ApJSS*, 28, 19
- PlanckCollaboration, (2016), *AAP*, 594, A13
- Press, W., & Schechter, P., (1974), *ApJ*, 187, 425
- Rhoads, J. E., Malhotra, S., Dey, A., et al., (2000), *ApJ*, 545, L85
- Shapley, H., & Ames, A., (1932), *AHCO*, 88, 41
- Sheth, R., Mo, H. J., & Tormen, G., (2001), *MNRAS*, 323, 1
- Shi, F., Yang, X., Wang, H., et al., (2016), *ApJ*, 833, 241
- Shimizu, I., & Umemura, M., (2010), *MNRAS*, 406, 913
- Shioya, Y., Taniguchi, Y., Sasaki, S. S., et al., (2009), *ApJ*, 696, 546
- Sobral, D., Best, P. N., Geach, J. E., et al., (2009), *MNRAS*, 398, 75
- Sobral, D., Best, P. N., Geach, J. E., et al., (2010), *MNRAS*, 404, 1551
- Sobral, D., Matthee, J., Best, P., et al., (2017), *MNRAS*, 466, 1242
- Springel, V., Frenk, C. S., & White, S. D. M., (2006), *Nature*, 440, 1137
- Springel, V., White, S. D. M., Jenkins, A., et al., (2005), *Nature*, 435, 629
- Steidel, C. C., Bogosavljevic, M., Shapley, A. E., et al., (2011), *ApJ*, 736, 160
- Steidel, C. C., Giavalisco, M., Pettini, M., et al., (1996), *ApJ*, 462, L17
- Strauss, M. A., Weinberg, D. H., Lupton, R. H., et al., (2002), *AJ*, 124, 1810
- Tasca, L. M. A., Le Fevre, O., Ribeiro, B., et al., (2017), *A&A*, 600, A110
- Urrutia, T., Wisotzki, L., Kerutt, J., et al., (2019), *A&A*, 624, 24
- Wechsler, R. H., & Tinker, J. L., (2018), *ARAA*, 56, 435
- White, S. D. M., & Frenk, C. S., (1991), *ApJ*, 379, 52
- White, S. D. M., & Rees, M. J., (1978), *MNRAS*, 183, 341
- Wisotzki, L., Bacon, R., Blaizot, J., et al., (2016), *A&A*, 587, A98
- Wisotzki, L., Bacon, R., Brinchmann, J., et al., (2018), *Nature*, 562, 229
- Wyithe, J. S. B., & Dijkstra, M., (2011), *MNRAS*, 415, 3929
- Xue, R., Lee, K. S., Dey, A., et al., (2017), *ApJ*, 837, 172
- Yang, X., Mo, H. J., Jing, Y. P., et al., (2005a), *MNRAS*, 358, 217
- Yuma, S., Ohta, K., Yabe, K., et al., (2010), *ApJ*, 720, 1016
- Zehavi, I., Blanton, M. R., Frieman, J. A., et al., (2002), *ApJ*, 571, 172
- Zehavi, I., Zheng, Z., Weinberg, D., et al., (2011), *ApJ*, 736, 59
- Zehavi, I., Zheng, Z., Weinberg, D. H., et al., (2005), *ApJ*, 630, 1
- Zel'dovich, Y. B., (1970), *A&A*, 5, 84
- Zhang, H., Cai, Z., Liang, Y., et al., (2023), [arxiv:2301.07358](https://arxiv.org/abs/2301.07358)
- Zheng, Z., Cen, R., & Trac, H., (2011a), *ApJ*, 726, 38
- Zheng, Z., Coil, A., & Zehavi, I., (2007), *ApJ*, 667, 760

## The MUSE-Wide survey: Three-dimensional clustering analysis of Lyman- $\alpha$ emitters at $3.3 < z < 6^*$

Y. Herrero Alonso<sup>1</sup>, M. Krumpel<sup>1</sup>, L. Wisotzki<sup>1</sup>, T. Miyaji<sup>2</sup>, T. Garel<sup>3</sup>, K. B. Schmidt<sup>1</sup>, C. Diener<sup>4</sup>, T. Urrutia<sup>1</sup>, J. Kerutt<sup>3</sup>, E. C. Herenz<sup>5</sup>, J. Schaye<sup>6</sup>, G. Pezzulli<sup>7</sup>, M. V. Maseda<sup>8</sup>, L. Boogaard<sup>6</sup>, and J. Richard<sup>9</sup>

<sup>1</sup> Leibniz-Institut für Astrophysik Potsdam (AIP), An der Sternwarte 16, 14482 Potsdam, Germany

<sup>2</sup> Universidad Nacional Autónoma de México, Instituto de Astronomía (IA-UNAM-E), AP 106, Ensenada 22860, BC, Mexico

<sup>3</sup> Observatoire de Genève, Université de Genève, 51 Ch. des Maillettes, 1290 Versoix, Switzerland

<sup>4</sup> Institute of Astronomy, University of Cambridge, Madingley Road, Cambridge CB3 0HA, UK

<sup>5</sup> European Southern Observatory, Av. Alonso de Córdova 3107, 763 0355 Vitacura, Santiago, Chile

<sup>6</sup> Leiden Observatory, Leiden University, PO Box 9513, 2300 RA Leiden, The Netherlands

<sup>7</sup> Department of Physics, ETH Zurich, Wolfgang-Pauli-Strasse 27, 8093 Zurich, Switzerland

<sup>8</sup> Kapteyn Astronomical Institute, University of Groningen, Landleven 12, 9747 AD Groningen, The Netherlands

<sup>9</sup> Univ. Lyon, Univ. Lyon1, ENS de Lyon, CNRS, Centre de Recherche Astrophysique de Lyon UMR 5574, 69230 Saint-Genis-Laval, France

### ABSTRACT

We present an analysis of the spatial clustering of 695 Ly $\alpha$ -emitting galaxies (LAEs) in the MUSE-Wide survey. All objects have spectroscopically confirmed redshifts in the range  $3.3 < z < 6$ . We employed the K-estimator, an alternative clustering statistic, adapted and optimized for our sample. We also explore the standard two-point correlation function (2pcf) approach, which is however less suited for a pencil-beam survey such as ours. The results from both approaches are consistent. We parametrize the clustering properties in two ways, (i) following the standard approach of modelling the clustering signal with a power law (PL), and (ii) adopting a halo occupation distribution (HOD) model of the two-halo term. Using the K-estimator and applying HOD modelling, we infer a large-scale bias of  $b_{\text{HOD}} = 2.80^{+0.38}_{-0.38}$  at a median redshift of the number of galaxy pairs  $\langle z_{\text{pair}} \rangle \simeq 3.82$ , while the best-fit power-law analysis gives  $b_{\text{PL}} = 3.03^{+1.51}_{-0.52}$  ( $r_0 = 3.60^{+3.10}_{-0.90}$  comoving  $h^{-1}\text{Mpc}$  and  $\gamma = 1.30^{+0.36}_{-0.45}$ ). The implied typical dark matter halo (DMH) mass is  $\log(M_{\text{h}}/[h^{-1}M_{\odot}]) = 11.34^{+0.23}_{-0.27}$  (adopting  $b = b_{\text{HOD}}$  and assuming  $\sigma_8 = 0.8$ ). We study possible dependencies of the clustering signal on object properties by bisecting the sample into disjoint subsets, considering Ly $\alpha$  luminosity, UV absolute magnitude, Ly $\alpha$  equivalent width, and redshift as variables. We find no evidence for a strong dependence on the latter three variables but detect a suggestive trend of more luminous Ly $\alpha$  emitters clustering more strongly (thus residing in more massive DMHs) than their lower Ly $\alpha$  luminosity counterparts. We also compare our results to mock LAE catalogs based on a semi-analytic model of galaxy formation and find a stronger clustering signal than in our observed sample, driven by spikes in the simulated  $z$ -distributions. By adopting a galaxy-conserving model we estimate that the Ly $\alpha$ -bright galaxies in the MUSE-Wide survey will typically evolve into galaxies hosted by halos of  $\log(M_{\text{h}}/[h^{-1}M_{\odot}]) \approx 13.5$  at redshift zero, suggesting that we observe the ancestors of present-day galaxy groups.

\*A version of this chapter is published in *Astronomy & Astrophysics* as Herrero Alonso et al. 2021, Volume 653, A136.

## 2.1 Introduction

The distribution of galaxies in the Universe forms a well defined network known as the cosmic web. This structure was formed when gravitational instabilities produced by primordial density fluctuations grew until they reached a critical density. Their collapse formed gravitationally bound dark matter halos (DMHs). These halos grow hierarchically through accretion and mergers with other halos. Their gravitational interaction with baryonic matter caused gas to fall into the growing potential wells, making the gas cool by radiation and collapse to form stars and galaxies.

The evolution of the baryonic matter distribution follows the underlying dark matter (DM) but, especially in the early stages of galaxy formation, the details of this relation and how it evolved over time are still unclear. Galaxy clustering analyses aim to constrain the masses of the typical DMHs by which these galaxies are hosted and are therefore a crucial element towards understanding the formation and evolution of galaxies (Coil et al., 2012).

A common way to quantify galaxy clustering is through correlation functions (e.g. Gawiser et al., 2007; Zehavi et al., 2011; Ouchi et al., 2017), which express the probability of finding a tuple (usually a pair) of galaxies at a certain separation (e.g. Peebles, 1980). The clustering strength (large-scale bias) and the typical DMH masses can be inferred from measured correlation functions in various ways. A widespread traditional approach is to approximate the two-point correlation function (2pcf) as a power law (Davis & Peebles, 1983), while more recent methods such as halo occupation distribution (HOD) modelling (e.g. Zheng & Weinberg, 2007) distinguish between the different contribution of the correlation function. In these models, pairs of galaxies either belong to the same DMH or to different DMHs.

These procedures have often been applied to galaxy surveys. At low redshifts, the major surveys cover large areas of the sky, in particular SDSS (e.g. Strauss et al., 2002; Ahumada et al., 2020) along with its successors, 2MASS (Skrutskie et al., 2006), or the 2dF Galaxy Redshift survey (Colless et al., 2001). These samples at similar luminosities revealed a modest evolution of the clustering strength between  $z = 1$  and  $z = 0$  together with significant clustering dependencies on various galaxy properties, such as luminosity,

color, morphology, galaxy type, etc. (e.g. Norberg et al., 2002; Zehavi et al., 2002; Li et al., 2006; Zehavi et al., 2011).

At high redshifts ( $z > 2$ ), galaxy samples are more limited, however. Gathering a statistically relevant number of objects and covering representative volumes of the sky is a difficult task. Photometric selection techniques are often preferred because spectroscopic observations of many faint objects are observationally too expensive. The two most common techniques involve exploiting the drop in the continuum bluewards of  $912 \text{ \AA}$  (Steidel & Hamilton, 1992) to search for Lyman-break galaxies (LBGs) and the use of narrow-band (NB) filters to target, for instance, the Ly $\alpha$  emission line of young, star-forming galaxies (Ly $\alpha$  emitters, LAEs).

While each selection method provides us with its own somewhat biased view of the distribution of galaxies, LAEs are particularly interesting with regard to probing the lower range of stellar masses ( $10^8 - 10^9 M_{\odot}$ ), highlighting a subset of galaxies of copiously forming stars (star formation rates of  $1 - 10 M_{\odot} \text{ yr}^{-1}$ ). By combining the clustering analysis of LAEs with cosmological simulations, we can connect LAEs to their descendants in the local Universe.

Statistically substantial LAE samples ( $> 10^2$  objects) based on narrow-band surveys were presented by Cowie & M. (1998), Rhoads et al. (2000), Ouchi et al. (2003), Gawiser et al. (2007), Ouchi et al. (2017), and Sobral et al. (2017) and others. Generally, the NB selection method only provides LAE candidates implying that samples are contaminated by interlopers, which can be a problem for clustering studies. Obviously, since all objects selected by a given NB filter are assumed to be at the same redshift, their clustering can only be explored through the analysis of transverse angular correlations (Ouchi et al., 2003; Gawiser et al., 2007; Ouchi et al., 2010; Ouchi et al., 2017; Khostovan et al., 2019). In order to study the full three-dimensional (3D) spatial clustering behaviour of galaxies and its evolution over cosmic time, large-scale spectroscopic surveys of high-redshift galaxies with individually measured redshifts are required (Le Fèvre et al., 2005; Lilly et al., 2007; Newman et al., 2013; Guzzo et al., 2014; Le Fèvre et al., 2015). It has been found that the clustering strength of high-redshift galaxies is significantly higher at similar luminosities than at intermediate and low redshifts (Durkalec et al., 2014), possibly also

depending on luminosity and stellar mass (e.g. Ouchi et al., 2003; Ouchi et al., 2017; Durkalec et al., 2018).

Ideally, it would be optimal to perform spectroscopy of all existing objects over a large area of the sky, with a wide redshift coverage. While such surveys are still beyond our current means, panoramic integral field units (IFUs) are currently opening up an avenue for exploring this approach, at least over modest areas. In particular, the Multi Unit Spectroscopic Explorer (MUSE, Bacon et al., 2010) on the ESO-VLT has already produced significant samples of high-redshift galaxies with unprecedented source densities of several tens or even hundreds of objects per arcmin<sup>2</sup> (Inami et al., 2017; Urrutia et al., 2019). In this paper we explore the potential of using  $\approx 700$  LAEs selected from the MUSE-Wide survey (Herenz et al., 2017; Urrutia et al., 2019) for clustering studies. Our sample differs from previous studies of LAE clustering based on narrow-band imaging, but also from generic spectroscopic surveys requiring the preselection of targets from broad-band photometry.

In a pilot study, Diener et al. (2017) used 238 LAEs from the first 24 MUSE-Wide fields to demonstrate that MUSE-selected LAEs do indeed reveal a significant clustering signal, even though the uncertainties were still large. Here, we extend this work with a larger (threefold) sample and a refined set of analysis methods and tools. The paper is structured as follows. First, we briefly describe the data used for this work and characterize the sample. In Sect. 5.3, we explain our methods for measuring and analysing the clustering properties of our LAE sample. In Sect. 5.4, we present the results of our measurements, including a study of clustering dependencies with different galaxy parameters. In Sect. 5.5, we discuss our results and compare our findings to predictions from a semi-analytic galaxy formation model. In Sect. 5.6, we present our conclusions. The Appendix of the paper is mainly dedicated to a discussion of the LAE clustering results, using the traditional two-point correlation function.

Throughout the paper, all distances are measured in comoving coordinates and given in units of  $h^{-1}\text{Mpc}$  (unless otherwise stated), where  $h = H_0/100$ . We use a  $\Lambda\text{CDM}$  cosmology and adopt  $\Omega_M = 0.3$ ,  $\Omega_\Lambda = 0.7$ , and  $\sigma_8 = 0.8$  (Hinshaw et al., 2013). All uncertainties represent  $1\sigma$  (68.3%) confidence intervals.

## 2.2 Data

### 2.2.1 The MUSE-Wide survey

MUSE-Wide is an untargeted 3D spectroscopic survey (Herenz et al., 2017; Urrutia et al., 2019) executed by the MUSE consortium as one of the Guaranteed Time Observations (GTO) programs. The survey covers parts of the CANDELS/GOODS-S and CANDELS/COSMOS fields and also includes eight MUSE pointings in the so-called HUDF09 parallel fields (see Urrutia et al. 2019 for details). The spectroscopic data provided by MUSE complement the rich multiwavelength data available in these fields, from which physical properties such as star formation rates or stellar masses can be derived. The full survey comprises 100 MUSE fields of 1 arcmin<sup>2</sup> each (although there is some overlap between adjacent fields), with a depth of 1 hour exposure time, each split into  $4 \times 900$  s with 90 deg rotation between the exposures. Most fields were observed in dark time, with a seeing better than 1.0 arcsec. The spectra cover the range of 4750–9350 Å, implying a Ly $\alpha$  redshift range of  $2.9 < z < 6.7$ .

The data reduction process we used is detailed in Urrutia et al. (2019). Emission line sources were detected and their line fluxes were measured with the Line Source Detection and Cataloguing (LSDCat, Herenz & Wisotzki, 2017) software. LSDCat cross-correlates a reduced and flux-calibrated data cube with a 3D source template to find emission line sources above a given significance threshold. The resulting emission line flux limit of the survey is typically around  $\sim 10^{-17}$  erg s<sup>-1</sup> cm<sup>-2</sup> for LAEs, but with considerable spread between fields and also depending on the spatial extent of the Ly $\alpha$  emission (Herenz et al., 2019).

After the automatic detection of emission lines, a source catalog for each field was produced through visual inspection using the Qt-Classify tool (Kerutt, 2017). After an initial redshift guess of each object from LSDCat, refined redshifts of the LAEs were measured by fitting an asymmetric Gaussian profile to the Ly $\alpha$  emission line. Ly $\alpha$  fluxes were measured using the LSDCat measure functionality, adopting a 3D aperture of three Kron-like radii (Kron, 1980); together with the redshifts, this also provides the Ly $\alpha$  luminosities.

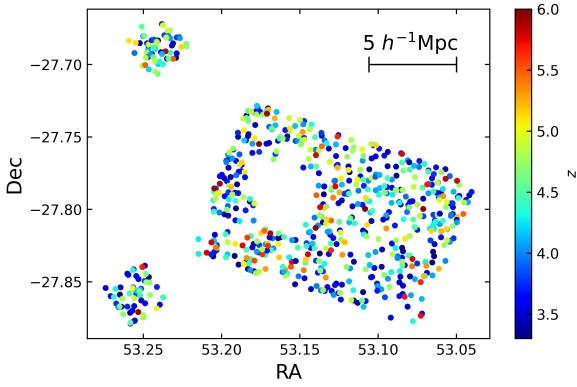


**Figure 2.1:** Spatial distribution of 695 LAEs covering part of the CANDELS/GOODS-S region and the HUDF parallel fields on the left. The individual LAEs span a total of 68 fields from the MUSE-Wide survey and are color-coded by their Ly $\alpha$  spectroscopic redshift,  $3.3 < z < 6$ . The  $5 h^{-1}\text{Mpc}$  bar for the mean redshift of the sample  $\bar{z} \approx 4.23$  indicates the actual transverse extent of the footprint.

Since our sample is based on emission lines without prior broadband selection, it includes galaxies with very faint continua but high equivalent widths – which can sometimes go undetected in deep Hubble Space Telescope (HST) data (Maseda et al., 2018). We identified the UV counterparts for our sample and measure their continuum flux densities and absolute UV magnitudes in various HST bands, as described in detail by Kerutt et al. (in prep.). Our Ly $\alpha$  equivalent widths are based on combining the Ly $\alpha$  fluxes measured by LSDCat and continuum flux measurements from the HST counterparts. In cases where no continuum counterpart was detected, an upper limit to the continuum flux density was used to calculate lower limits to the absolute magnitudes and equivalent widths.

## 2.2.2 LAE sample

In this paper, we focus on 68 fields of the MUSE-Wide survey located in the CANDELS/GOODS-S region, along with the HUDF09 parallel fields. Some of these fields are not yet included in the currently publicly available MUSE-Wide data; these will be part of the planned final data release. We chose to not take into account the nine central fields in the MUSE-Deep area because of their different depth and selection function, in line with our aim to approach (as much as possible) a homogeneous sample and minimize systematic effects. Furthermore, we also discard

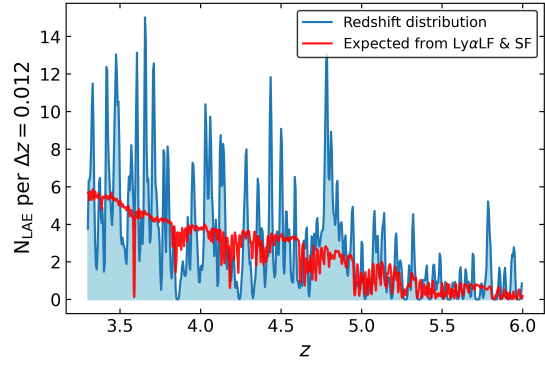


**Figure 2.2:** KDE-filtered redshift distribution of the 695 LAEs of our sample, taken from 68 fields of the MUSE-Wide survey. The sample spans a redshift range of  $3.3 < z < 6$ . The kernel is chosen to be a Gaussian with standard deviation  $\sigma_z = 0.005$ . The expected  $z$ -distribution of an unclustered population following the Ly $\alpha$  luminosity function of Herenz et al. (2019) and the selection function of the MUSE-Wide survey is overlotted in red.

the 23 MUSE-Wide fields in the COSMOS region from this analysis because of their on average somewhat lower data quality. We kept the eight MUSE-Wide pointings in the HUDF09 fields (see Fig. 2.1) since they give additional power to constrain the clustering signal at larger separations. In Appendix 3.A, we demonstrate that including the UDF09 parallel fields has no significant impact on our clustering results despite a minor decrease in the uncertainties.

While MUSE is formally capable of detecting LAES with  $2.91 < z < 6.65$ , we limit the redshift range for this investigation to  $3.3 < z < 6$ , as the details of the selection function at redshifts close to the limits are still a matter of investigation. Thus, we arrive at a final number of 695 LAEs, distributed over  $62.53 \text{ arcmin}^2$  (accounting for small field-to-field overlaps), implying an LAE density of slightly more than 11 objects per  $\text{arcmin}^2$ . The sample has a mean redshift of  $\bar{z} \approx 4.23$ , the median redshift is 4.12. The transverse extent of the footprint at  $\bar{z}$  is  $\sim 20 h^{-1} \text{ Mpc}$ .

The spatial distribution of our LAEs is shown in Fig. 2.1, and the distribution over redshifts is presented in Fig. 2.2. For the latter, we replaced the usual histogram counts-per-bin by a quasi-continuous kernel density estimator (KDE) to better represent the underlying probability distribution and avoid binning artefacts. Superimposed on the KDE-filtered  $z$  distribution, we also show the distribution expected for an unclustered population of objects following the Ly $\alpha$  luminosity function (LF) of Herenz et al. (2019)



**Table 2.1:** Properties of the LAE samples.

LAE sample name	$N_{\text{gal}}$	$\langle z \rangle$	$\log\langle L_{\text{Ly}\alpha}/[\text{erg s}^{-1}] \rangle$	$\langle EW_{\text{Ly}\alpha} \rangle/[\text{\AA}]$	$\langle M_{\text{UV}} \rangle$
Full sample	695	4.12	42.39	118.3	-18.4
Redshift < 4.12	348	3.63	42.31	109.9	-18.4
Redshift > 4.12	347	4.79	42.39	111.8	-18.4
$\log L_{\text{Ly}\alpha} < 42.36$	349	4.03	42.14	110.0	-17.9
$\log L_{\text{Ly}\alpha} > 42.36$	346	4.30	42.57	113.7	-19.0
$EW_{\text{Ly}\alpha} < 87.9$	254	4.03	42.37	53.6	-19.5
$EW_{\text{Ly}\alpha} > 87.9$	255	4.05	42.45	167.3	-18.3
$M_{\text{UV}} < -18.8$	256	4.07	42.57	61.8	-19.6
$M_{\text{UV}} > -18.8$	253	3.92	42.19	168.6	-17.6

**Notes:** Physical properties marked with  $\langle \rangle$  represent median values for the galaxies (not pairs) in the sample.

and also factoring in the selection function of the MUSE-Wide survey. The curve has been normalized to the footprint size of our 68 fields.

While the formal average accuracy of our redshifts is  $\Delta z \simeq 0.0007$  or  $\pm 41$  km/s (limited by the accuracy of fitting the line), it is well-known that Ly $\alpha$  peak redshifts are typically offset by up to several hundreds of km/s from systemic ones (e.g. Hashimoto et al. 2015; Muzahid et al. 2020; Schmidt et al. 2021), which would introduce a systematic error in the redshift-derived 3D positions of the LAEs along the line-of-sight (LOS) of the order of  $\sim 3$  Mpc. We mitigate this systematic uncertainty by applying a correction to the Ly $\alpha$  redshifts following the two recipes described in Verhamme et al. (2018): When the Ly $\alpha$  line presents two peaks with the red peak larger than the blue peak, we apply Eq. (1) from Verhamme et al. (2018). When only a single peak is visible, we employ the correction given by Eq. (2) in Verhamme et al. (2018). We show in Appendix 2.B that our method of measuring the clustering properties is not sensitive to the details of this correction.

The range of Ly $\alpha$  luminosities ( $L_{\text{Ly}\alpha}$ ) of our galaxies is  $40.91 < \log(L_{\text{Ly}\alpha}/[\text{erg s}^{-1}]) < 43.33$ , with a median Ly $\alpha$  luminosity of  $\langle \log(L_{\text{Ly}\alpha}/[\text{erg s}^{-1}]) \rangle = 42.36$ , the range of UV absolute magnitudes is  $-22.4 < M_{\text{UV}} < -16.8$ , with a median of  $\langle M_{\text{UV}} \rangle = -18.4$ , and the range of rest frame equivalent widths is  $10.2 < EW_{\text{Ly}\alpha} < 794.9$   $\text{\AA}$ , with a median of  $\langle EW_{\text{Ly}\alpha} \rangle = 118.3$   $\text{\AA}$ .

### 2.2.3 LAE subsets

In order to explore the dependence of the clustering amplitude on physical properties of LAEs, we

divide the original sample into subsamples based on different available properties. In each case we split the full sample at the median value of the LAE property under question to have (nearly) the same number of objects in each of the two subsets. The subsamples are summarized in Table 2.1 and defined in greater detail in the following.

A first split in redshift around  $\langle z \rangle = 4.12$  leads to a low- $z$  subset of 348 LAEs with median redshift  $\langle z_{\text{low}} \rangle = 3.56$  and a high- $z$  subset of 347 LAEs with  $\langle z_{\text{high}} \rangle = 4.59$ , respectively. The median Ly $\alpha$  luminosities and equivalent widths of the two redshift subsamples are nearly the same (differences of 0.08 dex and 2  $\text{\AA}$ , respectively). There is no difference between the median  $M_{\text{UV}}$ .

In order to explore possible clustering dependencies on Ly $\alpha$  luminosity, we generate two subsamples divided by Ly $\alpha$  luminosities. We split the full sample at  $\langle \log(L_{\text{Ly}\alpha}/[\text{erg s}^{-1}]) \rangle = 42.36$ . The low- and high- $L_{\text{Ly}\alpha}$  subsamples hold 349 and 346 LAEs, respectively. Their median redshifts are  $\langle z_{\text{low L}} \rangle = 4.03$  and  $\langle z_{\text{high L}} \rangle = 4.30$ . The median  $\log(L_{\text{Ly}\alpha})$  of the subsamples differs by 0.43 dex.

While at  $z \simeq 3$  most of our LAEs have a photometric HST counterpart, at  $z > 5$  only around 50% of the objects are detectable in the available HST images (Kerutt et al. in prep.). Hence, for those objects we can only adopt  $M_{\text{UV}}$  and  $EW_{\text{Ly}\alpha}$  lower limits, which would skew the  $EW_{\text{Ly}\alpha}$  and  $M_{\text{UV}}$  distributions for the higher redshift subset. Therefore we decided to eliminate the LAEs without HST counterparts when splitting by  $EW_{\text{Ly}\alpha}$  or  $M_{\text{UV}}$ . This reduces our sample size from 695 to 509 LAEs.

We then split the HST-detected sample by equivalent width at  $\langle EW_{\text{Ly}\alpha} \rangle = 87.9$ . The low-

and high- $EW_{Ly\alpha}$  subsample consists of 254 and 255 LAEs, respectively. The median redshifts and luminosities of these samples are very similar (see Table 2.1).

Finally, we divided the HST-detected LAE sample by absolute magnitude at  $\langle M_{UV} \rangle = -18.8$ , leading to low- and high- $M_{UV}$  subsets (bright and faint, respectively) of 256 and 253 LAEs. The  $\langle M_{UV} \rangle$  values differ between these two subsamples by 1.59 dex, while the  $\langle \log(L_{Ly\alpha}) \rangle$  values differ by only 0.32 dex.

## 2.3 Methods

### 2.3.1 K-estimator

#### 2.3.1.1 Basic principles

The specifics of MUSE as a survey instrument present a serious challenge for the commonly used two-point correlation function (2pcf) to measure galaxy clustering. By design, MUSE surveys span a wide redshift range but cover only small (spatial) regions in the sky. The MUSE-Wide footprint has already the largest transverse footprint of all MUSE surveys, but its nature is still that of a pencil-beam survey. While transverse scales in the MUSE-Wide survey span up to  $\sim 20 h^{-1} \text{Mpc}$ , radial scales exceed the  $1000 h^{-1} \text{Mpc}$ . The limitations of the transverse extent impede the application of the ‘jackknife’ technique to compute realistic uncertainties (see Sect. 3.3.2.1), while methods such as bootstrapping fail in the 2pcf. Besides, given our spatial ranges, exploiting the redshift coverage rather than the spatial extent is strongly preferred. We thus explore possible alternatives to the 2pcf. In Diener et al. (2017) we applied the so-called K-estimator, introduced by Adelberger et al. (2005) to analyse the clustering of Lyman Break Galaxies, in a subset of our pencil-beam survey. Here, we build on our previous work by extending it to a larger dataset, but also paying attention to optimization aspects and comparing the method with the 2pcf.

The K-estimator focuses on radial clustering along the line of sight (LOS) by counting pair separations in redshift space at fixed transverse distances. In contrast to the 2pcf, no random sample is needed because the K-estimator computes the ratio between small and small+large scales. This quantity is directly related to the underlying correlation function. We adopt the following no-

tation: Considering two galaxies with indices  $i$  and  $j$ , their transverse distance is  $R_{ij}$  (equivalent to  $r_p$  in the 2pcf), and their LOS redshift-space separation is  $Z_{ij}$  (equivalent to  $\pi$  in the 2pcf). We then count the number  $N$  of pairs within a given  $R_{ij}$  bin, for two different ranges of  $Z_{ij}$ ,  $|a_1| < Z_{ij} < |a_2|$  and  $|a_2| < Z_{ij} < |a_3|$ . The K-estimator is defined as the ratio of the numbers of galaxy pairs  $N_{a_1,a_2}(R_{ij})$  and  $N_{a_2,a_3}(R_{ij})$  between these two consecutive cylindrical shells, namely:

$$K_{a_2,a_3}^{a_1,a_2}(R_{ij}) = \frac{N_{a_1,a_2}(R_{ij})}{N_{a_1,a_2}(R_{ij}) + N_{a_2,a_3}(R_{ij})}, \quad (2.1)$$

as a function of transverse separation  $R_{ij}$ . We set  $a_1 = 0 h^{-1} \text{Mpc}$  so that the K-estimator quantifies the excess of galaxy pairs in the range  $0 < Z_{ij} < a_2$  with respect to the larger LOS range of  $0 < Z_{ij} < a_3$ . In other words, the K-estimator can be expressed as  $K(R_{ij}) = N_{0,a_2}(R_{ij})/N_{0,a_3}(R_{ij})$ . This concept is schematically illustrated in Fig. 2.3. Here,  $(a_2 - 0)$  and  $(a_3 - a_2)$  are the lengths of the two cylinders within which the numbers of pairs are counted.

The transverse distance  $R_{ij}$  between LAE pairs is taken in bins of  $R_{ij}$ , corresponding to different cylindrical shells in Fig. 2.3. These shells are defined by their radii  $R_{ij}$  and their lengths  $a_2, a_3$  in the  $Z$  direction. For illustration purposes, we display  $R_{ij}$  in Fig. 2.3 using a linear scaling ( $R_{ij2} - R_{ij1} = R_{ij3} - R_{ij2}$  etc.), although in practice we adopt a logarithmic spacing of subsequent transverse separations. We note that in this figure each  $R_{ij}$  and  $Z_{ij}$  combination corresponds to a galaxy pair and not just a single galaxy.

$K_{a_2,a_3}^{a_1,a_2}$  is related to the 2pcf through the mean value of the correlation function  $\bar{\xi}$  (see Adelberger et al., 2005)

$$\langle K_{a_2,a_3}^{a_1,a_2}(R_{ij}) \rangle \simeq (a_2 - a_1) \cdot \sum_{i>j}^{\text{pairs}} [1 + \bar{\xi}_{a_1,a_2}] \times \\ \left\{ (a_2 - a_1) \cdot \sum_{i>j}^{\text{pairs}} [1 + \bar{\xi}_{a_1,a_2}] + (a_3 - a_2) \cdot \sum_{i>j}^{\text{pairs}} [1 + \bar{\xi}_{a_2,a_3}] \right\}^{-1}, \quad (2.2)$$

where  $\bar{\xi}_{a_1,a_2}$  is

$$\bar{\xi}_{a_1,a_2} = \frac{1}{a_2 - a_1} \int_{a_1}^{a_2} dZ_{ij} \cdot \xi(R_{ij}, Z_{ij}), \quad (2.3)$$

and corresponds to the mean correlation function that would be theoretically measured in the blue region in Fig. 2.3. The same is applied for  $\bar{\xi}_{a_2, a_3}$  in the red region of Fig. 2.3. The function  $\xi(R_{ij}, Z_{ij})$  can be represented by a power law through the Limber Equation (Limber, 1953) in spatial coordinates  $\xi(R_{ij}, Z_{ij}) = (\sqrt{R_{ij}^2 + Z_{ij}^2}/r_0)^{-\gamma}$  or modelled with a halo occupation distribution model.

The understanding of this estimator is quite intuitive. If galaxies were randomly distributed in space ( $\xi(r) = 0$ ), the expected number of galaxy pairs at each LOS separation would be equal. Thus, from Eq. (2.2) and with  $a_1 = 0$ ,  $K_{a_2, a_3}^{0, a_2}$  is simply the ratio of volumes between the two cylindrical shell segments,  $(a_2 - 0)/(a_2 - 0 + a_3 - a_2) = a_2/a_3$ . Hence if  $a_3 = 2a_2$ , the expectation value for an unclustered galaxy population would be  $K = 0.5$ ; if for a specific sample the value of  $K$  is significantly above 0.5, we have detected a clustering signal. We note, however, that while this criterion (applied by both Adelberger et al. 2005 and Diener et al. 2017) seems natural, there is no a priori reason to keep the restriction to  $a_3 = 2a_2$ . In fact, allowing for  $a_3/a_2 > 2$  provides the analysis with a more solid statistical baseline against which the clustering signal can be evaluated (addressed in Sect. 2.3.1.2).

Adelberger et al. (2005) applied Eq. (2.2) and the Limber equation to estimate the correlation length,  $r_0$ , while keeping the power law slope  $\gamma$  of the correlation function fixed. They first measured the K-estimator in a single  $R_{ij}$  bin  $R_{\text{cut}} < 5 h^{-1}\text{Mpc}$  which captures the  $R_{ij}$  scale for which the clustering signal is largest. They then applied Eqs. (2.2) and (2.3) to predict the expectation values  $\langle K \rangle$  for different assumed values of  $r_0$ , selecting the correlation length for which the predicted value of  $K$  was closest to the measured value as their best estimate. The same procedure was adopted by Diener et al. (2017) in their analysis of a MUSE-Wide subset of LAEs. We refer to this approach in the following as the ‘one-bin fit’ method.

In addition to this simple approach to estimate  $r_0$  at fixed  $\gamma$ , we also implemented a more elaborate procedure to fit the K-estimator with a power law correlation function with both  $\gamma$  and  $r_0$  as free parameters. For this purpose, we integrate  $\xi(r)$  over both  $Z_{ij}$  ranges as in Eq. (2.3), for each  $R_{ij}$  bin and for each combination of a grid in  $(r_0, \gamma)$ . Plugging the values of these integrals

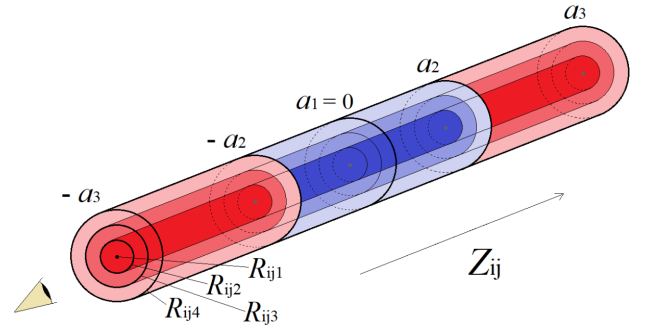


**Figure 2.3:** Illustration of the K-estimator. We show three nested cylinders representing three bins of transverse separations. The number of galaxy pairs inside each blue cylindrical shell from  $a_1 = 0$  to  $\pm a_2$  is  $N_{0, a_2}$ , the number of pairs in each red cylindrical shell between  $a_3 - a_2$  and  $-a_2 - (-a_3)$  is  $N_{a_2, a_3}$ . The K-estimator for each shell is then the ratio of pair counts between the inner (blue) segment to the total (blue plus red) segment. For illustration purposes we depict linear  $R_{ij}$  bins, although in practice we use a logarithmic binning scheme.

into Eq. (2.2) to calculate  $\langle K \rangle$  for each  $R_{ij}$  bin, we obtain a global  $\chi^2$  value for each grid point by summing over the squared deviations between predicted and observed values of  $K$  relative to the statistical error bars (obtained by bootstrapping as explained in Sect. 3.3.2.1). Our best-fit parameters are then finally taken as the  $(r_0, \gamma)$  grid point with the smallest  $\chi^2$ . For the estimation of confidence intervals, we face the complication that the  $K$  values in subsequent  $R_{ij}$  bins are correlated because each galaxy contributes to multiple pairs at various separations. We explain in Sect. 3.3.2.1 how we obtained realistic uncertainties for the fit parameters.

### 2.3.1.2 Optimizing the K-estimator

The parameters  $a_2$  and  $a_3$  in the definition of the K-estimator can in principle be chosen freely. We now explore for which values we obtain the best sensitivity for the clustering signal and the highest signal-to-noise ratio (S/N). We compute the S/N from the error bars of the correlation lengths. This procedure is similar to finding the optimal  $\pi_{\text{max}}$  saturation value in the case of the 2pcf, where  $\pi_{\text{max}}$  is increased until most of the correlated pairs are included, while even larger values of  $\pi_{\text{max}}$  only add noise to the measurement.

We performed a grid search with the full sample over the different combinations of  $K_{a_2, a_3}^{a_1, a_2}$ , but setting  $a_1 = 0$  throughout. Here, we vary  $a_2$  within  $5\text{--}25 h^{-1}\text{Mpc}$  in steps of  $2 h^{-1}\text{Mpc}$  and  $a_3$

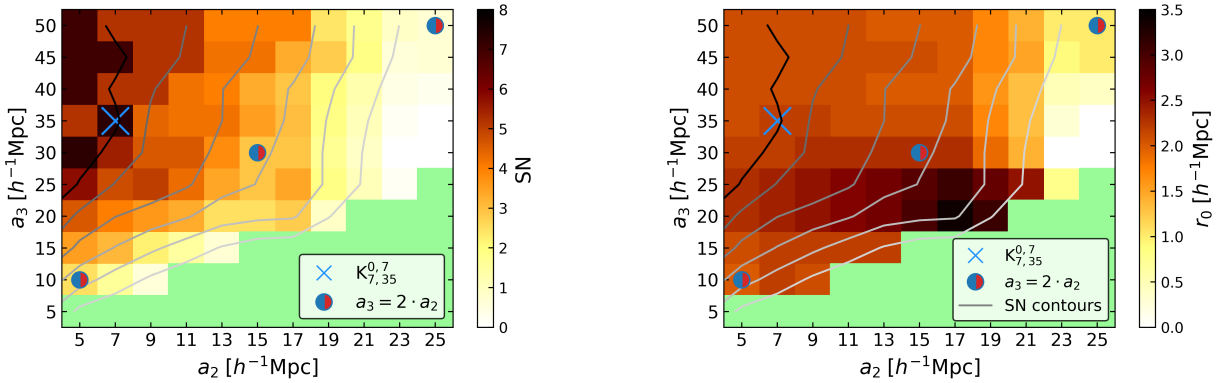


**Figure 2.4:** Results of our grid study to optimize the K-estimator. Left: S/N obtained for each evaluated combination of  $(a_2, a_3)$ , displayed as a color map. The green area indicates the ‘forbidden’ range where  $a_3 < a_2$ . The contours trace S/N increments of 2, slightly smoothed for display purposes. Right: Same parameters but for the correlation length  $r_0$ , except that the contours again follow the values of the S/N. The blue-red colored circles represent grid points with  $a_3 = 2a_2$  for which the blue-red cylinders in Fig. 2.3 are equally long. The blue cross indicated our adopted parameter combination for the clustering analysis, as it provides the highest S/N and reaches saturation at  $r_0$ .

within  $5\text{--}50 h^{-1}\text{Mpc}$  in steps of  $5 h^{-1}\text{Mpc}$ , with the additional restriction  $a_3 \geq a_2$ . We adopt 15 logarithmic bins in the range  $0.6 < R_{ij} < 12.8 h^{-1}\text{Mpc}$ , discarding  $R_{ij}$  bins with fewer than 16 galaxy pairs. We use the one-bin fit described above with a fixed canonical  $\gamma$  value of  $\gamma = 1.8$  (Adelberger et al. 2005; Durkalec et al. 2014; Ouchi et al. 2017) to calculate the correlation length,  $r_0$ , and the S/N for each combination  $(a_2, a_3)$ .

The results are shown in Fig. 2.4. The left panel reveals that the S/N is highest for small  $a_2$  and large  $a_3$  values, while it decreases towards  $a_2 \approx a_3$ . Parameter combinations with  $a_2 = a_3/2$  as adopted in the two previous studies that used the K-estimator (Adelberger et al., 2005; Diener et al., 2017) are represented by the colored circles; it is evident that these combinations are far from optimal with regard to bringing out the clustering signal with maximal significance.

The right panel of Fig. 2.4 shows that in the upper left range of the diagram where the S/N is highest, the best-fit value of  $r_0$  is also insensitive to the specific parameter combination. On the other hand, larger values of  $a_2$  and smaller values of  $a_3$  degrade the S/N. Comparable  $a_2$  and  $a_3$  values (tiny red and large blue cylinders in Fig. 2.3) result in  $N_{a_2, a_3}(R_{ij}) \ll N_{a_1, a_2}(R_{ij})$ , with  $N_{a_2, a_3}(R_{ij})$  strongly varying with the exact value of  $a_3$ . This translates into large uncertainties when computing  $r_0$  from the K-estimator (see Eq. 2.1). These errors are however not reflected in the right panel of Fig. 2.4 but are clearly visible

in the low S/N on its left panel. The largest  $r_0$  values therefore correspond to the most uncertain values but agree well within their uncertainties with the  $r_0$  value accepted by us. We adopt the combination  $a_2 = 7 h^{-1}\text{Mpc}$  and  $a_3 = 35 h^{-1}\text{Mpc}$ , marked with a blue cross in both plots, for the rest of this paper as the grid point giving the highest S/N and a  $r_0$  within the saturation values. Thus, in the following, we always refer to the specific estimator  $K_{7,35}^{0,7}$  which quantifies the ratio of the number of galaxy pairs with LOS separations between  $-7 < Z_{ij}/[h^{-1}\text{Mpc}] < 7$  and between  $-35 < Z_{ij}/[h^{-1}\text{Mpc}] < 35$  at given transverse distance  $R_{ij}$ . The expectation value of this estimator for an unclustered population is  $(a_2 - a_1)/(a_3 - a_1) = 0.2$ .

### 2.3.1.3 Error estimation

The individual data points from clustering statistics are correlated. One galaxy can contribute to galaxy pairs in more than one  $R_{ij}$  bin. In order to account for this correlation one would use the jackknife resampling technique and compute a covariance matrix (see e.g. Krumpel et al., 2010). However, that method requires a division of the sky area into several independent regions, each of which must be large enough to cover the full range of scales under consideration. Due to the small sky area of our survey, this approach is not feasible here. Poisson uncertainties, even if commonly used, might underestimate the real uncertainties. We therefore consider several al-

ternatives to derive meaningful uncertainties in Appendix 2.C and choose the most conservative approach.

Thus, we apply the bootstrapping technique detailed in Ling et al. (1986) (and similar as in Durkalec et al., 2014) to determine the statistical uncertainties of our data points. We create pseudo-data samples by randomly drawing 695 LAEs from our parent sample, allowing for repetitions. We generate 500 different pseudo-samples and compute the K-estimator in all of them. The standard deviations of  $K$  in each  $R_{ij}$  bin are adopted as error bars. We verify the robustness of our error approach in Appendix 2.C.

With the bootstrapped uncertainties and the uncorrelated  $\chi^2$  statistics, the uncertainties of the clustering parameters can be derived. However, we suspect that naively applying an uncorrelated  $\chi^2$  analysis with the standard confidence threshold can also lead to an underestimation of the clustering uncertainties. Therefore, we test this hypothesis by investigating the behavior of the error bars when the bin size is modified. While we would generally expect a decrease in the individual uncertainties when the bin size is increased, here we expect an increase in the error bars if the bin size is decreased.

We compute new bootstrapping error bars for five different  $R_{ij}$  bin sizes (half size, double size, three times larger, four times larger and five times larger than the current binning). The error bar sizes do not vary significantly when the  $R_{ij}$  bin size is modified, contrary to the expectation of the standard  $\chi^2$  method.

We therefore recalibrate the  $\chi^2$  analysis to determine realistic 68.3% and 95.5% confidence levels in the following way: with each of our bootstrapped samples delivering a best-fit minimal value of  $\chi_{\min,i}^2$  corresponding to  $(r_{0,i}, \gamma_i)$ , we assume that the posterior distribution of these  $\chi_{\min,i}^2$  approximately describes the true confidence regions. We compute the  $\chi_i^2$  values using the corresponding  $(r_{0,i}, \gamma_i)$  combinations and our real data. We sort these  $\chi_i^2$  into ascending order and adopt the 68.3% and 95.5% parameter ranges with respect to the sorted bootstrapped  $\chi_i^2$  values as marginalized single-parameter error bars. This posterior distribution is also used to provide combined confidence regions on both  $r_0$  and  $\gamma$ . Throughout the paper, we refer to this fitting approach as a ‘PL-fit’.

### 2.3.2 Two-point correlation function

The 2pcf is undoubtedly the most frequently used statistic to investigate galaxy clustering. Although we argued above that it is less suited than the K-estimator for a pencil-beam survey such as MUSE-Wide, we include a 2pcf analysis of our sample for comparison in Appendix 2.D. We note that this is in fact the first time that such an analysis has been performed on a 100% spectroscopically confirmed sample of LAEs. However, the challenge of estimating realistic uncertainties in the case of the 2pcf is even more problematic (due to the survey design) than for the K-estimator. We present in Appendix 2.D an in depth presentation and discussion of the 2pcf on our LAE sample. In summary, we show that the results from the K-estimator and 2pcf agree within their uncertainties.

### 2.3.3 Bias and typical Dark Matter Halo masses from power-law fits

The clustering strength is characterized by the large-scale bias factor  $b$ , which relates the distribution of galaxies to that of the underlying dark matter density. The bias factor has often been derived from the characteristic correlation length  $r_0$  and the PL slope  $\gamma$  by fitting a PL to the clustering signal (e.g. Peebles, 1980). Given  $b$ , we can also derive typical host DMH masses. Within the concept of linear bias, the evolution of  $b$  with redshift is given by the ratio of the density variance of galaxies  $\sigma_{8,\text{gal}}(z)$  over that of dark matter  $\sigma_{8,\text{DM}}(z)$ :

$$b(z) = \frac{\sigma_{8,\text{gal}}(z)}{\sigma_{8,\text{DM}}(z)}. \quad (2.4)$$

For a power-law 2pcf the relation between  $\xi(r)$  and the density variance  $\sigma_{8,\text{gal}}(z)$  (Peebles, 1980; Miyaji et al., 2007) is given by

$$\xi(r, z) = \left(\frac{r}{r_0}\right)^{-\gamma} \\ \sigma_{8,\text{gal}}(z)^2 = \xi(r_8, z) \times J_2, \quad (2.5)$$

where  $\xi(r_8, z)$  is the correlation function evaluated in spheres of comoving radius  $r_8 = 8 h^{-1}\text{Mpc}$  and  $J_2 = 72/[(3 - \gamma)(4 - \gamma)(6 - \gamma)2^\gamma]$ .

Simultaneously, for the DM case:

$$\sigma_{8,\text{DM}}(z) = \sigma_8 \frac{D(z)}{D(0)} \quad (2.6)$$

with  $D(z)$  as the linear growth factor.

Inserting Equations (2.5) and (2.6) into Eq. (2.4) we obtain the bias factor as a function of the growth factor

$$b(z) = \left[ \frac{r_8}{r_0(z)} \right]^{-\gamma/2} \frac{J_2^{1/2}}{\sigma_8 D(z)/D(0)}. \quad (2.7)$$

Following the bias evolution model described in Sheth et al. (2001), we can compute the large-scale Eulerian bias factor  $b_{\text{Eul}}$  and compare it to the bias given by Eq. 3.7 in order to estimate DMH masses. To calculate  $b_{\text{Eul}}$ , we consider linear overdensities in a sphere which collapses in an Einstein-de Sitter Universe at  $\delta_{\text{cr}} = 1.69$ . The linear root mean square fluctuations correspond to the mass at the epoch of observation  $\nu = \delta_{\text{cr}}/\sigma_{8,\text{DM}}(M_h, z)$ . The theory behind the  $\sigma_{8,\text{DM}}(M_h, z)$  calculation is developed in van den Bosch (2002).

### 2.3.4 Halo occupation distribution modelling

It is known that bias factors and DMH masses inferred from PL fits suffer from systematic errors (e.g. Jenkins et al. 1998 and references therein). A PL correlation function treats scales in the linear and non-linear regime alike and does not differentiate between pairs of objects belonging to the same DMH and pairs residing in different halos. Even for fits performed only in the linear regime, the correlation function still deviates from the PL shape. A more appropriate treatment is achieved through HOD modelling that explicitly combines the separate contributions from the one- and the two-halo terms.

The HOD model we use here is an improved version of the model set presented by (Miyaji et al., 2011; Krumpel et al., 2012; Krumpel et al., 2015; Krumpel et al., 2018). To maintain consistency with these studies, we use the bias-halo mass relation from Tinker et al. (2005), the halo mass function of Sheth et al. (2001), the dark matter halo profile of Navarro et al. (1997), and the concentration parameter from Zheng et al. (2007). We use the weakly redshift-dependent collapse overdensity  $\delta_{\text{cr}}$  (Navarro et al., 1997; van

den Bosch et al., 2013). We further include the effects of halo-halo collisions and scale-dependent bias by Tinker et al. (2005) as well as redshift space distortions using linear theory (Kaiser infall, Kaiser, 1987; van den Bosch et al., 2013) to the two-halo term only (see Appendix 2.E).

The mean occupation function is a simplified version of the five parameter model by Zheng et al. (2007), where we fix the halo mass at which the satellite occupation becomes zero to  $M_0 = 0$  and the smoothing scale of the central halo occupation lower mass cutoff to  $\sigma_{\log M} = 0$ .

In this simplification, the mean occupation distribution of the central galaxies can be expressed by

$$\langle N_c(M_h) \rangle = \begin{cases} 1 & (M_h \geq M_{\min}) \\ 0 & (M_h < M_{\min}) \end{cases} \quad (2.8)$$

and that of the satellite galaxies  $\langle N_s(M) \rangle$  as

$$\langle N_s(M_h) \rangle = \langle N_c(M_h) \rangle \cdot \left( \frac{M_h}{M_1} \right)^\alpha, \quad (2.9)$$

where  $M_{\min}$  is the mass scale of the central galaxy mean occupation,  $M_1$  is the mass scale of a DMH that hosts (on average) one additional satellite galaxy, and  $\alpha$  is the high-mass slope of the satellite galaxy mean occupation function.

We apply the model to obtain the  $\xi(r)$  based on HOD modelling and convert the calculated  $\xi(r)$  to the K-estimator using Eq. 2.2. The minimum transverse separation of our observed K-estimator is  $\sim 0.6 h^{-1}\text{Mpc}$ , where the one-halo term contribution to  $\xi(r)$  is typically a few to several percent. This is too low for obtaining robust constraints on the one-halo term to perform a full HOD modelling. We therefore restrict our analysis to an estimate of the bias parameter by fitting the expected K-estimator based on only the two-halo term to the observations. We hold  $\alpha = 1$  and  $\log M_1/M_{\min} = 1$  fixed and vary only  $M_{\min}$  to find the best-fit model and calculate the bias parameter. This probes the typical DMH mass for the sum of central and satellite galaxy halo occupations,  $N(M_h) = N_c(M_h) + N_s(M_h)$ , without being able to distinguish between these two. The details of the HOD models (e.g.  $M_1$  and  $\alpha$ ) do not affect the typical DMH mass estimations since we only fit the two-halo term. Some HOD modelling applications in the literature also use number density constraints (e.g. Equation 18 of Miyaji et al., 2011). This is, however, only

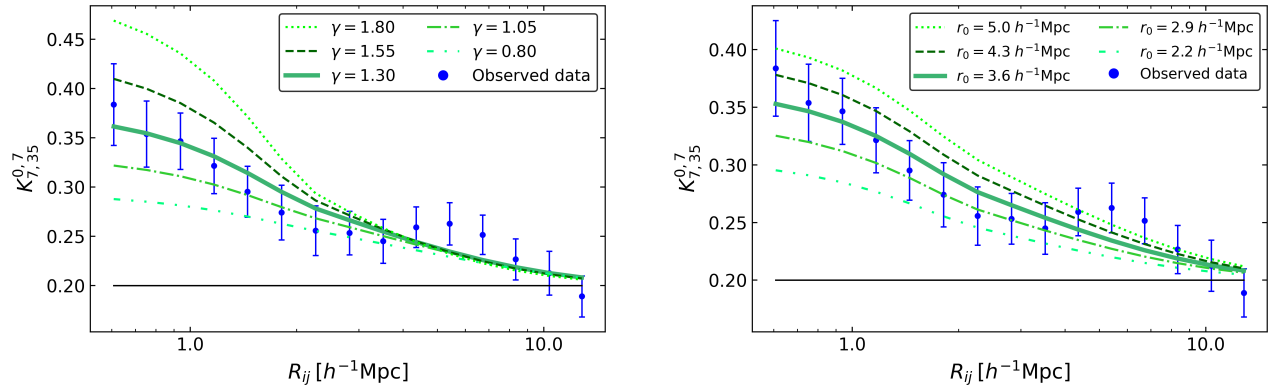


**Figure 2.5:** Measured values of the K-estimator as a function of transverse distance (points with error bars) compared to the expected behaviour for a population strictly following a power-law correlation function. Left: The five curves represent different power-law indices as given in the legend, for a fixed value of  $r_0 = 3.6 h^{-1}\text{Mpc}$ . Right: Same details for five different correlation lengths at fixed  $\gamma = 1.3$ . The central (thick solid) curves always indicate the minimum  $\chi^2$  best-fit values. The horizontal straight line shows the no-clustering expectation value of  $K$ . The error bars are calculated with the bootstrapping technique described in Sect. 3.3.2.1.

relevant if the one-halo term contributes significantly, which is not the case here. Thus, we do not need to employ any number density constraints. The HOD model is evaluated at the median redshift of  $N(z)^2$  where  $N(z)$  is the redshift distribution of the sampled galaxies. For our dataset,  $z_{\text{pair}} = 3.82$ .

As above for the PL-fit parameters (Sect. 3.3.2.1), we estimate the uncertainties of the inferred bias factor by fitting the 500 bootstrapped samples with the two-halo term HOD modelling and obtain the 500 best bias factors from the bootstrapped samples. Those best 500 HOD models are then compared to the observed K-estimator data points to compute the bootstrapped  $\chi^2$  values. We sort the bootstrapped  $\chi_{\text{min}}^2$  values in ascending order and use these to recalibrate the 68.3% ( $1\sigma$ ) confidence interval.

## 2.4 Results

### 2.4.1 K-estimator

Adopting the optimized K-estimator  $K_{7,35}^{0.7}$  (see Sect. 2.3.1.2), we measure the clustering of our LAE sample in 15 logarithmic bins of transverse separations  $R_{ij}$  between 0.6 and  $12.8 h^{-1}\text{Mpc}$ , with error bars calculated by bootstrapping the sample as explained in Sect. 3.3.2.1.

Figure 2.5 shows the results for the full LAE sample. It is evident that the values of  $K$  are significantly above the no-clustering expectation value of 0.2.

We can verify that our clustering results are not affected by the accuracy of our redshifts (see Appendix 2.B), also taking into account our statistical corrections for the expected offset between Ly $\alpha$ -based and systemic redshifts (see Sect. 2.2.2). We emphasize that the K-estimator is insensitive to these redshift errors because of the broad ( $\pm 7 h^{-1}\text{Mpc}$ ) window over which the numerator in Eq. (2.1) is evaluated.

A somewhat puzzling feature, at least at first sight, is the broad hump in the  $K(R_{ij})$  profile around  $4 \lesssim R_{ij}/[h^{-1}\text{Mpc}] \lesssim 7$ , suggesting a slight excess in the clustering strength for such separations (or alternatively, a dent at  $2 \lesssim R_{ij}/[h^{-1}\text{Mpc}] \lesssim 4$ ). We test the possibility that this feature might be introduced as an artefact of the sample footprint shape by dividing the sample into an ‘eastern’ and a ‘western’ half. Since we find the hump (or dent) in both subsets, as is also the case when splitting the sample by LAE properties (see Sect. 5.5), we rule out a systematic effect due to the footprint. Recalling the fact that the data points in Fig. 2.5 are strongly correlated, we underline that the significance of the feature is actually below  $2\sigma$ , and we consider it to most likely be due to a statistical fluctuation in the spatial distribution of the sample. The only robust test of this explanation would require an independent but statistically equivalent comparison sample, which we do not have at our disposal. However, we removed the data points of the hump or dent and tested the possible effect of this feature on our fits to the K-estimator. We find the same clustering parameters (within  $1\sigma$ )

**Table 2.2:** Clustering parameters from the different fit approaches to the K-estimator in our full sample.

Fit method	$\gamma$	$r_0$ [ $h^{-1}\text{Mpc}$ ]	$b_{\text{PL}}$	$b_{\text{HOD}}$	$\log(M_h / [h^{-1}M_\odot])$
HOD fit	–	–	–	$2.80^{+0.38}_{-0.38}$	$11.34^{+0.23}_{-0.27}$
Two-parameter PL-fit	$1.30^{+0.36}_{-0.45}$	$3.60^{+3.10}_{-0.90}$	$3.03^{+1.51}_{-0.52}$	–	–
One-parameter PL-fit	fixed 1.8	$2.60^{+0.72}_{-0.67}$	$2.02^{+0.22}_{-0.24}$	–	–
Single-bin fit	fixed 1.8	$2.10^{+0.20}_{-0.20}$	$1.66^{+0.14}_{-0.14}$	–	–

**Notes:** The typical DMH masses for the full sample are derived only from our HOD results.

The uncertainties in the bias factors reflect the statistical error on  $r_0$  only.

as in the next section. For the purpose of this paper we treat the hump or dent as an insignificant statistical fluctuation that is not related to a true clustering excess of the MUSE-Wide LAEs.

We also checked that our clustering signal is insensitive to including or excluding the objects from the 8 HUDF09 parallel fields ( $\Delta b = 0.03$ ; see Appendix 3.A), again confirming the robustness of the K-estimator on the survey footprint.

## 2.4.2 Power law fits

First, we applied the single-bin fit method to our clustering signal to compare our results to earlier studies, which also computed the K-estimator and evaluated its strength by using the single-bin fit approach. We derived the best-matching correlation length  $r_0$  at fixed  $\gamma = 1.8$ , as described in Sect. 2.3.1.1. The calculated value of  $K_{7,35}^{0,7}$  for  $R_{ij,\text{max}} < 5 h^{-1}\text{Mpc}$  corresponds to  $r_0 = 2.10 \pm 0.20 h^{-1}\text{Mpc}$ . The outcome of this single-bin fit depends somewhat on the adopted  $R_{ij,\text{max}}$ : lowering the limit to  $3 h^{-1}\text{Mpc}$  results in  $r_0 = 1.90^{+0.30}_{-0.20} h^{-1}\text{Mpc}$ , whereas increasing  $R_{ij,\text{max}}$  to  $7 h^{-1}\text{Mpc}$  delivers  $r_0 = 2.60^{+0.20}_{-0.10} h^{-1}\text{Mpc}$ . In principle, this dependence should be included in the error bar on  $r_0$ . We also vary the fixed value of  $\gamma$  between 1.0 and 2.0 and find that  $r_0$  does not change by more than  $1\sigma$ . Our single-bin fit results agree with those in Diener et al. (2017) but give much tighter constraints on  $r_0$ .

Motivated by these results we proceed to estimate both parameters simultaneously. Since in the single-bin approach the choice of  $R_{ij,\text{max}}$  does affect the fit result, we now switch to fitting the K-estimator over the full measured range of transverse separations using all bins in  $0.6 < R_{ij}/[h^{-1}\text{Mpc}] < 12.8$  (see Sect. 3.3.1).

To obtain a visual impression of how  $K_{7,35}^{0,7}(R_{ij})$  depends on  $\gamma$  and  $r_0$  separately, we overplot the expected curves for five different values of each

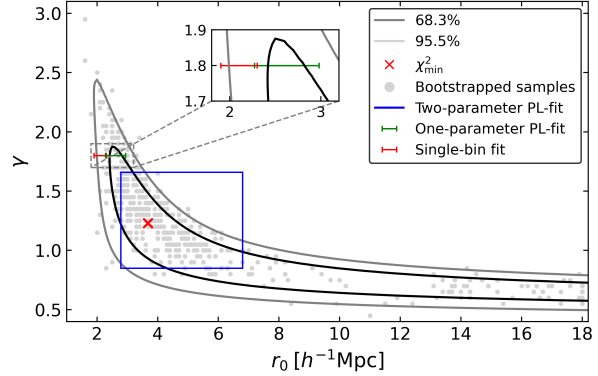


**Figure 2.6:** Simultaneous fit to  $r_0$  and slope  $\gamma$ . The black (dark grey) contour represents the 68.3% (95.5%) confidence. The red cross stands for the lowest  $\chi^2$  value at  $(r_0 = 3.65, \gamma = 1.25)$ . The points show the 500 best-fit values from the 500 bootstrapped samples. The blue rectangle indicates the 16% and 84% percentiles from the marginalized single-parameter posterior distributions of the bootstrapped samples. The green (red) error bar represents the correlation length from the one-parameter PL (single-bin) fit with fixed  $\gamma = 1.8$ . For a better visualization, we show a zoom onto the region containing these fits.

quantity into Fig. 2.5, always keeping the other parameter fixed. It can be seen that  $K$  reacts in different ways to changes in the two parameters. Increasing  $r_0$  leads to an elevated  $K$  at all  $R_{ij}$  scales, whereas increasing  $\gamma$  results in changes of  $K$  mainly at small transverse separations. Because the shape of  $K_{7,35}^{0,7}(R_{ij})$  changes differently for  $r_0$  and  $\gamma$ , it is in principle possible to fit both parameters simultaneously. We perform an uncorrelated  $\chi^2$  analysis over a grid of  $r_0$  and  $\gamma$  to find the best-fit parameters as described in Sect. 2.3.1.1.

Following the procedure laid out in Sect. 3.3.2.1 we compute confidence contours for  $r_0$  and  $\gamma$  by fitting the 500 bootstrapped samples in the same way. The marginalized single-parameter (1D) 16%–84% confidence regions are  $\gamma = 1.30^{+0.36}_{-0.45}$  and  $r_0 = 3.70^{+3.10}_{-0.92}$ . These and the corresponding 2-dimensional 68.3% and 95.5%



confidence contours are displayed in Fig. 2.6, along with the 500 best-fit parameter sets from the bootstrapped pseudo-data samples. For a visual comparison we also plot the estimations from the single-bin fit. We further include the results from a one-parameter PL-fit with fixed  $\gamma = 1.8$  for an easier comparison with the literature in Sect. 5.5.1.

The best-fit correlation length of  $2.1 h^{-1}\text{Mpc}$  obtained by the single-bin fit (at fixed  $\gamma = 1.8$ ) is lower than suggested by the one- and two-parameter fits and it is not compatible with its 68.3% probability contour. This was expected because the single-bin fit was not optimized for  $r_0$ , S/N and  $R_{ij}$  range. We also observe a large similarity between the medians of the marginalized single-parameter posterior distributions ( $r_0 = 3.60^{+3.10}_{-0.90} h^{-1}\text{Mpc}$ ,  $\gamma = 1.30^{0.36}_{0.45}$ ) and the combination of parameters that provide the lowest  $\chi^2$  value ( $r_0 = 3.65$ ,  $\gamma = 1.25$ ). It is also evident from Fig. 2.6 that the fit is quite degenerate between  $r_0$  and  $\gamma$  in the sense that parameter combinations with higher  $\gamma$  and lower  $r_0$  are only slightly less likely than the best-fit combination. Different  $R_{ij}$  scales are affected when modifying  $\gamma$  or  $r_0$  (see Fig. 2.5). This results in similarly good PL-fits when combinations of low  $\gamma$  and high  $r_0$  or high  $\gamma$  and low  $r_0$  are applied. Taking into account the sensitivity of the single-bin fit to the value of  $R_{ij,\text{max}}$ , the three results are in fact very similar. We therefore adopt the PL fitting approach also for our subsequent investigation of the dependence of clustering on LAE physical properties. This eases the comparison to the literature, where mainly PL fits are performed. The values and errors of the best-fit parameters from the different fit approaches are summarized in Table 2.2.

The confidence contours of our fit are essentially open towards large  $r_0$  and low  $\gamma$ . In fact, our bootstrap sample contains a sizeable proportion of instances with best-fit combinations in the lower right corner of Fig. 2.6 (11.8% with  $r_0 > 10 h^{-1}\text{Mpc}$ ). Upon investigation of these ‘solutions’, we find that they correspond to almost constant K-estimator values with respect to  $R_{ij}$ , driven by the tentative hump around  $5 h^{-1}\text{Mpc}$ . Whatever the actual origin of these extreme points, it seems clear that from the K-estimator alone without further priors we can only constrain plausible combinations of  $r_0$  and  $\gamma$  at one end of the distribution.

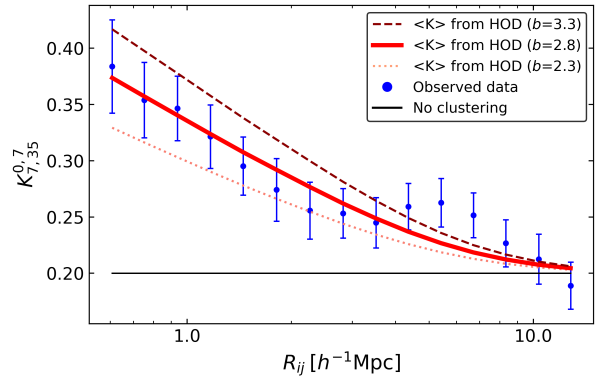


**Figure 2.7:** Dependence of the HOD fits to the K-estimator on the large-scale bias factor. The dotted, solid, and dashed red curves show three different bias factors  $b = 2.3, 2.8, 3.3$ , respectively. The thicker solid red curve shows the  $b$  that provides the lowest  $\chi^2$  value. The  $K$  values and their respective error bars are the same as in Fig. 2.5.

While it appears that the best-fit power-law index for our LAEs tends to be substantially shallower than the results from other studies based on NB imaging that use the fiducial  $\gamma$  value of  $\gamma = 1.8$  (e.g. Ouchi et al., 2010; Ouchi et al., 2017), we note that they are generally compatible at the  $1-2\sigma$  level. The same is true for the values obtained from our own sample using the 2pcf method (see Appendix 2.D).

### 2.4.3 Halo occupation distribution fit

We can then match the HOD model (Sect. 3.3.3) to our measured K-estimator. Similarly to Fig. 2.5 we first visualize the basic behaviour of the HOD model for different large-scale bias factors (shown in Fig. 2.7). Higher values of  $b$  increase the expectation values of  $K$  at most separation scales, but most strongly for small  $R_{ij}$ . Following the procedure described in Sect. 3.3.3 we recalibrate the confidence contours and obtain a best-fit large-scale bias of  $b_{\text{HOD}} = 2.80^{+0.38}_{-0.38}$ . The corresponding typical DMH mass is  $\log(M_{\text{h}}/[h^{-1}M_{\odot}]) = 11.34^{+0.23}_{-0.27}$ .

The best-fit HOD model behaves in several aspects similarly to the best-fit PL correlation function. Even if PL fits do not have a physical basis, the PL model seems to perform slightly better in terms of matching the observed  $K$  values and reaching a slightly lower  $\chi^2$  value, but these differences are not significant. The bias values derived from the two fits are also fully consistent as discussed in Sect. 2.5.3.

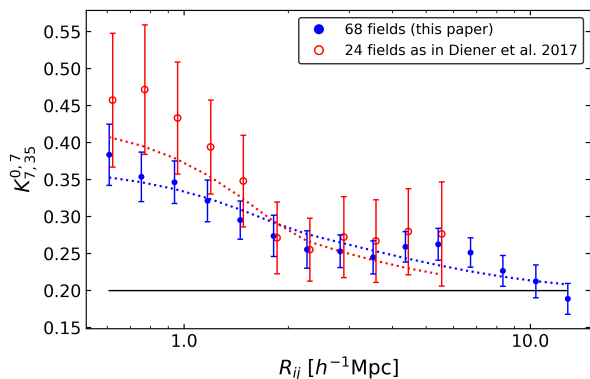


**Figure 2.8:** Measured values of the K-estimator of our sample of 68 MUSE-Wide fields (blue filled circles) compared to the subset of 24 fields considered in Diener et al. (2017, D17, open red circles). The error bars are again calculated with the bootstrapping technique described in Sect. 3.3.2.1. The blue dotted curve represents our two-parameter best PL-fit. The red dotted curve uses the best single-bin fit results of D17 ( $r_0 = 2.9_{-1.1}^{+1.0}$  cMpc for a fixed  $\gamma = 1.8$ ) applied to our PL-method (two-parameter PL-fit).

We investigate the effects of the redshift space distortions (RSD) in Appendix 2.E, where we show that the RSD do not have a significant effect on the HOD fit for K-estimator.

## 2.5 Discussion

### 2.5.1 Comparison to Diener et al. (2017)

We first compare our results with those of our pilot study (Diener et al., 2017, p. D17) which employed the non-optimized K-estimator  $K_{25,50}^{0.25}$  for a subset of 24 fields of our current sample. In order to visualize the statistical gain of our new investigation, we applied our improved  $K_{7,35}^{0.7}$  estimator to the 196 LAEs at  $3.3 < z < 6$  in the same 24 fields. The outcome of this comparison is shown in Fig. 2.8.

While the two datasets show excellent agreement given the uncertainties, as expected the error bars are much smaller in our new sample. The clustering signal of the 24 fields appears a bit higher, but the differences are at most  $1\sigma$ . The smaller footprint of the 24 fields dataset limits the range of transverse separations  $< 0.6 h^{-1}\text{Mpc}$ . The clustering curves from the two samples are fitted with a PL correlation function, based on the results from D17 for the 24 fields and on our best PL-fit for the 68 fields. Figure 2.8 also shows

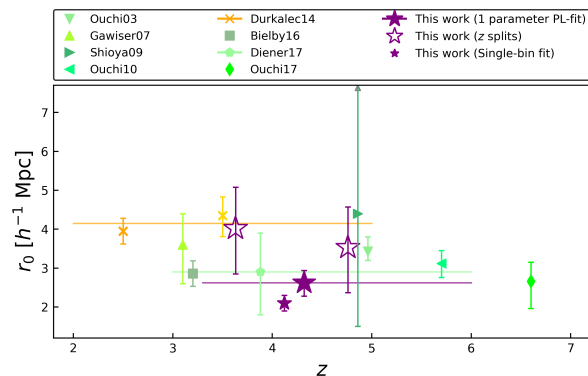


**Figure 2.9:** Comparison of the derived correlation lengths to the literature. The  $r_0$  values calculated in this study are represented with purple stars. Green symbols correspond to studies of samples based on Ly $\alpha$  selected galaxies. The samples from Durkalec et al., 2014 at  $z \sim 2.5$  and  $z \sim 3.5$  (dark and light yellow) are based on continuum-selected high- $z$  galaxies. The horizontal colored bars indicate the redshift ranges of the corresponding studies (spectroscopic surveys). The redshift range of the  $z$ -subsamples of this paper are not plotted for a better visibility. Values for  $r_0$  are plotted at the median redshift of the samples. The  $r_0$  from Ouchi et al. (2003) and Bielby et al. (2016) have been shifted by  $+0.1$  along the x-axis for visual purposes. Our one-parameter PL-fit with fixed  $\gamma = 1.8$  by  $+0.2$ . The upper limit of the  $r_0$  from Shioya et al. (2009) corresponds to  $r_0 = 10.1$  Mpc.

that the power-law fits to the 68 fields follow the data points much better than in the 24 fields since we performed a simultaneous fit of  $r_0$  and  $\gamma$ . Following the same procedure as in Sect. 3.3.2.1 for the 24 fields, we find  $r_0 = 2.85_{-0.76}^{+0.73} h^{-1}\text{Mpc}$  and  $\gamma = 1.62_{-0.82}^{+1.18}$ . These results are very close to the numbers obtained in D17 ( $r_0 = 2.9_{-1.1}^{+1.0}$  cMpc for a fixed  $\gamma = 1.8$ ), but our improved procedure substantially decreased the error bars for the same data.

### 2.5.2 Comparison with the literature

Most previously published works on the clustering of high-redshift galaxies are restricted to the estimation of  $r_0$  at fixed power-law index  $\gamma$ , with the latter typically assumed to be 1.8 or thereabouts. While our best-fit value for  $\gamma$  based on the K-estimator is considerably lower, Fig. 2.6 shows that  $\gamma$  values around 1.8 are still consistent with our data. To make a fair comparison, in Sect. 2.4.2 we recompute the best-fitting power law with  $\gamma$  fixed to 1.8; thus only allowing  $r_0$  to vary. Furthermore, the clustering strength and

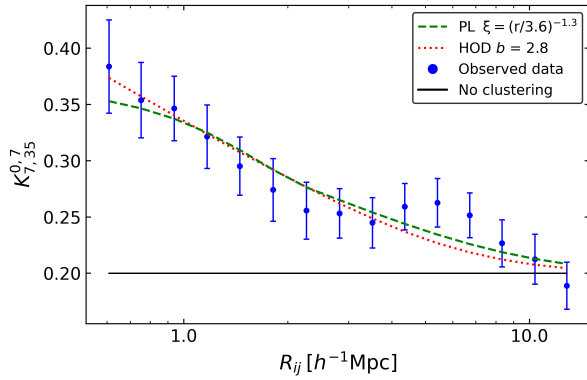


**Figure 2.10:** Best PL and HOD fits to the K-estimator. The dashed green curve shows the PL-fit (same as the solid curves in Fig. 2.5) while the dotted red curve represents the HOD fit (same as the thick curve in Fig. 2.7). The measurements of  $K_{7,35}^{0,7}$  are the same as in Figures 2.5 and 2.7.

thus the correlation length are predicted to evolve with cosmic time and, thus, the (average) redshifts of the samples must also be taken into account in any comparison.

We first considered clustering measurements of LAEs selected by NB surveys. Here, all objects are assumed to have the same redshift defined by the NB filter. Early studies (Ouchi et al., 2003; Gawiser et al., 2007; Shioya et al., 2009) focused on small samples of LAEs (up to 160 objects) at  $z = 3.1 - 4.86$  to compute angular correlations. The correlation lengths at fixed  $\gamma = 1.8$  (except Shioya et al., 2009, who calculated  $\gamma = 1.90 \pm 0.22$ ) are consistent with our recomputed PL-fits, in particular when considering the involved uncertainties. The correlation lengths are in the range of  $r_0 \approx 2.5 - 4.5 h^{-1}\text{Mpc}$ , higher values corresponding to higher redshift samples. More recent studies based on NB surveys (Ouchi et al., 2010; Bielby et al., 2016; Ouchi et al., 2017) at higher redshifts ( $z \approx 3 - 6.6$ ) hold much larger samples (up to 2000 objects), where they find slightly higher correlation lengths,  $r_0 = 3 - 5 h^{-1}\text{Mpc}$ . Given the similarity between these and lower redshift samples, our derived correlation lengths are also in fair agreement with most recent LAE clustering studies.

We then considered clustering measurements of high-redshift galaxies selected based on photometric redshifts or magnitude and colour-colour criteria (mainly Lyman-break galaxies). Durkalec et al. (2014, 2018) computed the real-space 2pcf on samples of more than 3000 objects at  $2 < z < 5$  distributed over more than  $0.8 \text{ deg}^2$ . The sample is more suited for clustering studies

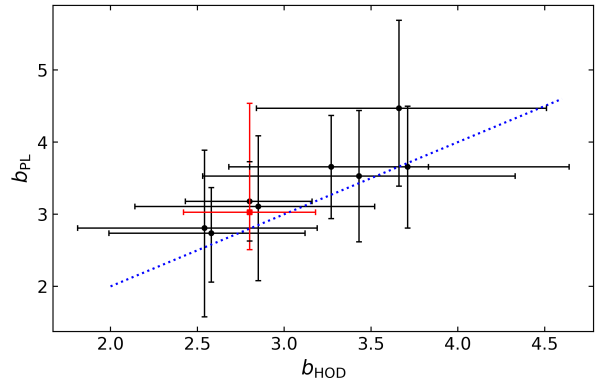


**Figure 2.11:** Comparison between the bias parameters derived from the PL and HOD fits listed in Tables 2.2 and 2.3. We highlight the bias factor from the full sample of LAEs with a red square. The dotted blue line shows a 1:1 correspondence.

than our MUSE-Wide survey because their large spatial coverage diminishes the effect of cosmic variance and allows the computation of the traditional 2pcf method. Thanks to the characteristics of the survey they perform a two-parameter PL-fit and derive a correlation slope of  $\gamma = 1.80^{+0.02}_{-0.06}$  and a correlation length of  $r_0 = 3.95^{+0.48}_{-0.54} h^{-1}\text{Mpc}$  at  $z \sim 2.5$ . At  $z \sim 3.5$  they obtain lower slopes  $\gamma = 1.60^{+0.12}_{-0.13}$  and higher lengths  $r_0 = 4.35 \pm 0.60$ . Our results not only agree with their clustering parameters but also point toward a lower slope for higher redshift galaxies. Moustakas & Somerville (2002) also reported a redshift dependence of  $\gamma$ ; in addition, the authors parameterized analytically the correlation slope as a function of redshift.

Figure 2.9 compiles the comparison of correlation lengths from the literature and those derived in this work with different fit approaches. We also plot the correlation lengths for our redshift subsamples (see Sect. 2.5.4).

Most literature values are in agreement with our findings, both with the  $r_0$  from the two-parameter PL-fit and from the one-parameter PL-fit with fixed  $\gamma = 1.8$  ( $r_0 = 2.60^{+0.72}_{-0.67} h^{-1}\text{Mpc}$ ). Not surprisingly, given the  $r_0$  dependence on  $R_{ij,\text{max}}$ , the value from the single-bin fit is lower than in most studies (including our robust PL-fit approach results).

A more appropriate but not so traditional comparison of the clustering strength is the bias factor, derived from  $\gamma$  and  $r_0$  (for PL-based correlation functions) or from HOD models. At  $z \sim 3$  Bielby et al. (2016) reported a bias factor of  $b_{\text{PL}} = 2.13 \pm 0.22$  and DMH masses of  $M_{\text{h}} = 10^{11 \pm 0.3} h^{-1}M_{\odot}$ , whilst at the same red-

shift, Durkalec et al. (2014) reported a somewhat larger bias value of  $b_{\text{HOD}} = 2.82 \pm 0.27$  and typical DMH masses of  $\log(M_{\text{h}}/[h^{-1}M_{\odot}]) = 11.75 \pm 0.23$ . As for Ouchi et al. (2017), they obtained a bias value of  $b_{\text{HOD}} = 3.9^{+0.7}_{-1.0}$  and typical DMH masses of  $\log(M_{\text{h}}/[h^{-1}M_{\odot}]) = 11.1^{+0.2}_{-0.4}$  at  $z = 5.7$ , whilst Ouchi et al. (2010) derived bias values in the range  $b = 3 - 6$  and typical DMH masses of  $M_{\text{h}} = 10^{11 \pm 1} h^{-1}M_{\odot}$  at  $z = 6.6$ . Our results fall between the values derived from studies at  $z = 3$  and  $z = 5.7$ .

Each study, however, probes different luminosity and EW ranges, an effect that may have an impact on the interpretation of the clustering results from the literature. Despite these differences, it is interesting to note the general agreement in the clustering parameters from the different studies at similar  $z$ . Consequently, the hosting DMH mass of galaxies are also very similar. We present our testing of the sample, aimed at characterizing such dependencies, in the next section.

### 2.5.3 PL vs HOD fits

The various fit methods performed on the K-estimator allow us to compare the derived PL-fit results to those from HOD modelling. We tested the performance of the different PL-fit approaches and we developed an improved fit method.

The clustering signal provided by the K-estimator was never robustly fitted in previous studies (Adelberger et al., 2005; Diener et al., 2017). The correlation length  $r_0$  was obtained by measuring the K-estimator in a single  $R_{ij}$  bin ( $R_{\text{cut}} < 5 \text{ cMpc}$ ) and comparing the result to the expectation values  $\langle K \rangle$  provided by Eq. 2.2 for different correlation lengths. In the process, a PL correlation function of fixed slope was assumed but never directly fit to the K-estimator. Instead, the correlation length that yields the closest match between  $\langle K \rangle$  and  $K_{\text{measured}}$  was chosen as the best correlation length. However, in Sect. 2.4.2, the result varies significantly depending on the chosen  $R_{\text{cut}}$ . Due to the simplicity of this approach and its dependence on  $R_{\text{cut}}$ , we fit the measured K-estimator as a function of  $R_{ij}$  with the model predictions (Eq. 2.2), providing a more reliable and accurate fit to the full  $R_{ij}$  range covered by the K-estimator.

Taking the K-estimator one step further, we also make use of HOD models. As explained in

Sect. 3.3.3, PL-based correlation functions do not distinguish between the one- and two-halo term regimes. PLs are just an approximation, whereas HOD models treat galaxies residing in one DMH and in different DMHs differently, being a more advanced and physically meaningful approach.

We measure the clustering only at  $R_{ij} > 0.6 h^{-1}\text{Mpc}$  so we do not cover the one-halo term of the correlation function. Hence, we fit the two-halo term of  $\xi(r)$  from the HOD model to our  $K$  values in order to obtain the large-scale bias of our sample.

In Fig. 2.10 we show both PL and HOD best-fits to the K-estimator from the  $\chi^2$  analysis described in Sect. 3.3.1. The performance of the curves is comparable and there are only tiny variations in the shape of the curves. Nonetheless, the PL-fit achieves the lowest  $\chi^2$ , indicating a modest better performance.

Even though the curves are nearly identical at intermediate separations ( $1 < R_{ij}/[h^{-1}\text{Mpc}] < 2.5$ ), at smaller and larger separations, the curves deviate from each other. The largest difference occurs at small separations ( $R_{ij} < 1 h^{-1}\text{Mpc}$ ), where the PL flattens but the HOD fit continues to increase. Less remarkable is the difference at large separations ( $R_{ij} > 2.5 h^{-1}\text{Mpc}$ ), where the PL-fit is somewhat higher than the HOD fit. In both cases, the differences are well within the uncertainties, and in the main range used to calibrate the bias factor ( $R_{ij} > 1 h^{-1}\text{Mpc}$ ), the variations between the fits are minute.

We show the comparison between the large-scale bias parameters calculated from the PL and HOD fits listed in Tables 2.2 and 2.3 in Fig. 2.11. The derived bias factors from the PL fits are slightly higher than the HOD values, while the HOD uncertainties are, on average, smaller ( $\approx 25\%$ ) than those from the PL fits. Using samples of AGN and a cross-correlation function approach, Krumpe et al. (2012) also compared PL and HOD clustering fits. They found higher bias factors and smaller uncertainties from the HOD fits because they included part of the one-halo term in the PL fit. As we have explained, strong variations between samples in the one-halo term cause a decrease in the bias factors derived from the PL fits. However, we do not include the one-halo term in any of our fits so we are not subjected to these variations.

**Table 2.3:** Derived clustering parameters from the subsamples.

LAE subsample	$r_0$ [ $h^{-1}\text{Mpc}$ ]	$b_{\text{PL}}$	$b_{\text{HOD}}$	$\log(M_{\text{h}} / [h^{-1}\text{M}_{\odot}])$
Redshift < 4.12	$4.02^{+1.17}_{-1.06}$	$3.18^{+0.55}_{-0.55}$	$2.80^{+0.36}_{-0.37}$	$11.39^{+0.23}_{-0.29}$
Redshift > 4.12	$3.53^{+1.16}_{-1.04}$	$3.66^{+0.71}_{-0.72}$	$3.27^{+0.56}_{-0.59}$	$11.07^{+0.31}_{-0.41}$
$\log L_{\text{Ly}\alpha} < 42.36$	$2.78^{+1.09}_{-1.02}$	$2.74^{+0.63}_{-0.68}$	$2.58^{+0.54}_{-0.59}$	$10.88^{+0.39}_{-0.62}$
$\log L_{\text{Ly}\alpha} > 42.36$	$4.08^{+1.60}_{-1.40}$	$3.66^{+0.84}_{-0.85}$	$3.71^{+0.93}_{-0.91}$	$11.57^{+0.38}_{-0.54}$
$EW_{\text{Ly}\alpha} < 87.9$	$2.89^{+1.98}_{-1.74}$	$2.81^{+1.08}_{-1.23}$	$2.54^{+0.65}_{-0.73}$	$10.84^{+0.47}_{-0.83}$
$EW_{\text{Ly}\alpha} > 87.9$	$4.14^{+1.84}_{-1.57}$	$3.53^{+0.91}_{-0.91}$	$3.43^{+0.90}_{-0.90}$	$11.44^{+0.41}_{-0.62}$
$M_{\text{UV}} < -18.8$	$6.30^{+2.97}_{-2.26}$	$4.47^{+1.22}_{-1.08}$	$3.66^{+0.85}_{-0.82}$	$11.63^{+0.36}_{-0.48}$
$M_{\text{UV}} > -18.8$	$3.35^{+1.84}_{-1.59}$	$3.11^{+0.98}_{-1.03}$	$2.85^{+0.67}_{-0.71}$	$11.06^{+0.41}_{-0.64}$

**Notes:** Power-law derived bias values ( $b_{\text{PL}}$  use a fixed slope of  $\gamma = 1.3$ ; see discussion in Sect. 2.5.4). The typical DMH masses are derived from our HOD results. The uncertainties in the bias factors and DMH masses reflect the statistical error on  $r_0$  only.

## 2.5.4 Clustering dependence on physical properties

We searched for clustering dependencies on LAE physical properties. We computed the K-estimator in the subsamples described in Sect. 3.2.4, but the lower number of objects in the subsets does not allow for a two-parameter PL-fit. We therefore take the prior from our full sample and assume that our subsamples present the same correlation slope as the parent sample ( $\gamma = 1.3$ ). We then performed the one-parameter PL-fit with fixed  $\gamma = 1.3$ . We also conducted HOD fits in the same way as we did for the full sample.

### 2.5.4.1 Redshift

Taking advantage of the large redshift range provided by MUSE, we investigate whether LAEs occupy denser regions of the Universe at earlier epochs by measuring their clustering strength with the K-estimator.

At the cost of enlarging the error bars (and as explained in Sect. 5.2), we split our sample in two bins around the median redshift,  $\langle z \rangle = 4.12$ . We computed the K-estimator in both subsamples, with the results given in the top left panel of Fig. 2.12.

The two curves are essentially indistinguishable within the error bars. Both follow the same trend and have similar shapes. Analogously to Sect. 2.4.2, we fit a PL correlation function  $\xi(r) = (r/r_0)^{-\gamma}$  with fixed slope  $\gamma = 1.3$ . For the low redshift subsample, we obtain  $b_{\text{low}} = 3.18^{+0.55}_{-0.55}$ . The resulting value for the high-redshift bin is

$b_{\text{high}} = 3.66^{+0.71}_{-0.72}$ . The best-fit parameters are listed in Table 2.3 along with the bias factors obtained from the HOD fit and their corresponding DMH masses.

The difference between the best-fit parameters (lower than  $1\sigma$ ) of the subsamples do not allow us to corroborate or contradict the general statement "LAEs reside in more massive DMHs at higher redshifts". However, other studies found higher bias factors of LAEs at higher redshifts (e.g. Ouchi et al., 2010). Even if the study of samples at fixed luminosities is needed, this has been interpreted as evidence for downsizing, with galaxies residing in the largest DMHs going through their 'LAE phase' early in the Universe, while Milky Way progenitors appear as LAEs at later times, around  $z \sim 3$ .

We confirm that our findings are not strongly affected by the selected redshift cut of the sample. Varying the cut by 10% in  $z$ , from  $z = 4.12$  to  $z = 4.53$ , changes the number of LAEs in each subsample by  $\sim 15\%$  (118 objects) and results in an increase in  $b$  within  $1\sigma$ , which is equivalent when considering the uncertainties; whereas, the  $z$  and  $L_{\text{Ly}\alpha}$  values are not independent. Therefore, the different luminosity distributions in the different redshift subsamples may bias the detection of a clustering dependence on redshift. To assure that the investigation of the clustering dependence on  $z$  is not driven by the different  $L_{\text{Ly}\alpha}$  distributions, we apply a 'matching' technique similar to Coil et al. (2009) and Krumpal et al. (2015). To do so, we compare individual bins between the two luminosity distributions of the  $z$ -subsamples. In each bin, we check which subsample contains more objects. We then select

the one with the higher number and randomly remove objects until we match the number counts of the other subsample in that bin. Once the two luminosity distributions are equivalent, we run the K-estimator in both subsamples with now matched  $L_{\text{Ly}\alpha}$  distributions but still different redshift distributions. We find fully consistent results when making a comparison with our original subsample definition. The clustering difference between the ‘matched’ and ‘unmatched’ subsamples varies within  $1\sigma$ . Therefore, we discard the possibility of a possible clustering dependence on  $z$  driven by  $L_{\text{Ly}\alpha}$  as well as a strong clustering dependence on  $z$ .

#### 2.5.4.2 Ly $\alpha$ luminosity

To learn about the DMHs where LAEs of different Ly $\alpha$  luminosities reside, we studied the clustering dependence on Ly $\alpha$  luminosity. We used two subsamples divided by the median Ly $\alpha$  luminosity of the full sample as explained in Sect. 5.2. The K-estimator was then computed for both. Details of the individual subsamples are given in Table 2.1 and the clustering correlations are illustrated in the top right panel of Fig. 2.12.

Although the statistical uncertainties are substantial, the top right panel of Fig. 2.12 suggests a trend in the sense that LAEs with higher Ly $\alpha$  luminosities appear to be more strongly clustered. This trend is also seen in the correlation lengths and bias factors, see Table 2.3. We verify that our results are not significantly altered by the chosen Ly $\alpha$  luminosity cut of the sample. Shifting the Ly $\alpha$  luminosity from  $\log(L_{\text{Ly}\alpha}/[\text{erg s}^{-1}]) = 42.36$  to  $\log(L_{\text{Ly}\alpha}/[\text{erg s}^{-1}]) = 43.21$  (120 objects shifted) does not change the results; we still find a tentative  $2\sigma$  clustering dependence on Ly $\alpha$  luminosity. Furthermore, we have also investigated that the possible clustering evolution trend with  $L_{\text{Ly}\alpha}$  is not caused by the different redshift distributions of the subsamples.

As already mentioned  $L_{\text{Ly}\alpha}$  and  $z$  are not independent. Thus, we also create matched distributions to exclude that dependence is driven by  $z$  and not  $L_{\text{Ly}\alpha}$ . In order to discard this possibility, we match the  $z$ -distributions of both subsamples such that the low- and high-  $L_{\text{Ly}\alpha}$  subsamples have exactly the same  $z$ -distribution. We compute the K-estimator for the subsamples with the matched  $z$ -distributions and find a more pronounced trend than that of the top right panel of Fig. 2.12. For both matched subsamples, the

$K$  values vary within  $\sim 7\%$  of the original subsamples. This translates into a difference lower than  $1\sigma$  between the ‘matched’ bias factors and those listed in Table 2.3. However, the ‘matched’ bias factors between the low and high  $L_{\text{Ly}\alpha}$  subsamples differ by almost  $2\sigma$ , suggesting a tentative weak clustering dependence in the way that more luminous LAEs cluster more strongly than less luminous LAEs.

The calculated bias factor for fainter LAEs is  $b_{\text{low}} = 2.58^{+0.54}_{-0.59}$ , while for luminous LAEs is  $b_{\text{high}} = 3.71^{+0.93}_{-0.91}$ . This trend is consistent with the statement that more luminous (in Ly $\alpha$ ) galaxies reside in more massive DMHs (Ouchi et al., 2003). While a more statistically significant result will require larger LAE samples, the trend we see is in agreement with Ouchi et al. (2003) and Khostovan et al. (2019), who found stronger clustering strengths for Ly $\alpha$  brighter LAEs in samples of  $41.85 \leq \log(L_{\text{Ly}\alpha}/[\text{erg s}^{-1}]) \leq 42.65$  at  $z \approx 4.86$  and  $42 \leq \log(L_{\text{Ly}\alpha}/[\text{erg s}^{-1}]) \leq 43.6$  at  $2.5 < z < 6$ , respectively.

#### 2.5.4.3 Ly $\alpha$ equivalent width

We investigate the clustering dependence on the rest-frame Ly $\alpha$   $EW$  to explore the possibility of LAEs residing in different DMHs depending on the  $EW$  of the Ly $\alpha$  emission line. We use the two subsamples described in Table 2.1. The  $EW$  cut is made at the median  $EW_{\text{Ly}\alpha}$  of the sample of galaxies with HST counterparts as explained in Sect. 5.2. The K-estimator results are presented in the bottom left panel of Fig. 2.12 and the best-fit parameters from the PL- and HOD-based correlation functions are given in Table 2.3.

There are hardly any differences between the curves shown in the bottom left panel of Fig. 2.12. The low  $EW_{\text{Ly}\alpha}$  subsample presents a linear bias factor of  $b_{\text{low}} = 2.54^{+0.65}_{-0.73}$ , while the resulting value for the high  $EW_{\text{Ly}\alpha}$  bin is  $b_{\text{high}} = 3.43^{+0.90}_{-0.90}$ . Even though LAEs with higher  $EW_{\text{Ly}\alpha}$  seem to reach higher  $K$  values on average, the difference is smaller than  $1\sigma$ . Similar results were found by Ouchi et al. (2003).

We certify that the derived correlation lengths are not affected by the selected  $EW_{\text{Ly}\alpha}$  cut of the sample. Shifting the cut by 25% in  $EW_{\text{Ly}\alpha}$ , from  $EW_{\text{Ly}\alpha} = 87.9$  to  $EW_{\text{Ly}\alpha} = 110$ , changes the subsample number counts in 50 objects and results in a variation in  $r_0$  within  $1\sigma$ , equal within the error bars.

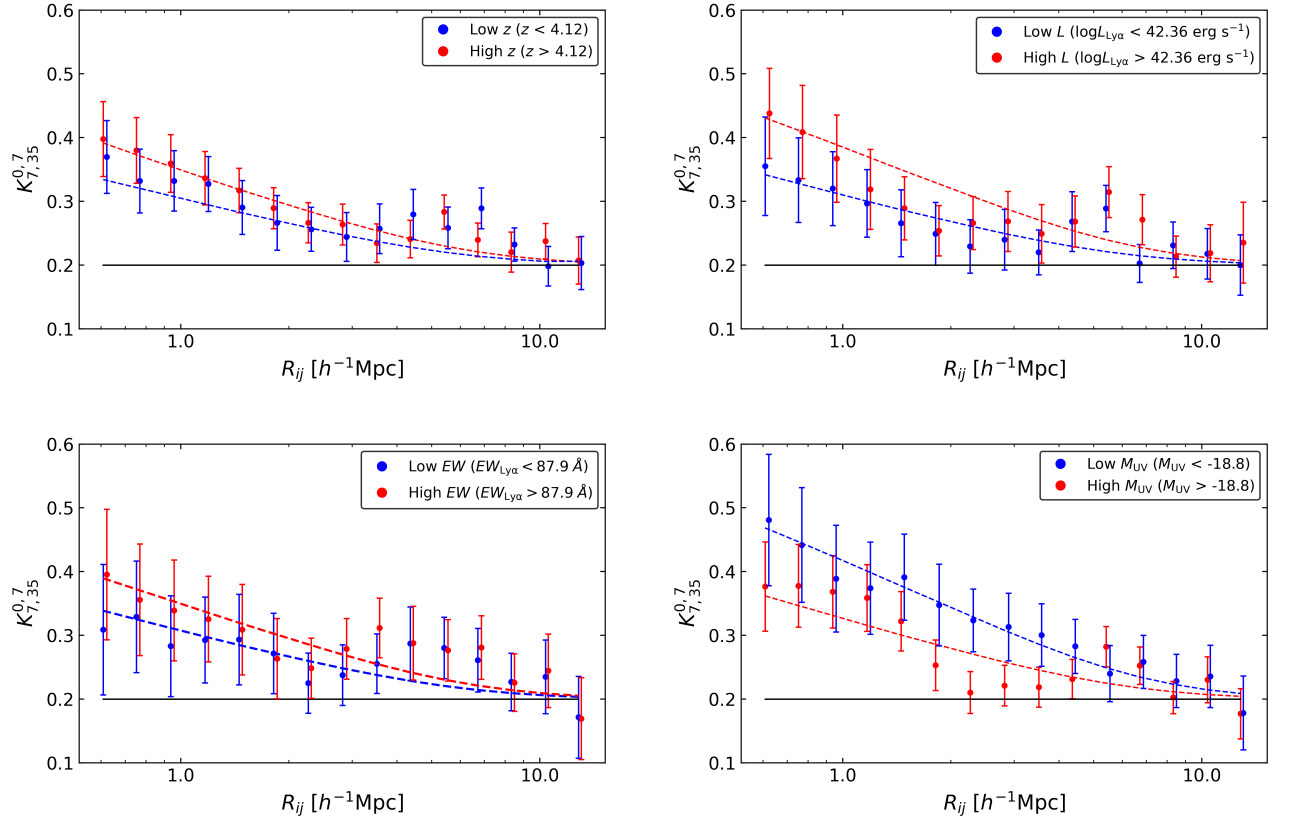


**Figure 2.12:** Clustering dependencies on object properties. Top left: Clustering variation in two different redshift subsamples. The blue dots show the clustering in the lower redshift bin while the red points show the higher redshift subsample. The dotted curves represent the best HOD fits. Top right: Same details but for two different Ly $\alpha$  luminosity subsamples. Bottom left: Same details but for  $EW_{Ly\alpha}$ . Bottom right: Same details but for UV absolute magnitude. The black line represents the K expectation value for an unclustered sample of galaxies and the  $1\sigma$  error bars are determined from the bootstrapping approach explained in Sect. 3.3.2.1.

#### 2.5.4.4 UV absolute magnitude

The UV absolute magnitude is related to the star formation rate which in turn is expected to scale with stellar and also the DMH mass. It is therefore interesting to explore the clustering dependence on UV absolute magnitude by dividing our full sample at the median  $M_{UV}$  into two subsamples. The characteristics of both bins are listed in Table 2.1. We compute the K-estimator in both subsamples and we illustrate the clustering correlations in the bottom right panel of Fig. 2.12. The clustering parameters are listed in Table 2.3.

We find large-scale bias factors in the bright- and faint- $M_{UV}$  subsamples (low and high  $M_{UV}$ , respectively) of  $b_{low} = 4.47^{+1.22}_{-1.08}$  and  $b_{high} = 3.11^{+0.98}_{-1.03}$ . Given the large uncertainties, we cannot claim the detection of a clustering dependence on  $M_{UV}$ , even if the bottom right panel of Fig. 2.12 seems to indicate a stronger clustering signal for more luminous LAEs than for fainter LAEs. While Durkalec et al. (2018) found that high- $z$  galaxies with  $M_{UV} < -20.2$  cluster more strongly than those with  $M_{UV} < -19.0$  ( $\Delta b = 0.43$ ), Ouchi et al. (2003) found no notable difference between their  $M_{UV}$  subsamples. Since Ouchi et al. (2003) recognize different clustering strengths as a function of Ly $\alpha$  luminosity, they claim that such dependence might dominate over a  $M_{UV}$  clustering dependence.

We checked that the derived correlation parameters are not significantly affected by the chosen  $M_{UV}$  cut of the sample. Shifting the  $M_{UV}$  cut, from  $M_{UV} = -18.8$  to  $M_{UV} = -19.18$  changes the number of counts in the subsamples by 62 objects while the correlation lengths vary within  $1\sigma$ , consistent within the uncertainties.

### 2.5.5 Cosmological simulations

We go on to compare our results with cosmological simulations to test whether our detected clustering signal is predicted by state of the art LAE models at high redshift and to gain some insight into the expected cosmic variance.

While a plethora of cosmological simulations are now available to describe the formation and evolution of galaxies at high redshift, the complex nature of the Ly $\alpha$  line emission and propagation in the gas requires careful numerical modelling in order to make predictions for the LAE population. Various approaches based on different numerical techniques and model as-

sumptions (i.e. cosmology, baryonic physics, etc) have incorporated Ly $\alpha$  radiation transfer effects over simple geometries in semi-analytic models (e.g. Garel et al., 2012; Orsi et al., 2012; Garel et al., 2015; Gurung-López et al., 2018) or in post-processing of hydrodynamical simulations (e.g. Forero-Romero et al., 2011; Dayal & Libeskind, 2012; Yajima et al., 2012). Even though there is no radiative transfer (RT) model that perfectly reproduces the Ly $\alpha$  emission lines and, therefore, no cosmological simulation that succeeds in fully replicating LAE observations, here we compare our results with the GALICS semi-analytic model which includes Ly $\alpha$  radiation transfer in expanding shells (Garel et al., 2015).

The underlying dark matter simulation used in this model is run with GADGET (Springel, 2005) and features a box of  $3 \times 10^6$  Mpc<sup>3</sup> with a DMH mass resolution of  $10^9 M_{\odot}$ . As shown in Garel et al. (2015), this model can reproduce the UV and Ly $\alpha$  luminosity functions at  $3 < z < 7$  down to Ly $\alpha$  fluxes of  $4 \times 10^{-17}$  erg s<sup>-1</sup> cm<sup>-2</sup>. Following the procedure described in Garel et al. (2016), we generate 100 mock light cones of  $17 \times 17$  arcmin<sup>2</sup> size to obtain physical parameters such as Ly $\alpha$  fluxes or 3D positions.

In order to resemble the real data, the selection function, spatial geometry, and redshift range of the 68 MUSE-Wide fields have been applied before computing the K-estimator for the 100 simulated samples. The selection function was shifted +0.28 dex in flux to recover the same total number of detections. The results given by the K-estimator in the 100 simulated samples are shown in Fig. 2.13, along with its average and uncertainties.

We find that the clustering in the simulated samples is much stronger than the clustering in the MUSE-Wide survey. Simulated samples present much larger K-values than in the observed data. The two-parameter PL-fit results in very large uncertainties in  $r_0$  (consistent with our observed  $r_0$ ) but also points to lower  $\gamma$  values. From the one-parameter PL-fit (fixed  $\gamma = 1.8$ ), we obtain  $r_0 = 5.80^{+1.23}_{-1.10} h^{-1}$  Mpc and derive a bias factor of  $b = 4.13^{+0.78}_{-0.71}$ . These are only  $\approx 1.9\sigma$  away from our one-parameter best-fit results. However, from the HOD fit we compute  $b = 4.80^{+0.32}_{-0.32}$  and  $\log(M_h/[h^{-1}M_{\odot}]) = 12.16^{+0.11}_{-0.11}$ . Considering the  $M_h$  values, this differs by  $3.2\sigma$  from our observations. We note that since the scope of this paper is not to give an extended comparison to simulations, we have restricted



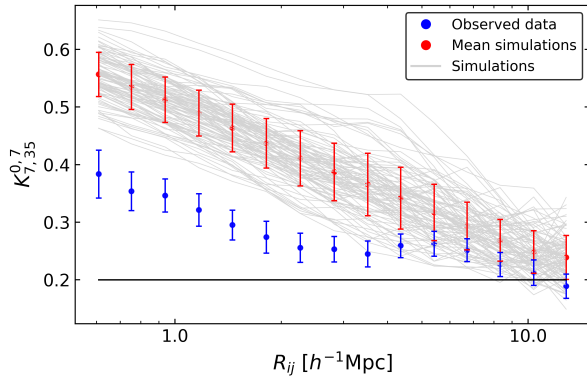


**Figure 2.13:** Comparison between the clustering signal in our real survey in blue (same as in Fig. 2.5) and in the 100 simulated samples. Each sample is drawn from a different light-cone realization. The values of the K-estimator for each of the 100 simulated catalogues is represented in gray. The standard deviation of the 100 K-estimator values and their average values are shown in red.

our comparison to one LAE model only, and we obviously cannot draw any general conclusion regarding a potential tension between the predicted and observed clustering of LAEs. Thus, we leave more detailed comparisons to future work. We briefly discuss aspects that may plausibly explain the mismatch below.

We first note that the mock light cones show prominent redshift spikes that are not present in the real data (see Fig. 2.14), a noticeable problem that was also discussed in Diener et al. (2017). The super structures seem to dominate the clustering signal and be responsible for most of the disagreement between our measurements and the simulation. The origin of this discrepancy is unclear and could be due to several reasons that need to be addressed in future simulation work, such as inaccuracies in the  $\text{Ly}\alpha$  RT modelling, the assumed cosmology, the baryonic physics modelling affecting the halo-galaxy relation, cosmic variance, intrinsic  $\text{Ly}\alpha$  luminosities, or poorly controlled LAE selection in the mocks.

In particular, a potential cause could arise from the fact that  $\text{Ly}\alpha$  luminosities in GALICS are angle-averaged, whereas the  $\text{Ly}\alpha$  escape fraction is supposedly highly anisotropic in real galaxies, such that observed  $\text{Ly}\alpha$  luminosities strongly vary from one sight line to another (Smith et al., 2019). Since the luminosity function of our LAEs is steep, this has the same effect as photometric scattering. Uncertainties in the selection function of GALICS and of observations due to field to field variation are poorly controlled and have a similar effect. This results in the selection

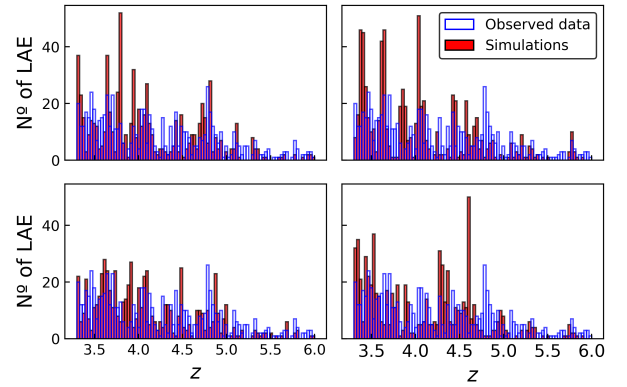


**Figure 2.14:** Redshift distribution from four simulated catalogues chosen randomly from the full set of light cones in red. The redshift distribution of the real LAEs from the 68 fields of the MUSE-Wide survey is shown in blue.

of more luminous galaxies at higher redshifts, which can boost the clustering signal.

Moreover, potential deviations on the  $\text{Ly}\alpha$  luminosity-halo mass relation in GALICS (e.g. star formation not sufficiently quenched in massive halos, such that  $L_{\text{Ly}\alpha} = 10^{42} \text{ erg s}^{-1}$  LAEs might reside in too massive halos) would also enhance the clustering. Besides, a duty cycle (e.g. Ouchi et al., 2010) further powers this mismatch because in GALICS most star forming galaxies emit  $\text{Ly}\alpha$ . Alternative modelling could lead to  $\text{Ly}\alpha$ -bright phases that only last a limited period of time, which could plausibly attenuate the strong spikes seen in the redshift distribution.

Since these simulations do not closely reproduce the clustering present in the real data, it is not possible to use them for improving the error estimates on the measurements over the approaches we considered in Appendix 2.C. Nevertheless, simulations can provide information on the individual contribution of the statistical uncertainty and the uncertainty due to cosmic variance. For the statistical uncertainty, we performed 500 K-estimator measurements on the same bootstrap-resampled light-cone (see Sect. 3.3.2.1 where we apply the same method to our real data). The uncertainty of the cosmic variance can be estimated by computing the standard deviation of the 100 different light-cone realizations. In comparing the individual data points, we find that the uncertainty due to the cosmic variance (red error bars in Fig. 2.13) is on average  $\sim 35\%$  larger than the error from the statistical approach only (similar to the blue error bars in Fig. 2.13 but for one light-cone). We have verified that similar results can be found if

we resample different light cones. Therefore, our quadratically combined uncertainties (statistical and cosmic variance) in the observed clustering may ultimately be  $\sim 70\%$  higher.

Finally, we used the light cones to check the effects of our special survey geometry. Even if we do not expect a strong effect on the K-estimator since we are measuring a contrast of galaxy pairs in two consecutive shells along LOS separations (see also Appendix 3.A), we compared the clustering of the 100 simulated catalogues in a 68 fields special geometry with the clustering present in the full area of the simulation without any forced geometry (just a simple square of  $17 \times 17$  arcmin<sup>2</sup>). We find that the signals agree very well.

### 2.5.6 The fate of LAEs over cosmic time

Applying an HOD modelling to the K-estimator determines a typical dark matter halo mass of  $\log(M_h/[h^{-1}M_\odot]) = 11.34_{-0.27}^{+0.23}$  for our LAEs. It is expected that these high redshift DMHs significantly grow all the way down to  $z = 0$ . We here explore the evolution of those DMHs from  $\langle z_{pair} \rangle \simeq 3.82$  to  $z = 0$  to find the typical descendants of our LAE sample.

Considering the galaxy-conserving evolution model of Fry (1996), which assumes the absence of mergers and that the motion of galaxies are driven by gravity only, the large-scale bias factor evolves as:

$$b(z) = 1 + (b_0 - 1)/D(z), \quad (2.10)$$

where  $b_0$  is the bias at  $z = 0$  and  $D(z)$  is the linear growth factor (e.g. Hamilton, 2001).

Using this model, we infer that the halos of LAEs with a median redshift of the number of pairs  $\langle z_{pair} \rangle \simeq 3.82$  evolve into halos with  $b_0 \approx 1.4$  by  $z = 0$ , which translates into typical DMH masses of  $\log(M_h/[h^{-1}M_\odot]) \sim 13.5$ . This is  $\approx 15$  times more massive than the Milky Way. Based on Ouchi et al. (2010) calculations, in a more realistic Press-Schechter formalism (e.g. Lacey & Cole, 1993), the bias evolution curve is slightly lower, meaning a bias closer to  $b_0 \approx 1.2$  rather than  $b_0 = 1.4$ .

Similar results are also derived from simulations. The information stored in the DM halo merger trees used in GALICS (Garel et al., 2016) allowed a similar study. They found median de-

scendant halo masses of  $M_h/[h^{-1}M_\odot] \approx 2 \cdot 10^{12}$  for  $z = 3$  LAEs, corresponding to the upper limit estimate of the Milky-Way halo mass. For  $z = 6$  LAEs they found median descendant halo masses of  $M_h/[h^{-1}M_\odot] \approx 5 \cdot 10^{13}$ , corresponding to group or cluster galaxy halos. These assessments are thoroughly in agreement with our estimations and reinforce the notion that our LAEs actually contain a diverse population of objects (as expected, since MUSE-Wide is a Ly $\alpha$ -flux limited survey over a wide  $z$  range).

Our work and the various studies presented in the literature cover wide  $z$  and Ly $\alpha$  luminosity ranges. If there are indeed clustering dependencies with one or both parameters, this would lead to different typical DMH masses, depending on the details of the sample selection. It is thus necessary to discuss the descendants with respect to different redshift and luminosity progenitors. The combination of clustering measurements of NB-selected LAEs and the galaxy-conserving model considered in this work, leads us to the conclusion that  $z = 5.7 - 6.6$  LAEs will evolve into DMH with bias values of  $b_0 = 1.5 - 2$  at  $z = 0$  (Ouchi et al., 2010). This is in agreement with our findings. These higher values, in comparison to those of Gawiser et al. (2007) at  $z = 3.1$ , indicate that descendants of LAEs at different redshifts differ. While most LAEs at  $4 < z < 7$  are probably the large galaxies of today, LAEs at  $z = 3$  are more likely to be the ancestors of Milky Way type galaxies.

Khostovan et al. (2019) considered narrowband-selected LAEs with typical  $L_{Ly\alpha} \sim 10^{42-43}$  erg s<sup>-1</sup> and intermediate-band-selected LAEs with typical  $L_{Ly\alpha} \sim 10^{43-43.6}$  erg s<sup>-1</sup> at  $2.5 < z < 6$ . Assuming halo mass accretion models, they found that the former evolved into galaxies residing in halos of typically  $\log(M_h/[h^{-1}M_\odot]) = 12 - 13$  (Milky Way-like) while the later evolved into galaxies residing in halos of  $\log(M_h/[h^{-1}M_\odot]) > 13$  (cluster-like) in the local Universe.

Since our LAEs are in the redshift range of  $3.3 < z < 6$  and present typical Ly $\alpha$  luminosities in the range  $40.9 < \log(L_{Ly\alpha}/[\text{erg s}^{-1}]) < 43.3$ , the derived descendant masses ( $\log(M_h/[h^{-1}M_\odot]) \sim 13.5$ ) are thoroughly in agreement with the cluster-like descendants found by Ouchi et al. (2010) and Khostovan et al. (2019). These results, along with those from literature, reveal that LAEs cover a wide range of present-day descendants, depending on their

luminosity and redshift, from Milky Way-type galaxies all the way to clusters of galaxies.

## 2.6 Conclusions

In this work, we examine the galaxy clustering properties of a sample of 695 LAEs from the MUSE-Wide survey in the redshift range of  $3.3 < z < 6$ . We applied an optimized version of the K-estimator and supported our results with the traditional two-point correlation function, measuring, for the first time, the spatial clustering as a function of distance in a spectroscopic sample of Ly $\alpha$ -selected galaxies.

Due to the characteristics of the survey (special geometry, large redshift range and limited angular coverage), we focus on the more appropriate clustering method, namely, the K-estimator. We then relied on the radial clustering and quantified the clustering signal following different approaches. We first obtained  $r_0 = 3.60^{+3.10}_{-0.90} h^{-1}\text{Mpc}$  and  $\gamma = 1.30^{+0.36}_{-0.45}$  by fitting the clustering signal with a power-law-based correlation function. We derived a bias parameter of  $b = 3.03^{+1.51}_{-0.52}$  and compared it to that derived from the second fit approach,  $b = 2.80^{+0.38}_{-0.38}$ , by scaling a halo occupation distribution model to the measured signal. The large-scale bias corresponds to typical dark matter halo masses of  $\log(M_h/[h^{-1}M_\odot]) = 11.34^{+0.23}_{-0.27}$ . In order to support the less known K-estimator method, we also computed the traditional 2pcf, whose results are consistent with those obtained with the K-estimator.

The results are also in general agreement with the last available measurements at similar redshifts, with bias factors slightly higher than those in the literature. Nevertheless, most of the previous studies have been carried out in surveys with somewhat different flux limits than that of the MUSE-Wide survey. This could play an important role since we may probe disparate stellar masses. The chosen cosmology and the redshift evolution of these parameters through different epochs also contribute to those slight differences.

We also explore possible clustering dependencies on physical properties. We exclude the possibility of a strong clustering dependence on Ly $\alpha$  equivalent width, UV absolute magnitude, and redshift. However, we see a tentative weak trend when we split the sample at the median Ly $\alpha$  lu-

minosity that is, more luminous LAEs cluster more strongly than less luminous LAEs.

We compare the clustering in the MUSE-Wide survey with the clustering in 100 light cones from a GADGET dark matter only cosmological simulation coupled to the GALICS semi-analytical modelling of LAEs. We find that even though the simulation mimics the flux and luminosity of the LAEs, it is far from successfully reproducing the observed clustering. Simulated data show a stronger clustering than measured in our sample. In order to better imitate the clustering of LAEs, determine the reliable 2pcf scales, compute more realistic uncertainties for our methods, and constrain a physically robust model for LAEs, future simulation studies need to address this challenge.

Assuming galaxy-conserving evolution models, we inferred that our DMHs should evolve into halos of  $\log(M_h/[h^{-1}M_\odot]) \sim 13.5$  in the local Universe. Since these models assume that the motion of galaxies is driven entirely by gravity, and that mergers do not occur, our evolved DMH masses would be slightly higher in a (more realistic) Press-Schechter formalism. We deduce that the DMHs of LAEs observed at  $3.3 < z < 6$  with  $40.9 < \log(L_{\text{Ly}\alpha}/[\text{erg s}^{-1}]) < 43.3$  have mainly evolved into halos hosting present-day galaxies or groups. These halos are  $\approx 15$  times more massive than that of the Milky Way.

A radial extension of the MUSE-Wide survey would benefit the development of LAE clustering studies. Larger areas of the sky would be covered (i.e. larger clustering scales), a larger sample of LAEs would be detected, and the higher S/N would further decrease the uncertainties in the measurements. This will be the case for HETDEX (Hill et al., 2008), which will provide a higher S/N and a much broader coverage of the sky, contributing to improving the understanding of the cosmology behind LAEs.

## Appendix

### 2.A Effect of the HUDF parallel fields on the K-estimator

In this work, we focus on 68 fields of the MUSE-Wide survey, including part of the CANDELS/GOODS-S region and the eight

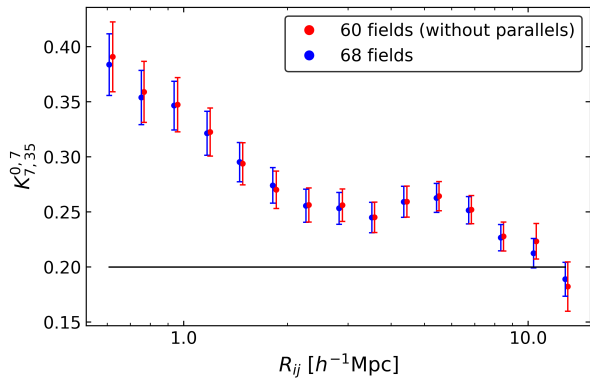


**Figure 2.A.1:**  $K_{7,35}^{0,7}$  estimator for the LAEs in 60 and 68 fields of the MUSE-Wide survey in red and blue, respectively. The black straight line shows the expected  $K$  value of an unclustered sample. All error bars are Poissonian. The red dots have been shifted along the x-axis for visual purposes.

parallel HUDF fields. In order to assess a homogeneous sample, cover a larger area of the sky, and maximize the number of detected galaxies, we include the eight HUDF parallel fields. In this section we explore the possible effects on the clustering measurements of including the parallel fields. We study the clustering in the 68 fields (same as throughout the paper) and that present in the 60 fields (without including the eight parallel HUDF fields). The characteristics of the first sample are described in Sect. 5.2, while the second sample covers a total of 54.74 arcmin<sup>2</sup> and has 581 LAEs.

The  $K$ -estimator is then run in both samples and shown in Fig. 2.A.1. We demonstrate the insignificant effect on our main results due to the inclusion or exclusion of the parallel fields. The two curves are indistinguishable within the approximated Poissonian uncertainties  $\sqrt{N_{a1,a2}}/(N_{a1,a2} + N_{a2,a3})$  (see Sect. 4.2 in Adelberger et al. 2005) but due to the lower number of LAEs in the 60 fields the uncertainties are somewhat larger (8%) than those of the 68 fields.

The minimal effect on the clustering signal, the larger area of the sky covered, which makes it more representative in terms of cosmic variance, and the larger number of LAEs in the sample, which reduce the uncertainties, lead us to include the eight parallel HUDF fields in our analysis of the main sample.

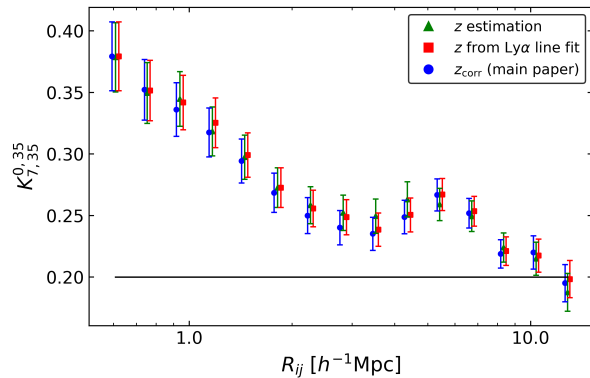


**Figure 2.B.1:**  $K_{7,35}^{0,7}$  estimator for the LAEs in the MUSE-Wide survey. The green triangles represent the  $K$ -estimator values of the sample of LAEs with redshift estimations from QtClassify, the red squares show the  $K$  values when the redshifts are obtained from the Ly $\alpha$  line fit with asymmetric Gaussians and the blue circles show the same previous redshifts but including the correction for the offset between the Ly $\alpha$  and the systemic redshift (same as in all plots in the main paper where the  $K$ -estimator results are shown). The black straight line shows the expected  $K$  value of an unclustered sample. All sets of data points are plotted along with Poisson errors. The blue circle and red square values have been shifted along the x-axis for visual purposes.

## 2.B Effect of Ly $\alpha$ derived redshifts on the $K$ -estimator

Inferring the redshift of galaxies from their Ly $\alpha$  lines introduces an offset (i.e. a few hundreds of km/s) with respect to their systemic redshift (Hashimoto et al., 2015). This offset translates into small uncertainties in the derived positions of the galaxies (i.e.  $\sim 3$  Mpc) that would affect the clustering measurements when scrutinized through traditional methods (see e.g. Gurung-López et al., 2021). The  $K$ -estimator compares galaxy pair counts in two consecutive shells along LOS separations. Thus, the offset introduced in the separations affects both shells equally, being simultaneously compensated. However, since we are working with much larger scales than  $\sim 3$  Mpc, even from a theoretical point of view, the  $K$ -estimator is not expected to be sensitive to these redshift offsets.

We prove this in Fig. 2.B.1, considering the same sample of LAEs, but obtaining the redshift of the galaxies in different manners. We first use the redshift estimates from QtClassify (see

Sect. 5.2) and then we use more precise redshifts obtained by fitting asymmetric Gaussian profiles to the Ly $\alpha$  emission lines. Finally, from those precise redshifts we correct the redshift following Verhamme et al. (2018) as described in Sect. 2.2.2. We run the K-estimator for these three samples, which only differ by their source redshift estimates. In Fig. 2.B.1, we show the minimal impact of the redshift uncertainties in our results, showing that the three different redshift samples provide negligible variations in the K-estimator values. The K-estimator on the sample with redshift estimations provides large-scale bias factors of  $b = 3.00^{+1.73}_{-0.56}$  from PL fits, while using the sample with the corrected redshifts (main paper)  $b = 3.03^{+1.51}_{-0.52}$ .

## 2.C Error estimates in the K-estimator

When computing the clustering signal with the K-estimator, we have to recognize that the individual data points are correlated. Various galaxy pairs can be part of more than one  $R_{ij}$  bin and the same galaxy may be counted in more than one galaxy pair. The extent of how bin  $i$  correlates with bin  $j$  is usually expressed with the covariance matrix. However, the small area covered by our survey does not allow us to calculate a covariance matrix. Therefore, we investigated several error approaches for our K-estimator measurements.

We applied the bootstrapping technique described in Ling et al. (1986), which creates pseudo-data sets by sampling  $N$  sources with replacement from the real sample of  $N$  galaxies. In other words, we randomly draw objects from the real sample, allowing multiple selections of the same object, to generate a pseudo-sample with the same number of objects  $N$  as the real sample. We repeat the process 500 times, obtaining a large set of pseudo-samples, which vary moderately from the original data. We compute the K-estimator in the 500 pseudo-samples,  $N_{\text{boots}} = 500$ . The scatter from all the measurements is adapted for our uncertainty estimations.

We also considered a second technique, in which we generate random samples. Ideally, 500 different realizations from cosmological simulations should be applied but we showed in Sect. 4.4.5 that the simulated data cannot directly be compared to our clustering measurements.

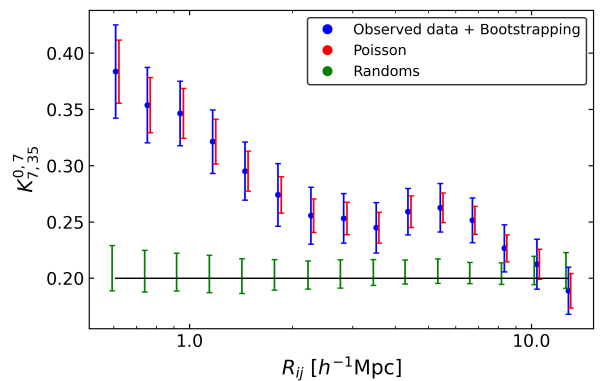


**Figure 2.C.1:**  $K_{7,35}^{0,7}$  estimator of the LAEs in the 68 fields of the MUSE-Wide survey with the different error approaches. Approximated Poisson errors (i.e.  $\sqrt{N_{a1,a2}}/(N_{a1,a2} + N_{a2,a3})$ ) are shown in red, while the blue and green uncertainties are obtained from the bootstrapping and the random sample generation methods, respectively. Both sort of error bars have been shifted in the  $R_{ij}$  direction for illustration purposes. As usual, the black line represents an unclustered sample of galaxies.

Therefore, we use the selection and luminosity functions of the survey (Herenz et al., 2019) to obtain the real  $z$ -distribution of our LAEs (see Sect. 5.2 and red curve in Fig. 2.2). Randomly clustered samples with the same number of objects as the real sample are created from the real redshift distribution. Each new galaxy is located at a random position within the MUSE-Wide survey footprint, with a specific redshift provided by the combination of LF and SF. Following this procedure, we generate 500 different random samples and compute  $K_{a2,a3}^{0,a2}$  in each of the samples. For each bin, the uncertainty has been obtained as the standard deviation from the resulting  $K_{a2,a3}^{a1,a2}$  of the different 500 random samples.

We show the two main uncertainty approaches for the K-estimator in Fig. 3.C.1. We also include the approximated Poisson errors  $\sqrt{N_{a1,a2}}/(N_{a1,a2} + N_{a2,a3})$  calculated by the error propagation of Eq. 2.1.

While the random errors are 20% smaller than Poisson errors, we find that the uncertainties from bootstrapping are moderately larger ( $\sim 35\%$ ) than the Poissonian ones. In order to remain conservative (and even if all uncertainties are comparable), we decided to compute the error bars in our K-estimator analyses following the classical bootstrapping approach. Hence, uncertainties due to cosmic variance are not represented yet in our error estimates of the real data. In other words, repeating the same LAE clustering studies in different regions of the sky can

lead to clustering signals outside our expected uncertainty range. The cosmic variance contribution to the total error budget was explored in Sect. 4.4.5. Including this contribution results in  $\sim 70\%$  larger uncertainties. However, this additional uncertainty does not impact our results when comparing the subsamples because they are obtained in the same sky field.

## 2.D Two-point correlation function analysis

### 2.D.1 2pcf method

Overall, 2pcf is the most commonly used statistical approach to explore the clustering in a sample of objects. Traditionally, those samples cover a broad spatial coverage that accounts for cosmic variance and allows the computation of a covariance matrix to estimate clustering uncertainties. With the MUSE-Wide survey, we are facing the opposite scenario: small spatial coverage and a wide redshift range.

In reconstructing the 2pcf, we follow standard recipes (Landy & Szalay, 1993). To recall,  $\xi(r)$  quantifies the excess probability  $P$  over a random Poisson distribution of finding a pair of galaxies separated by a distance  $r$  (Peebles, 1980)

$$dP = n[1 + \xi(r)]dV, \quad (2.D.1)$$

where  $dV$  is the infinitesimal volume occupied by the pair and  $n$  is the average number density of galaxies.

Galaxy distances along the light of sight (LOS) cannot be measured directly. Instead the redshift information of the galaxies is used, which is affected by their peculiar velocities. In order to eliminate this effect, the so-called redshift space distortions (RSD), we compute the correlation function in a 2D grid. We measure the separation of pairs in the perpendicular distance to the LOS direction,  $r_p$ , and parallel to the LOS direction,  $\pi$ . We then count pairs of LAEs within given separations and compare them to those in a random sample of galaxies by means of the Landy-Szalay estimator (Landy & Szalay, 1993)

$$\xi(r_p, \pi) = \frac{DD(r_p, \pi) - 2DR(r_p, \pi) + RR(r_p, \pi)}{RR(r_p, \pi)}, \quad (2.D.2)$$

where  $DD$ ,  $RR$  and  $DR$  are the normalized data-

data, random-random and data-random pairs. In other words, expressing the actual number of pairs as  $n_{\text{pair},DD}(r_p, \pi)$ ,  $n_{\text{pair},DR}(r_p, \pi)$  and  $n_{\text{pair},RR}(r_p, \pi)$ :

$$\begin{aligned} DD &= n_{\text{pair},DD}(r_p, \pi) / [N_D(N_D - 1)] \\ DR &= \frac{1}{2} n_{\text{pair},DR}(r_p, \pi) / (N_D N_D) \\ RR &= n_{\text{pair},RR}(r_p, \pi) / [N_R(N_R - 1)]. \end{aligned} \quad (2.D.3)$$

$N_D$  and  $N_R$  are the total number of galaxies in the real and random sample, respectively.

We then calculate the projected correlation function  $\omega(r_p)$  by integrating  $\xi(r_p, \pi)$  along the  $\pi$ -direction (Davis & Peebles, 1983)

$$\omega_p(r_p) \approx 2 \int_0^{\pi_{\text{max}}} \xi(r_p, \pi) d\pi, \quad (2.D.4)$$

where  $\omega_p$  is the projected 2pcf and  $\pi_{\text{max}}$  is the maximum allowed LOS distance between pairs of galaxies to be considered as a pair. Also,  $\pi_{\text{max}}$  is chosen such that it accounts for most correlated pairs and the amplitude of  $\omega_p(r_p)$  is able to converge. Very large values would mainly increase the noise since there are not many correlated pairs at large LOS distances. In contrast, very low values would not include most correlated pairs and would effectively underestimate  $\omega_p(r_p)$ .

We compute  $\pi$  within  $10 - 300 h^{-1}\text{Mpc}$  in steps of  $10 h^{-1}\text{Mpc}$  and  $r_p$  in the range of  $0.375 < r_p/[h^{-1}\text{Mpc}] < 13.155$  in 9 logarithmic bins. We then calculate the projected correlation function  $\omega_p(r_p)$  for each  $\pi$  value and fit the analytical solution:

$$\omega_p(r_p) = r_p \left( \frac{r_0}{r_p} \right)^\gamma \frac{\Gamma(1/2) \Gamma((\gamma - 1)/2)}{\Gamma(\gamma/2)}, \quad (2.D.5)$$

where  $\Gamma(x)$  is the Gamma function. The fittings are performed in the range  $0.584 < r_p/[h^{-1}\text{Mpc}] < 13.155$  (two-halo term only) for each of the  $\omega_p(r_p)$  curves.

We measure the correlation length of the curves using Eq. 2.D.5 with a fixed slope of  $\gamma = 1.8$ . In order to be conservative, we use  $\pi_{\text{max}} = 60 h^{-1}\text{Mpc}$ . Similar  $\pi_{\text{max}}$  values are obtained with the simulation described in Sect. 4.4.5. Literature  $\pi_{\text{max}}$  values in similar LAE clustering studies used less conservative values ( $15-20 h^{-1}\text{Mpc}$ ; Durkalec et al., 2014, 2018).

**Table 2.D.1:** Best-fit clustering parameters from 2pcf measurements.

$r_0$ [ $h^{-1}$ Mpc]	$\gamma$	$b_{\text{PL}}$	$b_{\text{HOD}}$	$\log(M_{\text{h}}/[h^{-1}M_{\odot}])$
$2.24^{+0.25}_{-0.35}$	$1.85^{+0.25}_{-0.25}$	$1.66^{+0.36}_{-0.42}$	$2.05^{+0.14}_{-0.14}$	$10.51^{+0.16}_{-0.17}$

**Notes:** The correlation length and slope, the linear bias factor assuming a PL correlation function, the linear bias factor and typical dark matter halo masses from the HOD model are indicated. The uncertainties in the bias factors and DMH masses reflect the statistical error on  $r_0$  only.

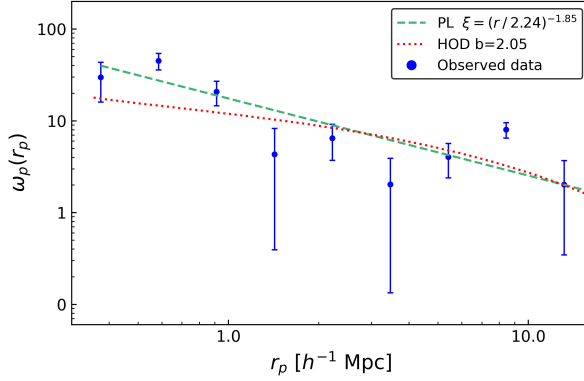


**Figure 2.D.1:** Best PL and HOD fits to the projected 2pcf  $\omega_p(r_p)$  for  $\pi_{\text{max}} = 60 h^{-1}$ Mpc. The dashed green curve shows the PL-fit while the dotted red curve represents the HOD fit. The error bars are determined from the random approach explained in appendix 2.D.2.

Besides the  $\pi_{\text{max}}$  determination, the measurement of the 2pcf also demands the modelling of a random sample of galaxies with the same geometry, selection effects and observational conditions as the real sample. Hence, we constructed a random sample from the real  $z$ -distribution of the sample (red curve in Fig. 2.2) obtained from the SF and the LF of the MUSE-Wide survey (Herenz et al., 2019). The number of random objects is chosen to be 100 times the number of galaxies in the real sample. This makes the variance of  $DR$  and  $RR$  in Eq. 2.D.2 negligible. We verified that increasing the number of random galaxies or using different random samples have an insignificant effect on our estimates. Each random galaxy is then located at a random position of the sky within the MUSE-Wide survey footprint, with a redshift taken from the real  $z$ -distribution. Given that our  $\pi_{\text{max}}$  is much smaller than the radial comoving distance corresponding to our sample redshift range, over which the random sample is constructed, the effects for the integral constraint are negligible for our  $\omega_p(r_p)$ .

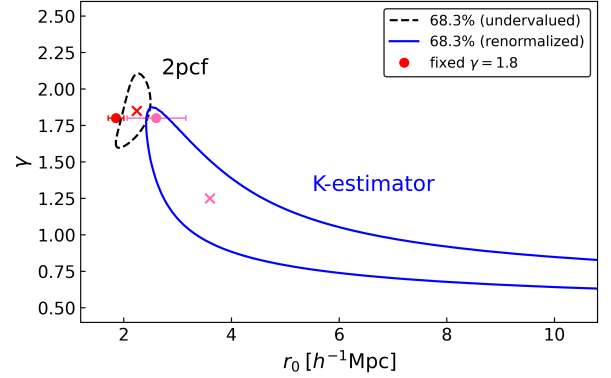


**Figure 2.D.2:** Analogous to Fig. 2.6, here showing the contours from the 2pcf method in black-gray. For a direct comparison to the K-estimator, its contours have been represented in blue, as well as the  $r_0$  computed from both methods when fixing the slope of the PL to the standard value, shown with dots. Please note that we consider the contours of the 2pcf to be likely underestimated (see text for further details).

## 2.D.2 Error estimates

The bootstrapping approach applied in the K-estimator method allows for replacement and galaxy repetitions. This produces an overlap of galaxies, which introduces an unrealistic clustering excess in the 2pcf. While this does not affect the K-estimator because it measures a contrast of galaxy pairs between two LOS regions and overlaps of galaxies cancel out in both areas, the 2pcf is severely affected. We therefore do not consider the bootstrapping approach as a possible error determination technique for the 2pcf.

We consider an alternative approach by generating random samples. Analogous to the error estimates in the K-estimator, 100 different light cones from cosmological simulations should be used instead; however, it was shown in Sect. 4.4.5 that the simulated data should not be directly compared to our measurements. Thus, we created random samples from the real redshift distribution of our LAEs. The random samples have

the same number of objects as the MUSE-Wide survey. The real redshift distribution is calculated from the luminosity and the selection function of the sample (Herenz et al., 2019) as described in Sect. 5.2. We denote the newly created random sample by  $R'$  to distinguish from the random sample  $R$  in Eq. 2.D.2. The 2pcf in the random samples is calculated by replacing  $D$  by  $R'$  in Eq. 2.D.2 for 100 different newly generated random samples  $R'$  (i.e.  $N_{\text{ran}} = 100$ ). The scatter of the 100 runs is used as our uncertainty estimation.

This approach is compared to Poissonian errors calculated by error propagation in Eq. 2.D.2,  $[(\delta_{DD}/RR)^2 + 4 \cdot (\delta_{DR}/RR)^2 + ((2DR - DD) \cdot \delta_{RR}/RR^2)^2]^{1/2}$ . We find that the Poissonian uncertainties underestimate the true clustering errors compared to the random-sample approach (uncertainties from the random error approach are  $\sim 65\%$  larger than Poisson errors). However, even the uncertainties from the random error approach should be understood only as a first guess. The combination of the 2pcf and the special design of our MUSE-Wide survey leave this as the only option to estimate the extent of the uncertainties on the 2pcf.

### 2.D.3 Results

We present the projected correlation function  $\omega_p(r_p)$  for  $\pi_{\text{max}} = 60 h^{-1}\text{Mpc}$  over the range of  $0.375 < r_p/[h^{-1}\text{Mpc}] < 13.155$  in Fig. 2.D.1. The error bars in  $\omega_p(r_p)$  have been computed following the random-sample approach described in Appendix 2.D.2.

Despite the small area covered by the MUSE-Wide survey, the  $\omega_p(r_p)$  curve shows a clear clustering signal. The large number of galaxies in the MUSE-Wide survey allow us to fit the clustering signal with a PL-based correlation function, where both correlation length and slope are constrained simultaneously. Thus, we set  $r_0$  and  $\gamma$  as the free parameters to be determined from the fit.

We then use Eq. 2.D.5 to fit  $\omega_p(r_p)$  in the two-halo term,  $0.584 < r_p/[h^{-1}\text{Mpc}] < 13.155$ . We also use this  $r_p$  range to fit the curve with the HOD model described in Sect. 3.3.3, same as for the K-estimator. The measured best-fit parameters are listed in Table 2.D.1 and shown in Fig. 2.D.1. The probability contours from the  $r_0$ - $\gamma$  grid of the PL-fit are shown in Fig. 2.D.2, along with those from the K-estimator to allow a direct

comparison (see Appendix 2.D.4 for a discussion of the different clustering methods and results).

With the PL-fit, we find  $r_0 = 2.24_{-0.35}^{+0.25} h^{-1}\text{Mpc}$  with a correlation slope  $\gamma = 1.85 \pm 0.25$ . These parameters correspond to  $b = 1.66_{-0.42}^{+0.36}$ . These results are in agreement with the derived correlation lengths from the one-bin fit (fixed  $\gamma = 1.8$ ) and from the PL-fit (free  $r_0$  and  $\gamma$ ) to the K-estimator (contours in Fig. 2.D.2). However, for the 2pcf case,  $\gamma$  is much closer to the canonical value than the K-estimator. When considering HOD fits, we obtain  $b = 2.05 \pm 0.14$ , somewhat lower ( $1.3\sigma$ ) than the  $b = 2.80 \pm 0.38$  obtained with the K-estimator. The differences in the derived linear bias factors from PL and HOD fits are discussed in detail in Sect. 2.5.3.

In order to better constrain the correlation parameters, we fix the correlation slope and determine only the correlation length. Following this procedure (and in an effort to remain consistent with the literature), we fix the slope to  $\gamma = 1.8$  and derive from the one-parameter fit  $r_0 = 1.85 \pm 0.15 h^{-1}\text{Mpc}$ . This value agrees at a one sigma level with the one derived from the K-estimator ( $r_0 = 2.60_{-0.67}^{+0.72} h^{-1}\text{Mpc}$ ; fixed  $\gamma = 1.8$ ).

### 2.D.4 K-estimator vs 2pcf

The various clustering methods studied in this paper allow us to compare not only their respective results but also their success as methods themselves in these sort of surveys. While the 2pcf is well known, the K-estimator is still relatively unexplored. However, for galaxy surveys that cover small areas of the sky, but span wide redshift ranges the K-estimator seems to be a more suitable clustering method than the commonly used 2pcf. Both methods have important similarities but also present critical differences. First of all, the concept of measuring clustering itself differs. While the 2pcf measures the spatial clustering by comparing pairs of galaxies to those in random samples, the K-estimator compares the contrast of galaxy pairs in two consecutive shells along LOS distances, without introducing any random sample and focusing on redshift clustering rather than on spatial clustering. Secondly, choosing the most suitable K-estimator or the upper integration limit  $\pi_{\text{max}}$  in the 2pcf share some concepts. The  $\pi_{\text{max}}$  value where the 2pcf saturates collects the maximum number of galaxy pairs and tries to discard noise from distant uncorrelated pairs. The  $a_2$  and  $a_3$



values of the K-estimator boost the clustering signal by finding the two shells along LOS separations where the highest contrast of galaxy pairs is encountered. Therefore,  $\pi_{\max}$  just represents an upper integration limit in LOS distances and  $a_2$  and  $a_3$  are the length of the shells with the highest difference in pair counts. Typically,  $a_3$  should be below the upper integration limit  $\pi_{\max}$ . Finally, both methods quantify the clustering of a sample of galaxies by counting galaxy pairs in 3D space.

Although the two methods present a clustering signal over equal transverse distances,  $R_{ij}$  and  $r_p$ , and the  $a_i$  values are within the  $\pi_{\max}$  limit, the fitting parameters are somewhat distinct. This was expected because, first, the 2pcf in this type of surveys has issues. Its performance is affected by the small spatial coverage of the data and the survey geometry. We do not see a clear saturation point of the  $\omega(r_p)$  curves for the different  $\pi_{\max}$  values and, in addition, error estimations, such as the jackknife method, fail. Hence, we believe that we are exploring the limit of the method. Secondly, the fits for both methods are carried out in different ways (see Sect. 3.3.1 and Appendix 2.D.3). While we fit  $\omega_p(r_p)$  with its analytical solution (Eq. 2.D.5), the K-estimator is either compared to the expectation value of  $K_{a_2, a_3}^{a_1, a_2}$  (Eq. 2.2) through the one-fit approach or fitted with a PL with the PL-fit approach. If we allow  $r_0$  and  $\gamma$  to freely vary in the fit for both methods, the correlation lengths, bias factors and DMH masses obtained from the K-estimator and the 2pcf are  $r_0 = 3.60_{-0.90}^{+3.10} h^{-1}\text{Mpc}$ ,  $\gamma = 1.30_{-0.45}^{+0.36}$ ,  $b_{\text{HOD}} = 2.80_{-0.38}^{+0.38}$ ,  $\log(M_h/[h^{-1}\text{M}_\odot]) = 11.34_{-0.27}^{+0.23}$  and  $r_0 = 2.24_{-0.35}^{+0.25} h^{-1}\text{Mpc}$ ,  $\gamma = 1.85 \pm 0.25$ ,  $b_{\text{HOD}} = 2.05_{-0.14}^{+0.14}$  and  $\log(M_h/[h^{-1}\text{M}_\odot]) = 10.51_{-0.17}^{+0.16}$ , respectively. Even if the HOD fits from the K-estimator are higher ( $1.3\sigma$ ) than those computed with the 2pcf, the 68.3% confidence intervals of the PL-fits agree.

A noteworthy addition to our discussion is the uncertainty dissimilarities between the methods, where the difference in the probability contour sizes of Fig. 2.D.2 come from. It is important to notice that the uncertainties in the K-estimator were obtained through the bootstrapping approach. However, bootstrapping causes overlaps of galaxies to which the K-estimator is insensitive, but in the 2pcf case, this causes a significant boost in the clustering signal. Thus, we have to consider the random sample approach as the

only way to give some educated guess on the 2pcf uncertainties, even if it most likely still underestimates the real uncertainties. Therefore, the 2pcf contour shown in Fig. 2.D.2 is also most likely underestimated.

For the 2pcf we had to apply the standard (uncorrelated)  $\chi^2$  analysis with likely underestimated uncertainties, while for the K-estimator we were able to renormalize the  $\chi^2$  analysis and used conservative uncertainty estimates as described in Sect. 3.3.2.1. Despite these fundamental differences the clustering results derived from both methods still agree within their combined  $2\sigma$  uncertainties.

The K-estimator is a more suitable clustering statistic than the 2pcf in these kind of surveys for the following reasons: (i) The K-estimator exploits the large redshift coverage rather than the spatial extent (more than  $1000 h^{-1}\text{Mpc}$  along the LOS direction vs only  $20 h^{-1}\text{Mpc}$  over transverse separations); (ii) it does not require a random sample so integral constraint issues do not take place; (iii) we can use bootstrapping uncertainties when the jackknife technique is not an option; and (iv) with the K-estimator we provide a straightforward recipe to obtain rough  $a_2$  and  $a_3$  values (unlike  $\pi_{\max}$  in the 2pcf).

## 2.E Effect of redshift space distortions on our measurements

Both PL and HOD fit approaches show a high performance on the K-estimator. Nevertheless, none of them account for the redshift space distortions present in the observations of the high-redshift Universe. Galaxy structures are observed to be ‘falling into’ large-scale overdensities, which varies the projected velocity along the LOS direction from that linked to its cosmological redshift. As explained in Sect. 3.3.3, we include the effects of the redshift distortion in the HOD model using the linear theory to the two-halo term only. Therefore, the large-scale streaming motion towards overdense regions (i.e. Kaiser infall, Kaiser, 1987) is corrected in the linear regime.

In order to account for these effects, we implement the HOD correlation function in redshift space,  $\xi(s)$ , accounting thus for RSD. We represent the HOD fit to the K-estimator both from

the spatial space,  $\xi(r)$ , (same as in Sect. 5.4) and the redshift space,  $\xi(s)$ , in Fig. 2.E.1.

The HOD fit from the redshift space correlation function (i.e. with RSD) is slightly higher than that from the real space correlation function (i.e. without RSD) at small separations ( $R_{ij} < 1 h^{-1}\text{Mpc}$ ), showing the minimal RSD effect on the K-estimator. This small rise translates into an increase in the derived bias factor, from  $b = 2.80^{+0.38}_{-0.38}$  to  $b = 2.84^{+0.33}_{-0.34}$ , indistinguishable within the  $1\sigma$  error bars.

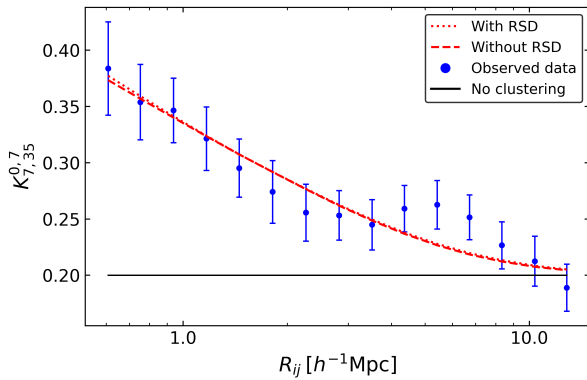


**Figure 2.E.1:** Best HOD fits to the K-estimator from  $\xi(r)$  (same as the thick curve in Fig. 2.7) and  $\xi(s)$ . The dotted red curve represents the HOD that takes into account the effect of the RSD, while the dashed red curve shows the HOD fit without RSD. The black line represents an unclustered sample of galaxies.

## References

- Adelberger, K. L., Steidel, C. C., Pettini, M., et al., (2005), *ApJ*, 558, A33
- Ahumada, R., Prieto, C. A., Almeida, A., et al., (2020), *ApJSS*, 249, 3
- Bacon, R., Accardo, M., Adjali, L., et al., (2010), *Proc. SPIE*, 7735, 773508
- Bielby, R. M., Tummuangpak, P., Shanks, T., et al., (2016), *MNRAS*, 456, 4061
- Coil, A. L., Georgakakis, A., Newman, J. A., et al., (2009), *ApJ*, 701, 1484
- Coil, A. L., Georgakakis, A., Newman, J. A., et al., (2012), 6, *Planets, Stars and Stellar Systems* (Springer, Dordrecht)
- Colless, M., Dalton, G., Maddox, S., et al., (2001), *MNRAS*, 328, 1039
- Cowie, L. L., & M., H. E., (1998), *ApJ*, 115, 1319
- Davis, M., & Peebles, P. J. E., (1983), *ApJ*, 267, 465
- Dayal, P., & Libeskind, N. I., (2012), *MNRAS*, 419, L9
- Diener, C., Wisotzki, L., Schmidt, K. B., et al., (2017), *MNRAS*, 471, 3186
- Durkalec, A., Le Fèvre, O., Pollo, A., et al., (2014), *A&A*, 583, A128
- Durkalec, A., Le Fèvre, O., Pollo, A., et al., (2018), *A&A*, 612, A42
- Forero-Romero, J. E., Yepes, G., Gottlöber, S., et al., (2011), *MNRAS*, 415, 3666
- Fry, J. N., (1996), *ApJ*, 461, L65
- Garel, T., Blaizot, J., Guiderdoni, B., et al., (2012), *MNRAS*, 422, 310
- Garel, T., Blaizot, J., Guiderdoni, B., et al., (2015), *MNRAS*, 450, 1279
- Garel, T., Guiderdoni, B., & Blaizot, J., (2016), *MNRAS*, 455, 3436
- Gawiser, E., Francke, H., Lai, K., et al., (2007), *ApJ*, 671, 278
- Gurung-López, S., Orsi, A., Bonoli, S., et al., (2018), *MNRAS*, 486, 1882
- Gurung-López, S., Saito, S., Baugh, C. M., et al., (2021), *MNRAS*, 500, 603
- Guzzo, L., Scodreggio, M., Garilli, B., et al., (2014), *A&A*, 566, A108
- Hamilton, A., (2001), *MNRAS*, 322, 419
- Hashimoto, T., Verhamme, A., Ouchi, M., et al., (2015), *ApJ*, 812, 157
- Herenz, E. C., Urrutia, T., Wisotzki, L., et al., (2017), *A&A*, 606, A12
- Herenz, E. C., & Wisotzki, L., (2017), *A&A*, 602, A111
- Herenz, E. C., Wisotzki, L., Saust, R., et al., (2019), *A&A*, 621, A107
- Hill, G. J., MacQueen, P. J., Smith, M. P., et al., (2008), *ASP*, 7014, 701470
- Hinshaw, G., Larson, D., Komatsu, E., et al., (2013), *AJSS*, 208, 19
- Inami, H., Bacon, R., Brinchmann, J., et al., (2017), *A&A*, 608, 26
- Jenkins, A., Frenk, C. S., Pearce, F. R., et al., (1998), *ApJ*, 499, 20
- Kaiser, N., (1987), *MNRAS*, 227, 1
- Kerutt, J., (2017), *Astrophysics Source Code Library*
- Khostovan, A. A., Sobral, D., Mobasher, B., et al., (2019), *MNRAS*, 489, 555
- Kron, R., (1980), *ApJS*, 43, 305
- Krumpe, M., Miyaji, T., & Coil, A. L., (2010), *ApJ*, 713, 558
- Krumpe, M., Miyaji, T., Coil, A. L., et al., (2012), *ApJ*, 746, 1
- Krumpe, M., Miyaji, T., Coil, A. L., et al., (2018), *MNRAS*, 474, 1773
- Krumpe, M., Miyaji, T., Husemann, B., et al., (2015), *ApJ*, 815, 21
- Lacey, C., & Cole, S., (1993), *MNRAS*, 262, 627

- Landy, S. D., & Szalay, A. S., (1993), *ApJ*, 412, 64
- Le Fèvre, O., Guzzo, L., Meneux, B., et al., (2005), *A&A*, 439, 877
- Le Fèvre, O., Tasca, L., Cassata, P., et al., (2015), *A&A*, 576, A79
- Li, C., Kaummann, G., Jing, Y., et al., (2006), *MNRAS*, 368, 21
- Lilly, S. J., Le Fèvre, O., Renzini, A., et al., (2007), *ApJS*, 172, 70
- Limber, D. N., (1953), *ApJ*, 117, 134
- Ling, E. N., Frenk, C. S., Barrow, J. D., et al., (1986), *MNRAS*, 223, 21P
- Maseda, M. V., van der Wel, A., Rix, H. W., et al., (2018), *ApJ*, 854, 29
- Miyaji, T., Krumpel, M., Coil, A., et al., (2011), *ApJ*, 726, 83
- Miyaji, T., Zamorani, G., Cappelluti, N., et al., (2007), *ApJS*, 172, 396
- Moustakas, L. A., & Somerville, R. S., (2002), *ApJ*, 577, 1
- Muzahid, S., Schaye, J., Marino, R. A., et al., (2020), *MNRAS*, 496, 1013
- Navarro, J. F., Frenk, C. S., & White, S. D. M., (1997), *ApJ*, 490, 493
- Newman, J. A., Cooper, M. C., Davis, M., et al., (2013), *ApJSS*, 208, 5
- Norberg, P., Baugh, C. M., Hawkins, E., et al., (2002), *MNRAS*, 332, 827
- Orsi, A., Lacey, C. G., & Baugh, C. M., (2012), *MNRAS*, 425, 87
- Ouchi, M., Harikane, Y., Shibuya, T., et al., (2017), *PASJ*, 70, S13
- Ouchi, M., Shimasaku, K., Furusawa, H., et al., (2003), *ApJ*, 582, 60
- Ouchi, M., Shimasaku, K., Furusawa, H., et al., (2010), *ApJ*, 723, 869
- Peebles, P. J. E., (1980), Princeton, N.J., Princeton Univ. Press
- Rhoads, J. E., Malhotra, S., Dey, A., et al., (2000), *ApJ*, 545, L85
- Schmidt, B. K., Kerutt, J., Wisotzki, L., et al., (2021), *A&A*, 645, A80
- Sheth, R., Mo, H. J., & Tormen, G., (2001), *MNRAS*, 323, 1
- Shioya, Y., Taniguchi, Y., Sasaki, S. S., et al., (2009), *ApJ*, 696, 546
- Skrutskie, M. F., Cutri, R. M., Stiening, R., et al., (2006), *AJ*, 131, 1163
- Smith, A., Ma, X., Bromm, V., et al., (2019), *MNRAS*, 484, 39
- Sobral, D., Matthee, J., Best, P., et al., (2017), *MNRAS*, 466, 1242
- Springel, V., (2005), *MNRAS*, 364, 1105
- Steidel, C. C., & Hamilton, D., (1992), *AJ*, 104, 941
- Strauss, M. A., Weinberg, D. H., Lupton, R. H., et al., (2002), *AJ*, 124, 1810
- Tinker, J. L., Weinberg, D. H., & Zheng, Z., (2005), *MNRAS*, 368, 85
- Urrutia, T., Wisotzki, L., Kerutt, J., et al., (2019), *A&A*, 624, 24
- van den Bosch, F. C., (2002), *MNRAS*, 331, 98
- van den Bosch, F. C., More, S., Cacciato, M., et al., (2013), *MNRAS*, 430, 725
- Verhamme, A., Garel, T., Ventou, E., et al., (2018), *MNRAS*, 478, 60
- Yajima, H., Li, Y., & Zhu, Q., (2012), *AASMA*, 219, 129
- Zehavi, I., Blanton, M. R., Frieman, J. A., et al., (2002), *ApJ*, 571, 172
- Zehavi, I., Zheng, Z., Weinberg, D., et al., (2011), *ApJ*, 736, 59
- Zheng, Z., Coil, A., & Zehavi, I., (2007), *ApJ*, 667, 760
- Zheng, Z., & Weinberg, D., (2007), *ApJ*, 659, 1



## Clustering dependence on Lyman- $\alpha$ luminosity from MUSE surveys at $3 < z < 6^*$

Y. Herrero Alonso<sup>1</sup>, T. Miyaji<sup>2</sup>, L. Wisotzki<sup>1</sup>, M. Krumpe<sup>1</sup>, J. Matthee<sup>3</sup>, J. Schaye<sup>4</sup>, H. Aceves<sup>2</sup>, H. Kusakabe<sup>5</sup>, and T. Urrutia<sup>1</sup>

<sup>1</sup> Leibniz-Institut für Astrophysik Potsdam (AIP), An der Sternwarte 16, 14482 Potsdam, Germany

<sup>2</sup> Universidad Nacional Autónoma de México, Instituto de Astronomía (IA-UNAM-E), AP 106, Ensenada 22860, BC, Mexico

<sup>3</sup> Department of Physics, ETH Zurich, Wolfgang-Pauli-Strasse 27, 8093 Zurich, Switzerland

<sup>4</sup> Leiden Observatory, Leiden University, PO Box 9513, 2300 RA Leiden, The Netherlands

<sup>5</sup> Observatoire de Genève, Université de Genève, 51 Ch. des Maillettes, 1290 Versoix, Switzerland

### ABSTRACT

We investigate the dependence of Ly $\alpha$  emitter (LAE) clustering on Ly $\alpha$  luminosity and connect the clustering properties of  $\approx L^*$  LAEs with those of much fainter ones, namely,  $\approx 0.04L^*$ . We use 1030 LAEs from the MUSE-Wide survey, 679 LAEs from MUSE-Deep, and 367 LAEs from the to-date deepest ever spectroscopic survey, the MUSE Extremely Deep Field. All objects have spectroscopic redshifts of  $3 < z < 6$  and cover a large dynamic range of Ly $\alpha$  luminosities:  $40.15 < \log(L_{\text{Ly}\alpha}/\text{erg s}^{-1}) < 43.35$ . We apply the Adelberger et al. K-estimator as the clustering statistic and fit the measurements with state-of-the-art halo occupation distribution (HOD) models. We find that the large-scale bias factor increases weakly with an increasing line luminosity. For the low-luminosity ( $\log\langle L_{\text{Ly}\alpha}/[\text{erg s}^{-1}] \rangle = 41.22$ ) and intermediate-luminosity ( $\log\langle L_{\text{Ly}\alpha}/[\text{erg s}^{-1}] \rangle = 41.64$ ) LAEs, we compute consistent bias factors  $b_{\text{low}} = 2.43^{+0.15}_{-0.15}$  and  $b_{\text{interm.}} = 2.42^{+0.10}_{-0.09}$ , whereas for the high-luminosity ( $\log\langle L_{\text{Ly}\alpha}/[\text{erg s}^{-1}] \rangle = 42.34$ ) LAEs we calculated  $b_{\text{high}} = 2.65^{+0.13}_{-0.11}$ . Consequently, high-luminosity LAEs occupy dark matter halos (DMHs) with typical masses of  $\log(M_h/[h^{-1}M_\odot]) = 11.09^{+0.10}_{-0.09}$ , while low-luminosity LAEs reside in halos of  $\log(M_h/[h^{-1}M_\odot]) = 10.77^{+0.13}_{-0.15}$ . The minimum masses to host one central LAE,  $M_{\text{min}}$ , and (on average) one satellite LAE,  $M_1$ , also vary with Ly $\alpha$  luminosity, growing from  $\log(M_{\text{min}}/[h^{-1}M_\odot]) = 10.3^{+0.2}_{-0.3}$  and  $\log(M_1/[h^{-1}M_\odot]) = 11.7^{+0.3}_{-0.2}$  to  $\log(M_{\text{min}}/[h^{-1}M_\odot]) = 10.7^{+0.2}_{-0.3}$  and  $\log(M_1/[h^{-1}M_\odot]) = 12.4^{+0.4}_{-0.6}$  from low- to high-luminosity samples, respectively. The satellite fractions are  $\lesssim 10\%$  ( $\lesssim 20\%$ ) at  $1\sigma$  ( $3\sigma$ ) confidence level, supporting a scenario in which DMHs typically host one single LAE. We next bisected the three main samples into disjoint subsets to thoroughly explore the dependence of the clustering properties on  $L_{\text{Ly}\alpha}$ . We report a strong ( $8\sigma$ ) clustering dependence on Ly $\alpha$  luminosity, not accounting for cosmic variance effects, where the highest luminosity LAE subsample ( $\log(L_{\text{Ly}\alpha}/\text{erg s}^{-1}) \approx 42.53$ ) clusters more strongly ( $b_{\text{highest}} = 3.13^{+0.08}_{-0.15}$ ) and resides in more massive DMHs ( $\log(M_h/[h^{-1}M_\odot]) = 11.43^{+0.04}_{-0.10}$ ) than the lowest luminosity one ( $\log(L_{\text{Ly}\alpha}/\text{erg s}^{-1}) \approx 40.97$ ), which presents a bias of  $b_{\text{lowest}} = 1.79^{+0.08}_{-0.06}$  and occupies  $\log(M_h/[h^{-1}M_\odot]) = 10.00^{+0.12}_{-0.09}$  halos. We discuss the implications of these results for evolving Ly $\alpha$  luminosity functions, halo mass dependent Ly $\alpha$  escape fractions, and incomplete reionization signatures.

\*A version of this chapter is published in *Astronomy & Astrophysics* as Herrero Alonso et al. 2023, Volume 671, A5.

### 3.1 Introduction

Dark matter halos (DMHs) serve as sites of galaxy formation but their co-evolution is still a matter of investigation. Observations deliver snapshots of the luminosities of galaxies at given redshifts, while numerical analyses succeed at simulating the evolution and copiousness of DMHs. Linking these two constituents is not straightforward but, because the spatial distribution of baryonic matter is biased against that of dark matter (DM), the former indirectly traces the latter. The evolutionary stage of the two distributions depends on both the epoch of galaxy formation and the physical properties of galaxies (see Wechsler & Tinker 2018 for a review). Thus, studying the dependence of the baryonic-DM relation on galaxy properties is essential for better understanding the evolution of the two components.

Exploring the spatial distribution of high-redshift ( $z > 2$ ) galaxies and its dependence on physical properties provides an insight into the early formation and evolution of the galaxies we observe today. Clustering statistics yield observational constraints on the relationship between galaxies and DMHs, as well as on their evolution. Traditional studies of high- $z$  galaxies (Steidel et al., 1996; Hu et al., 1998; Ouchi et al., 2003; Gawiser et al., 2007; Ouchi et al., 2010; Khostovan et al., 2019) model the large-scale ( $R \gtrsim 1 - 2 h^{-1}\text{cMpc}$ ) clustering statistics with a two parameter power-law correlation function that takes the form  $\xi = (r/r_0)^{-\gamma}$  (Davis & Peebles, 1983) to derive the large-scale linear galaxy bias and the associated typical DMH mass. To make full use of the clustering measurements, the smaller separations of the nonlinear regime ( $R \lesssim 1 - 2 h^{-1}\text{cMpc}$ ) are modelled by relating galaxies to DMHs within the nonlinear framework of halo occupation distribution (HOD) modelling. In this context, the mean number of galaxies in the DMH is modelled as a function of DMH mass, further assessing whether these galaxies occupy the centers of the DMHs or whether they are satellite galaxies.

Although clustering studies of high-redshift galaxies are plentiful, HOD modelling has been rarely used to interpret the results. While several works have focused on Lyman-break galaxy (LBG) surveys, only one study fit a sample of Lyman- $\alpha$  emitters (LAEs) with HOD models (Ouchi et al., 2017). Durkalec et al. (2014), Malkan

et al. (2017), Hatfield et al. (2018), and Harikane et al. (2018) applied the full HOD framework to sets of LBGs to put constraints on the central and satellite galaxy populations, while Ouchi et al. (2017) partially exploited the power of HOD models in a sample of LAEs to infer the threshold DMH mass for central galaxies.

The number of studies that have investigated the correlations between clustering strength and physical properties of high-redshift galaxies is slightly higher. In [OII] and [OIII] emission-line-selected galaxy samples, Khostovan et al. (2018) found a strong halo mass dependence on the line luminosity and stellar mass. Durkalec et al. (2018) also observed a correlation with stellar mass, together with a further dependence on UV luminosity, in a sample of LBGs. However, these correlations become somewhat unclear near the epoch of reionization ( $z \approx 6$ ). Based on LAEs surveys, Ouchi et al. (2003), Bielby et al. (2016), and Kusakabe et al. (2018) revealed tentative trends ( $\approx 1\sigma$ ) between luminosity (both UV and Ly $\alpha$ ) and clustering strength, while only Khostovan et al. (2019) reported a clear ( $5\sigma$ ) correlation between inferred DMH mass and Ly $\alpha$  luminosity.

In a previous study (Herrero Alonso et al., 2021), we used 68 MUSE-Wide fields to measure the LAE clustering with the K-estimator method presented in Adelberger et al. (2005). We computed the clustering at large scales ( $R > 0.6 h^{-1}\text{Mpc}$ ) to derive the linear bias factor and the typical DMH mass of LAEs. By splitting our main sample into subsets based on physical properties of LAEs, we also found a tentative  $2\sigma$  dependence on Ly $\alpha$  luminosity. Here, we extend this work with larger and more deeply spectroscopically confirmed samples and a refined set of analysis methods. We measured the clustering at smaller scales, applied full HOD modelling, and studied the dependence of the clustering properties on Ly $\alpha$  luminosity.

The paper is structured as follows. In Sect. 5.2, we describe the data used for this work and we characterize the LAE samples. In Sect. 5.3, we explain our method for measuring and analyzing the clustering properties of our galaxy sets. We present the results of our measurements in Sect. 5.4. In Sect. 5.5, we discuss our results and their implications, and we investigate the clustering dependence on Ly $\alpha$  luminosity. We give our conclusions in Sect. 5.6.

Throughout this paper, all distances are measured in comoving coordinates and given in

units of  $h^{-1}\text{Mpc}$  (unless otherwise stated), where  $h = H_0/100 = 0.70 \text{ km s}^{-1} \text{ Mpc}^{-1}$ . We assume the same  $h$  to convert line fluxes to luminosities. Thus, there are implicit  $h_{70}^{-2}$  factors in the line luminosities. We use a  $\Lambda\text{CDM}$  cosmology and adopt  $\Omega_M = 0.3$ ,  $\Omega_\Lambda = 0.7$ , and  $\sigma_8 = 0.8$  (Hinshaw et al., 2013). All uncertainties represent  $1\sigma$  (68.3%) confidence intervals.

## 3.2 Data

The MUSE spectroscopic surveys are based on a wedding cake design, namely: a first spatially wide region (bottom of the cake) is observed with a short exposure time (1 hour), while deeper observations (10 hours exposure) are carried out within the first surveyed area (middle tier of the cake). Contained in the last observed region, an even deeper survey (140 h) is then built up (at the top of the cake). These three surveys are known as: MUSE-Wide (Herenz et al., 2017; Urrutia et al., 2019), MUSE-Deep (Bacon et al., 2017; Inami et al., 2017; Bacon et al., 2021), and MUSE Extremely Deep Field (MXDF; Bacon et al. 2021). Each of them can be seen as a different layer of a wedding cake, where higher layers become spatially smaller and correspond to deeper observations. In what follows, we give further details on survey and galaxy sample construction.

### 3.2.1 MUSE-Wide

The spectroscopic MUSE-Wide survey (Herenz et al., 2017; Urrutia et al., 2019) comprises 100 MUSE fields distributed in the CANDELS/GOODS-S, CANDELS/COSMOS and the Hubble Ultra Deep Field (HUDF) parallel field regions. Each MUSE field covers  $1 \text{ arcmin}^2$ . While 91 fields were observed with an exposure time of one hour, nine correspond to shallow (1.6 hours) reduced subsets of the MUSE-Deep data (see next section; as well as Bacon et al., 2017), located within the HUDF in the CANDELS/GOODS-S region. However, we do not include the objects from this region since they overlap with the MUSE-Deep sample (see next section and gap in the left panel of Fig. 3.2.1). The slight overlap between adjacent fields leads to a total spatial coverage of  $83.52 \text{ arcmin}^2$ . The red circles in Fig. 3.2.1 display the spatial distribution of the LAEs from the MUSE-Wide survey. We refer to Urrutia et al. (2019) for further de-

tails on the survey build up, reduction and flux calibration of the MUSE data cubes.

In this paper, we extend (x2 spatially, 50% more LAEs) the sample used in Herrero Alonso et al. (2021) and include all the 1 h exposure fields from the MUSE-Wide survey. Despite the somewhat worse seeing (generally) in the COSMOS region (right panel of Fig.3.2.1), we demonstrate in Appendix 3.A that adding these fields does not significantly impact our clustering results but helps in minimizing the effects of cosmic sample variance.

We also expanded the redshift range of the sample. While MUSE spectra cover  $4750\text{--}9350 \text{ \AA}$ , implying a  $\text{Ly}\alpha$  redshift interval of  $2.9 < z < 6.7$ , we limited the redshift range to  $3 < z < 6$  (differing from the more conservative range of Herrero Alonso et al. 2021;  $3.3 < z < 6$ ) as the details of the selection function near the extremes are still being investigated. Section 2 of Herrero Alonso et al. (2021) describes the aspects relevant to our analysis on the construction of a sample of LAEs, as well as the strategy to measure line fluxes and redshifts. The redshift distribution of the sample is shown in red in the top panel of Fig. 3.2.2. Systematic uncertainties introduced in the redshift-derived 3D positions of the LAEs have negligible consequences for our clustering approach (see Sect. 2.2 in Herrero Alonso et al. 2021).

Within  $83.52 \text{ arcmin}^2$  and in the selected redshift interval, we detected a total of 1030 LAEs. This implies a LAE density of more than 13 objects per  $\text{arcmin}^2$  or  $n \approx 1 \cdot 10^{-3} h^3 \text{Mpc}^{-3}$  (for  $3 < z < 6$ ). At the median redshift of the sample  $\langle z \rangle = 4.0$ , the transverse extent of the footprint is  $\approx 43 h^{-1}\text{Mpc}$ . The range of  $\text{Ly}\alpha$  luminosities is  $40.92 < \log(L_{\text{Ly}\alpha}/[\text{erg s}^{-1}]) < 43.35$  (see red circles in Fig. 3.2.2), with a median value of  $\log\langle L_{\text{Ly}\alpha}/[\text{erg s}^{-1}] \rangle = 42.34$  (or  $\approx L^*$  in terms of characteristic luminosity  $L^*$ ; Herenz et al. 2019), which makes this sample the highest luminosity data set of our three considered surveys. The  $\text{Ly}\alpha$  luminosity distribution is shown in red in the right panel of Fig. 3.2.2. The main properties of the MUSE-Wide LAEs are summarized in Table 5.2.1.

### 3.2.2 MUSE-Deep

MUSE-Deep (10 hour MOSAIC; Bacon et al., 2017; Inami et al., 2017; Bacon et al., 2021) encompasses nine fields located in the CANDELS/GOODS-S region of the HUDF, each

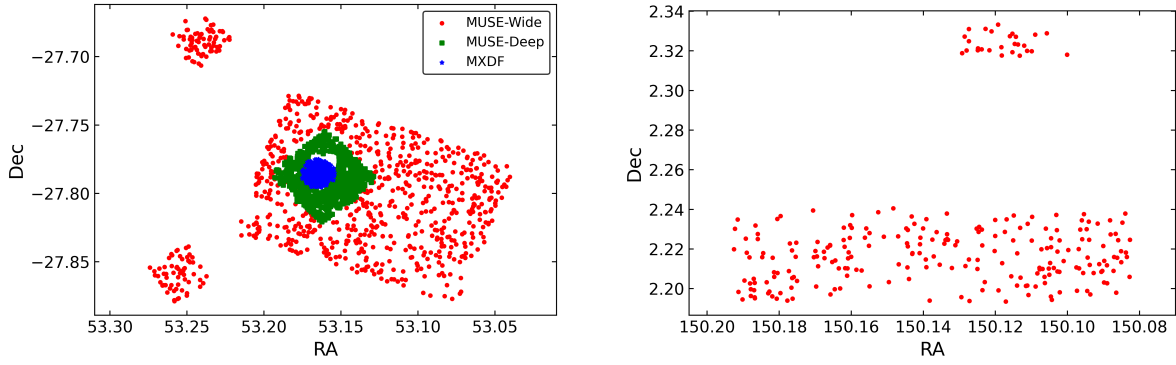


**Figure 3.2.1:** Spatial distribution of the LAEs from the MUSE-Wide survey (red circles), MUSE-Deep (green squares) and MXDF (blue stars). The overlapping objects between the MXDF and MUSE-Deep samples have been removed from the MUSE-Deep LAE set, while those LAEs overlapping in MUSE-Deep and MUSE-Wide have been removed from the MUSE-Wide LAE sample. The MUSE-Wide survey covers part of the CANDELS/GOODS-S region and the HUDF parallel fields (left panel) as well as part of the CANDELS/COSMOS region (right panel). See Figure 1 in Urrutia et al. (2019) for the layout of the MUSE-Wide survey without individual objects, Figure 1 in Bacon et al. (2017) for that of MUSE-Deep, and Figure 2 in Bacon et al. (2021) for that of MUSE-Deep (MOSAIC) and MXDF together.

spanning  $1 \text{ arcmin}^2$  and observed with a 10 h exposure time. The total spatial coverage is  $9.92 \text{ arcmin}^2$ . We represent the spatial distribution of the survey in green in Fig. 3.2.1. We did, however, remove the MUSE-Deep objects that are selected in the deepest survey, described in the next section. We refer to Bacon et al. (2017), Bacon et al. (2021) for a detailed description on survey construction and data reduction.

The sources in MUSE-Deep were blindly detected and extracted using ORIGIN (Mary et al., 2020), based on a matched filtering approach and developed to detect faint emission lines in MUSE datacubes. While the redshift measurements and line classifications were carried out with pyMarZ, a python version of the redshift fitting software MarZ (Hinton et al., 2016), the line flux determination was conducted with pyPlatefit, which is a python module optimized to fit emission lines of high-redshift spectra. The redshift distribution of the sample is shown in green in the top panel of Fig. 3.2.2, also within  $3 < z < 6$ .

The LAE density of the MUSE-Deep sample is  $8 \cdot 10^{-3} h^3 \text{Mpc}^{-3}$  (68 LAE per  $\text{arcmin}^2$  in the whole redshift range). The survey spans  $\approx 8.7 h^{-1} \text{Mpc}$  transversely. The range of  $\text{Ly}\alpha$  luminosities is  $40.84 < \log(L_{\text{Ly}\alpha}/[\text{erg s}^{-1}]) < 43.12$ , represented with green squares in Fig. 3.2.2, together with its distribution (right panel). MUSE-Deep is our intermediate luminous dataset, with a median luminosity of  $\log\langle L_{\text{Ly}\alpha}/[\text{erg s}^{-1}] \rangle = 41.64$ . The sample properties are recorded in Table 5.2.1.

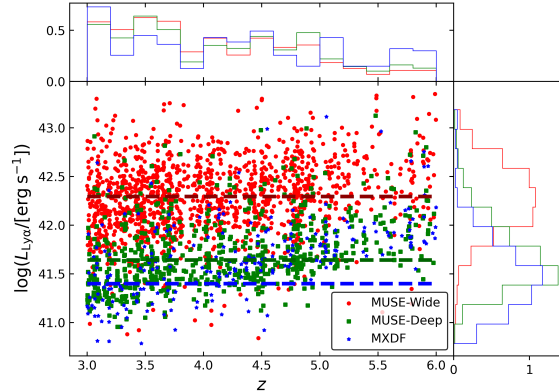


**Figure 3.2.2:**  $\text{Ly}\alpha$  luminosity-redshift for the LAEs in MUSE-Wide (red circles), MUSE-Deep (green squares) and MXDF (blue stars). The dashed colored lines correspond to the median  $\log L_{\text{Ly}\alpha}$  values of the corresponding samples. The redshift and  $L_{\text{Ly}\alpha}$  distributions are shown in the top and right panel, respectively.

### 3.2.3 MUSE Extremely Deep

The MUSE Extremely Deep Field (Bacon et al., 2021) is situated in the CANDELS/GOODS-S region and overlaps with MUSE-Deep and MUSE-Wide. It is composed of a single quasi circular field with inner and outer radii of  $31''$  and  $41''$ , respectively. While a 140 hour exposure was employed to observe the totality of the field, the inner field is 135 hours deep, decreasing to 10 hours depth at the outer radius. This makes MXDF the deepest spectroscopic survey to date. For further details see Bacon et al. (2021) and the blue



**Table 3.2.1:** Properties of the LAE samples.

	Area	Number LAEs	$\langle z \rangle$	$n$	$\log L_{\text{Ly}\alpha}$	$\log \langle L_{\text{Ly}\alpha} \rangle$
MUSE-Wide	83.52	1030	4.0	$1 \cdot 10^{-3}$	40.92 – 43.35	42.34 ( $\approx L^*$ )
MUSE-Deep	9.92	679	4.1	$8 \cdot 10^{-3}$	40.84 – 43.12	41.64 ( $\approx 0.2L^*$ )
MXDF	1.47	367	4.2	$3 \cdot 10^{-2}$	40.15 – 43.09	41.22 ( $\approx 0.08L^*$ )

**Notes:** Properties marked with  $\langle \rangle$  represent median values for the galaxies in the samples. The area is given in arcmin<sup>2</sup>, the number density in  $h^3\text{Mpc}^{-3}$ , and the Ly $\alpha$  luminosities in erg s<sup>-1</sup>.

**Table 3.2.2:** Properties of the LAE subsamples.

	Number LAEs	$\langle z \rangle$	$\log \langle L_{\text{Ly}\alpha} / [\text{erg s}^{-1}] \rangle$
MUSE-Wide low L	( $\log L_{\text{Ly}\alpha} < 42.34$ )	515	3.7
MUSE-Wide high L	( $\log L_{\text{Ly}\alpha} > 42.34$ )	515	4.1
MUSE-Deep low L	( $\log L_{\text{Ly}\alpha} < 41.64$ )	340	3.7
MUSE-Deep high L	( $\log L_{\text{Ly}\alpha} > 41.64$ )	339	4.5
MXDF low L	( $\log L_{\text{Ly}\alpha} < 41.22$ )	183	4.0
MXDF high L	( $\log L_{\text{Ly}\alpha} > 41.22$ )	184	4.5

**Notes:** Properties marked with  $\langle \rangle$  represent median values for the galaxies in the subsamples.

data points in Fig.3.2.1, where the MXDF field is overplotted on the previous surveys.

The survey assembly and data reduction is described in Bacon et al. (2021) and is similar to the one applied to MUSE-Deep (Bacon et al., 2017). The source extraction in MXDF and the redshift and flux measurements are conducted following the same procedure as was done for MUSE-Deep. The redshift distribution of the sample is shown in blue in the top panel of Fig. 3.2.2.

Contained within  $\approx 1.47$  arcmin<sup>2</sup> and over the same redshift range as for the previous catalogues, we detected 367 LAEs, corresponding to a LAE density of  $n \approx 3 \cdot 10^{-2} h^3\text{Mpc}^{-3}$  (432 LAEs per arcmin<sup>2</sup> at  $3 < z < 6$ ). With a median redshift of  $\langle z \rangle = 4.2$ , the footprint covers  $\approx 2.8 h^{-1}\text{Mpc}$  (transversely). The Ly $\alpha$  luminosities span  $40.15 < \log(L_{\text{Ly}\alpha} / [\text{erg s}^{-1}]) < 43.09$  (see blue stars in Fig. 3.2.2 and its distribution in the right panel). The median Ly $\alpha$  luminosity is  $\log \langle L_{\text{Ly}\alpha} / [\text{erg s}^{-1}] \rangle = 41.22$  (or  $\approx 0.08L^*$ ), more than one order of magnitude fainter than for MUSE-Wide. This makes MXDF the faintest ever observed sample of non-lensed LAEs. The main properties are listed in Table 5.2.1.

### 3.2.4 LAE subsamples

We bisected the main samples into disjoint subsets based on their median Ly $\alpha$  luminosity to investigate the clustering dependence on this quan-

tity. We did not merge the main LAE datasets because their distinct Ly $\alpha$  luminosities, together with their slightly different location on the sky, might introduce systematics in the clustering measurements. The subsample properties are summarized in Table 3.2.2 and described in the following.

We split the MUSE-Wide sample at the median Ly $\alpha$  luminosity  $\log \langle L_{\text{Ly}\alpha} / [\text{erg s}^{-1}] \rangle = 42.34$ . The two subsamples consist of 515 LAEs each. The low-luminosity subset has a median redshift and Ly $\alpha$  luminosity of  $\langle z_{\text{low}} \rangle = 3.7$  and  $\log \langle L_{\text{Ly}\alpha\text{low}} / [\text{erg s}^{-1}] \rangle = 42.06$ , while the high-luminosity subsample has  $\langle z_{\text{high}} \rangle = 4.1$  and  $\log \langle L_{\text{Ly}\alpha\text{high}} / [\text{erg s}^{-1}] \rangle = 42.53$ . The median redshift of the number of galaxy pairs for the low-luminosity subset is  $z_{\text{pair}} \approx 3.4$ , and that for the high-luminosity one is  $z_{\text{pair}} \approx 4.1$ .

We next bisected the MUSE-Deep set at the median Ly $\alpha$  luminosity  $\log \langle L_{\text{Ly}\alpha} / [\text{erg s}^{-1}] \rangle = 41.64$ . The low-luminosity subsample has 340 LAEs and presents a median redshift and Ly $\alpha$  luminosity of  $\langle z_{\text{low}} \rangle = 3.7$  and  $\log \langle L_{\text{Ly}\alpha\text{low}} / [\text{erg s}^{-1}] \rangle = 41.46$ . The high-luminosity subset is formed by 339 LAEs with  $\langle z_{\text{high}} \rangle = 4.5$  and  $\log \langle L_{\text{Ly}\alpha\text{high}} / [\text{erg s}^{-1}] \rangle = 41.89$ . While for the low-luminosity subsample  $z_{\text{pair}} \approx 3.5$ , for the high-luminosity one  $z_{\text{pair}} \approx 4.4$ .

We also divide the sample with the largest dynamic range of Ly $\alpha$  luminosities (MXDF) at the

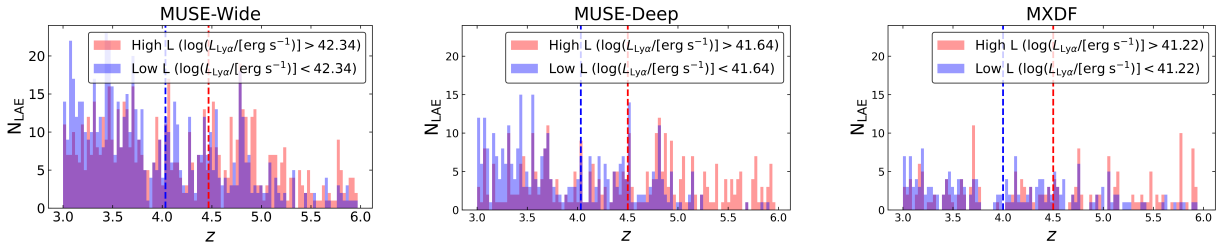


**Figure 3.2.3:** Redshift distribution of the subsamples bisected at the median  $\text{Ly}\alpha$  luminosity of MUSE-Wide, MUSE-Deep and MXDF (panels from left to right). Blue (red) colors show the low- (high-) luminosity subsets. The vertical dashed lines represent the median redshift of the corresponding subsample.

median  $\text{Ly}\alpha$  luminosity  $\log\langle L_{\text{Ly}\alpha}/[\text{erg s}^{-1}] \rangle = 41.22$ . While the lower luminosity subset contains 183 LAEs with  $\langle z_{\text{low}} \rangle = 4.0$  and  $\log\langle L_{\text{Ly}\alpha\text{low}}/[\text{erg s}^{-1}] \rangle = 40.97$ , the higher luminosity subsample consists of 184 LAEs with  $\langle z_{\text{high}} \rangle = 4.5$  and  $\log\langle L_{\text{Ly}\alpha\text{high}}/[\text{erg s}^{-1}] \rangle = 41.54$ . For the low-luminosity subset, we have  $z_{\text{pair}} \approx 3.9$ , and for the high-luminosity one, we have  $z_{\text{pair}} \approx 4.8$ .

The redshift distribution of each subsample is shown in Fig. 3.2.3. The corresponding median redshifts are represented with a vertical dashed line. Despite the similar median redshifts between the subsample pairs, the redshift distributions are significantly different, with a higher amount of spike-trough contrasts in the high-luminosity subsets.

## 3.3 Methods

### 3.3.1 K-estimator

Galaxy clustering is commonly measured by two-point correlation function (2pcf) statistics. Samples investigated by this method typically span several square degrees on the sky. With MUSE, we encounter the opposite scenario. By design, MUSE surveys cover small spatial extensions on the sky and provide a broad redshift range. Although the MUSE-Wide survey is the largest footprint of all MUSE samples, its nature is still that of a pencil-beam survey. Its transverse scales are of the order of  $40 h^{-1}\text{Mpc}$ , while in redshift space it reaches almost  $1500 h^{-1}\text{Mpc}$ . If we consider the deeper samples, the difference is even more prominent:  $8.7$  vs  $1500 h^{-1}\text{Mpc}$  for MUSE-Deep and  $2.8$  versus  $1500 h^{-1}\text{Mpc}$  for MXDF. It is thus paramount to exploit the radial scales and utilize alternative methods to the traditional 2pcf.

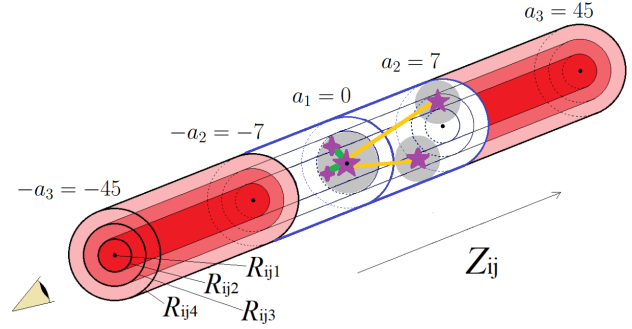


**Figure 3.3.1:** Sketch of the K-estimator, representing the relative geometry that probe the one- and two-halo term scales. The empty blue and filled red cylinders, delimited by  $|a_2| = 7 h^{-1}\text{Mpc}$  and  $|a_3| = 45 h^{-1}\text{Mpc}$  respectively, illustrate the line-of-sight distance  $Z_{ij}$  intervals within which we count galaxy pairs at fixed transverse separations  $R_{ij}$ , represented by nested cylinders. Pairs of LAEs connected with green lines within the same DMH (filled gray circle) contribute to the one-halo term (small  $R_{ij}$  scales), while pairs belonging to two different DMHs (yellow lines) probe the two-halo term (larger  $R_{ij}$  separations).

In Herrero Alonso et al. (2021) we applied the so-called K-estimator, introduced by Adelberger et al. (2005), to a subset of our current sample. Here, we build on our previous work by extending the dataset and measuring the small-scale clustering required to perform full HOD modelling. The details of the K-estimator are given in Sect. 3.1 of Herrero Alonso et al. (2021). In the following, we provide a brief description of the method.

The K-estimator measures the radial clustering along line-of-sight distances,  $Z_{ij}$ , by counting galaxy pairs (formed by galaxy  $i$  and galaxy  $j$ ) in redshift space at fixed transverse separations,  $R_{ij}$ . Although the K-estimator does not need a random sample to carry out the clustering measurements, its nature is very similar to that of the projected two-point correlation function. We bin by  $R_{ij}$ , shown with distinct radii in the cylin-

ders of Fig. 3.3.1, and count the number of pairs within individual transverse bins, for two different ranges of  $Z_{ij}$ , represented in red and blue in Fig. 3.3.1. The K-estimator as a function of  $R_{ij}$  is then defined as the ratio of galaxy pairs within the first  $Z_{ij}$  interval (blue cylinder) and the total  $Z_{ij}$  range (red and blue cylinder), quantifying the excess of galaxy pairs in the first  $Z_{ij}$  bin with respect to the total one. We optimize the choice of the  $Z_{ij}$  ranges, and thus the K-estimator, by seeking out the estimator that delivers the best sensitivity for the clustering signal (i.e., the highest signal-to-noise ratio, S/N; see Sect. 3.1.2 in Herrero Alonso et al. 2021). Although slightly different than in Herrero Alonso et al. (2021), we find nearly identical K-estimators for each of the current samples ( $K_{7,45}^{0,7}$  for MUSE-Wide,  $K_{7,45}^{0,7}$  for MUSE-Deep, and  $K_{7,40}^{0,7}$  for MXDF), whose clustering signals only differ in their S/N. We chose the same K-estimator for the three data sets,  $K_{7,45}^{0,7}$ .

The K-estimator is directly related to the average underlying correlation function (see Eq. 2 in Herrero Alonso et al. 2021). In fact, its definition is proportional to a combination of projected two-point correlation functions corresponding to the blue and red cylinders of Fig. 3.3.1. While the traditional 2pcf method integrates the correlation function  $\xi(R_{ij}, Z_{ij})$  over line-of-sight separations up to a maximum line-of-sight distance  $\pi_{\max}$ , the K-estimator integrates up to  $a_2$  and  $a_3$ . The correlation function  $\xi(R_{ij}, Z_{ij})$  can be approximated with a power-law following Limber (1953) equations as we did in Herrero Alonso et al. (2021), or modelled with a halo occupation distribution (HOD) model (see Sect. 3.3.3). For reference, randomly distributed galaxies in space ( $\xi(R_{ij}, Z_{ij}) = 0$ ) provide  $K_{7,45}^{0,7}(R_{ij})$  values equal to 7/45 (see Eq. 2 in Herrero Alonso et al. 2021). Samples with data points significantly above 7/45 dispense clustering signals.

### 3.3.2 Error estimation

#### 3.3.2.1 Error estimation for the MUSE-Wide survey

Applying clustering statistics delivers correlated data points. One single galaxy might be part of more than one galaxy pair and can therefore contribute to several  $R_{ij}$  bins, especially if they are adjacent. In order to quantify the actual correlation between data points, we applied the jackknife resampling technique, followed by the

computation of the covariance matrix (see e.g., Krumpel et al., 2010; Miyaji et al., 2011). For the MUSE-Wide sample, we employed ten logarithmic bins in the range  $0.16 < R_{ij} < 27.5 h^{-1}\text{Mpc}$ , discarding lower  $R_{ij}$  scales since they host very few galaxy pairs.

We then found a compromise between the number of independent regions (jackknife zones) and the size of the jackknife zones and divide the sky coverage into  $N_{\text{jack}} = 10$  regions, each of which extends  $\approx 4 h^{-1}\text{Mpc}$  in both RA and Dec directions (see Appendix 3.B for a visual representation of the sky division). The limited spatial extent of the survey does not allow for a higher number of jackknife zones. We then constructed  $N_{\text{jack}}$  jackknife subsamples, excluding one jackknife zone at a time, and computed the K-estimator for each of the subsets. The K-estimator measurements are then used to derive the covariance matrix  $M_{ij}$ , which quantifies the correlation between bins  $i$  and  $j$ . The matrix is expressed as

$$M_{ij} = \frac{N_{\text{jack}} - 1}{N_{\text{jack}}} \left[ \sum_{k=1}^{N_{\text{jack}}} \left( K_k(R_i) - \langle K(R_i) \rangle \right) \times \left( K_k(R_j) - \langle K(R_j) \rangle \right) \right], \quad (3.1)$$

where  $K_k(R_i)$ ,  $K_k(R_j)$  are the K-estimators from the  $k$ -th jackknife samples and  $\langle K(R_i) \rangle$ ,  $\langle K(R_j) \rangle$  are the averages over all jackknife samples in the  $i$ ,  $j$  bins, respectively. The error bar for the K-estimator at the  $i$ th bin comes from the square root of the diagonal element ( $\sqrt{M_{ii}}$ ) of the covariance matrix, our so-called "jackknife uncertainty." This approach could not be followed in Herrero Alonso et al. (2021) because of the smaller sky coverage. Instead, we used a galaxy bootstrapping approach. In Appendix 3.C, we compare the two techniques and show that bootstrapping uncertainties are  $\approx 50\%$  larger than the jackknife error bars, in agreement with Norberg et al. (2009), who found that bootstrapping overestimates the uncertainties.

We next search for the best-fit parameters by minimizing the correlated  $\chi^2$  values according

to

$$\chi^2 = \sum_{i=1}^{N_{\text{bins}}} \sum_{j=1}^{N_{\text{bins}}} \left( K(R_i) - K(R_i)^{\text{HOD}} \right) \times M_{ij}^{-1} \left( K(R_j) - K(R_j)^{\text{HOD}} \right), \quad (3.2)$$

where  $N_{\text{bins}} = 10$  is the number of  $R_{ij}$  bins,  $K(R_i)$ ,  $K(R_j)$  are the measured K-estimators and  $K(R_i)^{\text{HOD}}$ ,  $K(R_j)^{\text{HOD}}$  are the K-estimators predicted by the HOD model for each  $i$ ,  $j$  bin, respectively.

Regardless of the larger sample considered in this work, we are still limited by the spatial size of the survey, which only permits a small number of jackknife zones. The insufficient statistics naturally lead to a higher noise contribution in the covariance matrix, which cause the  $\chi^2$  minimization to mathematically fail (i.e., cases of  $\chi^2 < 0$ ) when the full covariance matrix is included. Hence, we only incorporated the main diagonal of the matrix and its two contiguous diagonals. In Appendix 3.B, we discuss the high level of noise in the matrix elements corresponding to bins that are significantly apart from each other. We also verify the robustness of our approach and show that our clustering results are not altered (within  $1\sigma$ ) by this choice.

### 3.3.2.2 Error estimation for the deeper surveys

The small sky coverage of the deeper surveys does not allow us to follow the same error estimation approach as for the MUSE-Wide survey. In Appendix 3.C, we not only compare the bootstrapping technique applied in Herrero Alonso et al. (2021) to the jackknife approach performed in MUSE-Wide, but we also consider the Poisson uncertainties. We demonstrate that Poisson and jackknife errors are comparable in our sample. In fact, we show that while bootstrapping uncertainties are  $\approx 50\%$  larger than jackknife errors, Poisson uncertainties are only  $\approx 7\%$  higher. Thus, and similarly to Adelberger et al. (2005), Diener et al. (2017), and Khostovan et al. (2018), we stick to Poisson uncertainties for the MUSE-Deep and MXDF samples. For these datasets, we measure the K-estimator in eight and six logarithmic bins in the ranges  $0.09 < R_{ij}/[h^{-1}\text{Mpc}] < 4.75$  and

$0.09 < R_{ij}/[h^{-1}\text{Mpc}] < 1.45$ , respectively, constrained by the spatial extent of the surveys.

We then perform a standard  $\chi^2$  minimization to find the best fitting parameters to the K-estimator measurements. Namely,

$$\chi^2 = \sum_{i=1}^{N_{\text{bins}}} \left( \frac{K(R_i) - K(R_i)^{\text{HOD}}}{\sigma_i} \right)^2, \quad (3.3)$$

where  $K(R_i)$ ,  $K(R_i)^{\text{HOD}}$ , and  $\sigma_i$  denote the measured K-estimator, the HOD modelled K-estimator and the Poisson uncertainty in the  $i$ th bin, respectively.

We note that the standard  $\chi^2$  minimization does not account for the correlation between bins. Although in Appendix 3.B we show that only contiguous bins are moderately correlated, we should take the resulting fit uncertainties with caution.

### 3.3.3 Halo occupation distribution modelling

The clustering statistics can be approximated with a power-law or modelled with state-of-the-art HOD modelling. Traditional clustering studies make use of power laws to derive the correlation length and slope, from which they infer large-scale bias factors and typical DMH masses. This simple approach deviates from the actual shape of the clustering statistic curve, even in the linear regime, and its inferred DMH masses suffer from systematic errors (e.g., Jenkins et al. 1998 and references therein). To overcome these concerns, physically motivated HOD models do not treat the linear and non-linear regime alike but differentiate between the clustering contribution from galaxy pairs that reside in the same DMH and pairs that occupy different DMHs.

In Herrero Alonso et al. (2021) we only modelled the two-halo term of the K-estimator with HOD modelling, which only delivered the large-scale bias factor and the typical DMH mass of the sample. We now extend into the non-linear regime (i.e.,  $R_{ij} < 0.6 h^{-1}\text{Mpc}$ ) of the one-halo term. We can then model the clustering measured by the K-estimator with a *full* HOD model, combining the separate contributions from the one- (1h, i.e., galaxy pairs residing in the same DMH) and the two-halo (2h, i.e., galaxy pairs

residing in different DMHs) terms:

$$\xi = \xi_{1h} + \xi_{2h}, \quad (3.4)$$

where  $\xi$  is the correlation function.

The HOD model we used is the same as in Herrero Alonso et al. (2021), an improved version of that described by Miyaji et al. (2011) and Krumpel et al. (2012), Krumpel et al. (2015), Krumpel et al. (2018). We assumed that LAEs are associated with DMHs, linked by the bias-halo mass relation from Tinker et al. (2005). From Tinker et al. (2005), we also included the effects of halo-halo collisions and scale-dependent bias. The mass function of DMHs, which is denoted by  $\phi(M_h)dM_h$ , is based on Sheth et al. (2001), and the DMH profile is taken from Navarro et al. (1997). We use the concentration parameter from Zheng et al. (2007), and the weakly redshift-dependent collapse overdensity from Navarro et al. (1997) and van den Bosch et al. (2013). We further incorporated redshift space distortions (RSDs) in the two-halo term using linear theory (Kaiser infall; Kaiser 1987 and van den Bosch et al. 2013). We did not model RSDs in the one-halo term because the peculiar velocity has negligible effects to our K-estimator as demonstrated in the following. The velocity dispersion ( $\sigma_v$ ) of satellites in a  $M_h$  halo can be estimated by  $\sigma_v^2 \approx GM_h/(2R_{vir})$ , where  $R_{vir}$  is the virial radius (Tinker, 2007). Its effect on the line-of-sight physical distance estimate is then  $\sigma_v/H(z)$ . For  $10^{11-12} h^{-1}M_\odot$  DMH masses, which are typical for our sample, with virial radii of  $\approx 0.02 - 0.05$  (physical)  $h^{-1}\text{Mpc}$ , the line-of-sight distance estimation is deviated by  $\approx 0.15 - 0.30 h^{-1}\text{Mpc}$ , corresponding to a peculiar velocity dispersion of  $\sigma_v \approx 80 - 170 \text{ km s}^{-1}$ . This is significantly small compared to our  $a_2 = 7 h^{-1}\text{Mpc}$ . We thus assume that the one-halo term contributes only to the  $Z_{ij} = 0 - 7 h^{-1}\text{Mpc}$  bin. We evaluated the HOD model at the median redshift of  $N(z)^2$ , where  $N(z)$  is the redshift distribution of the sampled galaxy pairs. For our three main datasets,  $z_{pair} \approx 3.8$ .

The mean halo occupation function is a simplified version of the five parameter model by Zheng et al. (2007). We fixed the halo mass at which the satellite occupation becomes zero to  $M_0 = 0$  and the smoothing scale of the central halo occupation lower mass cutoff to  $\sigma_{\log M} = 0$ , due to sample size limitations. We define the mean occupation distribution of the central

galaxy  $\langle N_c(M_h) \rangle$  as

$$\langle N_c(M_h) \rangle = \begin{cases} 1 & (M_h \geq M_{\min}) \\ 0 & (M_h < M_{\min}) \end{cases} \quad (3.5)$$

and that of satellite galaxies  $\langle N_s(M_h) \rangle$  as

$$\langle N_s(M_h) \rangle = \langle N_c(M_h) \rangle \cdot \left( \frac{M_h}{M_1} \right)^\alpha, \quad (3.6)$$

where  $M_{\min}$  is the minimum halo mass required to host a central galaxy,  $M_1$  is the halo mass threshold to host (on average) one satellite galaxy, and  $\alpha$  is the high-mass power-law slope of the satellite galaxy mean occupation function. The total halo occupation is given by the sum of central and satellite galaxy halo occupations,  $N(M_h) = N_c(M_h) + N_s(M_h)$ .

The dependencies of the HOD parameters on the shape of the K-estimator are detailed in Appendix 3.D. In short, for the HOD parameters there selected, the clustering amplitude of the two-halo term is ascertained by the hosting DMHs and is thus very sensitive to their mass,  $M_{\min}$ , and to the fraction of galaxies in massive halos with respect to lower-mass halos, linked to  $\alpha$ . The clustering in the one-halo term regime, however, is affected by the three parameters in a complex manner; roughly  $M_{\min}$  and  $\alpha$  vary the amplitude, and  $\alpha$  as well as (moderately)  $M_1$  modify the slope.

To find the best-fit HOD model, we construct a 3D parameter grid for  $M_{\min}$ ,  $M_1$ , and  $\alpha$ . We vary  $\log(M_{\min}/[h^{-1}M_\odot])$  in the range 9.5 – 11.2,  $\log(M_1/M_{\min})$  from 0.5 to 2.5, and  $\alpha$  within 0.2 – 4.3, all in steps of 0.1. For each parameter combination, we computed  $\xi$  (Eq. 3.4), converted it to the K-estimator using Eq. 2 in Herrero Alonso et al. (2021), and computed a  $\chi^2$  value (Eqs. 3.2 or 3.3). We then used the resulting 3D  $\chi^2$  grid to estimate the confidence intervals for the HOD parameters. For each point on a 2D plane, we search for the minimum  $\chi^2$  for the contouring along the remaining parameter. The contours we plot are at  $\Delta\chi^2 = 3.53$  and 8.02, which correspond to Gaussian 68% ( $1\sigma$ ) and 95% ( $2\sigma$ ) confidence levels, respectively, applying the  $\chi^2$  distribution for three degrees of freedom. The projections of the 68% probability contours on the three interesting parameters are then used to compute the uncertainty of each HOD parameter.

For each point in the three parameter grid, we

also computed the large-scale galaxy bias factor,  $b$ , and the fraction of satellite galaxies per halo,  $f_{\text{sat}}$ , as follows:

$$b = \frac{\int \langle N(M_h) \rangle b_h(M_h) \phi(M_h) dM_h}{\int \langle N(M_h) \rangle \phi(M_h) dM_h}, \quad (3.7)$$

$$f_{\text{sat}} = \frac{\int \langle N_s(M_h) \rangle \phi(M_h) dM_h}{\int \langle N(M_h) \rangle \phi(M_h) dM_h}, \quad (3.8)$$

where  $b_h(M_h)$  denotes the large-scale halo bias. The typical DMH mass is determined by the large-scale galaxy bias factor. We ultimately compute the bias and  $f_{\text{sat}}$  distributions from the HOD models that fall within the 68% confidence (for the three-parameter space) contours. These distributions are then used to assess the uncertainties in the bias and  $f_{\text{sat}}$ .

## 3.4 Results from HOD modelling

### 3.4.1 Fit results from the MUSE-Wide survey

Using the K-estimator  $K_{7,45}^{0.7}$ , we compute the clustering of our LAE sample in ten logarithmic bins in the range  $0.16 < R_{ij}/[h^{-1}\text{Mpc}] < 27.5$ , with error bars calculated following the jackknife resampling technique described in Sect. 3.3.2.1. In the left top panel of Figure 3.4.1, we show the measured clustering signal, with all MUSE-Wide data points significantly above the 7/45 baseline, which represents the expected clustering of an unclustered population.

Following the procedure laid out in Sect. 3.3.3, we obtain constraints on the HOD parameters. From the grid search and the  $\chi^2$  minimization, we find the best HOD fit to the K-estimator, colored in black in the same figure and dissected into the one- and two-halo term contributions. It can be seen from the residuals (bottom) that the model is in remarkable agreement with the measurements.

A somewhat intriguing feature, at least at first sight, is the kink in the two-halo term profile at  $0.2 < R_{ij}/[h^{-1}\text{Mpc}] < 0.4$ . This reflects the effect of the halo-halo collision introduced in the HOD model formalism by Tinker et al. (2005), where the galaxy pairs within the same DMH cannot contribute to the two-halo term.

Our fitting allows us to find the best-fit HOD from Eqs. 3.5 and 3.6. In the right top panel of Fig. 3.4.1, we represent the best HODs for the central, satellite, and total LAEs from the MUSE-Wide survey. While the halo mass needed to host one (central) LAE is  $\log(M_h/[h^{-1}M_\odot]) > 10.6$ , satellite galaxies are only present if the DMHs are at least one order of magnitude more massive ( $\log(M_h/[h^{-1}M_\odot]) > 11.6$ ).

As described in Sect. 3.3.3, we also compute the confidence regions for the HOD parameters. We show the probability contours (red) in Fig. 3.4.2. The wobbliness of the curves, especially those involving  $\alpha$ , is caused by making use of a discrete grid. For our sample, the contours are constrained to have  $\alpha > 1$ ,  $\log(M_1/M_{\text{min}}) > 1$ , and  $\log(M_{\text{min}}/[h^{-1}M_\odot]) > 10.4$ .

We list the best-fit HOD parameters in Table 3.4.1. While the minimum DMH mass required to host a central galaxy is  $\log(M_{\text{min}}/[h^{-1}M_\odot]) = 10.7^{+0.2}_{-0.3}$ , that needed to host one central and (on average) one satellite is  $\log(M_1/[h^{-1}M_\odot]) = 12.4^{+0.4}_{-0.6}$  (i.e.,  $\log(M_1/M_{\text{min}}) = 1.7^{+0.4}_{-0.6}$ ). The power-law slope of the number of satellites is found to be  $\alpha = 2.8^{+0.9}_{-0.7}$ . The inferred typical DMH mass is  $\log(M_h/[h^{-1}M_\odot]) = 11.09^{+0.10}_{-0.09}$ , corresponding to a large-scale bias factor of  $b = 2.65^{+0.13}_{-0.11}$ . The high values of  $\log M_1$  and  $\alpha$ , considering the typical DMH mass of LAEs, suggest a low number of satellite galaxies detected in our sample.

Seeking robust information about the number of satellite galaxies, we compute the satellite fraction  $f_{\text{sat}}$  (Eq. 3.8) for each parameter combination. We find  $f_{\text{sat}} \lesssim 0.10$  at the  $3\sigma$  confidence level, being  $f_{\text{sat}} = 0.012^{+0.018}_{-0.009}$ . That is,  $\approx 3\%$  ( $1\sigma$  upper limit) of the LAEs in the MUSE-Wide survey are satellites. In other words, at most  $\approx 2$  out of  $\approx 65$  DMHs in our sample host one satellite LAE.

### 3.4.2 Fit results from MUSE-Deep

We measure the clustering of the MUSE-Deep LAE sample with the same K-estimator in eight logarithmic bins within  $0.09 < R_{ij}/[h^{-1}\text{Mpc}] < 4.75$ . We compute Poisson uncertainties as laid out in Sect. 3.3.2.2 and display the result in the middle left panel of Fig. 3.4.1. Overplotted on the clustering signal, we show the best HOD fit, split into the one- and two-halo term contributions. The good quality of the fit is quantified with the residuals in the bottom panel of the figure.

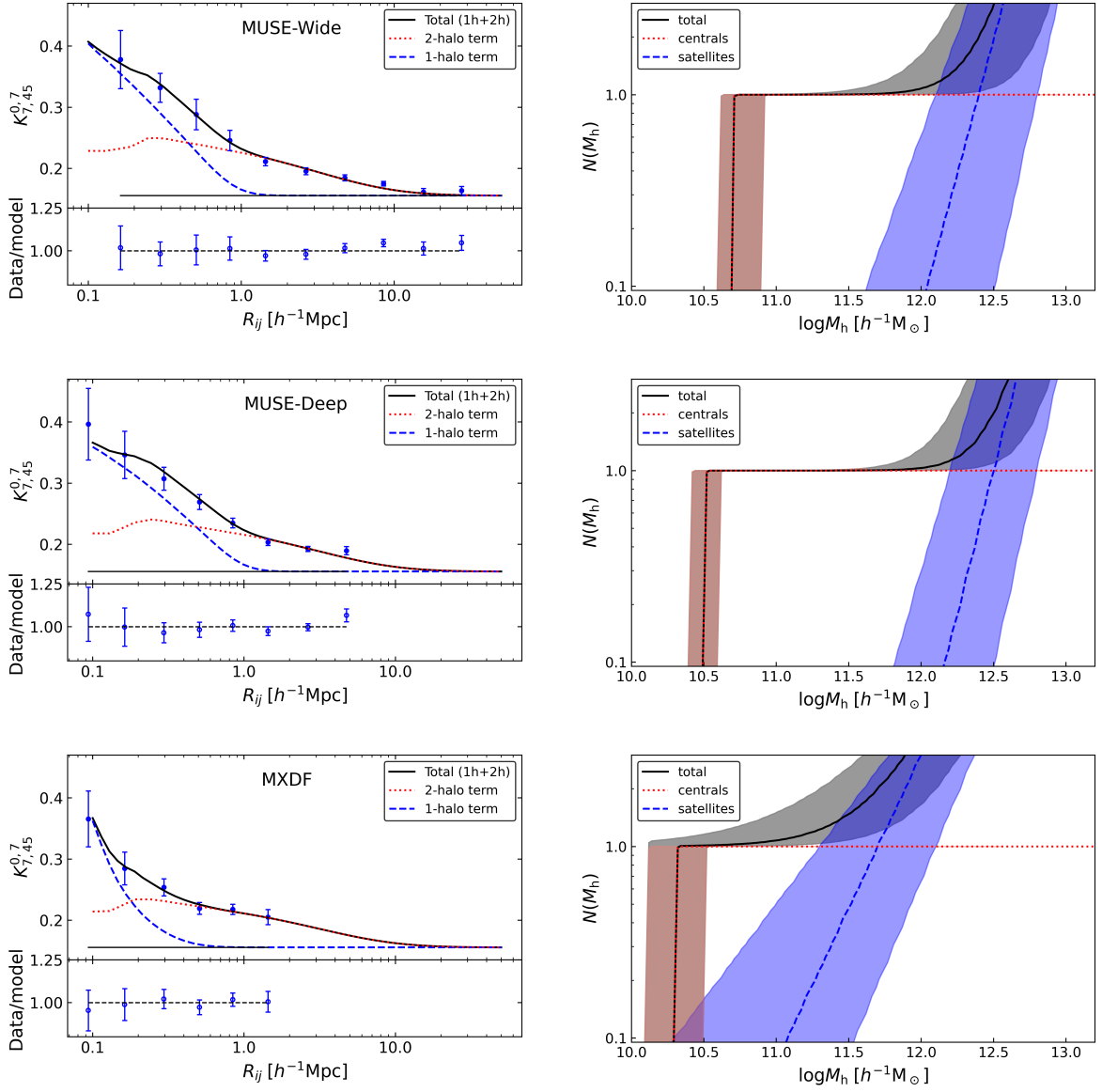


**Figure 3.4.1:** Best-fit HOD models to the LAE clustering measurements (blue data points) from MUSE samples. Top left: Blue dashed, red dotted, and black continuous curves show the one-halo, two-halo, and total clustering terms from the MUSE-Wide sample, respectively. The black straight line shows the expected  $K$  value of an unclustered sample. The residuals are shown below. The uncertainties are computed with the jackknife technique described in Sect. 3.3.2.1. Top right: Best-fit HODs for central (red dotted), satellite (blue dashed), and total LAEs (black continuous) from the MUSE-Wide survey. Shaded regions correspond to  $1\sigma$  confidence space. Middle: Same but for MUSE-Deep and using Poisson error bars. Bottom: Same but for MXDF and Poisson uncertainties.

**Table 3.4.1:** Best-fit HOD parameters for the main samples of LAEs.

	$\langle z \rangle$	$\log M_{\min}$	$\log(M_1/M_{\min})$	$\alpha$	$f_{\text{sat}}$	$b$	$\log M_h$
MUSE-Wide	4.0	$10.7^{+0.2}_{-0.3}$	$1.7^{+0.4}_{-0.6}$	$2.8^{+0.9}_{-0.7}$	$0.012^{+0.018}_{-0.009}$	$2.65^{+0.13}_{-0.11}$	$11.09^{+0.10}_{-0.09}$
MUSE-Deep	4.1	$10.5^{+0.2}_{-0.1}$	$1.9^{+0.3}_{-0.2}$	$3.0^{+0.4}_{-0.5}$	$0.004^{+0.009}_{-0.002}$	$2.42^{+0.10}_{-0.09}$	$10.89^{+0.09}_{-0.09}$
MXDF	4.2	$10.3^{+0.2}_{-0.3}$	$1.4^{+0.3}_{-0.2}$	$1.5^{+0.5}_{-0.5}$	$0.08^{+0.02}_{-0.05}$	$2.43^{+0.15}_{-0.15}$	$10.77^{+0.13}_{-0.15}$

**Notes:**  $\langle z \rangle$  is the median redshift of the sample.  $M_{\min}$ ,  $M_1$  are the threshold DMH masses in  $h^{-1}M_{\odot}$  to host a central and a satellite LAE, respectively.  $\alpha$  is the high-mass power-law slope of the number of satellite galaxies,  $f_{\text{sat}}$  is the satellite fraction,  $b$  is the large-scale bias factor and  $M_h$  is the typical DMH mass of the galaxy sample.

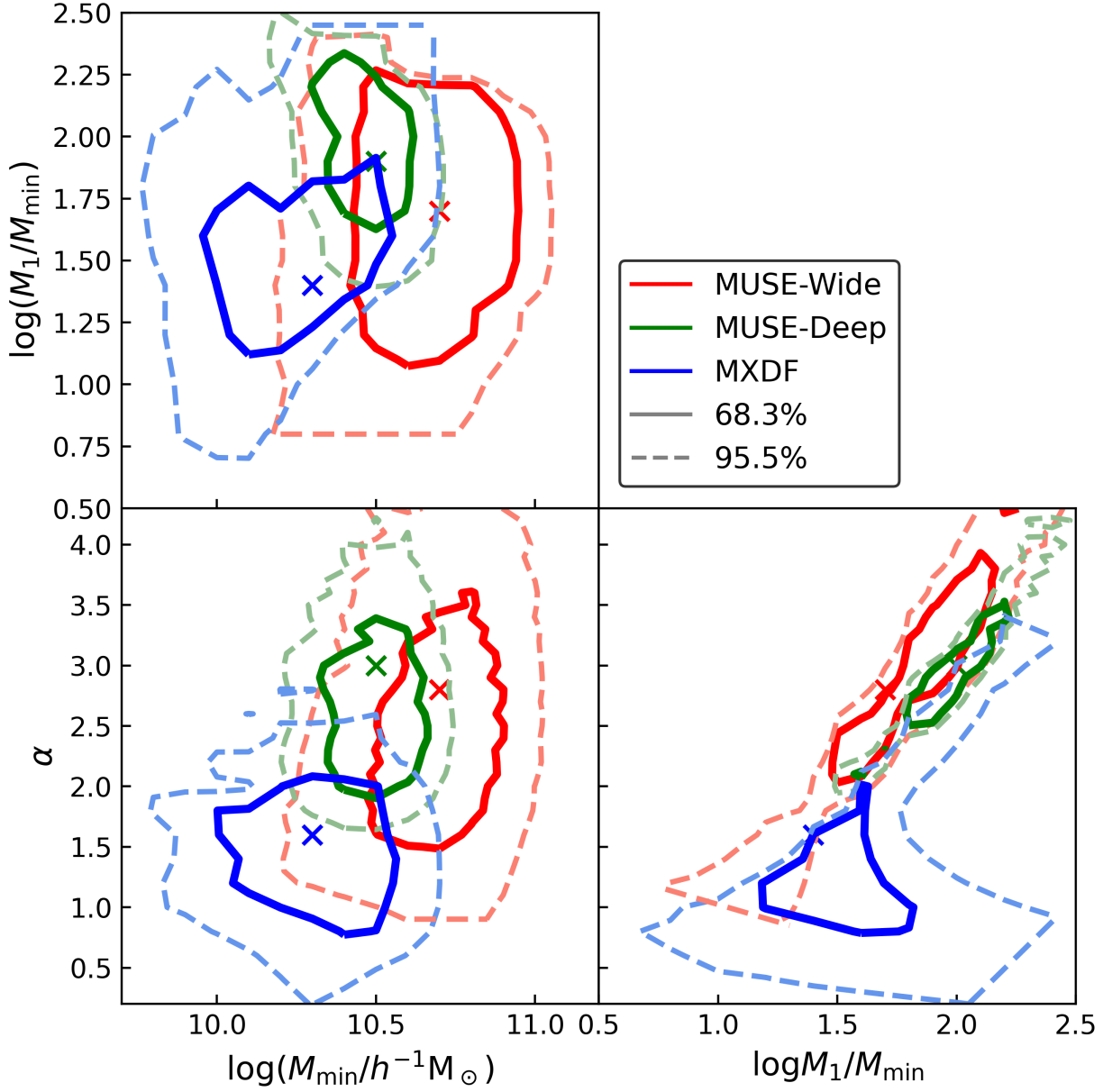


**Figure 3.4.2:** Confidence contours in the three HOD parameter space. Red corresponds to MUSE-Wide, green to MUSE-Deep, and blue to MXDF. The thick (dashed) contours represent the 68.3% (95.5%) confidence, at  $\Delta\chi^2 = 3.53$  (8.02) level. The crosses stand for best-fit ( $\chi_{\min}^2$ ), searched along the remaining parameter for each 2D parameter plane.



Following the procedure described in Sect. 3.3.2.2, we compute the confidence intervals for the HOD parameters and list them in Table 3.4.1. We plot the probability contours (green) in Fig. 3.4.2, which overlap significantly with those from the MUSE-Wide sample. Central LAEs can occupy DMHs if these are at least as massive as  $\log(M_{\min}/[h^{-1}\text{Mpc}]) = 10.5_{-0.1}^{+0.2}$ , whereas, in order to host satellite LAEs, the halos must have masses  $\log(M_1/[h^{-1}\text{Mpc}]) = 12.4_{-0.2}^{+0.3}$  ( $\log(M_1/M_{\min}) = 1.9_{-0.2}^{+0.3}$ ). These values correspond to a large-scale bias and typical DMH mass  $b = 2.42_{-0.09}^{+0.10}$  and  $\log(M_h/[h^{-1}M_{\odot}]) = 10.89_{-0.09}^{+0.09}$ , which are similar to those found in the MUSE-Wide survey. The derived satellite fraction is  $f_{\text{sat}} = 0.004_{-0.002}^{+0.009}$ , consistent with that from the MUSE-Wide LAE sample.

We then compute the best-fit HOD for central, satellite and total LAEs (middle right panel of Fig. 3.4.1). In line with the best-fit HOD parameters and somewhat lower than the values found for the MUSE-Wide survey, the smallest DMH that can host a central LAE has a mass of  $\log(M_h/[h^{-1}M_{\odot}]) > 10.4$ , more than one order of magnitude lower than that required to host one additional LAE (satellite).

### 3.4.3 Fit results from the MUSE Extremely Deep Field

We make use of six logarithmic bins in the range  $0.09 < R_{ij}/[h^{-1}\text{Mpc}] < 1.45$  and Poisson errors (see Sect. 3.3.2.2) to quantify the clustering of the sample of LAEs from MXDF. We show the K-estimator measurements in the bottom left panel of Fig. 3.4.1, along with the corresponding best HOD fit.

The probability contours are plotted in blue in Fig. 3.4.2, significantly apart from those of MUSE-Wide and MUSE-Deep. While the minimum DMH mass to host a central LAE is  $\log(M_{\min}/[h^{-1}\text{Mpc}]) = 10.3_{-0.3}^{+0.2}$ , that to host one central and one satellite LAE is  $\log(M_1/[h^{-1}\text{Mpc}]) = 11.7_{-0.2}^{+0.3}$  ( $\log(M_1/M_{\min}) = 1.4_{-0.2}^{+0.3}$ ). These values are somewhat lower than those found for the MUSE-Wide survey and correspond to a bias factor and typical halo mass of  $b = 2.43_{-0.15}^{+0.15}$  and  $\log(M_h/[h^{-1}M_{\odot}]) = 10.77_{-0.15}^{+0.13}$ , respectively. The inferred satellite fraction is  $f_{\text{sat}} = 0.08_{-0.05}^{+0.02}$  ( $f_{\text{sat}} \lesssim 0.2$  at the  $3\sigma$  confidence level), tentatively higher than that found in the MUSE-Wide survey.

From the best-fit HOD parameters, we cal-

culate the HODs for central, satellite and total LAEs and show them in the bottom right panel of Fig. 3.4.1. Significantly lower than in the MUSE-Wide survey, central LAEs reside in DMHs if these are more massive than  $\log(M_h/[h^{-1}M_{\odot}]) > 10.2$ . For the satellite case, and similarly to the previous LAE samples, they only exist if the halos are around one order of magnitude more massive.

It is worth pointing out that the three HOD parameters have some degree of degeneracy, printed out in the diagonally elongated probability contours in  $\log M_1/M_{\min} - \alpha$  space in the bottom right panel of Fig. 3.4.2. This can be understood as follows: a higher  $\alpha$  in the models causes an increase of satellites at high mass halos, but this can be compensated by producing less satellites by increasing  $\log M_1/M_{\min}$ . While this correlation is clearly visible for the MUSE-Wide and MUSE-Deep samples, the MXDF dataset only seems to be affected in the 95% confidence contour. We did not observe clear correlations between other parameters with any of our samples. Appendix 3.A shows how our K-estimator varies with the parameters. The causes of parameter degeneracies are also noticeable in Fig. 3.D.1. We note however that while the correlation between the HOD parameters leads to the perturbed shape of the probability contours, the lowest (MXDF) and highest luminosity (MUSE-Wide) sample contours are detached from each other. Thus, for the purposes of this study, simultaneously fitting the three HOD parameters and showing their correlations is preferable over, for instance, fixing  $\alpha$  to a dubious value.

## 3.5 Discussion

### 3.5.1 Clustering dependence on $\text{Ly}\alpha$ luminosity

The complex radiative transfer processes that the  $\text{Ly}\alpha$  photons are subject to make the search for correlations between  $\text{Ly}\alpha$  luminosity and other physical properties a difficult task. Despite this complication, Yajima et al. (2018) predicted a correlation between simulated  $L_{\text{Ly}\alpha}$  and halo mass based on halo merger trees and  $\text{Ly}\alpha$  radiative transfer calculations. Khostovan et al. (2019) is, however, the only study so far that has reported a clear ( $5\sigma$ ) relation between these quantities using observational data. Motivated by these

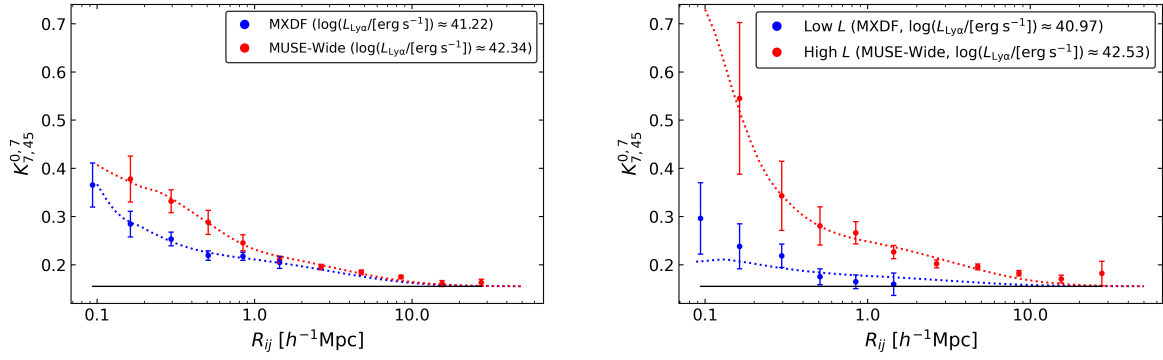


**Figure 3.5.1:** Clustering dependence on  $\text{Ly}\alpha$  luminosity. Left: K-estimator measurements in the MUSE-Wide survey (red;  $\langle L_{\text{Ly}\alpha} \rangle \approx 10^{42.34} \text{ erg s}^{-1}$ ) and MXDF (blue;  $\langle \log L_{\text{Ly}\alpha} \rangle \approx 10^{41.22} \text{ erg s}^{-1}$ ). The dotted curves represent the best HOD fits. The black straight line shows the expected K-estimator of an unclustered sample. Right: Same for the high  $L_{\text{Ly}\alpha}$  subset (red) from the MUSE-Wide survey and the low  $L_{\text{Ly}\alpha}$  subsample (blue) from MXDF.

results, we exploited the large dynamic range of  $\text{Ly}\alpha$  luminosities that we cover to investigate the relation between  $\text{Ly}\alpha$  luminosity and DMH mass. As a first step, we compare the K-estimator measurements in the MUSE-Wide survey (highest luminosity LAE sample:  $\langle L_{\text{Ly}\alpha} \rangle \approx 10^{42.34} \text{ erg s}^{-1}$ , but still fainter than those in Khostovan et al. (2019)) and in MXDF (faintest LAE sample;  $\langle L_{\text{Ly}\alpha} \rangle \approx 10^{41.22} \text{ erg s}^{-1}$ ) and show the outcome of this comparison in the left panel of Fig. 3.5.1.

The relatively luminous LAEs from the MUSE-Wide survey cluster slightly more strongly ( $b_{\text{Wide}} = 2.65^{+0.13}_{-0.11}$ ) than the low-luminosity LAEs from MXDF ( $b_{\text{MXDF}} = 2.43^{+0.15}_{-0.15}$ ). The clustering measurements and bias factor ( $b = 2.42^{+0.10}_{-0.09}$ ) in MUSE-Deep ( $\log(L_{\text{Ly}\alpha}/[\text{erg s}^{-1}]) = 41.64$ ) fall between those from MUSE-Wide and MXDF. We convert the bias factors from the three main samples of this study into typical DMH masses and plot them as a function of their median  $\text{Ly}\alpha$  luminosity with colored symbols in Fig. 3.5.2.

Although the three main datasets sample the same region of the sky, their transverse coverage is limited and somewhat differs. Therefore, our results are affected by cosmic sample variance. Ideally, this uncertainty is estimated from the variance of clustering measurements from simulated mocks in different lines of sight. Inferring cosmic variance from a large set of mocks that are able to reproduce the observed clustering of our LAEs is however beyond the scope of this paper.

We further investigate the possible dependence on  $L_{\text{Ly}\alpha}$  by splitting the main LAE samples into disjoint subsets (see Table 3.2.2). We compute the K-estimator in each  $L_{\text{Ly}\alpha}$  subsam-

ple, find the best HOD fit and list the large-scale bias factors and the typical DMH masses in Table 3.5.1. We also plot the typical DMH masses in Fig. 3.5.2 (empty symbols) as a function of the median  $L_{\text{Ly}\alpha}$  of the subsamples. We find that typical halo mass increases from  $10^{10.00}$  to  $10^{11.43} M_{\odot}$  between  $10^{40.97}$  and  $10^{42.53} \text{ erg s}^{-1}$  in line luminosity.

For each subsample pair, the high-luminosity subset always clusters more strongly than the low-luminosity one and, in this case, cosmic sample variance effects can be completely neglected because subset pairs span the exact same area on the sky. The most pronounced difference is found when splitting the MXDF sample, the dataset with the largest dynamic range of  $\text{Ly}\alpha$  luminosity. The best HOD fits deliver  $b_{\text{low}} = 1.79^{+0.08}_{-0.06}$  and  $b_{\text{high}} = 3.10^{+0.24}_{-0.22}$  ( $3.9\sigma$  significant).

Despite its higher luminosity, we infer a less massive DMH for the MUSE-Deep high-luminosity subsample than for the main dataset. This is due to the higher  $z_{\text{pair}}$  of the subset (see Sect. 3.2.4 and 3.3.3). Because we evaluate the HOD model at  $z_{\text{pair}}$ , a higher redshift corresponds to HOD models in which the halo mass function presents a lower number density of massive halos and, thus, deliver less massive typical DMHs. The same reasoning applies when comparing the high-luminosity MXDF and low-luminosity MUSE-Deep subsamples and the high-luminosity MUSE-Deep and low-luminosity MUSE-Wide subsets. While each subsample pair presents similar median luminosities, the former also has similar  $z_{\text{pair}}$ , unlike the latter one (see Sect. 3.2.4). This translates

**Table 3.5.1:** Best HOD fit large-scale bias factor and typical DMH mass for the LAE subsamples.

	Subsample	$\langle z \rangle$	$b$	$\log(M_h/[h^{-1}M_\odot])$
MUSE-Wide high L	4.1	$3.13^{+0.08}_{-0.15}$	$11.43^{+0.04}_{-0.10}$	$11.43^{+0.04}_{-0.10}$
MUSE-Wide low L	3.7	$2.45^{+0.10}_{-0.12}$	$10.92^{+0.09}_{-0.11}$	$10.92^{+0.09}_{-0.11}$
MUSE-Deep high L	4.5	$2.41^{+0.12}_{-0.10}$	$10.40^{+0.12}_{-0.10}$	$10.40^{+0.12}_{-0.10}$
MUSE-Deep low L	3.7	$2.20^{+0.09}_{-0.11}$	$10.68^{+0.09}_{-0.13}$	$10.68^{+0.09}_{-0.13}$
MXDF high L	4.5	$3.10^{+0.24}_{-0.22}$	$10.96^{+0.15}_{-0.15}$	$10.96^{+0.15}_{-0.15}$
MXDF low L	4.0	$1.79^{+0.08}_{-0.06}$	$10.00^{+0.12}_{-0.09}$	$10.00^{+0.12}_{-0.09}$

**Notes:**  $\langle z \rangle$  is the median redshift of the subsample. The uncertainties do not include cosmic sample variance.

into similar DMH masses for the first pair but significantly distinct masses for the second.

We last consider the most extreme cases, the low-luminosity subset from MXDF and the high-luminosity one from the MUSE-Wide survey. We show the measured clustering in the two subsamples in the right panel of Fig. 3.5.1. The high-luminosity LAEs cluster  $8\sigma$  more strongly than the low-luminosity LAEs, without accounting for cosmic variance. We find that LAEs with  $\log(L_{\text{Ly}\alpha}/[\text{erg s}^{-1}]) \approx 42.53$  reside in DMHs of  $\log(M_h/[h^{-1}M_\odot]) = 11.43^{+0.04}_{-0.10}$  and that lower luminosity LAEs ( $\log(L_{\text{Ly}\alpha}/[\text{erg s}^{-1}]) \approx 40.97$ ) are hosted by DMHs of masses ranging  $\log(M_h/[h^{-1}M_\odot]) = 10.00^{+0.12}_{-0.09}$ . These results fit well within the assumed framework in which star-forming galaxies that reside in more massive halos present higher star formation rates and thus show more luminous nebular emission lines (Kusakabe et al., 2018). This dependence can then be weakened by low  $\text{Ly}\alpha$  escape fractions in high mass halos.

Following Sect. 5.4.1 of Herrero Alonso et al. (2021), we matched the redshift distributions of the three main samples and of each subsample pair to verify that the difference in clustering amplitude is not driven by the different redshift distribution of the datasets. For each main sample, we compare individual bins between their corresponding  $z$ -distributions and select the one that contains a higher number of objects. We then randomly remove LAEs until we match the number counts of the non-selected samples in that bin. Once all bins have been inspected, we obtain "matched"  $z$ -distributions (i.e., equivalent), but with still different  $\text{Ly}\alpha$  luminosity distributions. We ran the K-estimator in the three "matched" datasets and find consistent results with the original ones.

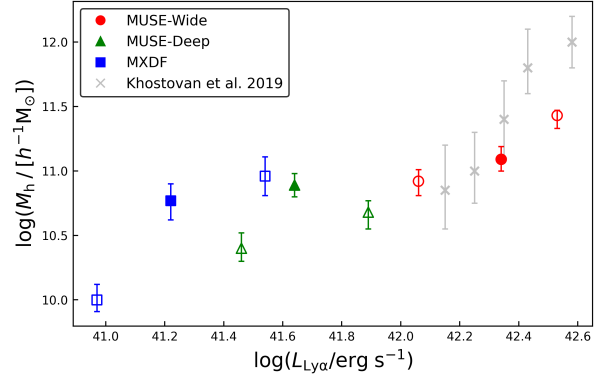


**Figure 3.5.2:** Typical dark matter halo mass against observed median  $\text{Ly}\alpha$  luminosity. Filled and unfilled symbols correspond to the values derived from the samples and subsamples described in Sect. 5.2, respectively. Red circles, green triangles and blue squares belong to MUSE-Wide, MUSE-Deep and MXDF, respectively. Gray crosses represent the results from Khostovan et al. (2019) in the  $\text{Ly}\alpha$  luminosity interval relevant for this study.

We follow the same approach for the subsamples such that the low- and high-luminosity subsets have exactly the same  $z$ -distribution. We find that the clustering difference between the "matched" and original subsamples varies within  $1\sigma$ . Besides, as we did for  $L_{\text{Ly}\alpha}$ , we also searched for a possible clustering dependence on redshift and found no trend. Thus, we discarded the possibility of a possible clustering dependence on  $\text{Ly}\alpha$  luminosity driven by  $z$ .

Our results are not driven by AGN or low-redshift emission line contamination either. The  $\text{Ly}\alpha$ -emitting AGN fraction for  $L_{\text{Ly}\alpha} < 10^{43} \text{ erg s}^{-1}$  is close to zero (Spinoso et al. 2020 and references therein) and the four known X-ray detected AGNs (Luo et al., 2017), which only affect MUSE-Wide and MUSE-Deep, were not included in our datasets. Besides, Urrutia et al. (2019) performed a stacking experiment of X-ray images

centered on MUSE-Wide LAEs, yielding no signal. The presence of low-redshift interlopers in our spectroscopic samples is also unlikely. [OII] emitters are the typical contaminants of high-redshift LAE samples but the high resolution of the MUSE instrument allows to distinguish the [OII] emission line doublet with high confidence.

These results are in line with the tentative trends seen in Ouchi et al. (2003), Kusakabe et al. (2018), and Herrero Alonso et al. (2021) and the clear dependence found in Khostovan et al. (2019). While Ouchi et al. (2003) noted a slight difference in the correlation amplitude of two  $L_{Ly\alpha}$  subsamples (30 and 57 LAEs in each subset at  $z = 4.86$  with  $\log(L_{Ly\alpha}/[\text{erg s}^{-1}]) > 42.2$  and  $\log(L_{Ly\alpha}/[\text{erg s}^{-1}]) < 42.2$ , respectively), Kusakabe et al. (2018) observed a tendency ( $< 2\sigma$ ) of larger bias factors corresponding to higher luminosity LAEs. They used four deep survey fields at  $z = 2$  with limiting  $Ly\alpha$  luminosities within the range of  $41.3 < \log(L_{Ly\alpha}/[\text{erg s}^{-1}]) < 42$  computed from NB387 magnitudes.

More significant is the dependence found in Khostovan et al. (2019) and Herrero Alonso et al. (2021). While the latter measured a  $2\sigma$  difference in bias factors or DMH masses between two subsets of 349 and 346 LAEs at  $z \approx 4$  with  $\log(L_{Ly\alpha}/[\text{erg s}^{-1}]) \approx 42.14$  and  $\log(L_{Ly\alpha}/[\text{erg s}^{-1}]) \approx 42.57$ , the former used various surveys with discrete redshift slices between  $2.5 < z < 6$  and  $42.0 < \log(L_{Ly\alpha}/[\text{erg s}^{-1}]) < 43.6$  to find that halo mass clearly ( $5\sigma$ ) increases with increasing line luminosity. For a direct comparison, we plot in Fig. 3.5.2 (gray crosses) the DMH masses computed by Khostovan et al. (2019) from samples with similar redshifts ( $z \approx 3$ ) and  $Ly\alpha$  luminosities ( $\log(L_{Ly\alpha}/[\text{erg s}^{-1}]) \approx 42$ ) to our current LAE samples. Our results are in good agreement and extend to much fainter  $Ly\alpha$  luminosities.

Our results, along with those from the literature, demonstrate that having a broad dynamic range of  $L_{Ly\alpha}$  (nearly extending two orders of magnitude) and a large number of LAEs in the samples is crucial to detect the clustering dependence on  $L_{Ly\alpha}$ .

### 3.5.2 Comparison to Herrero Alonso et al. (2021)

In this section we compare our results with the findings of our previous study (Herrero Alonso

et al., 2021, hereafter HA21), where we measured the clustering of a subset (68 fields of the MUSE-Wide survey) of our current sample (91 fields of the MUSE-Wide survey) and fitted the corresponding signal with a two-halo term only HOD modelling. In order to envisage the methodological and statistical improvement of our new investigation, we applied our  $K_{7,45}^{0,7}$  estimator to the sample considered in HA21 (695 LAEs at  $3.3 < z < 6$ ). We compare the outcome to our current clustering measurement in Fig. 3.5.3.

The two datasets show good agreement within the uncertainties, with smaller errors for the current sample. Besides the higher number of LAEs and larger spatial coverage, the error estimation was carried out following different procedures. While the spatial coverage of the full MUSE-Wide survey allows us to compute the covariance matrix from the jackknife resampling technique, the smaller transverse extent covered by the 68 fields did not allow the split of the surveyed area into a significant number of jackknife zones. Thus, in HA21, we chose bootstrapping error bars as our next most conservative and realistic approach.

The slightly puzzling hump seen in Sect. 4 of HA21 at  $4 \lesssim R_{ij}/[h^{-1}\text{Mpc}] \lesssim 7$  is no longer visible in our new dataset. This confirms the judgement in HA21 that the feature was consistent with a statistical fluctuation resulting from the correlation between datapoints.

In HA21, we limited the range of transverse separations to  $R_{ij} > 0.6 h^{-1}\text{Mpc}$ , excluding the smallest scales of the one-halo term. Thus, we fitted the signal with a two-halo term only HOD model (red dotted curve in Fig. 3.5.3) in contrast to the full HOD modelling performed in this work (blue dotted curve). While the former only constrained the large-scale bias factor and the typical DMH mass of LAEs, the latter further determines the number of central and satellite galaxies, as well as the required DMH mass to host each type of galaxy. Despite these dissimilarities, the two fits are in good agreement: the bias factor ( $b = 2.80_{-0.38}^{+0.38}$ ) and the typical DMH mass of LAEs ( $\log(M_{\text{DMH}}/[h^{-1}M_{\odot}]) = 11.34_{-0.27}^{+0.23}$ ) from HA21 are consistent with those derived in this work ( $b = 2.65_{-0.11}^{+0.13}$  and  $\log(M_{\text{DMH}}/[h^{-1}M_{\odot}]) = 11.09_{-0.09}^{+0.10}$ ). The higher accuracy of our current measurements originates from the larger sample, the availability of more realistic error bars, and constraints from the one-halo term.

### 3.5.3 Comparison with the literature

A common way to infer the host DMH masses of LAEs is to quantify the galaxy clustering of the detected population through clustering statistics, which is then traditionally approximated with power-laws or fit with physically motivated HOD models.

Following the traditional approach, Gawiser et al. (2007), Ouchi et al. (2010) and Bielby et al. (2016) focused on the clustering of a few hundred LAEs at  $z = 3.1 - 6.6$  to obtain typical DMH masses in the range  $10^{10} - 10^{11} M_{\odot}$ . Similar masses were found by Khostovan et al. (2018) in a much larger sample ( $\approx 5000$  LAEs) in discrete redshift slices within  $2.5 < z < 6$ , adopting the same procedure. A major improvement in terms of methodology was presented in Lee et al. (2006), Durkalec et al. (2014), Ouchi et al. (2017), and Durkalec et al. (2018), who considered samples of high- $z$  galaxies (2000-3000 mainly LAEs and Lyman-break galaxies, LBGs) and quantified the clustering with HOD modelling. While Ouchi et al. (2017) found that their LAEs at  $z = 5.7$  (6.6) are hosted by DMHs with typical masses of  $\log(M_h/M_{\odot}) = 11.1_{-0.4}^{+0.2}$  ( $10.8_{-0.5}^{+0.3}$ ), Lee et al. (2006) and Durkalec et al. (2014, 2018) computed  $\log(M_h/h^{-1}M_{\odot}) \approx 11.7$  for their sample of galaxies at  $z = 4 - 5$  and  $z = 3$ , respectively. Considering that we have performed a full HOD modelling at the median redshift of our number of galaxy pairs ( $z_{\text{pair}} = 3.8$ ) and that the DMH masses are predicted to evolve with cosmic time, our derived typical DMH masses  $\log(M_h/h^{-1}M_{\odot}) \approx 10.77 - 11.09$  are in good agreement with the literature.

Besides the computation of typical DMH masses, modelling the one-halo term of the clustering statistics with HOD models delivers the minimum DMH mass required to host a central galaxy,  $M_{\text{min}}$ , that is needed for a satellite galaxy,  $M_1$ , and the power-law slope of number of satellites,  $\alpha$ . These three parameters constrain the satellite fraction,  $f_{\text{sat}}$ . Ouchi et al. (2017) partially exploited the power of HOD models in a sample of  $\approx 2000$  LAEs to obtain  $\log(M_{\text{min}}/M_{\odot}) = 9.5_{-1.2}^{+0.5}$  ( $9.1_{-1.9}^{+0.7}$ ) at  $z = 5.7$  (6.6). Our derived minimum masses to host a central galaxy at  $z_{\text{pair}} = 3.8$  are considerably larger ( $\log(M_{\text{min}}/M_{\odot}) \approx 10.3 - 10.7$ ), which can be explained by the different Ly $\alpha$  luminosities covered in the two studies, and by the fact that several

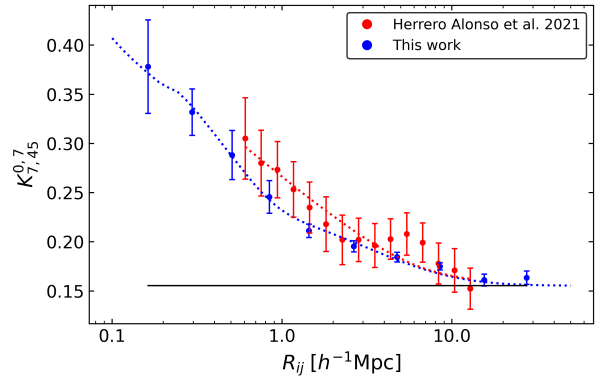


**Figure 3.5.3:** Clustering of the full MUSE-Wide sample (blue; this work) compared to the subset considered in HA21 (red). The former measurements show jackknife uncertainties (see Sect. 3.3.2.1) and the latter bootstrapping errors (see Sect. 3.1.3 in HA21). The blue dotted curve represents our best-fit from full HOD modelling. The red dotted curve displays the two-halo term only best HOD fit found in Sect. 4.3 of HA21. The black straight line shows the expected  $K$  value of an unclustered sample.

HOD parameters were fixed in Ouchi et al. (2017), namely,  $\sigma_{\log M} = 0.2$ ,  $\log M_0 = 0.76M_1 + 2.3$ ,  $\log M_1 = 1.18 \log M_{\text{min}} - 1.28$ , and  $\alpha = 1$ , which are not compatible with ours. This was the only previous study that performed HOD modelling in a sample of LAEs.

Lee et al. (2006) and Durkalec et al. (2014) made use of the full potential of HOD models to reproduce the clustering of their LBG population at  $z = 4 - 5$  and  $2.9 < z < 5$ , respectively. Although it is still under debate whether LBGs and LAEs are the same galaxy population (Garel et al. 2015 and references therein), Lee et al. (2006) computed a minimum DMH mass to host a central LBG of  $\log(M_{\text{min}}/M_{\odot}) \approx 10.8$ , to host a satellite LBG of  $\log(M_1/M_{\odot}) \approx 12.0$ , and a power-law slope  $\alpha$  for the number of satellites of  $\alpha \approx 0.7$ , with considerable uncertainties. Similarly, Durkalec et al. (2014) found  $\log(M_{\text{min}}/M_{\odot}) = 11.18_{-0.70}^{+0.56}$ ,  $\log(M_1/M_{\odot}) = 12.55_{-0.88}^{+0.85}$ , and  $\alpha = 0.73_{-0.30}^{+0.23}$ . While their halo masses are in agreement with our findings, their slope is somewhat shallower. This is partially expected given the dissimilarities in the galaxy populations (i.e., disparate observational selection techniques detect distinct galaxy populations).

### 3.5.4 Satellite fraction

In the above discussions on HOD modelling, we limit ourselves to the HOD model form expressed by Eqs. 3.5 and 3.6, which is rather restrictive.

The underlying assumption of the model is that the center of the halo with mass  $M_h > M_{min}$  is always occupied by one galaxy in the sample (or at least at a  $M_h$ -independent constant probability). This form may be appropriate for instance, for luminosity or stellar mass thresholding samples, but there is no reason that this has to be the case for samples selected by other criteria.

We note that the inferred value of  $f_{sat}$  is sensitive to the form of the parameterized model of the central and satellite HODs. In this work and in the literature, a power-law form of the satellite HOD is customarily assumed. In this case, a lower  $\alpha$  would increase the model  $\langle N_s(M_h) \rangle$  at the lower  $M_h$  end, near  $M_{min}$ , and yield fewer satellites in higher mass halos. Since the halo mass function drops with increasing mass,  $f_{sat}$  is mainly determined by the HOD behavior around  $M_h \sim M_{min} \sim 10^{10.5} h^{-1} M_\odot$ , where the halo mass function is large and the virial radius is  $r_{vir} \approx 0.08 h^{-1} Mpc$  at  $z \sim 3.8$  (Zheng et al., 2007). These scales are too small to be well constrained by our observations. Our observed one-halo term mainly constrains the satellite fraction at larger mass halos ( $M_h \sim M_{min} \sim 10^{13} h^{-1} M_\odot$ , where  $r_{vir} \approx 0.5 h^{-1} Mpc$  at the same redshift). Thus, the  $f_{sat}$  values from the HOD modelling should be viewed with caution and may well reflect the artefacts of the assumed form of the model. On the other hand, the sheer presence of a significant one-halo term indicates the existence of some satellites at higher halo masses. The extent of the one-halo term up to  $R_{ij} \approx 0.5 h^{-1} Mpc$  shows that there are indeed satellites up to  $M_h \sim 10^{13} h^{-1} M_\odot$ .

In spite of the above caveats, the small satellite fraction of the LAEs is likely to be robust. The small  $f_{sat}$  values for the assumed HOD model indicate that not only central-satellite pairs are rare, but also satellite-satellite pairs are as well, suggesting that only a small fraction of halos contain multiple LAEs. The small  $M_{min}$  values themselves are also an indication that a large majority of the halos (at the low mass end) that contain a LAE are indeed dominated by one galaxy and in this case, the LAE is probably the central galaxy.

### 3.5.5 Implications

The clustering results of this study do not only have implications on the baryonic-DM relation, but also on evolving  $Ly\alpha$  luminosity functions,

signatures of incomplete reionization, and halo mass-dependent  $Ly\alpha$  escape fractions. We address these aspects in the following.

The relation between halo mass (or clustering strength) and  $Ly\alpha$  luminosity (Table 3.5.1 and Fig. 3.5.2) demonstrates that high-luminosity LAEs tend to reside in higher density environments than lower luminosity ones. As a result, overdense regions contain a larger fraction of high-luminosity sources (and a lower fraction of less luminous ones) than environments of lower density. These inferences affect the  $Ly\alpha$  LF measurements at  $3 < z < 6$ . While we expect a shallower faint-end slope of the  $Ly\alpha$  LF in overdense regions, the slope should steepen in average or low density environments. As a consequence, surveys for relatively high-luminosity ( $L_{Ly\alpha} \approx 10^{42} \text{ erg s}^{-1}$ ) LAEs are implicitly biased against the lowest density regions and thus gives a biased shape for the LF, which should not be extrapolated towards lower  $Ly\alpha$  luminosities.

Assuming that our  $L_{Ly\alpha} - M_h$  relation still holds at higher redshifts, the  $Ly\alpha$  LF at  $z \geq 6$  would be even more affected, not only because of the above discussion but also because higher redshift bins are mainly populated by high-luminosity sources, contrary to lower redshift bins (typical case for telescopes with higher sensitivity at bluer wavelengths). Thus, it is important to be careful when interpreting  $Ly\alpha$  LFs, especially near the epoch of reionization (EoR), where a shallow to steep variation in the slope of the LF from higher ( $z \approx 7$ ) to lower redshifts ( $z \approx 5.7$ ) is commonly interpreted as a sign of incomplete reionization (Konno et al., 2014; Matthee et al., 2015; Santos et al., 2016).

Simulations at those higher redshifts also tend to find that high-luminosity LAEs are more likely to be observed than low-luminosity ones because they are able to ionize their surroundings and form HII regions around them (i.e., ionized bubbles; Matthee et al., 2015; Hutter et al., 2015; Yoshioka et al., 2022). These allow  $Ly\alpha$  photons to redshift out of the resonance wavelength and escape the region. Lower luminosity LAEs are then observed if they reside within the ionized bubbles of higher luminosity LAEs or if they are able to transmit enough flux through the IGM (Matthee et al., 2015). If our  $L_{Ly\alpha} - M_h$  relation is still valid at these redshifts, our results would support this simulation paradigm since high-luminosity LAEs (situated in overdense regions) could form large ionized bubbles more

efficiently than low-luminosity sources which tend to be located in lower density environments (Tilvi et al., 2005).

Theoretical studies e.g., Furlanetto et al., 2006; McQuinn et al., 2007 have modelled the size distribution of these HII regions and predicted an increase in the apparent clustering signal of LAEs towards the epoch of reionization (i.e., towards a more neutral IGM). Large ionized bubbles become rarer as the ionizing fraction declines. This patchy distribution of HII regions, which mostly surrounds large galaxy overdensities, boosts the apparent clustering of LAEs. This is commonly interpreted as another sign of incomplete reionization (e.g., Matthee et al., 2015; Hutter et al., 2015). Comparisons between observed intrinsic LAE clustering and model predictions have therefore been used to infer the fraction of neutral hydrogen at the EoR e.g., Ouchi et al., 2017. Nevertheless, if the clustering dependence on Ly $\alpha$  luminosity continues to  $z \approx 6$ , this comparison should be performed with caution. Because the observed high redshift bins ( $z \geq 6$ ) mainly contain high-luminosity LAEs, a strong clustering signal at  $z \approx 6$  may be wrongly interpreted as incomplete reionization when, in fact, it may only reflect the natural relation between Ly $\alpha$  luminosity and clustering strength.

We speculate that our results also play a role in the amount of escaping Ly $\alpha$  photons (Ly $\alpha$   $f_{\text{esc}}$ ). Durkalec et al. (2018) observed a dependence between halo mass and absolute UV magnitude ( $M_{\text{UV}}$ ). The interpretation of their relation goes as follows:  $M_{\text{UV}}$  traces star formation rate (SFR; e.g., Walter et al. 2012), which, in turn, tracks stellar mass ( $M_*$ ; e.g., Salmon et al. 2015), which correlates with halo mass (e.g., Moster et al. 2010). Because we observe a similar relation of  $M_h$  with  $L_{\text{Ly}\alpha}$ ,  $L_{\text{Ly}\alpha}$  is presumably also a tracer of star formation. If this is correct, the object-to-object variations in Ly $\alpha$  escape fraction cannot be so large that they obscure the trend of SFR –  $M_*$  –  $M_h$ . Given the typical Ly $\alpha$  luminosities of our sample, this is in agreement with the model suggestions of Schaerer et al. (2011a) and Garel et al. (2015), where the Ly $\alpha$   $f_{\text{esc}}$  is of the order of unity for sources with SFR  $\approx 1 M_\odot \text{ yr}^{-1}$ . The Ly $\alpha$  luminosity would then be a good tracer of the SFR for less luminous LAEs.

### 3.6 Conclusions

We report a strong clustering dependence on Ly $\alpha$  luminosity from the clustering measurements of three MUSE Ly $\alpha$  emitting galaxy (LAE) samples at  $3 < z < 6$ . Following the pencil-beam design of MUSE surveys from spatially large and shallow observation to spatially small and deep observation, we use 1030 LAEs from the full MUSE-Wide survey (1 h exposure time), 679 LAEs from MUSE-Deep (10 h), and 367 LAEs from MXDF (140 h). We thus connect the clustering properties of  $L^*$  LAEs with those of much fainter ones in the MXDF. We applied an optimized version of the K-estimator as the clustering statistic, coupled to state-of-the-art halo occupation distribution (HOD) modelling.

From our full HOD analysis, we derive constraints on the HOD of high-luminosity ( $\log(L_{\text{Ly}\alpha}/[\text{erg s}^{-1}]) \approx 42.34$ ), intermediate ( $\log(L_{\text{Ly}\alpha}/[\text{erg s}^{-1}]) \approx 41.64$ ) and low-luminosity ( $\log(L_{\text{Ly}\alpha}/[\text{erg s}^{-1}]) \approx 41.22$ ) LAEs. We modelled the LAE HOD with three parameters: the threshold dark matter halo (DMH) mass for hosting a central LAE ( $M_{\text{min}}$ ), for hosting (on average) one satellite LAE ( $M_1$ ), and the power-law slope of the number of satellites per halo ( $\alpha$ ) as a function of halo mass. For the high-luminosity sample we derived a typical DMH mass of  $\log(M_h/[h^{-1}M_\odot]) = 11.09^{+0.10}_{-0.09}$ , corresponding to a bias factor of  $b = 2.65^{+0.13}_{-0.11}$ . These findings, although more accurate, are in agreement with the results based on the two-halo term only HOD modelling performed in Herrero Alonso et al. (2021) for a subset of our MUSE-Wide sample. For the lower luminosity samples we found lower DMH masses. While for the  $\log(L_{\text{Ly}\alpha}/[\text{erg s}^{-1}]) \approx 41.64$  dataset we inferred  $\log(M_h/[h^{-1}M_\odot]) = 10.89^{+0.09}_{-0.09}$  ( $b = 2.42^{+0.10}_{-0.09}$ ), for the low-luminosity LAE sample we computed  $\log(M_h/[h^{-1}M_\odot]) = 10.77^{+0.13}_{-0.15}$  ( $b = 2.43^{+0.15}_{-0.15}$ ).

We also derived threshold DMH masses for centrals and satellites for each sample. We found that the minimum DMH mass to host a central LAE is  $\log(M_{\text{min}}/[h^{-1}M_\odot]) = 10.3^{+0.2}_{-0.3}$ ,  $10.5^{+0.2}_{-0.1}$ ,  $10.7^{+0.2}_{-0.3}$  for low-, intermediate-, and high-luminosity LAEs, respectively. The threshold halo mass for satellites and the power-law slope of the number of satellite LAEs also increase with Ly $\alpha$  luminosity, from  $\log(M_1/[h^{-1}M_\odot]) = 11.7^{+0.3}_{-0.2}$  and  $\alpha = 1.5 \pm 0.5$  to  $\log(M_1/[h^{-1}M_\odot]) = 12.4^{+0.3}_{-0.2}$  and  $\alpha = 3.0^{+0.4}_{-0.5}$  and to  $\log(M_1/[h^{-1}M_\odot]) = 12.4^{+0.4}_{-0.6}$  and  $\alpha =$

$2.8^{+0.9}_{-0.7}$ . These HOD constraints imply a decreasing number of detected satellite LAEs with luminosity. Indeed we infer satellite fractions of  $f_{\text{sat}} \lesssim 10, 20\%$  (at  $3\sigma$  confidence level) for high- and low-luminosity LAEs, respectively. This suggests that the most common scenario for current MUSE surveys is that in which DMHs mainly host a single detected LAE.

Motivated by these results, we aimed to further explore the clustering dependence on  $\text{Ly}\alpha$  luminosity. Exploiting the large dynamic range of  $L_{\text{Ly}\alpha}$  from MXDF, we split the main LAE sample at its median  $L_{\text{Ly}\alpha}$ . We found a  $3.9\sigma$  difference between the clustering of the low-luminosity ( $\log(L_{\text{Ly}\alpha}/[\text{erg s}^{-1}]) \approx 40.97$ ,  $b_{\text{low}} = 1.79^{+0.08}_{-0.06}$ ) and the high-luminosity subset ( $\log(L_{\text{Ly}\alpha}/[\text{erg s}^{-1}]) \approx 41.54$ ,  $b_{\text{high}} = 3.10^{+0.24}_{-0.22}$ ). We then selected the highest luminosity LAE subset from the MUSE-Wide survey ( $\log(L_{\text{Ly}\alpha}/[\text{erg s}^{-1}]) \approx 42.53$ ) and the lowest luminosity LAE subsample from MXDF ( $\log(L_{\text{Ly}\alpha}/[\text{erg s}^{-1}]) \approx 40.97$ ), resulting in a clear clustering dependence where the high-luminosity LAEs from MUSE-Wide cluster more strongly ( $b_{\text{high}} = 3.13^{+0.08}_{-0.15}$  or  $\log(M_{\text{h}}/[h^{-1}M_{\odot}]) = 11.43^{+0.04}_{-0.10}$ ) than the low-luminosity ones from MXDF ( $b_{\text{low}} = 1.79^{+0.08}_{-0.06}$  or  $\log(M_{\text{h}}/[h^{-1}M_{\odot}]) = 10.00^{+0.12}_{-0.09}$ ) at  $8\sigma$  significance, excluding cosmic variance effects. The ongoing Hobby-Eberly Telescope Dark Energy Experiment (HETDEX; Gebhardt et al. 2021) survey will complement these results at the high-luminosity end and at somewhat lower redshifts ( $1.9 < z < 3.5$ ).

The implications of this framework are however not only relevant for LAE clustering studies, but also for reported measurements of evolving  $\text{Ly}\alpha$  luminosity functions, detections of incomplete reionization at  $z \approx 6$ , and the relation between  $\text{Ly}\alpha$  escape fraction and halo mass. Our results are also crucial for the much debated relevance of unresolved satellite LAEs (fainter than those in MXDF) for the measured  $\text{Ly}\alpha$  surface brightness profiles.

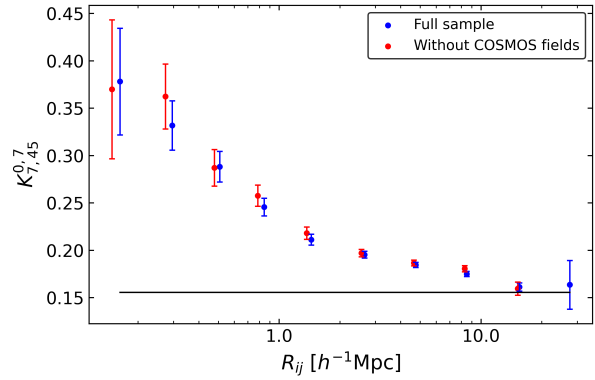


**Figure 3.A.1:** Clustering of the LAEs in the full MUSE-Wide sample (blue, see Fig. 3.2.1) and without the CANDELS/COSMOS fields (red, see right panel of Fig. 3.2.1). The black baseline represents the expected clustering of an unclustered sample. The error bars are Poissonian. The red measurements have been shifted along the x-axis for visual purposes.

## Appendix

### 3.A Effect of different fields on the clustering measurements

In this work, we have analyzed the clustering of LAEs in the full MUSE-Wide sample, including the CANDELS/COSMOS fields and the HUDF parallel fields. Here, we explore the possible effects on the MUSE-Wide clustering results when including or excluding various sets of fields. In appendix A of Herrero Alonso et al. (2021), we showed that the HUDF parallel fields did not alter the clustering results, their exclusion or inclusion mainly affected the clustering uncertainties. We therefore explore the effect of including the CANDELS/COSMOS region by comparing the clustering of the full MUSE-Wide survey with that present in a subsample without the CANDELS/COSMOS fields. The number of LAEs in the CANDELS/COSMOS region is 250.

It is clear from Fig. 3.A.1 that the clustering in both samples is in good agreement. The large-scale bias factors derived from the two curves are indistinguishable (within  $1\sigma$ ). The uncertainties corresponding to the smaller sample are (on average) 20% larger than in the full MUSE-Wide sample. We conclude that the inclusion of these fields has no notable effect on our clustering results but helps in reducing cosmic sample variance uncertainties.



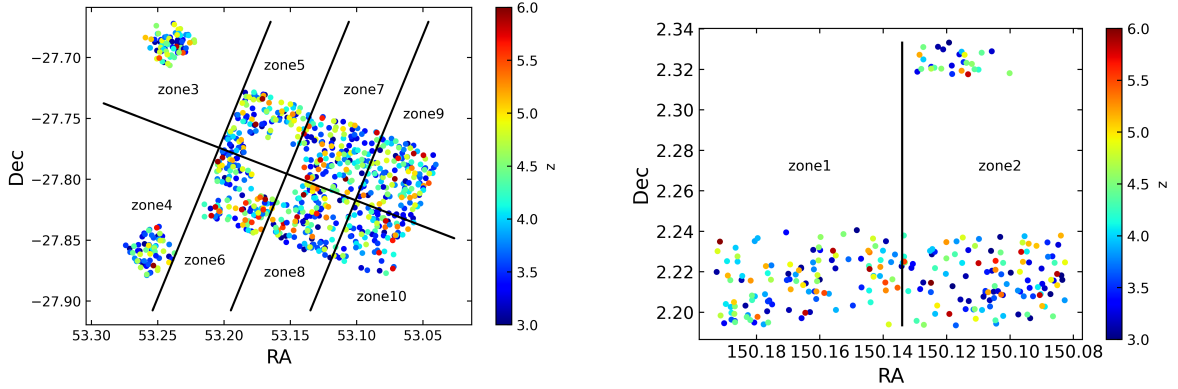


**Figure 3.B.1:** Ten Jackknife zones in the spatial coverage of the full MUSE-Wide survey ( $83.52 \text{ arcmin}^2$ ). Each Jackknife zone has a spatial extent of  $\approx 4 h^{-1} \text{ Mpc}$  in both RA and Dec directions.

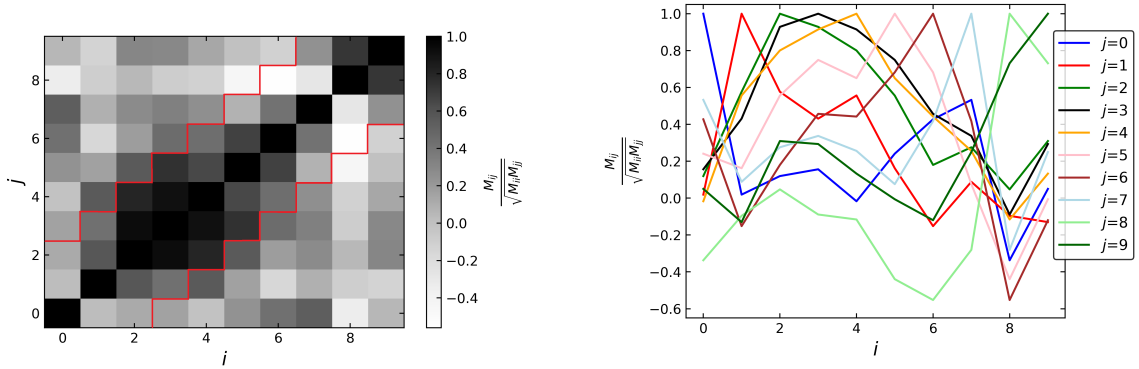


**Figure 3.B.2:** Covariance matrix computed from ten independent K-estimator measurements from the jackknife resampling technique. Left: Normalized covariance matrix for bins  $i$  and  $j$ . The red region defines the main diagonal and the two adjacent diagonals used for our reduced covariance matrix. Right: Normalized covariance matrix elements as a function of bin  $i$  for each bin  $j$  (colored).

### 3.B Covariance matrix

A common approach to quantify the correlation of the clustering data points is to resample the set of galaxies with the jackknife technique, followed by the calculation of the covariance matrix. To apply the jackknife method, we find a compromise between the number and the size of the jackknife zones. Thus, we split the sky area into ten independent regions (see Fig. 3.B.1) with a spatial extent of  $\approx 4 h^{-1}\text{Mpc}$  in both RA and Dec directions. We then construct ten different subsamples, each of them excluding one jackknife zone, and compute the K-estimator in each subset. These measurements are then used to build up the covariance matrix using Eq. 3.1 (see Sect. 3.3.2.1).

Considering that the probability of one galaxy pair to contribute to various adjacent bins is higher than that to contribute to several distant bins, one would naively expect a higher correlation in the former case. This is indeed what the (normalized) covariance matrix reflects in the left panel of Fig. 3.B.2. In fact, the noise in the matrix elements corresponding to notably separate bins is substantial. In the right panel of Fig. 3.B.2, we plot the normalized matrix elements as a function of bin  $i$  for each bin  $j$  to better illustrate the high level of noise in the matrix, especially for bins  $i > 6$ , where most curves become negative. This is likely due to the limited spatial size of the survey, which does not allow neither for a higher number of jackknife zones nor for spatially larger zones.

As a result of the considerable noise in the matrix on account of barely correlated bins significantly apart from each other, the minimization of the  $\chi^2$  values (Eq. 3.2) including the full covariance fails (i.e., various  $\chi^2$  values become negative). We therefore limit the use of the covariance matrix to its main diagonal and two adjacent diagonals (see red section in the left panel of Fig. 3.B.2; our so-called reduced covariance matrix). This means we set the negative part of the curves in the right panel of Fig. 3.B.2 to zero (i.e., no correlation between those bins), in an attempt to smooth out the noise.

While incorporating more diagonals results mathematically problematic for the  $\chi^2$  minimization, we have verified that the number of adjacent diagonals (one or two) slightly

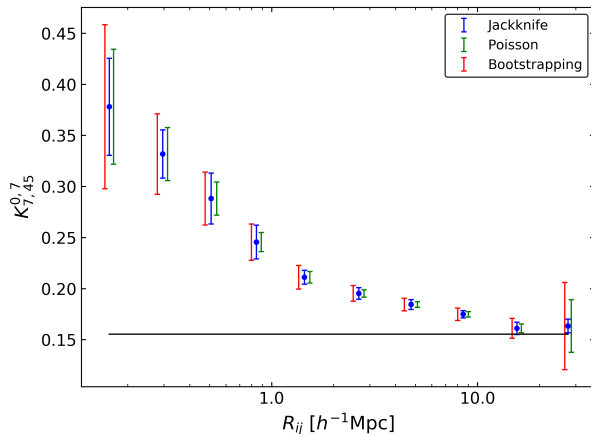


**Figure 3.C.1:** Error estimation method comparison for the sample of LAEs in the MUSE-Wide survey. Uncertainties from the covariance matrix and the jackknife resampling technique described in Sect. 3.3.2.1 are colored in blue, those from the bootstrapping approach used in Herrero Alonso et al. (2021) in red, and Poisson uncertainties in green.

modifies the  $\chi^2$  values but the probability contours represented in Fig. 3.4.2 remain unaltered. Thus, so do the best-fit HOD parameters.

Despite current limitations, jackknife is still the most robust method to compute the K-estimator uncertainties. While galaxy bootstrapping or Poisson error bars do not account for bin to bin correlations, our reduced covariance matrix only neglects the correlation between bins remarkably separated (expected to be minimal), but accounts for the correlation between nearby bins.

### 3.C Error estimation comparison

In order to quantify the correlation between the K-estimator bins, the covariance matrix must be computed. By splitting the sky area into independent regions, following the jackknife resampling technique, we create as many subsamples from the MUSE-Wide sample as jackknife zones (see Sect. 3.3.2.1). The K-estimator is then computed in each subset and the measurements are used to quantify the covariance matrix, whose diagonal provides the variance of each clustering data point. The square root of the diagonal represents the  $1\sigma$  uncertainties and are represented in blue in Fig. 3.C.1 (same along the main paper).

The jackknife resampling method requires a division of the sky area into several indepen-

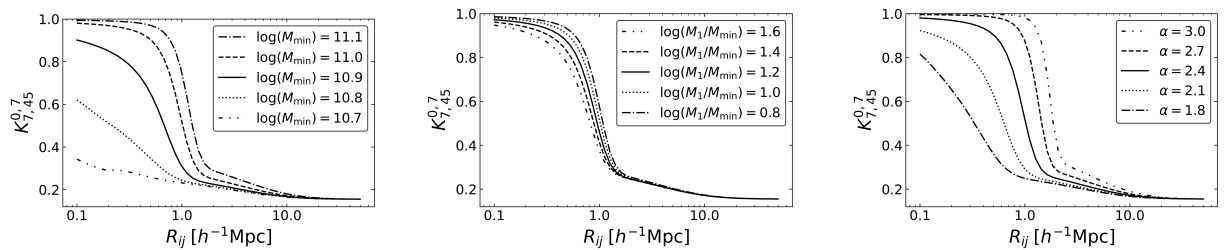


**Figure 3.D.1:** Effect of HOD parameters on the shape of the K-estimator. Left: Dependence on  $\log(M_{\min})$  for fixed  $\log(M_1/M_{\min}) = 1.2$  and  $\alpha = 2.4$ . Middle: Dependence on  $\log(M_1/M_{\min})$  for fixed  $\log(M_{\min}/[h^{-1}M_{\odot}]) = 10.9$  and  $\alpha = 2.4$ . Right: Dependence on  $\alpha$  for fixed  $\log(M_{\min}/[h^{-1}M_{\odot}]) = 10.9$  and  $\log(M_1/M_{\min}) = 1.2$ .

dent regions, each of which should ideally be large enough to cover the full range of scales under consideration. Out of the three samples examined in this study, this can only be partially achieved in the MUSE-Wide dataset. MUSE-Deep and MXDF do not allow for a spatial split into independent zones. We are thus left with two options for the deeper samples: the bootstrapping technique applied in Herrero Alonso et al. (2021), shown in red in Fig. 3.C.1, and Poisson uncertainties, shown in green.

We find that Poisson (bootstrapping) errors are, on average, 7% (46%) larger than those computed with the jackknife technique. These findings corroborate the results from Norberg et al. (2009), who found that the bootstrapping approach overestimates the uncertainties.

Similarly as for the MUSE-Wide survey, we find that bootstrapping uncertainties are  $\approx 40\%$  (on average) larger than Poisson in both MUSE-Deep and MXDF. We thus decide to use Poisson errors for the deeper samples in an attempt to at least overvalue the uncertainties.

We verified that the error estimation method does not significantly affect our clustering results. The best-fit parameters from MUSE-Deep and MXDF using bootstrapping error bars and the  $\chi^2$  minimization described in Sect. 3.1.3 of Herrero Alonso et al. (2021) are consistent with those delivered from Poisson statistics. Although in agreement, bootstrapping delivers  $\approx 45\%$  larger uncertainties than Poisson for the best-fit HOD parameters.

We last perform the same experiment in MUSE-Deep and MXDF but using scaled Poisson error bars. We decreased the Poisson in 7% (excess found in MUSE-Wide) and find that the best-fit parameters are  $\approx 10\%$  less uncertain than if Poisson errors are directly applied.

### 3.D Dependence of HOD parameters on the shape of the K-estimator

Here we visualize and qualitatively describe the effect of the HOD parameters on the K-estimator. Figure 3.D.1 shows the K-estimator for numerous HOD models. Each panel represents the result of varying one HOD parameter with the other two parameters fixed. Before detailing the major effects, it should be pointed out that the exact change in the shape of the K-estimator does not only depend on the varied parameter but also on the specific choice of the other two. Hence, these panels should merely be seen as illustrative examples.

The left panel of Fig. 3.D.1 shows the dependence of the K-estimator on  $M_{\min}$ . Higher values of  $\log M_{\min}$  (i.e., more massive halos) raise the expected K-estimator at all  $R_{ij}$  scales (one- and two- halo terms). At large scales, this occurs because more massive halos present larger bias factors, whereas at small scales, this is due to the decline in the contribution from less massive DMHs.

The middle panel of Fig. 3.D.1 shows the dependence of the K-estimator on  $M_1/M_{\min}$ . Larger  $\log(M_1/M_{\min})$  values (i.e., more massive halos) reduce the one-halo term clustering amplitude because of the decrease in the contribution from less massive DMHs. The clustering in the two-halo term does not depend on  $M_1$ .

The right panel of Fig. 3.D.1 shows the dependence of the K-estimator on  $\alpha$ . Higher values of  $\alpha$  increase the fraction of galaxies in massive DMHs with respect to smaller mass DMHs. Given that more massive halos are more strongly biased, the amplitude of the two-halo term increases. The change observed in the one-halo term is explained because galaxies hosted by

massive DMHs can contribute to the one-halo term on its largest scales, while galaxies residing in less massive halos can only contribute to the one-halo term at smaller  $R_{ij}$  scales. Since  $\alpha$  modifies the fraction of galaxies in massive DMHs to less mass DMHs, the corresponding fraction of the clustering contribution also varies. This alters the slope of the one-halo term.

## References

- Adelberger, K. L., Steidel, C. C., Pettini, M., et al., (2005), *ApJ*, 558, A33
- Bacon, R., Conseil, D., Mary, D., et al., (2017), *A&A*, 608, A1
- Bacon, R., Mary, D., Garel, T., et al., (2021), *A&A*, 647, A107
- Bielby, R. M., Tummuangpak, P., Shanks, T., et al., (2016), *MNRAS*, 456, 4061
- Davis, M., & Peebles, P. J. E., (1983), *ApJ*, 267, 465
- Diener, C., Wisotzki, L., Schmidt, K. B., et al., (2017), *MNRAS*, 471, 3186
- Durkalec, A., Le Fèvre, O., Pollo, A., et al., (2014), *A&A*, 583, A128
- Durkalec, A., Le Fèvre, O., Pollo, A., et al., (2018), *A&A*, 612, A42
- Furlanetto, S. R., Zaldarriaga, M., Hernquist, L., et al., (2006), *MNRAS*, 365, 1012
- Garel, T., Blaizot, J., Guiderdoni, B., et al., (2015), *MNRAS*, 450, 1279
- Gawiser, E., Francke, H., Lai, K., et al., (2007), *ApJ*, 671, 278
- Gebhardt, K., Cooper, E. M., Ciardullo, R., et al., (2021), *ApJ*, 923, 217
- Harikane, Y., Ouchi, M., Ono, Y., et al., (2018), *PASJ*, 70, S11
- Hatfield, P. W., Bowler, R. A. A., Jarvis, M. J., et al., (2018), *MNRAS*, 477, 3760
- Herenz, E. C., Urrutia, T., Wisotzki, L., et al., (2017), *A&A*, 606, A12
- Herenz, E. C., Wisotzki, L., Saust, R., et al., (2019), *A&A*, 621, A107
- Herrero Alonso, Y., Krumpke, M., Wisotzki, L., et al., (2021), *A&A*, 653, A136
- Hinshaw, G., Larson, D., Komatsu, E., et al., (2013), *AJSS*, 208, 19
- Hinton, S. R., Davis, T. M., Lidman, C., et al., (2016), *A&C*, 15, 61
- Hu, E. M., Cowie, L. L., McMahon, R. G., et al., (1998), *ApJ*, 502, L99
- Hutter, A., Dayal, P., & Müller, V., (2015), *MNRAS*, 450, 4025
- Inami, H., Bacon, R., Brinchmann, J., et al., (2017), *A&A*, 608, 26
- Jenkins, A., Frenk, C. S., Pearce, F. R., et al., (1998), *ApJ*, 499, 20
- Kaiser, N., (1987), *MNRAS*, 227, 1
- Khostovan, A. A., Sobral, D., Mobasher, B., et al., (2018), *MNRAS*, 478, 2999
- Khostovan, A. A., Sobral, D., Mobasher, B., et al., (2019), *MNRAS*, 489, 555
- Konno, A., Ouchi, M., Ono, Y., et al., (2014), *ApJ*, 797, 16
- Krumpe, M., Miyaji, T., & Coil, A. L., (2010), *ApJ*, 713, 558
- Krumpe, M., Miyaji, T., Coil, A. L., et al., (2012), *ApJ*, 746, 1
- Krumpe, M., Miyaji, T., Coil, A. L., et al., (2018), *MNRAS*, 474, 1773
- Krumpe, M., Miyaji, T., Husemann, B., et al., (2015), *ApJ*, 815, 21
- Kusakabe, H., Shimasaku, K., Ouchi, M., et al., (2018), *PASJ*, 70, 4
- Lee, K. S., Giavalisco, M., Gnedin, O., et al., (2006), *ApJ*, 642, 63
- Limber, D. N., (1953), *ApJ*, 117, 134
- Luo, B., Brandt, W. N., Xue, Y. Q., et al., (2017), *ApJSS*, 228, 2
- Malkan, M. A., Cohen, D. P., Maruyama, M., et al., (2017), *ApJ*, 850, 5
- Mary, D., Bacon, R., Conseil, S., et al., (2020), *A&A*, 635, A194
- Matthee, J., Sobral, D., Santos, S., et al., (2015), *MNRAS*, 451, 400
- McQuinn, M., Hernquist, L., Zaldarriaga, M., et al., (2007), *MNRAS*, 381, 75
- Miyaji, T., Krumpke, M., Coil, A., et al., (2011), *ApJ*, 726, 83
- Moster, B. P., Somerville, R. S., Maulbetsch, C., et al., (2010), *ApJ*, 710, 903
- Navarro, J. F., Frenk, C. S., & White, S. D. M., (1997), *ApJ*, 490, 493
- Norberg, P., Baugh, C. M., Gaztañaga, E., et al., (2009), *MNRAS*, 396, 19
- Ouchi, M., Harikane, Y., Shibuya, T., et al., (2017), *PASJ*, 70, S13
- Ouchi, M., Shimasaku, K., Furusawa, H., et al., (2003), *ApJ*, 582, 60
- Ouchi, M., Shimasaku, K., Furusawa, H., et al., (2010), *ApJ*, 723, 869
- Salmon, B., Papovich, C., Finkelstein, S. L., et al., (2015), *ApJ*, 799, 183
- Santos, S., Sobral, D., & Matthee, J., (2016), *MNRAS*, 463, 1678

- Schaerer, D., Hayes, M., Verhamme, A., et al., (2011a), *A&A*, 531, A12
- Sheth, R., Mo, H. J., & Tormen, G., (2001), *MNRAS*, 323, 1
- Spinoso, D., Orsi, A., López-Sanjuan, C., et al., (2020), *A&A*, 643, A149
- Steidel, C. C., Giavalisco, M., Pettini, M., et al., (1996), *ApJ*, 462, L17
- Tilvi, V., Malhotra, S., Rhoads, J. E., et al., (2005), *ApJL*, 891, L10
- Tinker, J. L., (2007), *MNRAS*, 374, 477
- Tinker, J. L., Weinberg, D. H., & Zheng, Z., (2005), *MNRAS*, 368, 85
- Urrutia, T., Wisotzki, L., Kerutt, J., et al., (2019), *A&A*, 624, 24
- van den Bosch, F. C., More, S., Cacciato, M., et al., (2013), *MNRAS*, 430, 725
- Walter, F., Decarli, R., Carilli, C., et al., (2012), *ApJ*, 752, 93
- Wechsler, R. H., & Tinker, J. L., (2018), *ARAA*, 56, 435
- Yajima, H., Sugimura, K., & Hasegawa, K., (2018), *MNRAS*, 477, 5406
- Yoshioka, T., Kashikawa, N., Inoue, A., et al., (2022), *ApJ*, 927, 32
- Zheng, Z., Coil, A., & Zehavi, I., (2007), *ApJ*, 667, 760



## The contribution of faint Lyman- $\alpha$ emitters to extended Lyman- $\alpha$ halos constrained by MUSE clustering measurements\*

Y. Herrero Alonso<sup>1</sup>, L. Wisotzki<sup>1</sup>, T. Miyaji<sup>2</sup>, J. Schaye<sup>3</sup>, J. Pharo<sup>1</sup> and M. Krumpke<sup>1</sup>

<sup>1</sup> Leibniz-Institut für Astrophysik Potsdam (AIP), An der Sternwarte 16, 14482 Potsdam, Germany

<sup>2</sup> Universidad Nacional Autónoma de México, Instituto de Astronomía (IA-UNAM-E), AP 106, Ensenada 22860, BC, Mexico

<sup>3</sup> Leiden Observatory, Leiden University, PO Box 9513, 2300 RA Leiden, The Netherlands

### ABSTRACT

Recent detections of extended Lyman- $\alpha$  halos around Ly $\alpha$  emitters (LAEs) have been reported on a regular basis, but their origin is still under investigation. Simulation studies predict that the outer regions of the extended halos contain a major contribution from the Ly $\alpha$  emission of faint, individually undetected LAEs. To address this matter from an observational angle, we used halo occupation distribution (HOD) modelling to reproduce the clustering of a spectroscopic sample of 1265 LAEs at  $3 < z < 5$  from the MUSE-Wide survey. We integrated the Ly $\alpha$  luminosity function to estimate the background surface brightness due to discrete faint LAEs. We then extended the HOD statistics inwards towards small separations and computed the factor by which the measured Ly $\alpha$  surface brightness is enhanced by undetected close physical neighbors. We considered various clustering scenarios for the undetected sources and compared the corresponding radial profiles. This enhancement factor from LAE clustering depends strongly on the spectral bandwidth  $\Delta\nu$  over which the Ly $\alpha$  emission is integrated and this value can amount to  $\approx 20 - 40$  for small values of  $\Delta\nu$  (around 200 – 400 km/s) as achieved by recent studies utilizing integral-field spectrographic data. The resulting inferred Ly $\alpha$  surface brightness of faint LAEs ranges between  $(0.4 - 2) \times 10^{20} \text{ erg s}^{-1} \text{ cm}^{-2} \text{ arcsec}^{-2}$ , with a very slow radial decline outwards. Our results suggest that the outer regions of observed Ly $\alpha$  halos ( $R \gtrsim 50 \text{ pkpc}$ ) could indeed contain a strong component from external (but physically associated) LAEs, and may even be dominated by them. It is only for a relatively shallow faint-end slope of the Ly $\alpha$  luminosity function that this contribution from clustered LAEs would be rendered insignificant. We also confirm that the observed emission from the inner regions ( $R \leq 20 - 30 \text{ pkpc}$ ) is too bright to be substantially affected by clustering. We compare our findings with predicted profiles from simulations and find good overall agreement. We outline possible future measurements to further constrain the impact of discrete undetected LAEs on observed extended Ly $\alpha$  halos.

### 4.1 Introduction

The Ly $\alpha$  line is a paramount cosmological feature for probing early star-forming galaxies and commonly assists in the detection of high-redshift galaxies, namely, Ly $\alpha$  emitters (LAEs). The ionizing photons produced by their young stars ionize

neutral hydrogen (HI) atoms in the neighbouring interstellar medium (ISM) and, after recombination, they have a probability of about 65% of being re-emitted as Ly $\alpha$  photons (Partridge & Peebles, 1967). As a result of the complex radiative transfer that the Ly $\alpha$  emission undergoes, a fraction of photons escape the ISM by resonantly

\*A version of this chapter is accepted for publication in *Astronomy & Astrophysics*.

scattering with HI throughout the circumgalactic and intergalactic media (CGM, IGM). In combination with several other factors, this effect causes the emission to become diffuse, giving rise to so-called extended Ly $\alpha$  halos.

Statistically relevant detections of extended Ly $\alpha$  halos (LAHs) have employed narrowband imaging observations (Hayashino et al., 2004; Nilsson et al., 2009; Finkelstein et al., 2011), which restrained the detectable surface brightness (SB) level to  $\sim 10^{-18}$  erg s $^{-1}$  cm $^{-2}$  arcsec $^{-2}$ . A significant step forward in terms of limiting SB is demonstrated in the studies of Steidel et al. (2011), Matsuda et al. (2012), Momose et al. (2014), and Xue et al. (2017), who adopted the image-stacking approach and extended the SB threshold by an order of magnitude, SB  $\sim 10^{-19}$  erg s $^{-1}$  cm $^{-2}$  arcsec $^{-2}$ . Recently, another major sensitivity improvement was made possible by the Multi-Unit Spectroscopic Explorer (MUSE) instrument at the ESO-VLT (Bacon et al., 2010), which evened out the limiting SB of individual object-by-object measurements to the limits obtained by the stacking of narrowband data. Wisotzki et al. (2016), Leclercq et al. (2017), Claeysens et al. (2022), and Kusakabe et al. (2022) reported the detection of ubiquitous extended LAHs at  $3 < z < 6$  and found that, on average, the LAHs detected by MUSE are a factor 4 – 20 more extended than their corresponding UV galaxy sizes, presenting median scale lengths of few physical kpc (pkpc). Combining the added depth of MUSE and the signal gain through stacking, Wisotzki et al. (2018) ascertained extended LAHs at much larger scales ( $\approx 60$  pkpc at  $z = 3$ ) than previous studies at similar redshifts ( $\approx 30$  pkpc). Recent works with Hobby-Eberly Telescope Dark Energy Experiment (HETDEX; Gebhardt et al. 2021) LAEs at  $1.9 < z < 3.5$  and Subaru LAEs at  $z = 2.2 - 2.3$  again roughly doubled the radii over which LAHs can be detected (160 pkpc and 200 pkpc, respectively; Niemeyer et al., 2022; Zhang et al., 2023).

Understanding the characteristics and, in particular, the nature of these extended LAHs provides information as to the spatial distribution and kinematic properties of the CGM (Zheng et al., 2011a) as well as, more fundamentally, to the processes of formation and evolution of galaxies (Bahcall & Spitzer, 1969). The main mechanisms that are believed to contribute to the existence of LAHs are (i) resonant scattering of Ly $\alpha$  photons produced in ionized HII regions of the ISM,

(ii) "in situ" recombination, (iii) fluorescence by photons from the metagalactic UV background, and (iv) collisional excitation from cooling gas accreted onto galaxies, also denoted as "gravitational cooling." Processes (i) and (ii) are consequences of local star formation through Lyman continuum radiation emitted from young and massive stars in star-forming galaxies: processes (iii) and (iv) are driven by external influences.

Comparisons between observational constraints and simulation studies have not yet delivered unique conclusions about the dominant origin of LAHs. Furthermore, while some simulation studies (e.g., Dijkstra & Kramer, 2012; Gronke & Bird, 2017) were able to fully explain the observed extended Ly $\alpha$  emission with the processes mentioned above, others (Shimizu & Umemura, 2010; Lake et al., 2015; Mas-Ribas & Dijkstra, 2016; Mas-Ribas et al., 2017; Mitchell et al., 2021; Byrohl et al., 2021) argued that in addition to these factors there is a significant contribution from Ly $\alpha$  emission originating in faint satellite galaxies. This emission would be significant only by its collective effects, as most of these "satellite LAEs" are too faint to be detected individually at the sensitivity of current observations. Lake et al. (2015) assessed that in their simulations the cooling of gas accreted onto galaxies as well as nebular radiation from satellites are the major contributors in the outer halo ( $R > 2$  pkpc). Mitchell et al. (2021) found that scattering is the dominant mechanism in the inner regions of the SB profile ( $R < 7$  pkpc, SB of few SB  $\sim 10^{-19}$  erg s $^{-1}$  cm $^{-2}$ ), scattering and satellites contribute equally at intermediate scales ( $R \approx 10$  pkpc, SB  $\sim 10^{-19}$  erg s $^{-1}$  cm $^{-2}$ ), and satellites dominate the large scales ( $R > 20$  pkpc, SB  $\sim 10^{-20}$  erg s $^{-1}$  cm $^{-2}$  arcsec $^{-2}$ ). Similar conclusions were drawn in Byrohl et al. (2021), whereby the authors identified scattering as the major source of SB and held photons originating in dark matter halos (DMHs) in the vicinity of the central galaxy responsible for the flattening of the observed SB profiles at  $R > 100$  pkpc.

The existence of faint sources around more massive and brighter galaxies is certainly predicted by the hierarchical cold dark matter (CDM) model of structure formation. Because this is closely related to non-linear clustering, Mas-Ribas et al. (2017) considered several clustering scenarios, coupled to the analytic formalism described in Mas-Ribas & Dijkstra (2016), to in-



investigate the plausibility of faint sources generating LAHs. In line with the previously mentioned simulations, they found that faint LAEs are the major contributors to the Ly $\alpha$  SB profiles already at  $R > 4$  pkpc. In contrast, Kakiichi & Dijkstra (2018) applied a model based on galaxy-Ly $\alpha$  forest clustering data to build Ly $\alpha$  SB profiles that could match a multitude of observed Ly $\alpha$  SB profiles even without considering the contribution from faint LAEs.

Despite the theoretical efforts to distinguish between the numerous contributions to the extended LAHs, observational tests and evidence for the "faint LAE" scenario are scant, mainly because of the extremely low SB of the Ly $\alpha$  emission at large distances from galaxies. Bacon et al. (2021) detected very extended Ly $\alpha$  emission around LAE overdensities in the MUSE extremely deep field (MXDF), reaching far beyond individual LAHs, but from comparing their data with the semi-analytic model GALICS (Garel et al., 2015) they concluded that much (and possibly all) of the apparently diffuse emission can be accounted for by the collective contribution of discrete faint LAEs surrounding more luminous (detected) ones.

A key step that is still missing is an assessment of the magnitude of this contribution based on observations, rather than on theoretical predictions. In this paper, we address this issue by employing LAE clustering statistics in combination with halo occupation distribution (HOD) models to obtain observational constraints on the contribution of the faint LAEs to the extended LAHs. We built on our previous study (Herrero Alonso et al. 2023a, hereafter HA23), where we used the HOD framework to interpret the clustering of three MUSE LAE samples at  $3 < z < 6$ . Each dataset had a different exposure time and thus covered a distinct range of Ly $\alpha$  luminosities within  $40.15 < \log(L_{\text{Ly}\alpha}/[\text{erg s}^{-1}]) < 43.35$ . We found a strong ( $8\sigma$  significance) clustering dependence on  $L_{\text{Ly}\alpha}$ , where more luminous LAEs cluster more strongly and reside in more massive DMHs than faint LAEs.

The paper is structured as follows. In Sect. 5.2, we briefly describe the data used for this work. In Sect. 4.3, we summarize the clustering properties of our galaxy sample. We extrapolate the clustering features to estimate the contribution of undetected LAEs to the extended Ly $\alpha$  halos in Sect. 4.4, where we also compare our estimations

to recent observational and simulated results. We give our conclusions in Sect. 5.6.

Throughout the paper, comoving and physical distances are given in units of  $h^{-1}$ Mpc and pkpc, respectively, where  $h = H_0/100 = 0.70$ . We use a  $\Lambda$ CDM cosmology and adopt  $\Omega_M = 0.3$ ,  $\Omega_\Lambda = 0.7$ , and  $\sigma_8 = 0.8$  (Hinshaw et al., 2013). All uncertainties represent  $1\sigma$  (68.3%) confidence intervals.

## 4.2 Data

This paper is based on the results from two different spectroscopic MUSE samples. We used a sample of LAEs from the MUSE-Wide survey for the clustering constraints and we employed the data from two MUSE deep fields for the comparison to observed Ly $\alpha$  halos (see Sect. 4.4.4).

### 4.2.1 The MUSE-Wide survey

The main input to the HOD model of Sect. 4.3 is based on the clustering constraints of a subset of the LAE MUSE-Wide survey (Herenz et al., 2017; Urrutia et al., 2019), which is similar to the LAE dataset used in Herrero Alonso et al. (2023a). The sample is constructed from 100 fields, each spanning  $1 \text{ arcmin}^2$ , observed with an exposure time of one hour, and covering regions of CANDELS/GOODS-S, CANDELS/COSMOS and the Hubble Ultra Deep Field (HUDF) parallel fields. The survey also incorporates shallow (1.6 hours) subsets of MUSE-Deep data (Bacon et al., 2017; Bacon et al., 2022) within the HUDF in the CANDELS/GOODS-S region. We refer to Urrutia et al. (2019) for further details on survey build-up, reduction, and flux calibration of the MUSE data cubes.

In contrast to the study in HA23, here we focus on LAEs with redshifts within  $3 < z < 5$  (and use the same redshift interval for the comparison to Ly $\alpha$  SB profile measurements in Sect. 4.4.4). Because Ly $\alpha$  peak redshifts are typically offset by up to several hundreds of  $\text{km s}^{-1}$  from systemic ones (e.g., Hashimoto et al. 2015; Muzahid et al. 2020; Schmidt et al. 2021), we corrected the Ly $\alpha$  redshifts following the relations given in Verhamme et al. (2018), which assure an accuracy of  $\leq 100 \text{ km s}^{-1}$  (Schmidt et al., 2021). We refer to Herrero Alonso et al. (2021), hereafter HA21, and references therein for further details on the LAE sample construction.

Our sample comprises a total of 1265 LAEs with Ly $\alpha$  luminosities in the range  $40.84 < \log(L_{\text{Ly}\alpha}/[\text{erg s}^{-1}]) < 43.30$  and a median value of  $\langle \log(L_{\text{Ly}\alpha}/[\text{erg s}^{-1}]) \rangle = 42.27$ . While the Ly $\alpha$  luminosity and redshift distributions of the sample are presented in Fig. 4.2.1, Figs. 1, and B.1 of HA23 show the spatial coverage of the LAE dataset. Taking into account the field-to-field overlaps, the actual surveyed area corresponds to  $90.2 \text{ arcmin}^2$  and extends  $\approx 43 h^{-1} \text{Mpc}$  at the median redshift of the sample  $\langle z \rangle = 3.8$ . This implies a LAE density of  $\approx 2 \cdot 10^{-3} h^3 \text{Mpc}^{-3}$ .

## 4.2.2 MUSE Deep fields

In Sect. 4.4.4, we compare our results to Ly $\alpha$  radial SB profiles, using the same data and measured in a similar way as by Wisotzki et al. (2018). The parent sample is a combination of LAEs detected by MUSE in the Hubble Deep Field South (Bacon et al., 2015) and in the Hubble Ultra-Deep Field (Bacon et al., 2017), as well as the definition of the final sample proceeds as in Wisotzki et al. (2018), with the exception that here we are only considering a single set of objects with redshifts of  $3 < z < 5$ .

To further facilitate a comparison to the clustering predictions, we also modified the construction of the resulting Ly $\alpha$  SB profile as follows: instead of the individually optimized spectral extraction windows for each LAE used by Wisotzki et al. (2018), we adopted a fixed velocity bandwidth of  $600 \text{ km s}^{-1}$  centered on the peak of the Ly $\alpha$  emission of each galaxy. This bandwidth not only provides a good compromise between noise suppression and flux loss avoidance in the stacking approach, it also facilitates the redshift-space distortion modelling (described in Sect. 4.3). We denote the individually extracted Ly $\alpha$  images as "pseudo-narrowband" in order to distinguish them from genuine filter-based narrowband (NB) imaging data, which encompass much wider bandwidths of typically  $\approx 12000 - 25000 \text{ km s}^{-1}$ . Unlike Wisotzki et al. (2018), we also skipped the artificial truncation of the used pseudo-NB data at a radius of  $6''$  ( $\approx 40 \text{ kpc}$ ), and we now used the mean instead of the median to stack the images, to make the resulting profiles as similar as possible to the clustering calculations in their construction logic.

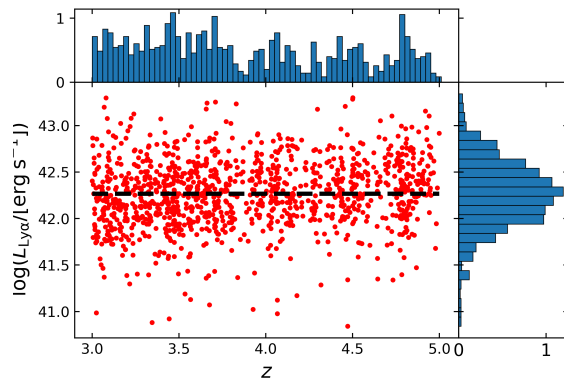


**Figure 4.2.1:** Distribution in Ly $\alpha$  luminosity-redshift space of the  $3 < z < 5$  LAEs selected from the spectroscopic MUSE-Wide survey. The dashed line corresponds to the median  $\log L_{\text{Ly}\alpha}$  of the sample. The normalized redshift and  $\log L_{\text{Ly}\alpha}$  distributions are shown in the top and right panels, respectively.

## 4.3 Clustering framework

In HA23 we measured the clustering of three LAE samples, including a subset of the MUSE-Wide survey, with the K-estimator of Adelberger et al. (2005). The K-estimator measures the radial clustering along line of sight distance,  $Z$ , by counting galaxy pairs in redshift space at fixed transverse separations,  $R$ . The K-estimator is directly related to the average underlying correlation function (see Eq. 2 in HA21). We refer to Sect. 3.1 in HA21 for further details.

We then fitted the K-estimator measurements with HOD modelling performed at the median redshift of the galaxy pairs of the sample. The HOD model we used is a simplified version of the five parameter model by Zheng et al. (2007). Because of sample size limitations, the halo mass at which the satellite occupation becomes zero and the scatter in the central halo occupation lower mass cutoff were fixed to  $M_0 = 0$  and  $\sigma_{\log M} = 0$ , respectively. The three free parameters are then the minimum halo mass required to host a central galaxy,  $M_{\text{min}}$ , the halo mass threshold to host (on average) one satellite galaxy,  $M_1$ , and the high-mass power-law slope of the satellite galaxy mean occupation function,  $\alpha$  (see Sect. 3.3 in HA23). Although we included redshift space distortions (RSDs) in the two-halo term using linear theory (Kaiser infall, Kaiser, 1987; van den Bosch et al., 2013), we ignored the effect of RSDs in the one-halo term given its negligible effect at the scales there considered.

The most relevant finding of HA23 for

this work is the strong clustering dependence on Ly $\alpha$  luminosity. Luminous ( $\log(L_{\text{Ly}\alpha}/[\text{erg s}^{-1}]) \approx 42.53$ ) LAEs cluster significantly ( $8\sigma$ ) more strongly and reside in  $\approx 25$  times more massive DMHs than less luminous ( $\log(L_{\text{Ly}\alpha}/[\text{erg s}^{-1}]) \approx 40.97$ ) LAEs. Hence, any fainter dataset is assumed to be less strongly clustered than those considered here or in HA23.

In Appendix 4.A, we demonstrate that the clustering strengths of the MUSE-Wide LAE subset considered in HA23 and our current sample are nearly identical. We convert the best-fit HOD model of the K-estimator found in HA23 to the traditional real-space two-point correlation function (2pcf) using Eq. 2 in HA21. In the left panel of Fig. 4.3.1 we represent the real-space 2pcf,  $\xi(r)$ , where  $r = \sqrt{R^2 + Z^2}$ , and where the contours show the expected circular symmetry. The model parameters correspond to a minimum DMH mass for central LAEs of  $\log(M_{\text{min}}/[h^{-1}M_{\odot}]) = 10.7$ , a threshold DMH mass for satellite LAEs of  $\log(M_1/[h^{-1}M_{\odot}]) = 12.4$  and a power-law slope of the number of satellites  $\alpha = 2.8$ . The corresponding satellite fraction, typical DMH mass, and virial radius are  $f_{\text{sat}} \approx 0.012$ ,  $\log(M_h/[h^{-1}M_{\odot}]) = 11.09_{-0.09}^{+0.10}$ , and  $R_{\text{vir}} \approx 36_{-2}^{+3}$  kpc, respectively (HA23).

Given the small bandwidths of the extracted pseudo-NB Ly $\alpha$  images from MUSE data (a few hundred km s $^{-1}$  or few comoving Mpc), we then included RSDs in the one-halo term (the so-called Fingers of God effect, FoG), following Tinker (2007). We convolved the line of sight component of the real-space 2pcf with the probability distribution function of galaxy pairwise velocities,  $P(v)$ . For each DMH mass,  $M_h$ , we assume a Gaussian distribution  $P(v, M_h)$  with velocity dispersion of central-satellite pairs determined by the streaming model namely,  $\sigma_v^2 \approx GM_h/(2R_{\text{vir}})$ , where  $R_{\text{vir}}$  is the virial radius. A Gaussian  $P(v, M_h)$  is supported by hydrodynamic simulations and observational analysis of rich SDSS clusters (see Tinker 2007 and references therein). We also included the extra contribution corresponding to the uncertainty in the Ly $\alpha$ -to-systemic redshift relation,  $\sigma_{v,\text{sys}} \sim 100$  km s $^{-1}$ . However, we ignore the contribution from satellite-satellite pairs given the negligible satellite fraction of the sample. The convolution kernel is then a superposition of weighted Gaussians with dispersion  $\sigma_v^2 \approx GM_h/(2R_{\text{vir}}) + \sigma_{v,\text{sys}}^2$ . We weight the Gaussians with the relative number of satellite galaxies,  $N_s$ , hosted by each DMH,

which involves an integral over the halo mass function  $\phi(M_h) dM_h$  (see Eq. 5 in Tinker 2007) as follows

$$P(v) = \frac{\int P(v, M_h) \langle N_s(M_h) \rangle \phi(M_h) dM_h}{\int \langle N_s(M_h) \rangle \phi(M_h) dM_h}. \quad (4.1)$$

In the right panel of Fig. 4.3.1, we present the redshift-space 2pcf i.e.,  $\xi(s) = \sqrt{R^2 + Z_s^2}$ , where  $Z_s$  is the line of sight comoving distance in redshift-space. The deviations from circular symmetry are clear. At large scales ( $s > 5 h^{-1}\text{Mpc}$ ), the coherent gravitational infall of galaxies onto forming structures (Kaiser infall, Kaiser, 1987; van den Bosch et al., 2013) flattens the  $\xi(s)$  contours. At small scales ( $Z_s < 5 h^{-1}\text{Mpc}$ ), the stretching of the  $\xi(s)$  contours for line of sight separations is caused by the peculiar velocities of galaxies when galaxy redshifts are used as proxies for distances. Because the distribution of LAEs at  $3 < z < 5$  is affected by the FoG effect only at  $Z_s \lesssim 5 h^{-1}\text{Mpc}$  (peculiar motions of  $< 500$  km s $^{-1}$ ) and is negligible at larger separations, we only include the FoG effect when considering velocity widths  $< 500$  km s $^{-1}$  (see Sect. 4.4.2).

## 4.4 Contribution of faint LAEs to extended Ly $\alpha$ halos

Taking advantage of the clustering constraints, we now seek to assess the contribution of undetected LAEs to the extended Ly $\alpha$  halos. Those objects are much fainter than those considered here or in HA23, and given the overall tendency of galaxies to cluster, they are expected to be found around our more luminous LAEs. Hence, some fraction of the measured extended Ly $\alpha$  flux must come from those undetected galaxies. While photons included in the central part of the Ly $\alpha$  halo are well distinguished from sky noise, the outskirts of the halo typically have such low SB values that they are close to the noise level. It is on these regions that we focus our attention.

The spatial distribution of these sources enhances the Ly $\alpha$  SB values measured within a given (pseudo-)NB width at any projected distance,  $R$ , from the observed LAE. This boost is quantified with the clustering enhancement factor,  $\zeta(R)$ . The contribution of these faint LAEs to

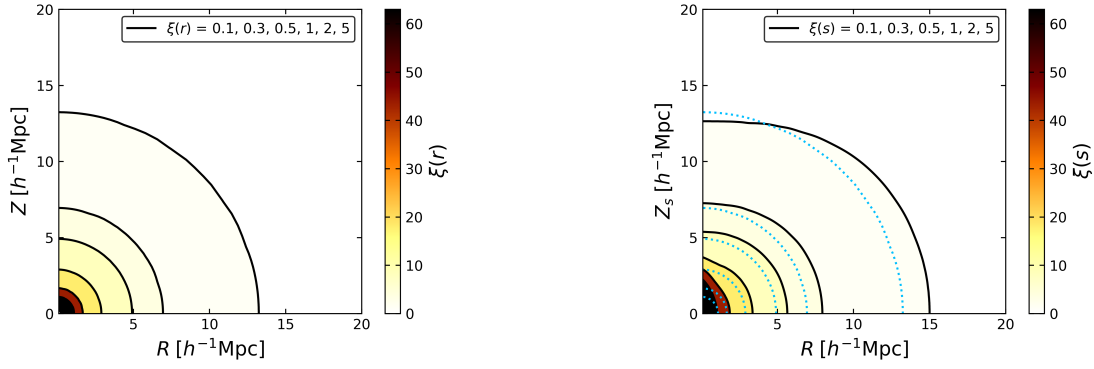


**Figure 4.3.1:** Best-fit HOD modelled real- and redshift-space 2pcf. Left: Real-space 2pcf,  $\xi(r)$ , for the sample of MUSE-Wide LAEs at  $3 < z < 5$ . Note: the circular symmetry of the color-coded contours. Right: Redshift-space 2pcf,  $\xi(s)$ . The dotted blue contours show the real-space 2pcf from the left panel. Note: the elongation of the 2pcf contours along the line-of-sight direction,  $Z_s$ , at small scales (FoG effect) and the flattening at larger transverse separations,  $R$ , (Kaiser infall). The contour levels are indicated in the legend.

the apparent Ly $\alpha$  SB profiles also depends on the number of undetected LAEs, which is obtained from the Ly $\alpha$  luminosity function (LF;  $\phi(L)dL$ ). The projected Ly $\alpha$  SB profile of undetected LAEs from a given pseudo-narrow band (NB) is:

$$SB(R) = \zeta(R) \cdot \int_{L_{\min}}^{L_{\det}(z)} L \times \phi(L) dL. \quad (4.2)$$

where  $L_{\det}(z)$  is the detection limit for individual LAEs and  $L_{\min}$  is the adopted lower limit for integrating the LF.

We go on to discuss the two ingredients of Eq. 4.2 in turn, first the luminosity function and then the enhancement factor.

#### 4.4.1 Ly $\alpha$ luminosity function

We quantify the number density of LAEs as a Schechter function (Schechter, 1976):

$$\phi(L)dL = \frac{\phi^*}{L^*} \left( \frac{L}{L^*} \right)^{\alpha_{LF}} e^{-(L/L^*)} dL, \quad (4.3)$$

where  $L^*$  denotes the characteristic luminosity,  $\phi^*$  the normalization density, and  $\alpha_{LF}$  the faint-end slope of the LF.

The matter of greatest importance with respect to our current study is the value of  $\alpha_{LF}$  because it largely governs the luminosity density ratio of undetected to detected LAEs. While earlier determinations of the Ly $\alpha$  LF were not able to constrain this parameter very well, this is now improving because of deeper LAE samples, particularly those of different MUSE surveys (Drake et al., 2017; Herenz et al., 2019; de la Vieuville

et al., 2019). The emerging trend is that the faint end of the LF is quite steep, with  $\alpha_{LF}$  approaching uncomfortably close to  $-2$ , which is the limiting value for which the luminosity density would diverge when integrating the LF to  $L = 0$ . Yet even with slightly less extreme slopes, the adopted lower integration limit has a significant impact on the resulting numbers. This probably indicates that the Schechter function approximation breaks down at very low luminosities. Here, we simply bypass this uncertainty by considering different lower integration limits, as discussed below.

We also assumed that  $\alpha_{LF}$  is constant within our current redshift range. While Drake et al. (2017) found a tentative indication for a steepening of the faint-end slope towards high  $z$ , most other studies concluded that the Ly $\alpha$  LF shows little or no significant evolution with redshift for  $3 \lesssim z \lesssim 6$  (Ouchi et al., 2008; Sobral et al., 2018; Konno et al., 2018; Herenz et al., 2019; de la Vieuville et al., 2019). As our baseline LF prescription, we adopted the best-fit parameters of Herenz et al. (2019), with  $\log(\phi^*/[Mpc^{-3}]) = -2.71$ ,  $\log(L^*/[erg s^{-1}]) = 42.6$ , and  $\alpha_{LF} = -1.84$ .

The upper integration limit in Eq. 4.2 depends on the details of the specific LAE survey under consideration. Since below we compare our calculations with the observed Ly $\alpha$  SB profile constructed from MUSE deep field data, we adopted a flux- and redshift-dependent selection function constructed to characterise this sample.

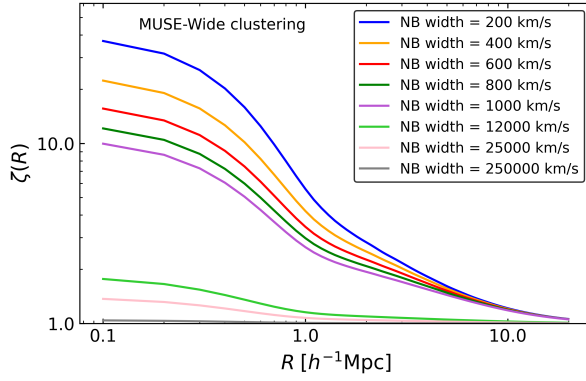


**Figure 4.4.1:** Clustering enhancement factor as a function of comoving transverse separation between LAE pairs. Each color corresponds to a different (FWHM) pseudo-NB width. For reference, we include typical NB widths of 12000 and 25000  $\text{km s}^{-1}$  (or 50 and 100 ) and a broad-band filter width of 250000  $\text{km s}^{-1}$  (or 1000 ). We assume that both resolved and undetected sources tend to cluster similarly to the MUSE-Wide LAE sample and include RSDs.

For the lower limit we use  $\log(L_{\min}/[\text{erg s}^{-1}]) = 38.5$  as our baseline value, but we also consider higher and lower values. As an extreme lower limit, we adopted  $\log(L_{\min}/[\text{erg s}^{-1}]) \approx 37$ , which could be generated by the HII region around a single O-type star with an absolute UV magnitude of  $M_{\text{UV}} \approx -6$ . More likely candidates for the smallest units that have to be considered are star clusters or dwarf galaxies with several tens or hundreds of such stars. We bracket the expected range by also adopting a "high" value of  $\log(L_{\text{Ly}\alpha}/[\text{erg s}^{-1}]) = 40$ .

Since our comparison  $\text{Ly}\alpha$  profile is a mean of LAEs in the redshift range  $3 < z < 5$ , we have to average the luminosity density also over this redshift range. In addition to a straight unweighted average, we also calculated a weighted mean that takes the actual redshift distribution of the sample into account. However, these two numbers differ by only a few percent.

#### 4.4.2 Clustering enhancement factor

The enhancement factor represents the boost in  $\text{Ly}\alpha$  SB due to the spatial distribution of undetected LAEs around our more luminous LAEs. This is computed from the cross-correlation function (CCF) between detected and undetected LAEs,  $\xi(R, Z)_{\text{CCF}}$ . We derived  $\zeta(R)$  from the 2pcf definition (Peebles, 1980) in Appendix 4.B and

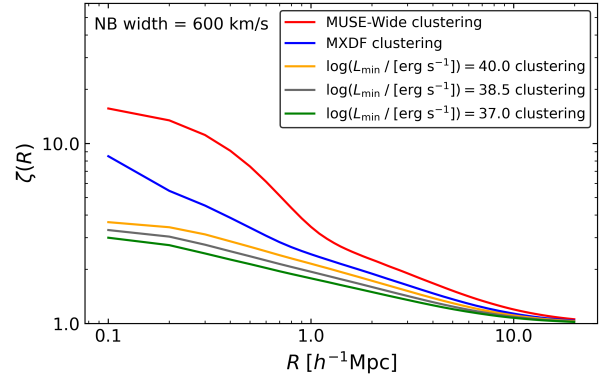


**Figure 4.4.2:** As in Fig. 4.4.1 but for a fixed (FWHM) pseudo-NB width of 600  $\text{km s}^{-1}$  and for different assumed clustering strengths for undetected sources, depending on their  $\text{Ly}\alpha$  luminosity. The red and blue enhancement factors assume that undetected LAEs cluster similarly to MUSE-Wide and MXDF LAEs, respectively. The orange, gray, and green factors assume an extrapolated HOD 2pcf for LAEs with  $\log(L_{\text{Ly}\alpha}/[\text{erg s}^{-1}]) \approx 40.0$ ,  $\log(L_{\text{Ly}\alpha}/[\text{erg s}^{-1}]) \approx 38.5$ , and  $\log(L_{\text{Ly}\alpha}/[\text{erg s}^{-1}]) \approx 37.0$ , respectively. In all cases, detected LAEs cluster similarly to what is seen for the MUSE-Wide sample.

give the outcome here:

$$\zeta(R) = \int_{-Z_{\text{NB}}}^{+Z_{\text{NB}}} [\xi(R, Z)_{\text{CCF}} + 1] \cdot dZ / \Delta Z, \quad (4.4)$$

where  $\Delta Z = +Z_{\text{NB}} - (-Z_{\text{NB}})$ . The radial comoving separations in redshift space,  $Z_{\text{NB}}$ , that is, by including the RSD effect, over which the integral is performed correspond to typical half-widths at half maximum of the (pseudo-)NBs applied in the measurement of  $\text{Ly}\alpha$  SB profiles ( $\sim 100 - 400 \text{ km s}^{-1}$ ; see, for instance, Wisotzki et al. 2018). In particular, because of the narrowness of  $Z_{\text{NB}}$ , it is imperative to model the RSD effects properly to estimate  $\xi(R, Z)_{\text{CCF}}$  from the HOD models.

Figure 4.4.1 shows the variation of the enhancement factor for various velocity widths (full width at half maximum, FWHM) applied in stacking experiments of (pseudo-)NB images of LAEs. As discussed below, we initially assume that detected and undetected LAEs share the same clustering properties. We thus employ the best-fit HOD modelled 2pcf of the right panel of Fig. 4.3.1, which corresponds to our sample of  $3 < z < 5$  MUSE-Wide LAEs.

While typical pseudo-NB widths of 200 – 800  $\text{km s}^{-1}$  (or 0.5 – 4 ) result in substantial enhancement factors of  $\approx 10-40$  at  $R = 0.1 \text{ h}^{-1}\text{Mpc}$ , the effective SB values measured with common

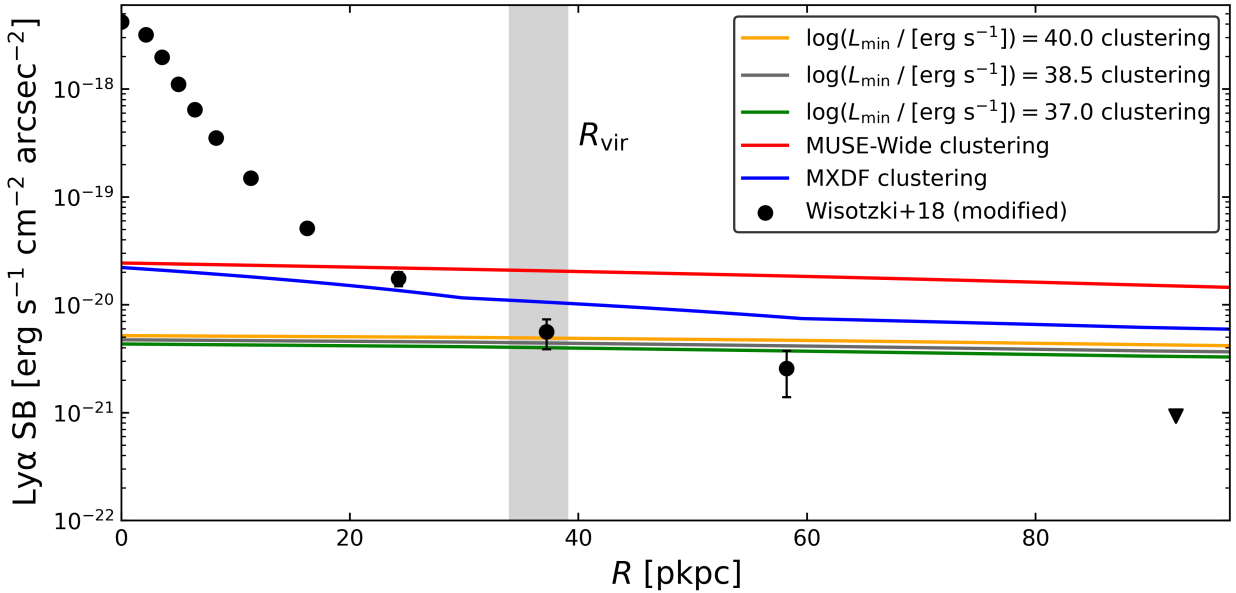


**Figure 4.4.3:** Contribution to the Ly $\alpha$  SB profiles from clustered and undetected LAEs with  $\log(L_{\min}/[\text{erg s}^{-1}]) = 38.5$ . Differently colored lines correspond to a different assumption for the clustering of undetected LAEs. Detected galaxies are assumed to cluster like those in the MUSE-Wide sample. The data points correspond to the modified stacking experiment of individual LAEs of Wisotzki et al. (2018) (see Sects. 5.2 and 4.4.4). The triangle denotes an upper limit. We employ a pseudo-NB width of  $600 \text{ km s}^{-1}$  and the Ly $\alpha$  LF of Herenz et al. (2019). The shaded gray region shows the typical virial radius of MUSE-Wide LAEs.

NB filters FWHM  $\approx 50 - 100 \text{ \AA}$  or  $12000 - 25000 \text{ km s}^{-1}$  are enhanced by only  $\zeta(R) \approx 1.5-2$  and thus barely boosted by clustering. Unsurprisingly, measurements through broad-band filters with FWHM  $\approx 1000 \text{ \AA}$  ( $250000 \text{ km s}^{-1}$ ) remain entirely unaffected ( $\zeta(R) \approx 1$ ). Thus, only for the narrow bandwidths achieved by IFU-based Ly $\alpha$  images is there a significant contribution of clustered LAEs to any underlying truly diffuse Ly $\alpha$  emission.

Unless explicitly specified, in the following we fix the bandwidth to  $Z_{\text{NB}} = 3 h^{-1} \text{ Mpc}$  (intermediate FWHM of  $Z = 6 h^{-1} \text{ Mpc}$  or  $600 \text{ km s}^{-1}$ : see Sect. 5.2), corresponding to a window spanning 2.5 in the rest frame around  $\lambda_{\text{Ly}\alpha} \approx 1216$ .

We also have to make assumptions about the clustering behaviour of the undetected sources to calculate the corresponding enhancement factor. Because the FoG effect is negligible at  $Z > 5 h^{-1} \text{ Mpc}$  (see Fig. 4.3.1), we did not include RSDs in the HOD modelling. The modelling process is described below.

As a first step, we assumed that detected and undetected LAEs present the same clustering properties. We show the corresponding boost factor in red in Fig. 4.4.2 (same as the red curve in Fig. 4.4.1 but without including RSDs; see the negligible difference between the two curves).

However, this is likely to be an overestimate: as demonstrated in HA23, the clustering strength depends significantly on Ly $\alpha$  luminosity ( $8\sigma$  in HA23) and, therefore, the even fainter undetected sources probably cluster less strongly than the MUSE-Wide LAEs. Since the enhancement factor depends directly on the clustering strength, this option only produces an upper limit on  $\zeta(R)$ .

Next, we modified the assumptions and allowed the undetected sources to have a clustering strength similar to the fainter LAEs detected at  $3 < z < 5$  in the MXDF (HA23), which are approximately one order of magnitude less luminous than the MUSE-Wide sample. As shown in Appendix 4.A for MUSE-Wide, the HOD model derived in HA23 for  $3 < z < 6$  is also able to describe the clustering of the current MXDF dataset. The resulting boost factor is shown in blue in Fig. 4.4.2. Although it is fainter than MUSE-Wide LAEs, the MXDF LAEs are still considerably more luminous than the hidden undetected ones. Hence, this boost factor is also an upper limit.

Finally, to obtain our best estimate of the actual enhancement factor of the undetected LAEs, we utilize the MUSE-Wide and MXDF HOD clustering probability contours of Sect. 4 of HA23

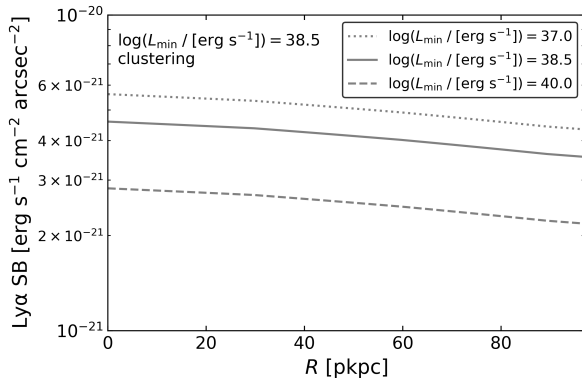


**Figure 4.4.4:** Ly $\alpha$  SB variation for plausible luminosities of the undetected LAEs. We assume that undetected sources cluster like the extrapolated HOD model for  $\log(L_{\min}/[\text{erg s}^{-1}]) = 38.5$ . Resolved sources cluster like those in the MUSE-Wide sample and the pseudo-NB width is  $600 \text{ km s}^{-1}$ . We use the Ly $\alpha$  LF from Herenz et al. (2019).

and extrapolate them to fainter luminosities. We first assumed that undetected LAEs have luminosities of  $\log L_{\text{Ly}\alpha} \approx 10^{40} \text{ erg s}^{-1}$  and obtained a HOD model with  $\log(M_{\min}/[h^{-1}M_{\odot}]) = 9.9$ ,  $\log(M_1/M_{\min}) = 1.1$  and  $\alpha = 0.1$ . We plot the resulting boost factor in orange in Fig. 4.4.2. We followed the same procedure for the other two lower integration limits (the resulting HOD models have  $\log(M_{\min}/[h^{-1}M_{\odot}]) = 9.4$ ,  $\log(M_1/M_{\min}) = 0.7$ ,  $\alpha = -1.6$ , and  $\log(M_{\min}/[h^{-1}M_{\odot}]) = 8.8$ ,  $\log(M_1/M_{\min}) = 0.3$ ,  $\alpha = -3.3$ , respectively), plotting their enhancement factors in gray and green. While the three last enhancement factors are based on extrapolations thereby untestable at present, we presume that these are probably closer to the truth than the one resulting from the assumption that faint LAEs cluster in the same way as much more luminous objects.

To build the Ly $\alpha$  SB profiles, we have to extrapolate the CCF models down to  $R = 0 \text{ kpc}$ , since our clustering measurements do not reach the smallest scales of the Ly $\alpha$  SB profiles ( $R < 30 \text{ pkpc}$ ). We also convert the comoving radii to physical kpc.

### 4.4.3 Ly $\alpha$ surface brightness profile from undetected LAEs

In Fig. 4.4.3, we build the expected Ly $\alpha$  SB profile from undetected LAEs with  $\log(L_{\min}/[\text{erg s}^{-1}]) = 38.5$  for a velocity width of the pseudo-NB of  $600 \text{ km s}^{-1}$ . The colors show the clustering scenarios considered in Sect. 4.4.2.

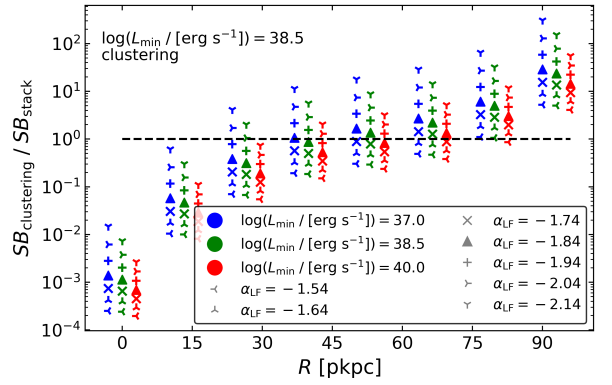


**Figure 4.4.5:** SB ratio of the Ly $\alpha$  SB profile from undetected LAEs and the redone stacked profile from Wisotzki et al. (2018) at  $3 < z < 5$ . The ratios at  $R = 90 \text{ pkpc}$  are lower limits. Undetected LAEs are assumed to cluster like the extrapolated HOD model for  $L_{\min} = 10^{38.5} \text{ erg s}^{-1}$  and resolved sources like those in the MUSE-Wide sample. The colors represent different minimum Ly $\alpha$  luminosities for the undetected sources. The symbols display various faint-end slopes of the Ly $\alpha$  LF. The dashed line shows a scenario in which the undetected LAEs alone fully explain the apparent Ly $\alpha$  SB profile. A pseudo-NB width of  $600 \text{ km s}^{-1}$  is assumed.

For comparison, we overplot the mean Ly $\alpha$  SB profile based on the stacking of LAEs in the MUSE Deep Fields (Sec. 5.2). We also indicate the typical virial radius of MUSE-Wide LAEs for guidance.

Before comparing the observed profile with the expected contribution from clustered faint LAEs (see Sect. 4.4.4 below), we have to evaluate the uncertainties and dependencies of our calculations with respect to the assumed input parameters.

We start by considering the different adopted clustering scenarios. By design, the maximum contribution is reached for the MUSE-Wide clustering assumption ( $\approx 2.5 \cdot 10^{-20} \text{ cgs}$ ), whereas the lowest extrapolated HOD model delivers SB levels lower by one order of magnitude ( $\approx 4 \cdot 10^{-21} \text{ cgs}$ ). Nevertheless, all versions of our estimates exceed the measurements at  $R > 60 \text{ kpc}$ .

The impact of using different lower integration limits for the LF is evaluated in Fig. 4.4.4. Here we assume that the clustering of faint LAEs follows the extrapolated HOD model for  $\log(L_{\min}/[\text{erg s}^{-1}]) = 38.5$  LAEs. The three curves show the variation in the SB contribution for various  $L_{\min}$  choices. As expected, the inclusion of fainter sources produces higher Ly $\alpha$  SB levels, although the difference is only a factor of  $\sim 2$  for the adopted range of  $L_{\min}$ .

In Fig. 4.4.5, we vary the value of the faint-end LF slope  $\alpha_{LF}$  in steps of  $\Delta\alpha = \pm 0.1$ , recomputing the SB profiles each time. The changes are substantial and demonstrate that the biggest single uncertainty in this estimate is still the faint-end shape of the Ly $\alpha$  LF. We also explored modifying the other LF parameters  $\phi^*$  and  $L^*$ , but these have a negligible effect on the predicted Ly $\alpha$  SB profiles.

#### 4.4.4 Comparison with observed surface brightness profile

It is clear from Fig. 4.4.3 that at  $R \lesssim 20$  pkpc the stacked Ly $\alpha$  SB is much higher than the level expected from undetected LAEs, irrespective of the clustering scenario, whereas for radii of  $\gtrsim 50$  pkpc, the observed SB level is always comparable to or lower than the contribution estimated from clustering. We note that even where the data points are formally below our calculations, for instance,  $R = 90$  kpc, the combination of error bars in the data with systematic uncertainties in the clustering and luminosity function evaluation imply that these two are not in contradiction.

When interpreting Fig. 4.4.3, we have to keep in mind that the two upper (red and blue) curves are upper limits in the sense that for these curves, the clustering of the undetected LAEs is assumed to be as strong as for (different sets of) detected LAEs. Allowing for a weaker clustering of the undetected objects shifts the radius of approximate equality outwards to at least  $\approx 40$  pkpc.

Figure 4.4.5 shows the inferred SB ratios (clustering/observed) instead of measured or calculated SB levels. For the fiducial baseline faint-end LF slope of  $\alpha_{LF} = -1.84$ , the Ly $\alpha$  emission from undetected LAEs can account for all of the measured Ly $\alpha$  SB profile at  $R \gtrsim 50$  pkpc, but only a fraction of 20% at  $R \sim 30$  pkpc. At these smaller distances to the central galaxy we presumably see genuine diffuse emission, powered by the above mentioned mechanisms.

These fractions (and the associated radii) are contingent on the uncertainties in the Ly $\alpha$  LF, especially its faint-end, which we here encapsulate by two parameters, the slope  $\alpha_{LF}$ , and the low-luminosity cutoff of  $L_{\min}$ . The effects of modifying any of these two are displayed in Fig. 4.4.5 by varying the symbols ( $\alpha_{LF}$ ) and colors ( $L_{\min}$ ). It is evident that varying  $L_{\min}$  has a much weaker effect than adopting a different LF slope.

An only slightly shallower LF would reduce the expected SB contribution of faint LAEs drastically to  $\approx 20 - 40\%$  at  $R \sim 50$  pkpc, whereas a steeper slope would imply that extended Ly $\alpha$  emission could be dominated by discrete objects already from distances of  $20 - 30$  pkpc outwards. It is worth mentioning that if undetected LAEs cluster similarly to the extrapolated HOD models, the minimum luminosity choices of  $\log(L_{\min}/[\text{erg s}^{-1}]) = 37, 40$  deliver indistinguishable SB ratios as those of Fig. 4.4.5. If undetected LAEs cluster like the LAEs in MUSE-Wide or MXDF, these ratios increase by (on average)  $\approx 70\%$  and  $\approx 30\%$ , respectively. In Appendix 4.C, we show how the SB ratio varies for different pseudo-NB widths.

These are very rough estimates. A sharp cut of the Ly $\alpha$  LF below a certain Ly $\alpha$  luminosity is, of course, implausible. A more realistic shape would probably involve some smooth turnover towards fainter luminosities. Such subtleties are however beyond the scope of this paper. Clearly more work is needed to study the faint parts of the Ly $\alpha$  luminosity function and its possible (non-)evolution with redshift. Nevertheless, our findings strongly support a scenario in which discrete but individually undetected LAEs are an important component of observed Ly $\alpha$  halos at  $R \gtrsim 30 - 50$  pkpc.

#### 4.4.5 Comparison with the simulations

Our results are in good agreement with the fundamental prediction from a number of simulation or modelling studies positing that faint LAEs in the vicinity of Ly $\alpha$  halos contribute to the observed extended emission and beyond some radii, they may even dominate (e.g., Lake et al., 2015; Mas-Ribas & Dijkstra, 2016; Mas-Ribas et al., 2017; Mitchell et al., 2021; Byrohl et al., 2021). Nevertheless, the models and also the predicted Ly $\alpha$  SB profiles due to "satellite" LAEs vary significantly between different studies. It is also worth mentioning that some of our undetected LAEs are, in principle, at the DMH center.

In the following we compare our Ly $\alpha$  SB profiles calculated from clustering with simulation studies that separate the satellite SB contribution from other powering mechanisms. We give the main differences below.

First, we consider the study of Lake et al. (2015), hereafter L15, where an adaptive mesh



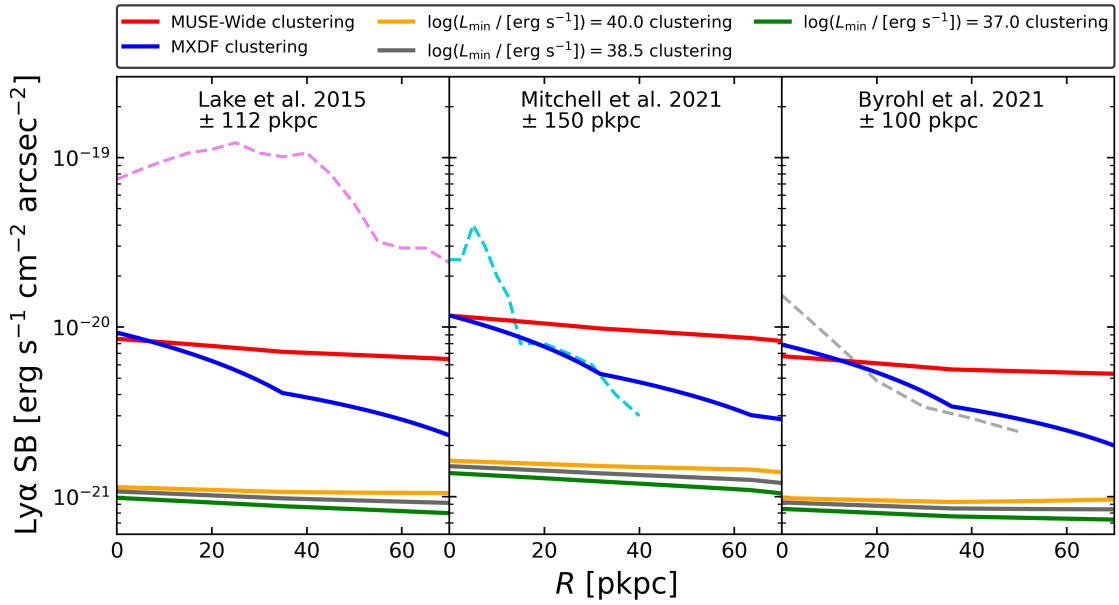


**Figure 4.4.6:** Comparison of our  $\text{Ly}\alpha$  SB profiles from undetected LAEs of  $\log(L_{\min}/[\text{erg s}^{-1}]) = 38.5$  (solid lines) and the satellite radial profiles predicted from simulations (dashed lines). The different colors of the solid curves correspond to the different clustering assumptions for the undetected LAEs displayed in the legend. Resolved LAEs are assumed to cluster in the same way as those in the MUSE-Wide sample. We adjusted our pseudo-NB width of Eq. 4.4 to the projection depth of the simulations. Left panel: Comparison to L15, whose applied projection depth is equivalent to a pseudo-NB width of  $66 \text{ km s}^{-1}$  at  $z_{\text{simul}} = 3.1$ . Middle panel: Comparison to M21 with a pseudo-NB width of  $94 \text{ km s}^{-1}$  at  $z_{\text{simul}} = 3.5$ . Right panel: Comparison to B21 with a pseudo-NB width of  $56 \text{ km s}^{-1}$  at  $z_{\text{simul}} = 3$ .

refinement hydrodynamical simulation of galaxy formation was used (Bryan & Norman, 2000; Joung et al., 2009). These authors modelled most potential sources of  $\text{Ly}\alpha$  photons and powering mechanisms namely, star formation from central and satellite galaxies, photon scattering, fluorescence from the UV background, supernova feedback (outflows), and gravitational cooling at  $z_{\text{simul}} = 3.1$ . The  $\text{Ly}\alpha$  emission was modelled using the Monte Carlo radiative transfer code of Zheng & Miralda-Escude (2002). The dark matter particle mass is  $1.3 \times 10^7 M_{\odot}$ , the simulation box size is  $120 h^{-1} \text{ Mpc}$ , and the spatial resolution  $\approx 111 \text{ pc}$ . Although the derived total  $\text{Ly}\alpha$  SB profiles match those measured in Matsuda et al. (2012), Xue et al. (2017) found that the simulated profile that included star formation from satellites considerably overpredicted the measured SB curves. To extract the SB profile, they employed a projection depth of  $224 \text{ pkpc}$  to include all scattered photons around the LAEs.

Next, Mitchell et al. (2021), hereafter M21, employed an adaptive mesh refinement zoom-in cosmological radiation hydrodynamics simulation of a single galaxy using the RAMSES-RT code (Rosdahl et al., 2013; Rosdahl & Teyssier, 2015). The stellar and DMH masses are  $M_{\star} = 10^{9.5} M_{\odot}$

and  $M_h = 10^{11.1} M_{\odot}$ , respectively. These authors modelled the same  $\text{Ly}\alpha$  powering mechanisms at  $3 < z < 4$  as L15. They also performed Monte Carlo radiative transfer to assess the  $\text{Ly}\alpha$  emission, tracing the emergent radiation along several different lines of sight and at different cosmic times. The simulation box is a sphere of  $150 \text{ kpc}$  radius and achieved a spatial resolution of  $14 \text{ pc}$ , with a characteristic dark matter particle mass of  $10^4 M_{\odot}$ . The simulated total  $\text{Ly}\alpha$  SB profile matched the one measured in Wisotzki et al. (2018), for which they used a projection depth of  $\pm 150 \text{ pkpc}$  at  $z_{\text{simul}} = 3.5$  around the LAE.

Finally, Byrohl et al. (2021), hereafter B21, utilized the outcome of the TNG50 (Nelson et al., 2019b; Pillepich et al., 2019) from the IllustrisTNG simulations (Pillepich et al., 2018b), coupled to their  $\text{Ly}\alpha$  full radiative transfer code VOROILTIS. They modelled the same  $\text{Ly}\alpha$  emission sources and powering mechanisms at  $2 < z < 5$  as L15 and M21 and further included a treatment for active galactic nuclei. TNG50 has a box size of  $50 \text{ Mpc}$ , attains a spatial resolution of  $\sim 100 \text{ pc}$  and a dark matter particle mass of  $4.5 \times 10^5 M_{\odot}$ . These authors were able to reproduce the  $\text{Ly}\alpha$  SB profiles measured in Leclercq

et al. (2017), for which they included all scattered photons from within  $\pm 100$  pkpc along the line of sight at  $z_{\text{simul}} = 3$  around the LAE.

Although most simulations deliver similar conclusions and their total Ly $\alpha$  SB profiles match a range of observations, the predicted contribution from satellites to the observed radial profiles at various scales varies significantly. We compare in Fig. 4.4.6 our clustering-based Ly $\alpha$  SB profiles (with  $\log(L_{\text{min}}/[\text{erg s}^{-1}]) = 38.5$ , but considering all clustering scenarios) to simulated satellite radial profiles. For this purpose, we recalculate our enhancement factors and SB profiles in order to approximately match our selected pseudo-NB width (i.e.,  $Z_{\text{NB}}$  in Eq. 4.4) to the projection depth applied in the simulations. We note that while the pseudo-NB width in observed spectral stacks cannot be narrower than the common linewidth, the typical bandwidths formally converted to real space depths are much greater than simulation boxes. To enable at least a rough comparison we used the simulated depths, which correspond to velocity intervals of  $\approx 60 - 100 \text{ km s}^{-1}$ . We also multiplied the simulated profiles by  $(1 + z_{\text{simul}})^4 / (1 + \langle z \rangle)^4$  to account for surface brightness dimming. The simulated contribution is due to the Ly $\alpha$  emission from satellites in L15 (dashed magenta) and M21 (dashed light blue), and to this plus a genuinely diffuse emission powered by these "other halos" in B21 (dashed light gray).

The profile from L15 is clearly flatter than those from M21 and B21 and is in this respect similar to our clustering-based SB profiles. This also agrees with the generally observed trend that the radial profiles tend to flatten at larger radii (Matsuda et al., 2012; Momose et al., 2014; Wisotzki et al., 2018; Niemeyer et al., 2022). On the other hand, the SB level predicted by L15 is much higher than ours, already by an order of magnitude than our two upper limit scenarios. The SB levels predicted by M21 and B21 are in better agreement with our upper limit SB estimates, although still higher than our extrapolated "low clustering" scenarios. This may reflect the fact that simulated galaxies in L15 present higher stellar and DMH masses ( $M_{\star} = 2.9 \cdot 10^{10} M_{\odot}$  and  $M_h = 10^{11.5} M_{\odot}$ ) than those of MUSE LAEs or those considered in M21 and B21. At small scales, the M21 and B21 simulated radial profiles are slightly steeper than the high clustering scenario curves of MUSE-Wide and MXDF.

The differences between our clustering-based

and the simulated SB profiles could be attributed to several factors. An overprediction of the simulated number of satellites would naturally lead to an overestimated contribution of discrete LAEs to the Ly $\alpha$  halos. This issue seems to be common to simulations and semi-analytical models, including the IllustrisTNG project and EAGLE simulations (e.g., Okamoto et al., 2010; Simha et al., 2012; Geha et al., 2017; Shuntov et al., 2022). In this context it is interesting to note that our upper limit clustering scenarios give results closer to the simulations than the extrapolations deemed to be more realistic.

Alternatively, there could also be a problem related to low number statistics, since the models by M21 and L15 are based on only one and nine galaxies, respectively. This is probably not an issue for B21, as they did not account for Ly $\alpha$  destruction by dust, which would otherwise lead to overestimated luminosities, and possibly influence the resulting LAH shapes as well. Finally, it is certainly possible that the differences may be partially driven by our assumptions. Our estimated fraction of undetected LAEs might be lower than the actual one, either because of a steeper luminosity function or because of a lower faint-end cutoff.

#### 4.4.6 How to measure the faint LAE SB contribution

While it seems safe to state that a significant contribution of faint LAEs to the apparent Ly $\alpha$  SB profiles must be expected, at least in qualitative agreement between our empirical framework and the predictions by cosmological simulations, it would be very desirable to further constrain their contribution directly from observations. Here, we embark on a few (partly speculative) considerations of how that might be achieved in the future.

One avenue of investigation could be a comparison between the behaviour of individual and stacked Ly $\alpha$  SB maps at large scales. In principle, this should contain essential information about the faint LAE SB contribution: Stacking at random angles invariably contains some degree of azimuthal averaging which smears out the contributions of individual neighboring LAEs, while individual LAEs have neighbors only in certain directions. Using the deepest existing data, it might be possible to estimate the incidence of clear asymmetries or other external dis-

turbances in individual Ly $\alpha$  halos and use this to constrain the frequency of marginally detectable close neighbours.

Another approach could be to compare the outcomes of different stacking methods, since these differ in terms of the sensitivity to asymmetries in the outskirts: a profile derived from a median-stack of Ly $\alpha$  images should show a different contribution from faint external LAEs than a profile obtained as the mean of several azimuthally averaged individual profiles.

What is also relevant is the bandwidth chosen to extract the LAE pseudo-NB images from the original IFU data, as this influences the contrast between the "background" contribution of unrelated and (with respect to the central galaxy) unclustered LAEs as well as the enhancement due to physical neighbor LAEs at similar redshifts. Varying this bandwidth will provide insights about the relative balance between these two.

Observations seem to show that on average, LAH profiles are remarkably self-similar over a wide range of Ly $\alpha$  luminosities. However, if at some radius the contribution from external LAEs prevails, then the self-similarity should break down around that radius, and profiles obtained at different luminosity levels should converge towards the same behaviour.

At fixed limiting sensitivity, the contribution of faint LAEs to the combined LAH profiles should also decrease rapidly with redshift, simply because of  $(1+z)^4$  dimming together with a (roughly) unevolving luminosity function. While Leclercq et al. (2017) did not find any significant Ly $\alpha$  halo size evolution with redshift, their sizes clearly refer to the "inner" LAHs and leave the outer regions still unconstrained. A slightly stronger boundary condition is the similarity of stacked Ly $\alpha$  profiles at  $z \approx 3.5, 4.5,$  and  $5.5$  in Wisotzki et al. (2018), which could suggest that at least at high redshifts there is indeed a genuinely diffuse component also in outer regions of LAHs. On the other hand, the same phenomenon could arise from a steepening Ly $\alpha$  LF, and/or an increasing clustering strength of LAEs towards higher redshifts, which would then counteract the cosmological dimming.

We can evaluate whether this scenario is actually realistic. We note that while in Ouchi et al. (2017), HA21, and HA23 no significant clustering dependence on redshift was found, Durkalec et al. (2014) and Khostovan et al. (2019) found

a clear increase of clustering strength with cosmic time. To calculate the increase of clustering strength needed to counteract the SB dimming (i.e.,  $(1+z)^{-4}$ ) in redshift bins of  $\Delta z = 1$ , we would need a factor  $\approx 1.25$  increase in the large-scale bias factor, from  $b \approx 2.65$  for  $3 < z < 4$  to  $b \approx 3.30$  for  $4 < z < 5$  and  $b \approx 4.15$  for  $5 < z < 6$ . These values are in broad agreement with the clustering growth found in Durkalec et al. (2014) and Khostovan et al. (2019).

Ultimately, building on these suggested analyses and experiments will require more and better data than currently available. Large LAE samples such as that from the Hobby-Eberly Telescope Dark Energy Experiment (HETDEX; Gebhardt et al. 2021) or future LAE integral field spectrographs such as BlueMUSE (Richard et al., 2019) may deliver the data quantity and quality to discern between genuinely diffuse Ly $\alpha$  emission in the circum- and intergalactic medium, on the one hand, and "fake diffuse" contributions from faint undetected LAEs, on the other hand.

## 4.5 Conclusions

In this paper, we turn the observed clustering properties of a sample of 1265 Ly $\alpha$  emitting galaxies (LAEs) at  $3 < z < 5$  from the MUSE-Wide survey into implications for the spatially extended Ly $\alpha$  emission in the circumgalactic medium (CGM) of LAEs. All sources have spectroscopic redshifts and their median Ly $\alpha$  luminosity is  $\log(L_{\text{Ly}\alpha}/[\text{erg s}^{-1}]) \approx 42.27$ .

We used halo occupation distribution (HOD) modelling to represent the clustering of our LAE set. Because the extended Ly $\alpha$  emission around LAEs is commonly measured using (pseudo-)narrow-band (NB) filters centered on the Ly $\alpha$  wavelength, we included redshift-space distortions both at large (Kaiser infall) and small (Finger of God effect) scales.

We then extrapolated the HOD statistics inwards towards smaller radii and combined them with assumptions about the Ly $\alpha$  emitter luminosity function (LF). We only considered the emission from undetected LAEs, which are less luminous than the ones in our current dataset. Together, these two ingredients are transformed into a (upper-limit) Ly $\alpha$  surface brightness (SB) profile, which belongs to individually undetected close neighbors that cluster like those in the MUSE-Wide sample. We derived a maximum SB

values of  $SB \approx 2.5 \cdot 10^{-20} \text{ erg s}^{-1} \text{ cm}^{-2} \text{ arcsec}^{-2}$ , assuming a luminosity of the undetected LAEs of  $\log(L_{\text{Ly}\alpha}/[\text{erg s}^{-1}]) = 38.5$ .

We considered various alternative clustering scenarios for the undetected sources. We first assumed that these follow the same clustering properties as the LAEs in the MUSE-Extremely Deep Field (MXDF; one order of magnitude fainter than those in MUSE-Wide but still more luminous than undetected LAEs) and compute the corresponding (upper limit) radial profile ( $SB \approx 2 \cdot 10^{-20} \text{ cgs}$ ). We then extrapolated the clustering properties of MUSE-Wide and MXDF LAEs down to  $\log(L_{\text{Ly}\alpha}/[\text{erg s}^{-1}]) \approx 37.0, 38.5, 40.0$  and used the resulting HOD models to estimate the actual Ly $\alpha$  SB profiles from undetected LAEs. We obtained a maximum SB of  $SB \approx 4 \cdot 10^{-21} \text{ cgs}$ .

We compared our  $\log(L_{\text{Ly}\alpha}/[\text{erg s}^{-1}]) = 38.5$  undetected Ly $\alpha$  SB profile to the LAE stacking experiment performed in Wisotzki et al. (2018) to address the question of whether undetected LAEs play a pivotal role in the formation of the extended Ly $\alpha$  halos. Assuming a simple Schechter LF with a reasonable intermediate faint-end slope ( $-1.94 \leq \alpha_{\text{LF}} \leq -1.84$ ) and a lower limit for Ly $\alpha$  luminosities of the undetected LAEs ( $\log(L_{\text{Ly}\alpha}/[\text{erg s}^{-1}]) \approx 38.5$ ), we find that the stellar irradiation from those undetected LAEs can dominate the excess surface brightness at large scales ( $R \gtrsim 50 \text{ pkpc}$ ). On the other hand, the Ly $\alpha$  SB profile at small scales ( $R \lesssim 20 \text{ pkpc}$ ) cannot be explained by undetected sources and may be better explained by a genuinely diffuse origin. More luminous LAEs ( $\log(L_{\text{Ly}\alpha}/[\text{erg s}^{-1}]) \approx 40$ ) reproduce at best 4%, 40%, and 100% of the extended emission at  $R = 15, 40, 65 \text{ pkpc}$ , respectively.

We also compared our estimated Ly $\alpha$  SB profiles with simulation studies. Although we agree that faint LAEs dominate the SB of the Ly $\alpha$  halos at large scales, the shape of the radial profiles and the contribution to the total Ly $\alpha$  SB profiles differ. While the simulated faint LAE SB profiles generally decrease rapidly with distance, our derived radial profiles have shallow slopes, likely leading to the flattening at  $R \gtrsim 30 \text{ pkpc}$  seen in observed Ly $\alpha$  SB profiles. Overall, most simulated profiles, together with our estimations, infer a faint LAE contribution of the same order of magnitude.

Although these faint LAEs are likely the most significant source of luminosity for the outer

parts of observed Ly $\alpha$  halos, beyond the scales probed by most observations of single objects ( $R > 50 \text{ pkpc}$ ), the actual point at which this contribution starts to become important depends crucially on the shape of the Ly $\alpha$  luminosity function, in particular, its faint end. We also suggest a few experiments to directly constrain the faint LAE SB contribution from observations.

## Appendix

### 4.A Clustering comparison from LAE subsets of the MUSE-Wide survey

In this work, we utilized the clustering constraints derived in HA23 for a subset of 1030 MUSE-Wide LAEs at  $3 < z < 6$  to estimate the contribution of undetected LAEs to the apparent Ly $\alpha$  halos observed at  $3 < z < 5$ . To be consistent with the Ly $\alpha$  halo measurements, we focused on a subsample of 1265 LAEs at  $3 < z < 5$  from the MUSE-Wide survey. In the following, we demonstrate that the LAEs in these two datasets have nearly identical clustering strengths.

In Fig. 4.A.1, we represent in blue the K-estimator measurements obtained in HA23 for the  $3 < z < 6$  LAE subsample and in red the corresponding measurement for the  $3 < z < 5$  LAE subset of this work. The clustering strengths are in excellent agreement. The clustering uncertainties for the former sample are (on average) 2% larger than for the latter dataset. The best-fit HOD model and, thus, the large-scale bias factor and typical DMH masses are indistinguishable.

### 4.B Clustering enhancement factor derivation

The surface brightness (SB) at cosmological distances is defined as

$$SB = \int_Z \epsilon(Z) \frac{[D_A(z)(1+z)]^2}{4\pi D_L(z)^2} dZ \approx \frac{\epsilon \Delta Z}{4\pi(1+z)^2}, \quad (4.B.1)$$

where  $\epsilon(Z)$  is the comoving volume emissivity as a function of radial comoving separation,  $Z$ , and  $D_L, D_A = D_L/(1+z)^2$  are the luminosity and angular size distances at redshift,  $z$ , respectively.

The radial comoving separation  $Z$  corresponds to the (pseudo-)NB width employed to stack LAE images in the measurement of  $\text{Ly}\alpha$  SB profiles. This definition considers the shape and expansion history of the universe and assumes that objects are randomly distributed.

To account for the clustering of galaxies, we include the excess probability  $dP$  of finding a galaxy,  $i$ , in a volume element  $dV$  at a separation  $R = \sqrt{R_{ij}^2 + Z_{ij}^2}$  from another galaxy,  $j$ , that is, the two-point correlation function ( $\xi(R)$ ; Peebles, 1980)

$$dP = n \cdot [1 + \xi(R)] \cdot dV \propto [1 + \xi(R)] \cdot \frac{dZ}{dz} dz, \quad (4.B.2)$$

where  $n$  is the mean number density of the galaxy sample and  $R_{ij}$  is the transverse separation between the galaxy pair. The two-point correlation function of interest is, in fact, a cross-correlation function between detected and undetected LAEs. This is because  $\text{Ly}\alpha$  SB profiles represent SB as function of distance from the central LAE outwards, not as function of observed LAE–observed LAE separation. Hence, the SB that accounts for galaxy clustering is:

$$SB = \int_Z \frac{\epsilon(Z)}{4\pi(1+z)^2} \cdot [1 + \xi(R)] \cdot \frac{dZ}{dz} dz \approx \frac{\epsilon}{4\pi(1+z)^2} \int_Z [1 + \xi(R)] \cdot dZ. \quad (4.B.3)$$

We derive the clustering enhancement factor  $\zeta(R)$  from the comparison between Eqs. 4.B.1 and 4.B.3 as:

$$\zeta(R) = 1 + \int_Z \xi(R) \cdot \frac{dZ}{\Delta Z}. \quad (4.B.4)$$

## 4.C Effect of the velocity bandwidth on the faint LAE contribution to the extended LAHs

To compute the faint LAE SB profiles (colored lines in Fig. 4.4.3) and to modify the stacking analysis of Wisotzki et al. (2018) (data points in Fig. 4.4.3), we adopted a fixed velocity bandwidth

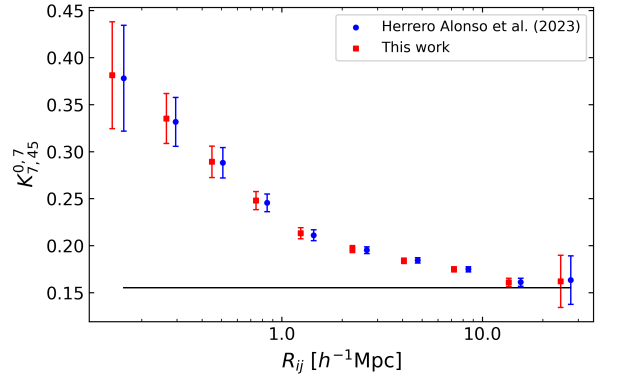


**Figure 4.A.1:** Clustering strength as measured by the K-estimator (Adelberger et al., 2005) for the LAE dataset considered in HA23 at  $3 < z < 6$  (blue) and that of the LAE sample at  $3 < z < 5$  used in this work (red). The black baseline represents the expected value for an unclustered sample. The error bars are Poissonian. The red measurements have been shifted along the x-axis for visual purposes.

of  $600 \text{ km s}^{-1}$ . The selected pseudo-NB width influences the  $\text{Ly}\alpha$  SB values of the stacked radial profile, the background  $\text{Ly}\alpha$  SB level due to discrete faint LAEs, and the clustering enhancement factor (Eq. 4.4). The general trend is that, for broader velocity widths, the stacked SB profile notably rises in the outer regions ( $R > 20 \text{ pkpc}$ ), the background SB slightly increases, and the clustering enhancement factor significantly declines (see Fig. 4.4.1). The interplay between these three factors is thus reflected in the SB ratio of Fig. 4.4.5.

In Fig. 4.C.1, we recompute the ratio between the faint LAE SB profile and the stacked one for a pseudo-NB width of  $400 \text{ km s}^{-1}$  (left panel) and  $800 \text{ km s}^{-1}$  (right panel). For broader bandwidths, the SB ratios decrease because the corresponding decline of the clustering enhancement factor exceeds the smaller rises in the stacked radial profile and the background SB level. While a broadening of the pseudo-NB width from  $400 \text{ km s}^{-1}$  to  $600 \text{ km s}^{-1}$  causes a maximum 40% drop of the SB ratios, an increase from  $600 \text{ km s}^{-1}$  to  $800 \text{ km s}^{-1}$  further decreases the SB ratios in at most 20%. We note that for a velocity offset of  $600 \text{ km s}^{-1}$  or  $800 \text{ km s}^{-1}$ , the stacked  $\text{Ly}\alpha$  SB value at  $R = 90 \text{ pkpc}$  is an upper limit (see e.g., Fig. 4.4.3). For  $400 \text{ km s}^{-1}$ , on the other hand, there is no detection.

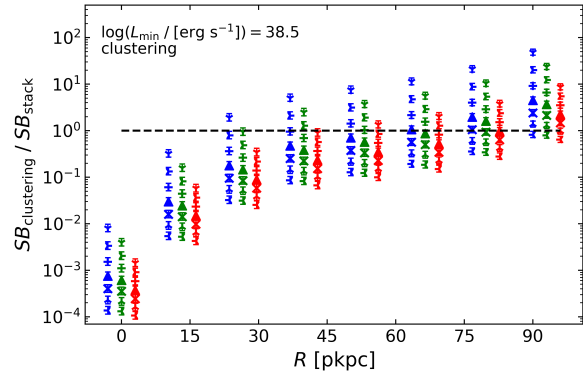
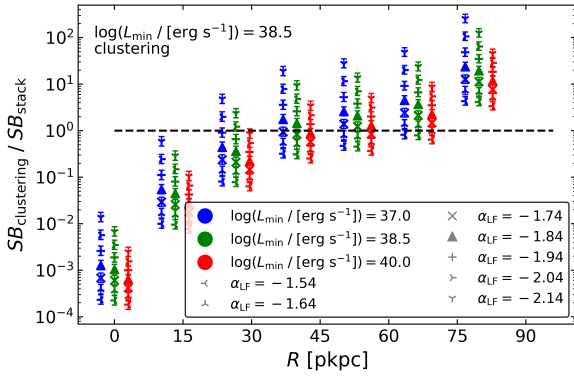


**Figure 4.C.1:** SB ratio of the Ly $\alpha$  SB profile from undetected LAEs and the modified stacked profile from Wisotzki et al. (2018). Left: Same as Fig. 4.4.5 but for a pseudo-NB width of 400 km s $^{-1}$ . Right: Same for a pseudo-NB width of 800 km s $^{-1}$ .

## References

- Adelberger, K. L., Steidel, C. C., Pettini, M., et al., (2005), *ApJ*, 558, A33
- Bacon, R., Accardo, M., Adjali, L., et al., (2010), *Proc. SPIE*, 7735, 773508
- Bacon, R., Brinchmann, J., Conseil, S., et al., (2022), *A&A*, 670, A4
- Bacon, R., Brinchmann, J., Richard, J., et al., (2015), *A&A*, 575, A75
- Bacon, R., Conseil, D., Mary, D., et al., (2017), *A&A*, 608, A1
- Bacon, R., Mary, D., Garel, T., et al., (2021), *A&A*, 647, A107
- Bahcall, J. N., & Spitzer, J. L., (1969), *ApJL*, 156, L63
- Bryan, G. L., & Norman, M. L., (2000), *IMA*, 117, 165
- Byrohl, C., Nelson, D., Behrens, C., et al., (2021), *MNRAS*, 506, 5129
- Claeyssens, A., Richard, J., Blaizot, J., et al., (2022), *A&A*, 666, 22
- de la Vieuville, G., Bina, D., Pello, R., et al., (2019), *A&A*, 628, A3
- Dijkstra, M., & Kramer, R., (2012), *MNRAS*, 424, 1672
- Drake, A. B., Garel, T., Wisotzki, L., et al., (2017), *A&A*, 608, A6
- Durkalec, A., Le Fèvre, O., Pollo, A., et al., (2014), *A&A*, 583, A128
- Finkelstein, S. L., Cohen, S. H., Windhorst, R. A., et al., (2011), *ApJ*, 735, 5
- Garel, T., Blaizot, J., Guiderdoni, B., et al., (2015), *MNRAS*, 450, 1279
- Gebhardt, K., Cooper, E. M., Ciardullo, R., et al., (2021), *ApJ*, 923, 217
- Geha, M., Wechsler, R. H., Mao, Y., et al., (2017), *ApJ*, 847, 4
- Gronke, M., & Bird, S., (2017), *ApJ*, 835, 2017
- Hashimoto, T., Verhamme, A., Ouchi, M., et al., (2015), *ApJ*, 812, 157
- Hayashino, T., Matsuda, Y., Tamura, H., et al., (2004), *AJ*, 128, 2073
- Herenz, E. C., Urrutia, T., Wisotzki, L., et al., (2017), *A&A*, 606, A12
- Herenz, E. C., Wisotzki, L., Saust, R., et al., (2019), *A&A*, 621, A107
- Herrero Alonso, Y., Krumpel, M., Wisotzki, L., et al., (2021), *A&A*, 653, A136
- Herrero Alonso, Y., Miyaji, T., Wisotzki, L., et al., (2023a), *A&A*, 671, A5
- Hinshaw, G., Larson, D., Komatsu, E., et al., (2013), *AJSS*, 208, 19
- Joung, M. R., Cen, R., & Bryan, G. L., (2009), *ApJL*, 692, L1
- Kaiser, N., (1987), *MNRAS*, 227, 1
- Kakiichi, K., & Dijkstra, M., (2018), *MNRAS*, 4, 5140
- Khostovan, A. A., Sobral, D., Mobasher, B., et al., (2019), *MNRAS*, 489, 555
- Konno, A., Ouchi, M., Shibuya, T., et al., (2018), *PASJ*, 70, S16
- Kusakabe, H., Verhamme, A., Blaizot, J., et al., (2022), *A&A*, 660, A44
- Lake, E., Zheng, Z., Cen, R., et al., (2015), *ApJ*, 806, 46
- Leclercq, F., Bacon, R., Wisotzki, L., et al., (2017), *A&A*, 608, A8
- Mas-Ribas, L., & Dijkstra, M., (2016), *ApJ*, 822, 84
- Mas-Ribas, L., Dijkstra, M., Hennawi, J. F., et al., (2017), *ApJ*, 841, 19
- Matsuda, Y., Yamada, T., Hayashino, T., et al., (2012), *MNRAS*, 425, 878

- Mitchell, P., Blaizot, J., Cadiou, C., et al., (2021), MNRAS, 501, 5757
- Momose, R., Ouchi, M., Nakajima, K., et al., (2014), MNRAS, 442, 110
- Muzahid, S., Schaye, J., Marino, R. A., et al., (2020), MNRAS, 496, 1013
- Nelson, D., Pillepich, A., Springel, V., et al., (2019b), MNRAS, 490, 3234
- Niemeyer, M. L., Komatsu, E., Byrohl, C., et al., (2022), ApJ, 929, 90
- Nilsson, K. K., Tapken, C., Moeller, P., et al., (2009), A&A, 498, 13
- Okamoto, T., Frenk, C. S., Jenkins, A., et al., (2010), MNRAS, 406, 208
- Ouchi, M., Harikane, Y., Shibuya, T., et al., (2017), PASJ, 70, S13
- Ouchi, M., Shimasaku, K., Akiyama, M., et al., (2008), ApJS, 176, 301
- Partridge, R. B., & Peebles, P. J. E., (1967), ApJ, 147, 868
- Peebles, P. J. E., (1980), Princeton, N.J., Princeton Univ. Press
- Pillepich, A., Nelson, D., Springel, V., et al., (2019), MNRAS, 490, 3196
- Pillepich, A., Springel, V., Nelson, D., et al., (2018b), MNRAS, 475, 648
- Richard, J., Bacon, R., Blaizot, J., et al., (2019), arxiv:1906.01657
- Rosdahl, J., Blaizot, J., Aubert, D., et al., (2013), MNRAS, 436, 2188
- Rosdahl, J., & Teyssier, R., (2015), MNRAS, 449, 4380
- Schechter, P., (1976), ApJ, 203, 297
- Schmidt, B. K., Kerutt, J., Wisotzki, L., et al., (2021), A&A, 645, A80
- Shimizu, I., & Umemura, M., (2010), MNRAS, 406, 913
- Shuntov, M., McCracken, H. J., Gavazzi, R., et al., (2022), A&A, 664, A61
- Simha, V., Weinber, D. H., Davé, R., et al., (2012), MNRAS, 423, 3458
- Sobral, D., Santos, S., Matthee, J., et al., (2018), MNRAS, 476, 4725
- Steidel, C. C., Bogosavljevic, M., Shapley, A. E., et al., (2011), ApJ, 736, 160
- Tinker, J. L., (2007), MNRAS, 374, 477
- Urrutia, T., Wisotzki, L., Kerutt, J., et al., (2019), A&A, 624, 24
- van den Bosch, F. C., More, S., Cacciato, M., et al., (2013), MNRAS, 430, 725
- Verhamme, A., Garel, T., Ventou, E., et al., (2018), MNRAS, 478, 60
- Wisotzki, L., Bacon, R., Blaizot, J., et al., (2016), A&A, 587, A98
- Wisotzki, L., Bacon, R., Brinchmann, J., et al., (2018), Nature, 562, 229
- Xue, R., Lee, K. S., Dey, A., et al., (2017), ApJ, 837, 172
- Zhang, H., Cai, Z., Liang, Y., et al., (2023), arxiv:2301.07358
- Zheng, Z., Cen, R., & Trac, H., (2011a), ApJ, 726, 38
- Zheng, Z., Coil, A., & Zehavi, I., (2007), ApJ, 667, 760
- Zheng, Z., & Miralda-Escude, J., (2002), ApJ, 578, 33





## Properties of MUSE Lyman- $\alpha$ halos at $2.9 < z < 6.7$ in different environments\*

Y. Herrero Alonso<sup>1</sup> and L. Wisotzki<sup>1</sup>

<sup>1</sup> Leibniz-Institut für Astrophysik Potsdam (AIP), An der Sternwarte 16, 14482 Potsdam, Germany

### ABSTRACT

We investigate how the properties of extended Lyman- $\alpha$  (Ly $\alpha$ ) halos (LAHs), ubiquitously observed around high-redshift Ly $\alpha$  emitters (LAEs), correlate with environment. We use two samples of 726 and 181 LAEs at  $2.9 < z < 6.7$  from the Multi-Unit Spectroscopic Explorer (MUSE) deep fields (MUSE-Deep) and ultra-deep field (UDF-10), respectively. We connect the LAEs to their corresponding LAH properties, which were individually measured in Leclercq et al. (2017), and obtain 142 and 42 LAEs with identified LAHs from the two datasets, respectively. We separately bin our LAE samples in redshift slices of  $\Delta z = 0.1$  and apply the Voronoi-Delaunay tessellation (VDT) to characterize small-scale ( $\approx 0.4$  pMpc) overdense regions. To consider larger-scale ( $\approx 2$  pMpc) LAE overdensities,  $\delta_{\text{LAE}}$ , we detect peaks in the kernel density estimator (KDE)-filtered redshift distribution of the datasets. We obtain local overdensities for the LAEs with LAH information within  $-1 < \delta_{\text{LAE}} < 11$ . We next explore how the halo scale length,  $r_s$ , and the halo fraction of the total Ly $\alpha$  flux,  $X_{\text{Ly}\alpha\text{-h}}$ , vary with  $\delta_{\text{LAE}}$  and find no correlation. The two overdensity finders deliver consistent results. We also investigate whether the  $r_s$  and  $X_{\text{Ly}\alpha\text{-h}}$  distributions of LAEs that reside inside and outside overdense regions differ and find mathematically indistinguishable distributions, means and medians (demonstrated with Kolmogorov-Smirnov and Mood's median tests). We compare our results with previous investigations based on stacking analyses of narrowband data and find an overall agreement. We discuss the implications of our findings for the origin of LAHs.

### 5.1 Introduction

The circumgalactic medium (CGM) mediates the interaction between galaxies and the intergalactic medium (IGM), influencing, thus, galaxy evolution. While gas inflows from the large-scale structure (LSS) of the universe fuel star formation in galaxies, galactic outflows eject part of this gas and regulate their star formation rates. This fraction of gas can then flow into the IGM or be re-accreted onto the galaxy. Besides, interactions with neighbouring galaxies also impact the CGM and, consequently, galaxy evolution (see Tumlinson et al. 2017 and references therein).

From an observational perspective, the CGM has been studied following numerous ap-

proaches. Investigations of absorption lines of background quasars or galaxies, stacking analyses of spectra, and emission-line maps are some of the most common techniques (Tumlinson et al., 2017). The diffuse Ly $\alpha$  emission observed ubiquitously around high-redshift Lyman- $\alpha$  (Ly $\alpha$ ) emitters (LAEs) has opened a new avenue to study the CGM. Outflows facilitate the escape of Ly $\alpha$  photons (produced in ionized HII regions of the interstellar medium, ISM) from the ISM (Behrens & Braun, 2014; Yang et al., 2016), which can resonantly scatter with neutral hydrogen and form diffuse Ly $\alpha$  gaseous halos (LAHs) around LAEs. Processes such as "in situ" recombination (e.g., Maiolino et al., 2017), collisional excitation from the cooling radiation of infalling

\*A version of this Chapter will be submitted for publication in *Astronomy & Astrophysics*.

gas (e.g., Rosdahl & Blaizot, 2011), Ly $\alpha$  fluorescence (e.g., Mas-Ribas & Dijkstra, 2016), emission from faint LAEs (e.g., Herrero Alonso et al., 2023b) may also originate and/or power the extended LAHs.

Because the origin of LAHs is still under investigation, extracting information about the CGM remains a challenging task. LAHs around LAEs are, however, repeatedly detected, both by stacking of narrowband data (Steidel et al., 2011; Matsuda et al., 2012; Momose et al., 2014a; Xue et al., 2017; Niemeyer et al., 2022; Kikuta et al., 2023; Zhang et al., 2023) and on an individual object-by-object basis (Wisotzki et al., 2016; Leclercq et al., 2017; Claeysens et al., 2022; Kusakabe et al., 2022) with Multi-Unit Spectroscopic Explorer (MUSE; Bacon et al. 2010) data.

Numerous are also the studies that sought for correlations between LAH and galaxy properties. While the characteristic exponential scale length of the LAHs ( $r_s$ ; typically of few pkpc) does not seem to vary with redshift (Wisotzki et al., 2016; Leclercq et al., 2017; Wisotzki et al., 2018), it appears to correlate with UV absolute magnitude (Momose et al., 2014b; Leclercq et al., 2017; Xue et al., 2017; Claeysens et al., 2022; Zhang et al., 2023). Other studies also found a correlation with Ly $\alpha$  luminosity and/or Ly $\alpha$  equivalent width (Xue et al., 2017; Momose et al., 2014b; Zhang et al., 2023). In terms of environment, the results are still inconclusive. While Matsuda et al. (2012) found that  $r_s$  is proportional to the square of the LAE overdensity where the LAEs reside, Momose et al. (2014b), Xue et al. (2017), and Kikuta et al. (2023) found that  $r_s$  is independent of environment.

Some of the trends found in stacking experiments of narrowband data yielded different conclusions than those drawn from the LAH characterization of individual LAEs (see, for instance, the  $r_s$  trends with Ly $\alpha$  luminosity from Momose et al. 2014b; Xue et al. 2017 and that from Leclercq et al. 2017). Because investigations about the possible environment effect on LAHs have only been explored in stacks, in this paper we address this matter with the LAH properties measured (on an individual object-by-object basis) by Leclercq et al. (2017) in MUSE deep and ultra deep data.

The paper is structured as follows. In Sect. 5.2, we briefly describe the data used for this work. In Sect. 5.3, we outline the various techniques we apply to identify overdense regions of differ-

ent scales. We investigate how the LAH properties correlate with environment in Sect. 5.4. In Sect. 5.5, we compare our findings to recent observational studies and discuss the implication of our results in the context of LAH origin. We give our conclusions in Sect. 5.6.

Throughout the paper, physical and comoving distances are given in units of pkpc and ckpc, respectively. We use a  $\Lambda$ CDM cosmology and adopt  $\Omega_M = 0.3$ ,  $\Omega_\Lambda = 0.7$ , and  $\sigma_8 = 0.8$  (Hinshaw et al., 2013). All uncertainties represent  $1\sigma$  (68.3%) confidence intervals, unless otherwise stated.

## 5.2 Data

This paper uses two different spectroscopic samples of LAEs, from the deep fields of MUSE (hereafter MUSE-Deep) and the MUSE ultra-deep field (UDF-10), as well as their measured LAH properties from Leclercq et al. (2017). We also considered using the LAH measurements from Wisotzki et al. (2016) in the Hubble Deep Field South (HDFS) but the small sample size, together with the different sky location, did not allow for a robust environment characterization.

### 5.2.1 MUSE Deep fields

MUSE-Deep (also known as MOSAIC; Bacon et al., 2017; Inami et al., 2017; Bacon et al., 2022) encompasses nine fields located in the CANDELS/GOODS-S region of the Hubble ultra deep field (HUDF), each spanning 1 arcmin<sup>2</sup> and observed with a 10 h exposure time. Due to field-to-field overlaps, the total spatial coverage is 9.92 arcmin<sup>2</sup>. We represent the spatial distribution of the survey in green in Fig. 5.2.1. We refer to Bacon et al. (2022) for a detailed description on survey construction and data reduction.

The sources in MUSE-Deep were blindly detected and extracted using ORIGIN (Mary et al., 2020). The redshift measurements and line classifications were carried out with pyMarZ, a python version of the redshift fitting software MarZ (Hinton et al., 2016).

We detect a total of 726 LAEs in the redshift interval of  $2.9 < z < 6.7$ . The redshift distribution of the LAE sample is shown in green in the left panel of Fig. 5.2.2. The physical transverse span of the survey is  $\approx 2$  pMpc (at the median redshift of  $\langle z \rangle = 4.0$ ). The range of Ly $\alpha$  lumi-

nosities is  $40.77 < \log(L_{\text{Ly}\alpha}/[\text{erg s}^{-1}]) < 43.38$ , with a median of  $\log\langle L_{\text{Ly}\alpha}/[\text{erg s}^{-1}] \rangle = 41.74$  (see Table 5.2.1).

## 5.2.2 MUSE ultra deep field

The UDF-10 (Bacon et al., 2017) is situated in the CANDELS/GOODS-S region and overlaps with MUSE-Deep. UDF-10 is composed of a single field of  $1 \text{ arcmin}^2$  and was observed with a 30 h exposure time. In Fig.5.2.1, we overplot the spatial distribution of the UDF-10 (orange) on the previous dataset.

The survey assembly and data reduction is described in Bacon et al. (2017) and is equivalent to the one applied in MUSE-Deep. The source extraction in UDF-10 and the redshift measurements are conducted following the same procedure as was done for MUSE-Deep.

Contained within  $1 \text{ arcmin}^2$  and over the same redshift range as the previous catalogue, we detect 181 LAEs. The redshift distribution of the LAE sample is shown in orange in the right panel of Fig. 5.2.2. At the median redshift of  $\langle z \rangle = 3.9$ , the footprint covers  $\approx 0.5 \text{ pMpc}$  (transversely). The  $\text{Ly}\alpha$  luminosities span  $40.16 < \log(L_{\text{Ly}\alpha}/[\text{erg s}^{-1}]) < 43.16$ . The median  $\text{Ly}\alpha$  luminosity is  $\log\langle L_{\text{Ly}\alpha}/[\text{erg s}^{-1}] \rangle = 41.66$ . These properties are listed in Table 5.2.1.

## 5.2.3 $\text{Ly}\alpha$ halo sample

From the complete MUSE-Deep and UDF-10 samples of LAEs (see previous sections), Leclercq et al. (2017) excluded LAEs in pairs that were closer than 50 (transverse) pkpc. The authors also removed LAEs that were close to the survey edges and those contaminated by emission lines from background sources, skylines, etc. When LAEs were detected in both UDF-10 and MUSE-Deep fields, only those in the UDF-10 were considered. They created  $10'' \times 10''$   $\text{Ly}\alpha$  pseudo-NB images of the remaining LAEs and further imposed a signal-to-noise (S/N) threshold of 6. A total of 184 LAEs fulfilled these criteria: 142 from MUSE-Deep ( $\approx 20\%$  of the MUSE-Deep LAE sample) and 42 from the UDF-10 ( $\approx 30\%$  of the UDF-10 LAE sample). The  $\text{Ly}\alpha$  luminosities of these LAEs range within  $40.77 < \log(L_{\text{Ly}\alpha}/[\text{erg s}^{-1}]) < 43.38$ , with a median of  $\log\langle L_{\text{Ly}\alpha}/[\text{erg s}^{-1}] \rangle = 42.23$  (see Table 5.2.1). We refer to Leclercq et al. (2017) for further details on the LAH sample construction.

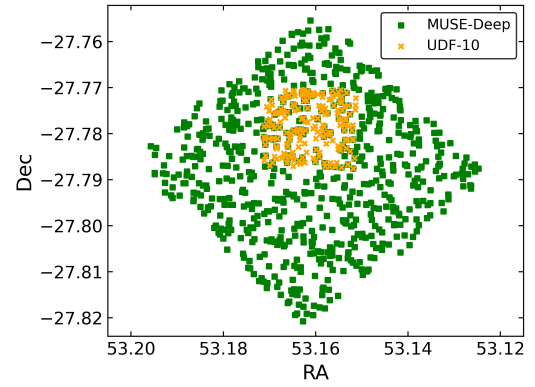


**Figure 5.2.1:** Spatial distribution of the LAEs from the MUSE-Deep (green squares) and UDF-10 (orange crosses) samples. The two surveys cover part of the CANDELS/GOODS-S region and span a redshift range of  $2.9 < z < 6.7$ .

To maximize the S/N of the pseudo-NB images, they chose spectral bandwidths within 2.5–20 (mean of 6.25). For each image, they computed a radial  $\text{Ly}\alpha$  SB profile by averaging the  $\text{Ly}\alpha$  flux in concentric annuli centered on the  $\text{Ly}\alpha$  emission. They then decomposed the profiles into a central (core emission) and an extended (emission from an extended halo) exponential component. They characterized the profiles as the sum of two circular, two-dimensional exponential distributions. The scale length of the former component was fixed to that obtained from a circular, 2D exponential fit to the UV continuum data from the Hubble Space Telescope (HST). The LAHs were thus characterized by three parameters: the LAH scale length ( $r_s$ ; halo component) and the fluxes of the  $\text{Ly}\alpha$  core,  $F_c$ , and halo,  $F_h$ . The fits included the point spread function (PSF) of MUSE.

Besides the LAH scale length delivered from the fits, we now compute the halo fraction of the total  $\text{Ly}\alpha$  flux  $X_{\text{Ly}\alpha\text{-h}}$  i.e.,  $X_{\text{Ly}\alpha\text{-h}} = \frac{F_h}{F_h + F_c}$ . The distributions of the LAH scale length and halo fraction are shown in the left and right panel of Fig. 5.2.3, respectively. The median values of the MUSE-Deep and UDF-10 LAH samples are displayed with dashed vertical lines and correspond to  $\langle r_s \rangle = 4.15, 3.21 \text{ pkpc}$  and  $\langle X_{\text{Ly}\alpha\text{-h}} \rangle = 0.66, 0.66$ , respectively (see Table 5.2.1). For the combined sample of LAHs, we obtain  $\langle r_s \rangle = 3.75 \text{ pkpc}$  and  $\langle X_{\text{Ly}\alpha\text{-h}} \rangle = 0.66$  (gray dashed lines).

**Table 5.2.1:** Properties of the LAE samples.

	Area/[arcmin <sup>2</sup> ]	LAEs	$\langle z \rangle$	$\log\langle L_{\text{Ly}\alpha}/[\text{erg s}^{-1}] \rangle$	LAHs	$\langle r_s/[\text{pkpc}] \rangle$	$\langle X_{\text{Ly}\alpha\text{-h}} \rangle$
MUSE-Deep	9.92	726	4.0	41.74	142	4.15	0.66
UDF-10	1.00	181	3.9	41.66	42	3.21	0.66

**Notes:** Properties marked with  $\langle \rangle$  represent median values for the galaxies in the samples. LAEs and LAHs refer to the number of LAEs and to the number of LAEs with available LAH information, respectively.

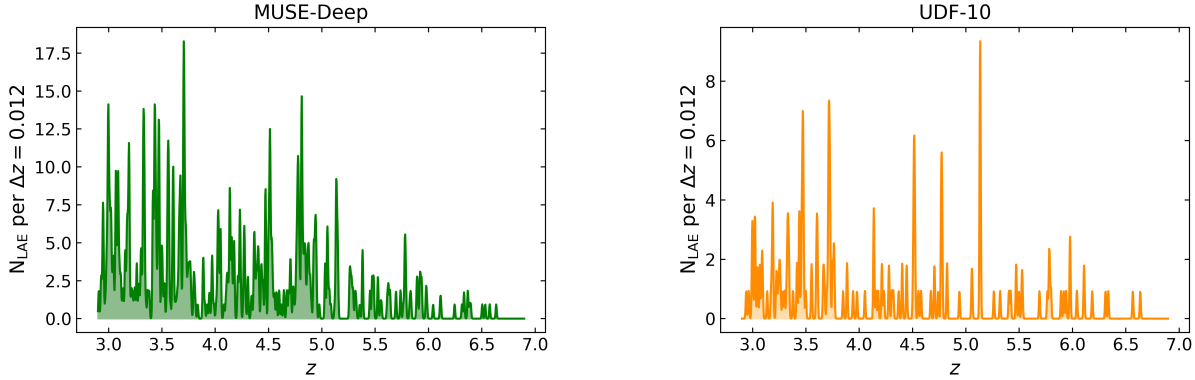


**Figure 5.2.2:** KDE-filtered redshift distributions of 726 and 181 LAEs from the MUSE-Deep (left) and UDF-10 (right) samples, respectively. The datasets span a redshift range of  $2.9 < z < 6.7$ . The chosen kernel is a Gaussian with a standard deviation of  $\sigma_z = 0.005$ , which corresponds to a full width at half maximum of  $\Delta z = 0.012$ .

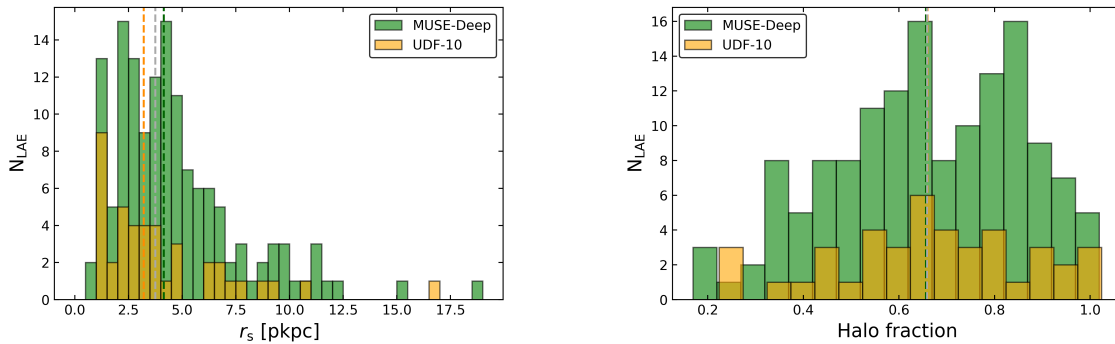


**Figure 5.2.3:** LAH property distributions of the MUSE-Deep (green) and UDF-10 (orange) samples of LAEs. Left: LAH scale length. Right: Halo fraction of the total Ly $\alpha$  flux. The colored dashed lines correspond to the median values of the distributions. The gray dashed line is the median of the total sample of LAHs.

## 5.3 Environment characterization

One common approach to identify overdense regions in galaxy samples is to smooth their sky distribution with a fixed or adaptive Gaussian kernel (e.g., Matsuda et al., 2012; Xue et al., 2017; Harikane et al., 2019). Other studies employ the Voronoi-Delaunay tessellation (e.g., Knobel et al., 2009; Shi et al., 2021; Jiménez-Andrade et al., 2023), a scale independent method that does not employ any binning scheme. Studies with small

sky coverages, on the other hand, bin the redshift distribution in comoving coordinates and identify overdensities by detecting peaks in the distribution (Bacon et al., 2021). Each of these methods targets different-scale overdensities. In this study, we use the Voronoi-Delaunay tessellation (VDT) to characterize small-scale (few virial radii;  $\approx 0.4$  pMpc) overdense regions and a kernel density estimator (KDE) for larger-scale (survey footprint size;  $\approx 2$  pMpc) overdensities.

### 5.3.1 Voronoi-Delaunay tessellation

A Voronoi tessellation is a partition of a two-dimensional set of points (RA, Dec) into convex regions or polygons (Voronoi cells). Each Voronoi cell contains one single point and a set of vertices, which are closer to that point than to any other in the plane. The tessellation is based on the Delaunay triangulation and has the mathematical property that the local surface density,  $\Sigma$ , is the inverse of the polygon area,  $A$ , i.e.,  $\Sigma = \frac{1}{A}$ . The galaxy overdensity,  $\delta$ , is defined as follows:

$$\delta = \frac{\Sigma - \langle \Sigma \rangle}{\langle \Sigma \rangle}, \quad (5.1)$$

where  $\langle \Sigma \rangle$  is the average surface density of the plane i.e.,  $\langle \Sigma \rangle = \langle \frac{1}{A} \rangle$ . Because we have a large redshift coverage, we bin the redshift range of our LAE samples in steps of  $\Delta z = 0.1$  and apply VDT to each resulting RA-Dec plane.  $\langle \Sigma \rangle$  is, in this case, the average surface density of all cells in all RA-Dec planes.

We define an overdense region as follows. We choose the galaxy with the highest local overdensity and place a circle of a given radius on it. The region delimited by the circle encloses the highest overdensity galaxy and those nearby. We consider this region as overdense if  $\delta > 3$  (similar to the  $\delta > 2.5$  considered in Matsuda et al. 2012; Kikuta et al. 2023). The radius that allows the enclosure of most high-overdensity galaxies is  $15R_{\text{vir}}$ , where  $R_{\text{vir}}$  is the virial radius. For our LAE samples,  $R_{\text{vir}} \approx 28$  pkpc (Herrero Alonso et al., 2021; Herrero Alonso et al., 2023a). Scales of  $\approx 0.4$  pMpc are consistent with typical protocluster sizes at  $z \approx 3$  (Chiang et al., 2013). We verify that selecting other overdensity thresholds ( $\delta > 3.5, 4.0, 4.5$ ) or smaller circle radii deliver results in agreement (although more uncertain) with those given in Sect. 5.4.

The RA-Dec plane of some redshift bins, however, present several overdense regions. We then place another circle of the same radius on the second overdense region (centered on its highest-overdensity galaxy). We visually inspect all RA-Dec planes and proceed alike for all visible overdensities in the field.

### 5.3.2 Kernel-density estimator

To consider larger-scale overdensities than those detected with the VDT, we replace the usual redshift histogram counts-per-bin by a quasi-

continuous kernel density estimator. We thus avoid binning artefacts and better represent the underlying redshift probability distribution. We compute the KDE-filtered redshift distribution of the two LAE samples and define overdense regions by selecting peaks in their distributions. To be consistent with the VDT method, we choose full widths of  $\Delta z = 0.1$  around the peak center. We consider as overdense region the entire RA-Dec plane of the redshift peak. This corresponds to scales of  $\approx 2$  pMpc (same as the survey footprint).

As kernel, we choose a Gaussian with a standard deviation of  $\sigma_z = 0.005$ . Redshift peaks higher than  $N_{\text{LAE}} = 3$  are considered to be overdense. As for the VDT, we also define overdensity with Eq. 5.1 but, in this case,  $\Sigma = \frac{N}{A}$ , where  $N$  is the number of LAEs within the selected redshift peak and  $A$  is the area of the survey footprint. We verified that different plausible values for  $\sigma_z$  or peak thresholds, deliver consistent results (within the uncertainties) with those presented in Sect. 5.4.

## 5.4 Ly $\alpha$ halo properties in different environments

### 5.4.1 Voronoi-Delaunay overdensities

We separately apply the VDT to the LAE samples from MUSE-Deep and UDF-10, as described in Sect. 5.3.1. To illustrate the method, we show the three highest local overdensities in Fig. 5.3.1, which were detected in the MUSE-Deep dataset. The LAEs are color-coded by their local overdensity, which is computed with Eq. 5.1.

We combine the local overdensity values from MUSE-Deep and UDF-10 and bin the overdensities within  $-1$ – $11$  in steps of  $0.75$ . For each bin, we only select the LAEs with available LAH measurements (the orange and green stars in Fig. 5.3.1 correspond to MUSE-Deep and UDF-10 LAEs whose LAH properties were measured in Leclercq et al. 2017, respectively). We obtain 53, 75, 33, 11, 6, 1, 4, 0, 0, 0, 0, 0, 0, 0, 0, 1 LAEs for these criteria. We represent their average LAH scale lengths and halo fractions in Fig. 5.3.2 (red).

There is no apparent correlation between LAH properties and the small-scale environment where the LAEs reside. While most scale lengths range between  $2$ – $8$  pkpc, the halo fractions vary

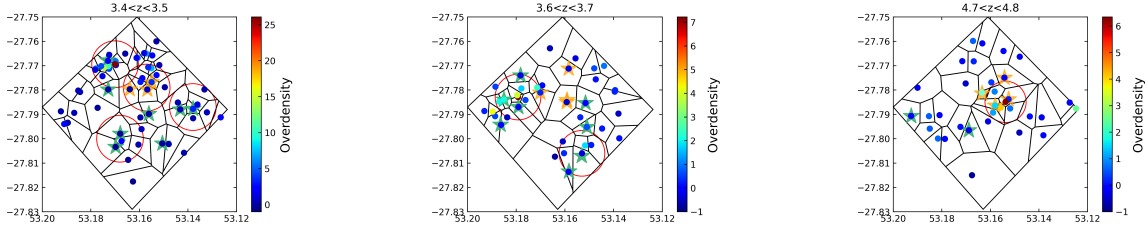


**Figure 5.3.1:** Voronoi-Delaunay tessellation of three redshift slices from the LAE sample from MUSE-Deep. The edges (outer black lines) correspond to the survey footprint. The LAEs (circles) are color-coded by their local overdensity. The green and orange stars denote LAEs with available LAH measurements in MUSE-Deep and UDF-10, respectively. The red circles indicate overdense regions.

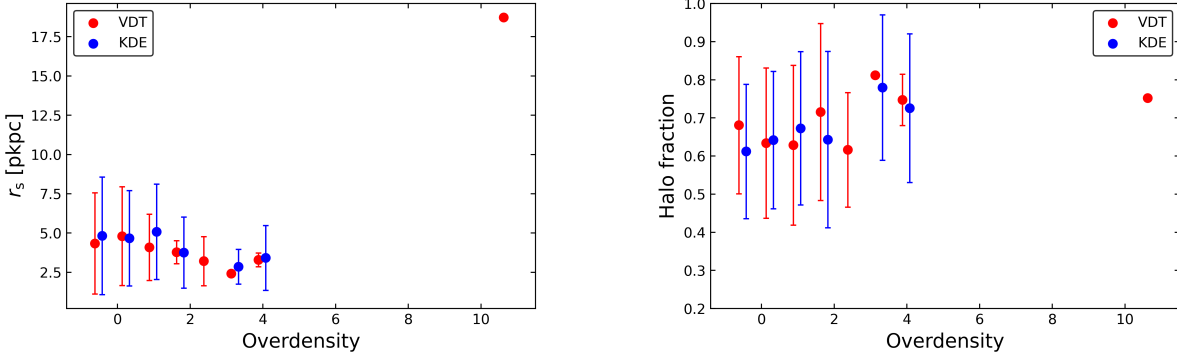


**Figure 5.3.2:** LAH scale length (left panel) and halo fraction of the total Ly $\alpha$  flux (right panel) as a function of LAE overdensity. Overdensity values were measured with the VDT (red) and the KDE (blue). The error bars correspond to the standard deviation of the LAH properties within the overdensity bins (see text).

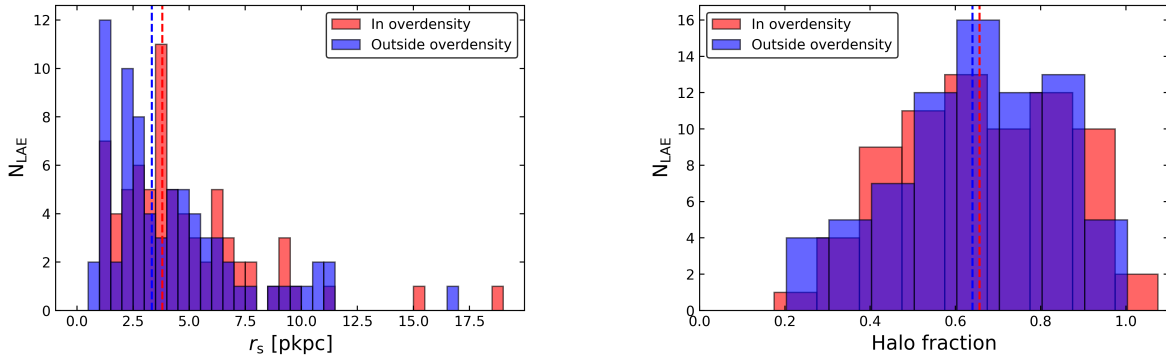


**Figure 5.3.3:** LAH property distributions of LAEs inside (red) and outside (blue) VDT-detected overdensities. Vertical dashed lines display the median of the distributions. Left: LAH scale length. Right: Halo fraction of the total Ly $\alpha$  flux.

**Table 5.3.1:** Properties of LAHs in different environments.

	$\langle r_s / [\text{pkpc}] \rangle_{\text{VDT}}$	$\langle r_s / [\text{pkpc}] \rangle_{\text{KDE}}$	$\langle X_{\text{Ly}\alpha-h} \rangle_{\text{VDT}}$	$\langle X_{\text{Ly}\alpha-h} \rangle_{\text{KDE}}$
In overdensity	3.8	3.8	0.66	0.66
Outside overdensity	3.3	4.2	0.64	0.64
$\chi^2$ (MM test)	0.53	1.89	0.20	0.02
$D$ (K-S test)	0.24	0.40	0.10	0.16

**Notes:** Properties marked with  $\langle \rangle$  represent median values. The subscripts VDT and KDE refer to the methods applied to measure the local overdensity of the LAEs with available LAH information.

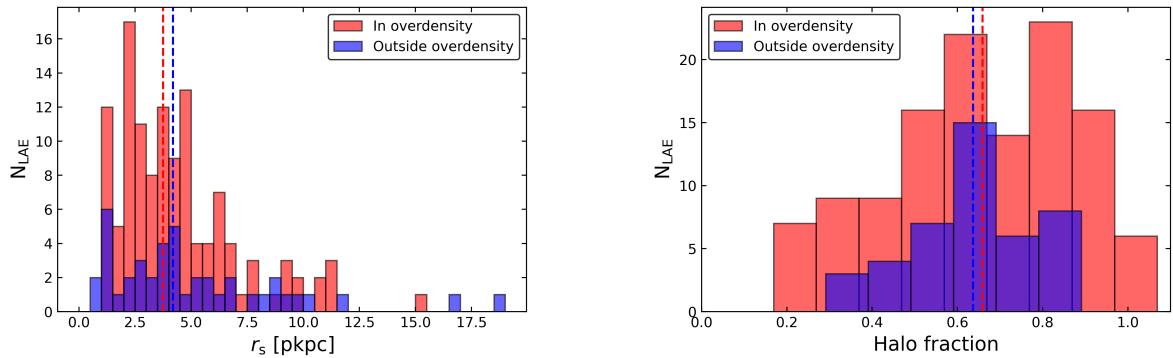


**Figure 5.3.4:** Same as Fig. 5.3.3, but for KDE-detected overdensities.

within 0.4–1.0. The data points without uncertainties correspond to the overdensity bins that host only one single LAE with LAH information and should, therefore, be seen with caution.

In Fig. 5.3.1, we also delimit the overdense regions with red circles (see Sect. 5.3). The largest overdensity (left panel of Fig. 5.3.1, at  $3.4 < z < 3.5$  and located in the northern end of the field) reaches local overdensity values of  $\approx 25$ . Although it contains 13 LAEs, only one has available LAH information. This LAE is located in a local overdensity of  $\approx 10.7$ . To confirm the robustness of the detected overdensities, we also applied other methods such as density maps (e.g., Chiang et al., 2014) and the  $k$ th nearest neighbors algorithm (Fix & Hodges, 1989) and, overall, found the same overdensities as with the VDT.

We now select the LAEs with LAH measurements that are located within the red circles (see Fig. 5.3.1) and compare their LAH property distributions to those from LAEs that reside outside overdensities. While 96 LAEs are inside overdense regions, 88 are outside overdensities. The left (right) panel of Fig. 5.3.3 shows the distribution of the LAH scale length (halo fraction) inside (red) and outside (blue) overdense regions. The vertical dashed lines display the median values of the histograms. LAEs that reside in overdensities present  $\langle r_s \rangle = 3.8$  pkpc (or mean of 4.7 pkpc) and  $\langle X_{\text{Ly}\alpha\text{-h}} \rangle = 0.66$  (same mean). For those located outside overdensities, we obtain  $\langle r_s \rangle = 3.3$  pkpc (mean of 4.3) and  $\langle X_{\text{Ly}\alpha\text{-h}} \rangle = 0.64$  (same mean; see Table 5.3.1).

The medians and LAH property distributions inside and outside overdensities are visually alike. To mathematically confirm the similarity of the medians and the histograms of Fig. 5.3.3, we perform the Mood’s median test (MM test)

and the two-sample Kolmogorov-Smirnov test (K-S test), respectively. While the MM test statistic  $\chi^2$  quantifies the likelihood that the two medians are statistically identical (null hypothesis of MM test), the K-S test statistic  $D$  (maximum vertical distance between the two cumulative normalized distributions) informs about the probability that the two samples are drawn from the same (unknown) probability distribution (null hypothesis of K-S test).  $\chi^2$  and  $D$  values larger than their corresponding confidence thresholds lead to the rejection of the null hypotheses. For a confidence level of 95%,  $\chi^2_{\text{threshold}} = 3.84$  and  $D_{\text{threshold}} = 0.22^*$ .

For the scale length and halo fraction distributions of Fig. 5.3.3, we obtain  $\chi^2 = 0.53, 0.20$  and  $D = 0.24, 0.10$ , respectively (see Table 5.3.1). Although the  $r_s$  distributions inside and outside overdense regions are statistically different ( $D_{r_s} > D_{\text{threshold}}$ ), those from  $X_{\text{Ly}\alpha\text{-h}}$ , as well as their medians (or means), are equivalent ( $D_{X_{\text{Ly}\alpha\text{-h}}} < D_{\text{threshold}}$  and  $\chi^2 < \chi^2_{\text{threshold}}$ ). We thus conclude that, when considering small-scale overdensities, there is no significant relation between the scale length and the halo fraction and the environment where the LAEs are embedded.

## 5.4.2 Kernel-density estimator overdensities

To consider larger-scale overdense regions than those detected with the VDT (see previous section), we apply the KDE method described in Sect. 5.3.2. We detect peaks in the redshift distributions of the MUSE-Deep and UDF-10 samples of LAEs (see Fig. 5.2.2) and compute their local overdensities with Eq. 5.1.

\* $D_{\text{threshold}}$  varies with the number of LAEs within the two distributions. See Eq. 15 in Sect. 3.3.1 of Knuth (1998).

We combine the overdensity values separately computed in MUSE-Deep and UDF-10 and bin the local overdensity within  $-1$ – $5$  in steps of  $0.75$ . Because we only consider LAEs with available LAH measurements, we detect 39, 41, 60, 37, 0, 3, 4, 0 LAEs within the bins. We note that the highest LAE overdensity detected by the VDT, it is now relaxed due to the larger area used to compute the surface density (Eq. 5.1) with the KDE. We represent the mean scale lengths and halo fractions of these overdensity subsamples in Fig. 5.3.2 (blue). The KDE trends are consistent with those derived from the VDT (red). The scale lengths and halo fractions mainly range between  $2$ – $8$  pkpc and  $0.4$ – $1.0$ , respectively. Hence, when considering Mpc-scale overdensities, we also do not find any correlation between LAH properties and environment.

The largest overdense region detected with the KDE is found at  $3.65 < z < 3.75$  (highest peak in the redshift distribution of the MUSE-Deep LAEs; see left panel of Fig. 5.2.2), coinciding with one of the most pronounced overdensities found with the VDT. It has an overdensity value of  $1.6$  and contains 64 LAEs, 17 of which have LAH information.

We also separate the LAEs that fall within the overdense redshift peaks (131 LAEs) from those located in lower density peaks (53 LAEs). We represent the distributions of the scale length (left panel) and halo fractions (right panel) of LAHs inside and outside overdense regions in Fig. 5.3.4. Their median values (dashed vertical lines) are  $\langle r_s \rangle = 3.8, 4.2$  pkpc (or mean values of  $4.4$  and  $5.2$  pkpc) and  $\langle X_{\text{Ly}\alpha\text{-h}} \rangle = 0.66, 0.64$  (same for the means), respectively (see Table 5.3.1). These values are very similar, if not identical, to those obtained with the VDT (previous section).

Although we now have better statistics than with the VDT because of the higher detection rate of LAEs within overdense regions, the shape of the  $r_s$  and  $X_{\text{Ly}\alpha\text{-h}}$  distributions inside and outside overdensities is still very similar to those obtained with the VDT. We also perform the MM and K-S tests on the histograms of Fig. 5.3.4 and list the results in Table 5.3.1. For a confidence level of 95%,  $\chi^2_{\text{threshold}} = 3.84$  and  $D_{\text{threshold}} = 0.25$ . We obtain  $\chi^2 = 1.89, 0.02$  and  $D = 0.40, 0.16$  for the scale length and halo fraction distributions, respectively. We thus conclude that, even when considering Mpc-scale overdensities, the  $r_s$  distributions inside and outside overdense regions are statistically dif-

ferent ( $D_{r_s} > D_{\text{threshold}}$ ) but those for  $X_{\text{Ly}\alpha\text{-h}}$  and the two medians (or means) are equivalent ( $D_{X_{\text{Ly}\alpha\text{-h}}} < D_{\text{threshold}}$  and  $\chi^2 < \chi^2_{\text{threshold}}$ ). Hence, we find no evidence for a dependence of LAH properties on environment, also when considering Mpc-scale overdensities.

## 5.5 Discussion

### 5.5.1 Comparison with the literature

Although there is no previous investigation of the possible dependence of the halo fraction of the total Ly $\alpha$  flux on environment, there are several the studies that addressed this matter for the LAH scale length. While Matsuda et al. (2012) found a clear increase of  $r_s$  with increasing LAE overdensity, Momose et al. (2014b), Xue et al. (2017), and Kikuta et al. (2023) found similar scale lengths for the LAEs that reside inside and outside overdense regions. Due to low sensitivity, these studies were based on stacking of narrowband data. This approach averages the LAH properties and cancels out any particular characteristic that individual LAHs may have. Hence, a statistical study of the LAH properties derived from individual LAEs located in different environments is preferred.

Previous studies that investigated the possible LAH scale length dependence on environment fitted the stacked Ly $\alpha$  SB profiles following different approaches. To characterize LAHs, Matsuda et al. (2012) and Momose et al. (2014b) fitted the profiles with a single-component exponential function, excluding their small scales ( $R < 3, 2''$ , respectively) to avoid PSF effects. It is worth mentioning that the exclusion of the central part of the radial profile may inflate the actual value of  $r_s$ . Xue et al. (2017) and Kikuta et al. (2023), on the other hand, opted for a two-component fit of the entire profile and included the PSF in their measurements. Moreover, Kikuta et al. (2023) did not assume that the scale lengths for the core and continuum-like components are equal. In opposition to previous studies, we remind that Leclercq et al. (2017) fitted individual LAHs with a two-component fit and accounted for the PSF of MUSE (see Sect.5.2.3).

Although all studies utilize the same definition of overdensity (Eq. 5.1), the way the surface density is computed differs. While Matsuda et



al. (2012) and Xue et al. (2017) smoothed the LAE sky distribution with a Gaussian kernel of  $\sigma = 1.5, 2'$  (or FWHM = 1.7, 10 pMpc), respectively, Momose et al. (2014b) and Kikuta et al. (2023) counted LAEs within circles of radius of  $10'$  and  $1.8'$  (or 5.0 and 0.8 pMpc), respectively, to calculate  $\Sigma$ . In contrast, we applied the VDT to consider small-scale overdensities (0.4 pMpc) and the KDE for Mpc-scale ones (2.0 pMpc; see Sect. 5.3).

To consider similar overdensity scales, in Fig. 5.5.1 we compare our KDE trend of scale length and LAE overdensity (same as in the left panel of Fig. 5.3.2) with the results from the literature. While our findings are in disagreement with those found in Matsuda et al. (2012) (and partially in Kikuta et al. 2023), they are consistent with the investigations of Momose et al. (2014b) and Xue et al. (2017).

The differences between our data points and those from the literature could be attributed to several factors (other than the distinct fits to the radial profiles and overdensity finders). Some of the LAEs in Matsuda et al. (2012) are located in fields which are known to host Ly $\alpha$  blobs (Yamada et al., 2012) and be extremely overdense. These characteristics likely affect scale length derivations (Xue et al., 2017). The LAH scale length derived for the highest overdensity bin in Kikuta et al. (2023) also disagrees with our  $r_s$  at similar overdensities. This data point, however, may be affected by the fact that the overdense region is, in reality, the protocluster HS1549 at  $z = 2.84$  (Trainor & Steidel, 2012). HS1549 is known to contain tens of active galactic nuclei, Ly $\alpha$  blobs and, furthermore, is located in a Mpc-scale diffuse Ly $\alpha$  emitting structure (Kikuta et al., 2019).

The agreement between our results and Momose et al. (2014b), Xue et al. (2017), and Kikuta et al. (2023) is, on the other hand, interesting given the distinct properties of the LAEs. Not only the LAH and overdensity characterizations differed, our LAEs are, in some cases, up to one order of magnitude less luminous than those from previous studies (see Sect. 5.2.3).

Despite the apparent lack of correlation between the LAH properties and LAE overdensity, we cannot definitively rule out the possibility of a LAH dependence on environment. Some of our Ly $\alpha$  SB profiles were not well constrained at large scales and our LAH sample is relatively small.

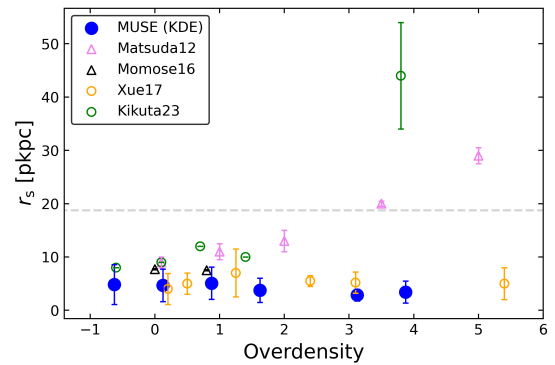


**Figure 5.5.1:** LAH scale length as a function of LAE overdensity. The blue circles represent our KDE measurements from the LAE samples of MUSE-Deep and UDF-10 (same as those of the left panel of Fig. 5.3.2). The dashed gray line shows the highest  $r_s$  value of our LAH sample. The pink, black, orange, and green symbols show the trends derived in Matsuda et al. (2012), Momose et al. (2014b), Xue et al. (2017), and Kikuta et al. (2023), respectively. Triangles and circles represent  $r_s$  values based on one- and two-component fits to the stacked Ly $\alpha$  SB profile, respectively.

Analyses on larger and deeper samples would not only allow a robust characterization of individual LAHs, but would also permit the examination of more diverse environments.

## 5.5.2 Implications

Galaxies are not isolated, but are surrounded by satellite galaxies. These can influence the central galaxy with their own emission, by losing their ISM through tidal stripping, ram pressure stripping, or galactic winds of their own. Processes such as cold accretion or inflows also interact with the central galaxy and can, thus, influence its evolutionary path. Therefore, an environment effect on LAHs would not be unreasonable. While the lack of correlation between the LAH scale length and halo fraction with the environment where LAEs reside (see Sect.5.4) does not yield information about satellites and inflows (distinct scales of interest), it supports a scenario in which the CGM scales probed by  $r_s$  and  $X_{\text{Ly}\alpha\text{-h}}$  are originated by internal processes.

Provided that our findings are not driven by a possible insufficient spatial coverage (unable to capture diverse environments), the inner regions of the CGM could be generated by outflows. Outflows facilitate the escape of scattered Ly $\alpha$  photons (Behrens & Braun, 2014; Yang et al., 20016), which is crucial for the emergence of LAHs. Moreover, theoretical and observational

studies (Yamada et al., 2012b; Song et al., 2020; Li et al., 2022; Blaizot et al., 2023) analysed the spectral shape of Ly $\alpha$  lines and found that most of them presented a redshifted and red-asymmetric profile. This fact suggests that the LAE star formation is dominated by burst-like events and gas outflows. The simulation results from Blaizot et al. (2023) further concluded that red-dominated lines preferentially arise during post-starburst outflows, which increase their luminosity and thus allows them to be detected with current instrumentation. Within this context, most our LAEs are in outflowing phases and environment does not necessarily play a role in forming LAHs.

## 5.6 Conclusions

In this paper, we investigate how the properties of Ly $\alpha$  halos (LAHs) correlate with environment. We use two samples of 726 and 181 LAEs at  $2.9 < z < 6.7$  from the MUSE deep fields (MUSE-Deep) and ultra-deep field (UDF-10), respectively. All sources have spectroscopic redshifts and the median Ly $\alpha$  luminosities of the datasets are  $\log(L_{\text{Ly}\alpha}/[\text{erg s}^{-1}]) \approx 41.74, 41.66$ . We match the LAEs to their individually-measured LAHs from Leclercq et al. (2017) and obtain 142 (from MUSE-Deep) and 42 (from UDF-10) LAEs with available LAH properties.

We use two methods to characterize distinct-scale environments. While we bin our LAE samples in  $\Delta z = 0.1$  redshift slices and apply the Voronoi-Delaunay tessellation (VDT) to consider small-scale ( $\approx 0.4$  pMpc) overdense regions, we detect peaks in the kernel density estimator (KDE)-filtered redshift distribution of the datasets to examine Mpc-scale ( $\approx 2$  pMpc) LAE overdensities. We compute the local surface density of our LAEs and explore how the halo scale length,  $r_s$ , and halo fraction of the total Ly $\alpha$  flux,  $X_{\text{Ly}\alpha\text{-h}}$ , vary with LAE overdensity.

We obtain overdensity values in the range -1–11 and find no clear LAH property dependence on environment. Neither the LAH scale length nor the halo fraction show any significant variation with the overdensity of the region where the LAEs reside. Both the VDT and the KDE yield consistent results.

We compare the  $r_s$  trend to those found in the literature. In contrast to the scale lengths of this study, those from previous studies were based on stacks of narrowband data. Despite this dif-

ference and the distinct LAE properties of this and other studies, our results are in agreement with the most recent literature.

We also investigate the possibility that the LAH property distributions of LAEs that are located inside and outside overdense regions differ. The  $r_s$  and  $X_{\text{Ly}\alpha\text{-h}}$  histograms of overdense and non-overdense regions are visually alike. We perform the Kolmogorov-Smirnov and Mood’s median tests to quantify the visual similarity of the distributions and medians, respectively, and find that they are mathematically indistinguishable. We discuss the implications of these results for the origin of LAHs.

## References

- Bacon, R., Accardo, M., Adjali, L., et al., (2010), *Proc. SPIE*, 7735, 773508
- Bacon, R., Brinchmann, J., Conseil, S., et al., (2022), *A&A*, 670, A4
- Bacon, R., Conseil, D., Mary, D., et al., (2017), *A&A*, 608, A1
- Bacon, R., Mary, D., Garel, T., et al., (2021), *A&A*, 647, A107
- Behrens, C., & Braun, H., (2014), *A&A*, 572, A74
- Blaizot, J., Garel, T., Verhamme, A., et al., (2023), *MNRAS*, 523, 3749
- Chiang, Y., Overzier, R., & Gebhardt, K., (2013), *ApJ*, 779, 127
- Chiang, Y., Overzier, R., & Gebhardt, K., (2014), *ApJL*, 782, L3
- Claeysens, A., Richard, J., Blaizot, J., et al., (2022), *A&A*, 666, 22
- Fix, E., & Hodges, J. L., (1989), *ISR*, 57, 238
- Harikane, Y., Ouchi, M., Ono, Y., et al., (2019), *ApJ*, 883, 142
- Herrero Alonso, Y., Krumpel, M., Wisotzki, L., et al., (2021), *A&A*, 653, A136
- Herrero Alonso, Y., Miyaji, T., Wisotzki, L., et al., (2023a), *A&A*, 671, A5
- Herrero Alonso, Y., Wisotzki, L., Miyaji, T., et al., (2023b), *A&A*, arxiv:2308.05105
- Hinshaw, G., Larson, D., Komatsu, E., et al., (2013), *AJSS*, 208, 19
- Hinton, S. R., Davis, T. M., Lidman, C., et al., (2016), *A&C*, 15, 61
- Inami, H., Bacon, R., Brinchmann, J., et al., (2017), *A&A*, 608, 26
- Jiménez-Andrade, E. F., Cantalupo, S., & Mag-nelli, B., (2023), *MNRAS*, 521, 2326

- Kikuta, S., Matsuda, Y., Cen, R., et al., (2019), PASJ, 71, 1
- Kikuta, S., Matsuda, Y., Inoue, S., et al., (2023), ApJ, arXiv:2302.12848
- Knobel, C., Lilly, S. J., Iovino, A., et al., (2009), ApJ, 697, 1842
- Knuth, D. E., (1998), The Art of Computer Programming, 2
- Kusakabe, H., Verhamme, A., Blaizot, J., et al., (2022), A&A, 660, A44
- Leclercq, F., Bacon, R., Wisotzki, L., et al., (2017), A&A, 608, A8
- Li, Z., Steidel, C. C., Gronke, M., et al., (2022), MNRAS, 513, 3414
- Maiolino, R., Russell, H. R., Cazzoli, S., et al., (2017), Nature, 544, 202
- Mary, D., Bacon, R., Conseil, S., et al., (2020), A&A, 635, A194
- Mas-Ribas, L., & Dijkstra, M., (2016), ApJ, 822, 84
- Matsuda, Y., Yamada, T., Hayashino, T., et al., (2012), MNRAS, 425, 878
- Momose, R., Ouchi, M., Nakajima, K., et al., (2014a), MNRAS, 442, 110
- Momose, R., Ouchi, M., Nakajima, K., et al., (2014b), MNRAS, 457, 2318
- Niemeyer, M. L., Komatsu, E., Byrohl, C., et al., (2022), ApJ, 929, 90
- Rosdahl, J., & Blaizot, J., (2011), MNRAS, 423, 344
- Shi, K., Toshikawa, J., Lee, K., et al., (2021), ApJ, 911, 46
- Song, H., Seon, K. I., & Hwang, H. S., (2020), ApJ, 901, 41
- Steidel, C. C., Bogosavljevic, M., Shapley, A. E., et al., (2011), ApJ, 736, 160
- Trainor, R. F., & Steidel, C. C., (2012), ApJ, 752, 39
- Tumlinson, J., Peebles, M. S., & Werk, J. K., (2017), ARAA, 55, 389
- Wisotzki, L., Bacon, R., Blaizot, J., et al., (2016), A&A, 587, A98
- Wisotzki, L., Bacon, R., Brinchmann, J., et al., (2018), Nature, 562, 229
- Xue, R., Lee, K. S., Dey, A., et al., (2017), ApJ, 837, 172
- Yamada, T., Matsuda, Y., Kousai, K., et al., (2012b), ApJ, 751, 29
- Yamada, T., Nakamura, Y., Matsuda, Y., et al., (2012), ApJ, 143, 79
- Yang, H., Malhotra, S., Gronke, M., et al., (20016), ApJ, 820, 130
- Zhang, H., Cai, Z., Liang, Y., et al., (2023), arxiv:2301.07358



# Conclusions and outlook

## 6.1 Summary

In this thesis, I studied various topics in the general framework of dark – baryonic matter relation, large-scale structure of the high-redshift universe traced by Lyman- $\alpha$  (Ly $\alpha$ ) emitters (LAEs), its properties and their extended Ly $\alpha$  gaseous halos (LAHs). These range from detailed clustering studies of LAEs detected with the Multi Unit Spectroscopic Explorer (MUSE) at redshifts of  $3 < z < 6$ , over investigations on the faint LAE clustering contribution to the LAHs, to a statistical study of the environment effect on the LAH properties.

In Chapter 2, I utilized a sample of 695 LAEs from the MUSE-Wide survey (1 h exposure time) to study the clustering properties of the dataset. As the clustering statistic, I applied an optimized version of the K-estimator from Adelberger et al. (2005) and supported our results with the traditional two-point correlation function, measuring, for the first time, the spatial clustering in a spectroscopic sample of Ly $\alpha$ -selected galaxies.

I then fitted the clustering signal with a power-law-based correlation function and obtained a correlation length of  $r_0 = 3.60_{-0.90}^{+3.10} h^{-1}$  Mpc and a correlation slope of  $\gamma = 1.30_{-0.45}^{+0.36}$ . That is, statistically, any MUSE-Wide-like galaxy has a neighbour at a distance within  $r_0$ . These correlation parameters translate into a large-scale bias factor of  $b = 3.03_{-0.52}^{+1.51}$ . Hence, LAEs cluster  $b$  times more strongly than the underlying dark matter. I also employed a more advanced fit approach i.e., scaling a halo occupation distribution model (HOD) to the large scales of the clustering signal. In line with the simple power-law fit, I obtained  $b = 2.80_{-0.38}^{+0.38}$  and a typical dark matter halo (DMH) mass of  $\log(M_h/[h^{-1}M_\odot]) = 11.34_{-0.27}^{+0.23}$ , which is in general agreement with the most recent literature.

I also compared our results with the clustering in 100 light cones from the GADGET dark-matter-only cosmological simulation coupled to the GALICS semi-analytical modelling of LAEs. Likely driven by the unrealistically spiky modelled redshift distribution, I found that the sim-

ulated clustering is far from successfully reproducing observations.

Assuming galaxy-conserving evolution models, I predicted that the DMHs of MUSE-Wide LAEs will typically evolve into halos of  $\log(M_h/[h^{-1}M_\odot]) \approx 13.5$  by  $z = 0$ . This suggests that the host DMHs of these LAEs are the DMH ancestors of present-day galaxy groups, which are  $\approx 15$  times more massive than the DMH of the Milky Way.

Although in Chapter 2 I excluded the possibility of a strong clustering dependence on Ly $\alpha$  equivalent width, UV absolute magnitude, and redshift, I found a tentative ( $2\sigma$ ) trend of a dependence on Ly $\alpha$  luminosity ( $L_{Ly\alpha}$ ). Later on, in Chapter 3, I found a strong clustering dependence on the latter. In Chapter 3, however, I included the deepest MUSE surveys namely, 1030 LAEs from the complete MUSE-Wide survey, 679 LAEs from MUSE-Deep (10 h exposure time), and 367 LAEs from the to-date deepest ever spectroscopic survey, the MUSE Extremely Deep Field (MXDF; 140 h). I thus connected the clustering properties of  $L^*$  LAEs with those of much fainter ones in the MXDF.

To fit the clustering signals from the new samples, I applied HOD modelling, including both the small and large scales. I modelled the LAE HOD as a function of DMH mass with three parameters: the threshold DMH mass to host a central LAE ( $M_{\min}$ ), to host (on average) one satellite LAE ( $M_1$ ), and the power-law slope of the number of satellites per DMH ( $\alpha$ ). Although with higher precision, I derived a similar typical DMH mass and bias factor for the high-luminosity sample (MUSE-Wide) to those inferred in Chapter 2 (based on large-scale only HOD modelling and on a subset of the current MUSE-Wide dataset). For the lower luminosity samples, I found lower DMH masses: while for the  $\log(L_{Ly\alpha}/\text{erg s}^{-1}) \approx 41.64$  dataset (intermediate luminosity; MUSE-Deep) I inferred  $\log(M_h/[h^{-1}M_\odot]) = 10.89_{-0.09}^{+0.09}$  ( $b = 2.42_{-0.09}^{+0.10}$ ), for the low-luminosity sample (MXDF;  $\log(L_{Ly\alpha}/[\text{erg s}^{-1}]) \approx 41.22$ ) I computed  $\log(M_h/[h^{-1}M_\odot]) = 10.77_{-0.15}^{+0.13}$  ( $b = 2.43_{-0.15}^{+0.15}$ ).

I then derived different threshold DMH masses for central and satellite LAEs for each sample. The minimum DMH masses needed to host a central LAE were  $\log(M_{\min}/[h^{-1}M_{\odot}]) = 10.3^{+0.2}_{-0.3}$ ,  $10.5^{+0.2}_{-0.1}$ ,  $10.7^{+0.2}_{-0.3}$  for low-, intermediate-, and high- luminosity LAEs, respectively. The corresponding threshold DMH mass and power-law slope for satellites varied from  $\log(M_1/[h^{-1}M_{\odot}]) = 11.7^{+0.3}_{-0.2}$  and  $\alpha = 1.5 \pm 0.5$  to  $\log(M_1/[h^{-1}M_{\odot}]) = 12.4^{+0.3}_{-0.2}$  and  $\alpha = 3.0^{+0.4}_{-0.5}$  and to  $\log(M_1/[h^{-1}M_{\odot}]) = 12.4^{+0.4}_{-0.6}$  and  $\alpha = 2.8^{+0.9}_{-0.7}$ , respectively. These values translated into a decreasing number of detected satellite LAEs with increasing luminosity i.e., satellite fractions of  $f_{\text{sat}} \lesssim 3, 10\%$  for high- and low-luminosity LAEs, respectively. Therefore, the most common scenario for LAEs is that in which DMHs mainly host a single detected LAE.

I then exploited the large dynamic range of  $L_{\text{Ly}\alpha}$  of the three surveys and split them at their median luminosities. Selecting the highest luminosity subset from the MUSE-Wide survey (median  $\log(L_{\text{Ly}\alpha}/\text{erg s}^{-1}) \approx 42.53$ ) and the lowest luminosity subsample from the MXDF (median  $\log(L_{\text{Ly}\alpha}/\text{erg s}^{-1}) \approx 40.97$ ) resulted in a clear clustering difference, where the highest luminosity subset clusters more strongly and resides in more massive halos ( $b_{\text{high}} = 3.13^{+0.08}_{-0.15}$  or  $\log(M_h/[h^{-1}M_{\odot}]) = 11.43^{+0.04}_{-0.10}$ ) than the lowest luminosity one ( $b_{\text{low}} = 1.79^{+0.08}_{-0.06}$  or  $\log(M_h/[h^{-1}M_{\odot}]) = 10.00^{+0.12}_{-0.09}$ ), at  $8\sigma$  significance.

I discussed the implications of these results in terms of reported measurements of evolving Ly $\alpha$  luminosity functions, detections of incomplete reionization at  $z \approx 6$ , and the relation between Ly $\alpha$  escape fraction and DMH mass. These results were also crucial for the much debated relevance of undetected LAEs (fainter than those in the MXDF) for the observed extended LAHs, which lead us to Chapter 4.

In Chapter 4, I turned the HOD-modelled clustering properties of a sample of 1265 LAEs at  $3 < z < 5$  from the MUSE-Wide survey into implications for the spatially extended Ly $\alpha$  emission in the circumgalactic medium (CGM) of LAEs. I also considered various alternative clustering scenarios for undetected LAEs and combined them with assumptions on the Ly $\alpha$  emitter luminosity function (LF), considering only the emission from undetected LAEs. I then integrated the Ly $\alpha$  LF to estimate the background surface brightness (SB) due to discrete faint LAEs and transformed these ingredients into Ly $\alpha$  SB

profiles (SB as a function of distance  $R$  from the center of the LAE) from clustered and individually undetected close neighbors. The resulting inferred faint radial profiles ranged between  $(0.4 - 2) \times 10^{20} \text{ erg s}^{-1} \text{ cm}^{-2} \text{ arcsec}^{-2}$ , with a very slow radial decline outwards, which likely leads to the flattening at  $R \gtrsim 30 \text{ pkpc}$  seen in observed total Ly $\alpha$  SB profiles.

I compared our faint LAE Ly $\alpha$  SB profiles to the total stacked radial profile computed in Wisotzki et al. (2018). I found that while the stellar irradiation from undetected LAEs can dominate the excess surface brightness at large scales ( $R \gtrsim 50 \text{ pkpc}$ ), the Ly $\alpha$  SB profile at  $R \lesssim 20 \text{ pkpc}$  cannot be described by undetected sources and may be better explained by a genuinely diffuse origin. I also compared our estimated Ly $\alpha$  SB profiles with simulation studies and found an overall agreement. I finally outlined possible future experiments to directly constrain the faint LAE SB contribution from observed data.

In Chapter 5, I investigated whether the properties of 184 observed LAHs from 726 MUSE-Deep and 181 ultra-deep field (UDF-10) LAEs at  $2.9 < z < 6.7$  were affected by environment. I used different definitions of overdensity to consider distinct-scale overdense regions. While I employed the Voronoi-Delaunay tessellation to characterize small-scale LAE overdensities ( $\approx 0.4 \text{ pMpc}$ ), I detected peaks in the kernel density estimator (KDE)-filtered redshift distribution of the samples to examine larger-scale ( $\approx 2 \text{ pMpc}$ ) overdensities. I found no correlation between the scale length of the LAHs,  $r_s$ , as well as the halo fraction of the total Ly $\alpha$  flux,  $X_{\text{Ly}\alpha\text{-h}}$ , with LAE overdensity. The two methods delivered consistent results.

I also selected LAEs located inside overdense regions and compared their  $r_s$  and  $X_{\text{Ly}\alpha\text{-h}}$  distributions with those from LAEs that reside outside overdensities. I found that the distributions and their medians are mathematically indistinguishable, which agrees with the last claims from the literature. I discussed the implications of these results for the origin of LAHs.

## 6.2 Future perspectives

### 6.2.1 The dark-baryonic matter relation

The main limitation of clustering studies with MUSE data is their small spatial coverage (at most tens of arcmin<sup>2</sup> on sky). Thus, our clustering measurements suffer from cosmic sample variance, specially those performed in MUSE-Deep and the MXDF (see Chapter 3). A large-scale spectroscopic 3D survey that covers large portions of the sky would significantly reduce cosmic sample variance and improve the statistics. This can already be pursued with HETDEX and Euclid, whose first data were released early this year (Cooper et al. 2023; Chavez Ortiz et al. 2023; see Sect. 6.2.3 for more details).

A spatial extension of MUSE surveys would also be beneficial. This would not only increase the S/N of clustering measurements (by detecting a higher amount of LAEs) and reduce cosmic variance (by covering larger areas of the sky), but it would also allow the simultaneous constraint of the five HOD parameters (see Chapter 3). In fact, if the sample were large enough, it would also be possible to include a sixth parameter in the modelling: the duty cycle of LAEs (fraction of DMHs hosting LAEs to those hosting any galaxy). This is due to (i) the on and off star formation of LAEs (e.g., driven by feedback), and (ii) the visibility of Ly $\alpha$  being somewhat line-of-sight dependent (at fixed star formation rate). Most studies point towards a duty cycle of few percent but the measurements are still uncertain (Kovac et al., 2007; Nagamine et al., 2010; Ouchi et al., 2017). The final LAE sample of HETDEX (and even the already available data) is also ideal to improve such experiments.

Somewhat related is the the underlying assumption of our HOD models: the center of the DMH with mass  $M_h > M_{\min}$  is always populated by one galaxy in the sample (or at least at a  $M_h$ -independent constant probability). This is very restrictive and should be relaxed in the future.

Clustering studies of LAEs would also benefit from the refinement of simulations coupled to radiative transfer models of Ly $\alpha$  emission. While most such simulations succeed at reproducing the Ly $\alpha$  and UV LFs of LAEs at  $3 < z < 6$ , they fail at replicating the LAE clustering properties. To achieve this goal, simulators have now access to the recipes provided in Chapter 3 (i.e., HODs,

large-scale bias factors, etc). The existence of simulations able to mimic LAE clustering would provide robust clustering uncertainties and realistic cosmic variance estimates (e.g., from hundreds of simulated light-cones).

### 6.2.2 The origin of Lyman- $\alpha$ halos

While clustering measurements primarily profit from wide sky coverages, the assessment of the faint LAE contribution to the extended LAHs benefits from long exposure times and deep spectroscopic data. Although from a purely astrophysical perspective deeper surveys than the MXDF with large sky coverages are desirable, the enormous observing time required makes this experiment unlikely to be carried out. Deeper LAE samples, however, would detect fainter LAEs, which would allow us to compute the clustering of those sources, instead of making assumptions on their clustering behaviour (as in Chapter 4). Furthermore, we could also observe these faint objects in MUSE pseudo-NB images, which would permit the constraint of their contribution to the LAHs directly from their incidence rate. Deeper data is also needed to constrain the faint-end slope of the Ly $\alpha$  LF, which plays an important role when estimating the faint LAE SB contribution (see Chapter 4). Because deeper observations would be extremely expensive, the lensed fields observed with MUSE are the current alternative. These fields reach luminosities as faint as  $L_{\text{Ly}\alpha} \approx 10^{39}$  erg s<sup>-1</sup> (more than one order of magnitude fainter than the MXDF). In the long term, lensed fields may also detect a fraction of the currently undetected faint LAEs. This is at present challenging given the significant lensing uncertainties e.g., magnification errors, in combination with several other factors.

Meanwhile, available non-lensed data should be further exploited. We should aim at measuring the incidence rate of faint neighbours around individual LAEs in the MXDF to disentangle their contribution from genuinely diffuse emission. There are several avenues to achieve this:

- Simultaneous inspection of spectra and pseudo-NB images of all LAEs in the MXDF. We should strive for detecting peaks and flux excesses in the spectrum and pseudo-NB image, respectively. This would be indicative of faint LAEs.
- Comparison of individual and stacked Ly $\alpha$

SB profiles. While stacked profiles seem to be significantly affected by faint LAEs at large scales (see Chapter 4), this contribution should vary in individual profiles. Diverse SB tails, asymmetries or other external disturbances would reveal the presence of close neighbours, because central LAEs alone should deliver self-consistent individual profiles. We could then use this to constrain the frequency of detectable faint LAEs.

- Comparison of distinct stacking approaches (see also Sect. 4.4.6 in Chapter 4). We can compare mean stacked profiles to median ones, center the stacking experiment on the Ly $\alpha$  peak and/or on the wavelength corresponding to the systemic redshift, select different bandwidths to extract the LAE pseudo-NB images from the IFU data, perform stacking analyses for various luminosity and redshift bins, etc. These experiments differ in the sensitivity to asymmetries in the outskirts of the LAH, which can be used to estimate the frequency of close neighbours.

While the first two avenues can be addressed with the available MXDF data (and with the deep data from the future integral field spectrograph BlueMUSE; see next section), the investigations that involve the split of the dataset into subsamples may require larger samples. Once again, HETDEX (and possibly BlueMUSE) fulfils the requirement (see Sect. 6.2.3).

To address this problem from a different angle, we can rely on intensity mapping. Intensity mapping studies compute the cross-correlation function between LAEs and the corresponding Ly $\alpha$  emission maps to constrain the integrated Ly $\alpha$  emission over large cosmological volumes (e.g., Kakuma et al., 2021; Kikuchihara et al., 2022). In that sense, stacked Ly $\alpha$  SB profiles and intensity mapping experiments are complementary. Despite the limited sky coverage of the MXDF (or MUSE-Deep), applying intensity mapping on these surveys could still map the extended emission out to few  $h^{-1}$ cMpc. These have the unique advantage, over common LAE samples, of identifying fainter LAEs and foreground contaminants. Besides, the comparison to intensity mapping results from non-resonant-line-selected star forming galaxies such as O[II] emitters would bring further light onto the physical processes

that power LAHs. While similar intensity mapping outcomes from LAEs and O[II] emitters at large scales would point towards satellite driven LAHs, distinct results would suggest that the large scales of the LAHs are powered by resonant mechanisms.

I also explored the possibility that LAHs are affected by environment (see Chapter 5), using the LAH properties measured in the MUSE-Deep and UDF-10 samples of LAEs. This study is, however, preliminary and further investigations are needed. I see the following directions:

- We should fit the LAH of all detected LAEs (independently of the S/N) in MUSE-Deep data and perform a similar analysis to that described in Chapter 5. Although this will deliver hundreds of new LAH properties and will improve the statistics of the investigation, the new LAH sample will still be relatively small. BlueMUSE will yield larger and fainter LAE samples than MUSE (see next section). As an alternative, we could also rely on the stacking of HETDEX LAEs in different environments.
- Different overdensity finders should be explored. While the finders we applied are robust at detecting overdense regions, algorithms such as the Friends-of-Friends are better suited to trace structure. Distinct definitions of overdensity may have an affect on the trends seen in Chapter 5.

The overdense regions of Chapter 5, together with the resulting ones from the proposals above, should also be used to confirm some of the predictions of Chapter 3. For instance, the relation I found between DMH mass and Ly $\alpha$  luminosity implied that the faint-end slope of the Ly $\alpha$  LF at  $3 < z < 6$  is shallower in overdense regions than in average or low density environments. This is also relevant for the faint LAE contribution to the extended LAHs of Chapter 4.

Ultimately, all the analyses and experiments I performed in this thesis and proposed in this section should also be applied to other (non-resonant) nebular lines at lower redshifts i.e., H $\alpha$ , O[II], O[III], etc. It may be that the observed diffuse emission in these emission-line-selected galaxies (see e.g., Zhang et al., 2016; Rajeshwari et al., 2023) is, in fact, produced by individually undetected sources or powered by the environment in which those galaxies are embedded.



## 6.2.3 Future instrumentation

Many of the experiments I proposed as possible future projects will greatly benefit from upcoming instrumentation or ongoing surveys. In the following, I outline the most relevant experiments.

HETDEX (Gebhardt et al., 2021) is an integral field spectroscopic experiment whose final survey is designed to cover a large area of the sky ( $> 540 \text{ deg}^2$ , contrary to the tens of  $\text{arcmin}^2$  of MUSE) and detect more than one million LAEs in the redshift range of  $1.8 < z < 3.5$  (opposed to the MUSE range of  $2.9 < z < 6.7$ ). The first HETDEX data were already released, which included more than 50000 LAEs over  $25 \text{ deg}^2$  on the sky (Cooper et al., 2023). Such characteristics are supreme to investigate the large-scale clustering of these sources. HETDEX will complement the results of this thesis at lower redshifts and at the high  $\text{Ly}\alpha$  luminosity end ( $42.7 < L_{\text{Ly}\alpha} / [\text{erg s}^{-1}] < 44.2$ ), delivering LAE clustering properties with minor cosmic sample variance uncertainties.

Investigations of the origin of LAHs will also be possible with HETDEX. Its complete sample of LAEs will be useful to investigate the faint LAE contribution to the LAHs (by performing stacks of LAE pseudo-NB images at various redshifts and  $\text{Ly}\alpha$  luminosities; see previous section) and the possible environment effect on LAHs (by characterizing stacks of LAEs in different environments). For these purposes, the future integral field spectrograph BlueMUSE (Richard et al., 2019), planned for the next decade, will be groundbreaking. BlueMUSE will complement the science cases of MUSE in the blue part of the spectrum ( $1.8 < z < 4$ ) and, because of the smaller dimming effects at lower redshifts, it will detect a significantly larger amount of faint LAEs. Therefore, BlueMUSE will be more sensitive to diffuse emission than MUSE, which may allow the differentiation between the truly diffuse component of LAHs and large-scale-structure artefacts.

The ongoing Texas Euclid Survey for Lyman Alpha (TESLA; first data publicly available in Chavez Ortiz et al. 2023) will assist in matters similar to HETDEX. The survey uses the IFU from HETDEX to observe  $10 \text{ deg}^2$  in the Euclid north ecliptic pole field. Once complete, TESLA will provide more than 50000 LAEs, allowing

large-scale clustering, and stacked LAH environment studies in a different region of the sky.

In the near future, a large amount of LAEs at  $2 < z < 7$  is also expected from the follow-up of the hyper supprime cam (HSC) fields with the prime focus spectrograph (PFS; Takada et al. 2014), to start on the Subaru telescope. The PFS will sample  $\sim 1400 \text{ deg}^2$  on the sky, which will permit similar investigations as those proposed for HETDEX.

The  $\text{Ly}\alpha$  detection is also among the science goals for spectroscopic instruments on the James Webb space telescope (JWST; Gardner et al. 2006). By probing Balmer lines, JWST will help disentangle the various mechanisms that produce LAHs. While  $\text{Ly}\alpha$  is powered by scattering, cooling radiation, fluorescence, star formation in the LAH, etc (see Sect. 1.3.2),  $\text{H}\alpha$  (accessible with JWST) is only affected by the latter two. The UV continuum, on the other hand, only becomes extended due to the star formation in the LAH e.g., undetected LAEs. The comparison between LAHs,  $\text{H}\alpha$  halos, and UV halos may clarify the relevant scales of the dominant powering mechanisms.

Spectroscopic instruments or survey telescopes planned for the next decade such as the multiplexed survey telescope (MUST), the Munaakea spectroscopic explorer (MSE) or the wide-field spectroscopic telescope (WST) may also deliver the data quantity and quality to further promote our knowledge on these matters.

## References

- Adelberger, K. L., Steidel, C. C., Pettini, M., et al., (2005), *ApJ*, 558, A33
- Chavez Ortiz, O. A., Finkelstein, S. L., Davis, D., et al., (2023), arXiv:2304.03258
- Cooper, E. M., Gebhardt, K., Davis, D., et al., (2023), arXiv:2301.01826
- Gardner, J. P., Mather, J. C., Clampin, M., et al., (2006), *SCR*, 123, 485
- Gebhardt, K., Cooper, E. M., Ciardullo, R., et al., (2021), *ApJ*, 923, 217
- Kakuma, R., Ouchi, M., Harikane, Y., et al., (2021), *ApJ*, 916, 22
- Kikuchihara, S., Harikane, Y., Ouchi, M., et al., (2022), *ApJ*, 931, 97
- Kovac, K., Somerville, R. S., Rhoads, J. E., et al., (2007), *ApJ*, 668, 15

- Nagamine, K., Ouchi, M., Springel, H., et al., (2010), PASJ, 62, 1455
- Ouchi, M., Harikane, Y., Shibuya, T., et al., (2017), PASJ, 70, S13
- Rajeshwari, D., Fossati, M., Fumagalli, M., et al., (2023), MNRAS, 522, 535
- Richard, J., Bacon, R., Blaizot, J., et al., (2019), arxiv:1906.01657
- Takada, M., Ellis, R. S., Chiba, M., et al., (2014), PASJ, 66, R1
- Wisotzki, L., Bacon, R., Brinchmann, J., et al., (2018), Nature, 562, 229
- Zhang, H., Zaritsky, D., Zhu, G., et al., (2016), ApJ, 833, 11

## Finding HST counterparts for MUSE data: QtCounterpart

### ABSTRACT

QtCounterpart is a graphical user interface (GUI) designed to find HST counterparts for sources detected in integral field data cubes. QtCounterpart was built in python for the HST counterpart assignment to emission line objects of MUSE data. Exploiting the full potential of the GUI, QtCounterpart displays a pseudo-narrowband image extracted from the MUSE data cube and four HST bands for each spectroscopically detected object. In addition, spectroscopic and photometric information for each source is also displayed. As an user-friendly tool, QtCounterpart does not depend on external software, can be executed on a normal PC or laptop, is intuitive to use, and is publicly available under <https://github.com/YohanaHerrero/QtCounterpart/tree/main>.

### A.1 General concept

Integral field spectroscopy (IFS) delivers three dimensional data cubes with one wavelength and two spatial coordinates. After the cubes have been carefully reduced (Urrutia et al., 2019), the Line Source Detection and Cataloguing (LSDCat, Herenz & Wisotzki 2017) software is used to create a catalogue of emission lines detected in the cube. A source catalogue is then produced through visual inspection using the QtClassify tool (Kerutt, 2017), which classifies the emission lines found by LSDCat and computes the redshift of the source. These algorithms, however, do not allow for any physical interpretation of the detected sources. In order to link their spectroscopic to their photometric data and to gather information about their morphology and orientation, which is indispensable to derive stellar masses, sizes, etc, we require HST counterparts.

#### A.1.1 Input data

As input, QtCounterpart requires one MUSE datacube, its corresponding spectroscopic catalogue of emission lines or sources, HST band images (maximum four) targeting the same area of the sky, and a photometric catalogue. Only the catalogues and one HST image are "must" arguments for the GUI, the rest is optional. If not passed, the corresponding information is omitted.

The MUSE datacube must have two spatial dimensions (RA and Dec), wavelength information and a proper WCS. The header must contain pixel information (keyword 'CD2\_2' or 'CDELTA2'), 'CD3\_3' (bin size of wavelength), and 'CRVAL3' (starting point of wavelength).

The HST images must also contain a proper WCS with pixel information, i.e. 'CRPIX' keyword. Besides, if later on you want to perform forced photometry for a photometrically unclassified HST detection, the HST header also needs to contain the keyword 'PHOTFLAM'.

The spectroscopic and photometric catalogues must, at least, contain RA and DEC in degrees. They can also contain additional info such as ID, confidence, lead line, signal-to-noise, flux, magnitude, photo\_z, redshift, wavelength. If this info is not provided, it will not be displayed in the interface and no narrowband image from the data cube will be extracted (in case no redshift or wavelength info is available).

Before running the GUI, I show an example of an useful setting of file and directory names:

Inside my work directory I have a directory named HST\_images (it contains HST images: a maximum of four are displayed in the GUI):

```
acs_435w_candels-cdfs-01_cut_v2.0.fits
acs_606w_candels-cdfs-01_cut_v2.0.fits
acs_814w_candels-cdfs-01_cut.fits
wfc3_160w_candels-cdfs-01_cut_v2.0.fits
```

Inside my work directory I have another directory named `Fields` (it contains the MUSE data cube and the spectroscopic catalogue e.g., the LSDCat output file):

```
DATACUBE_candels-cdfs-01_v2.0_dcsb_effnoised.fits
lsdcat_candels-cdfs-01.fits
```

In my work directory, I have the photometric catalogue:

```
catalog_photometry_candels-cdfs-01.fits
```

Because `ident_counterparts.py` is the main script of `QtCounterpart`, you can remind yourself of the files and parameters you need to pass to the GUI by doing `ident_counterparts.py --help`. The default names of the files (and parameters), their default location, and a brief explanation of what they are is also displayed. That is:

```
usage: ident_counterparts.py [-h] [-cube INPUTDATA] [-c CATALOG] [-p PCATALOG]
                             [-hstMAIN HSTIMAGEMAIN] [-hst1 HSTIMAGE1]
                             [-hst2 HSTIMAGE2] [-hst4 HSTIMAGE4] [-o OUTPUT]
                             [-c_RA COLUMN_RA] [-c_DEC COLUMN_DEC]
                             [-c_lambda COLUMN_LAM] [-c_z COLUMN_Z]
                             [-c_ID COLUMN_ID] [-c_sn COLUMN_SN]
                             [-c_line COLUMN_LINE]
                             [-c_confidence COLUMN_CONFIDENCE]
                             [-c_pRA COLUMN_PRA] [-c_pDEC COLUMN_PDEC]
                             [-c_pID COLUMN_PID] [-c_photoz COLUMN_PHOTOZ]
                             [-c_pmag_flux COLUMN_PMAG_FLUX]
```

Optional arguments:

```
-h, --help                show this help message and exit
-cube INPUTDATA, --inputdata INPUTDATA
                           Input flux cube FITS file (e.g. DC subtracted
                           effnoised cube). (default: None)
-c CATALOG, --catalog CATALOG
                           Input spectroscopic catalogue FITS file (e.g. from
                           LSDCat, consolidated MUSE catalogue, etc).
                           (default: /work/Fields/lsdcat_candels-
                           cdfs-47.fits)
-p PCATALOG, --pcatalog PCATALOG
                           Input photometric catalogue FITS file.
                           (default: /work/catalog_photometry_candels-
                           cdfs-47.fits)
-hstMAIN HSTIMAGEMAIN, --hstimageMAIN HSTIMAGEMAIN
                           HST main image for comparison. (default:
                           HST_images/acs_814w_candels-cdfs-47_cut_v1.0.fits)
-hst1 HSTIMAGE1, --hstimage1 HSTIMAGE1
                           HST1 image for comparison. (default:
                           HST_images/acs_435w_candels-cdfs-47_cut_v1.0.fits)
-hst2 HSTIMAGE2, --hstimage2 HSTIMAGE2
                           HST2 image for comparison. (default:
                           HST_images/acs_606w_candels-cdfs-47_cut_v1.0.fits)
```

```

-hst4 HSTIMAGE4, --hstimage4 HSTIMAGE4
        HST4 image for comparison. (default:
        HST_images/wfc3_160w_candels-cdfs-47_cut_v1.0.fits)
-o OUTPUT, --output OUTPUT
        Output catalogue FITS table.
        (default: /work/output_test.fits)
-c_RA COLUMN_RA, --column_RA COLUMN_RA
        Column name in input FITS spectroscopic catalogue for
        RA in degrees (default: RA)
-c_DEC COLUMN_DEC, --column_DEC COLUMN_DEC
        Column name in input FITS spectroscopic catalogue for
        DEC in degrees (default: DEC)
-c_lambda COLUMN_LAM, --column_LAM COLUMN_LAM
        Column name in input FITS spectroscopic catalogue for
        wavelength in Angstrom (default: LAMBDA)
-c_z COLUMN_Z, --column_z COLUMN_Z
        Column name in input FITS spectroscopic catalogue for
        redshift (default: Z)
-c_ID COLUMN_ID, --column_ID COLUMN_ID
        Column name in input FITS spectroscopic catalogue for
        ID (default: ID)
-c_sn COLUMN_SN, --column_sn COLUMN_SN
        Column name in input FITS spectroscopic catalogue for
        SN (default: S2N)
-c_line COLUMN_LINE, --column_LINE COLUMN_LINE
        Column name in input FITS spectroscopic catalogue for
        lead line (default: LINE_ID)
-c_confidence COLUMN_CONFIDENCE, --column_confidence COLUMN_CONFIDENCE
        Column name in input FITS spectroscopic catalogue for
        confidence (default: CONFIDENCE)
-c_pRA COLUMN_PRA, --column_pRA COLUMN_PRA
        Column name in input FITS photometric catalogue for RA
        in degrees (default: ra)
-c_pDEC COLUMN_PDEC, --column_pDEC COLUMN_PDEC
        Column name in input FITS photometric catalogue for DEC
        in degrees (default: dec)
-c_pID COLUMN_PID, --column_pID COLUMN_PID
        Column name in input FITS photometric catalogue for ID
        (default: id)
-c_photoz COLUMN_PHOTOZ, --column_photoz COLUMN_PHOTOZ
        Column name in input FITS photometric catalogue for
        photo_z (default: z_p)
-c_pmag_flux COLUMN_PMAG_FLUX, --column_pmag_flux COLUMN_PMAG_FLUX
        Column name in input FITS photometric catalogue for
        pflux or magnitude (default: F160W_LIMITING_MAGNITUDE)

```

An example on how to run the GUI would be:

```

-cube /work_directory/Fields/DATACUBE_candels-cdfs-01_v2.0_dcsb_effnoised.fit
-c lsdcat_candels-cdfs-01.fits -p catalog_photometry_candels-cdfs-01.fits -c_pRA

```

If I do not pass more files/parameters I am either using the default ones (e.g., default HST images) or I am not using them at all.

## A.1.2 Requirements

QtCounterpart uses a range of default packages included in standard installations of python. In order to run QtCounterpart you will need python version 3.7.x and the following standard packages:

```
numpy
matplotlib
math
scipy
pylab
```

You will also need somewhat special packages:

```
acstools
photutils
astropy
pyqtgraph
PyQt5
```

## A.2 Description of QtCounterpart

In this section I describe the functionality of QtCounterpart in detail. This can be seen as a guide on how to use the tool. I refer the reader to Fig. A.2.1 to look at the individual features of the GUI. Note that by keeping the mouse on top of each button/box of QtCounterpart a tip box is displayed to remind the user of its corresponding functionality.

The bottom left panel of the GUI shows the extracted pseudo-narrowband image of the MUSE detection ("MUSE narrowband"), which was recorded in the spectroscopic MUSE catalogue. The top left panel shows a HST band cutout ("Main HST image") corresponding to the same region of the sky where the detected MUSE object is located. Similarly, the four top small panels (small HST band images) show different HST bands of the same sky. The user decides which cut-outs are displayed.

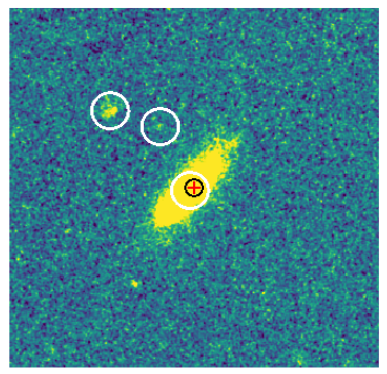
The numerical boxes below the small HST panels determine the resolution cuts of the HST bands. The contrast of the HST images can be modified by changing the cut number in the text boxes and clicking afterwards on the "Cuts" button. By using the "Reset images" button, the resolution of all HST images is set back to default (0.99). By double clicking on one of the small HST images, the user converts this into the main HST image of the GUI. It is also possible to zoom in or out on all displayed images by using the mouse.

The spectroscopic data from the MUSE catalogue is listed at the bottom of the GUI. Information such as MUSE ID, right ascension (RA), declination (Dec), wavelength ( $\lambda$ ) or redshift ( $z$ ), confidence of the source detection, the line that lead to the detection or the signal-to-noise (S/N) of the detection is given. Right on top, the photometric data from the photometric catalogue will be shown once a counterpart is selected. The photometric UV ID, the difference in RA and Dec between the spectroscopic and the photometric positions, the photometric redshift, and the magnitude will appear.

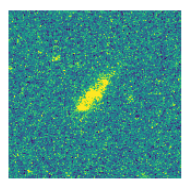
Inside the main HST image, the empty white circles show the position of the possible HST counterparts to the MUSE source, based on spatial assumptions (max 6" apart from the MUSE source). The user can click on any of the white circles to choose the most likely counterpart. This circle will then turn into red and the photometric information of the selected object will be displayed in the photometric information section. In order to guide the eye during the counterpart selection, the main HST image (and the MUSE narrowband) also contains the position of the MUSE object according to the spectroscopic data (crossed black circle). When the counterpart is selected, the user should tell the GUI how sure he/she is about his/her selection. For that purpose, the user should click on the "Confidence" bullet points. While "0" means the counterpart selection is uncertain, "3" means

Identifying Counterparts

**HST main image**

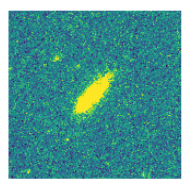


**acs\_435w**



Cuts:

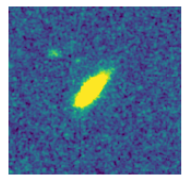
**acs\_606w**



**acs\_814w**



**wfc3\_160**



[Reset images](#)

**Photometric information**

UV ID:

$\Delta$  RA:

$\Delta$  Dec:

photo-z:

Confidence:  0  1  2  3

No match to MUSE in HST

Counterpart not in catalog

More than one counterpart

[Clear counterparts](#)

Comments:

**MUSE information**

MUSE ID: 147001004

RA: 53.142

DEC: -27.746

Lambda: 8386.8

z: 0

Confidence: 3

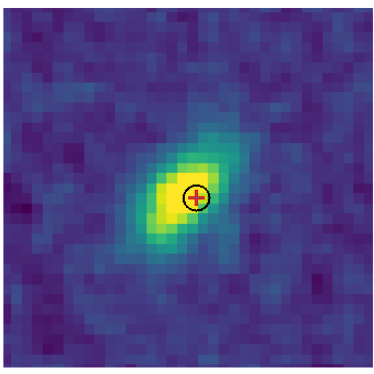
Lead line: Ha

S/N: 18.18

[Jump to MUSE ID:](#)

[Jump to next unclassified ID](#)

**MUSE narrowband**



[previous](#) [next](#)

Figure A.2.1: Screenshot of QtCounterpart.

the assignment is certain. The user can then click on "next" to save all information and find the counterpart for the next object in the MUSE catalogue. All information is saved in a fits output Table (see Sect. A.2.1).

There might be cases in which the MUSE object has no counterpart in the HST data, the object is not listed in the photometric catalogue or there is more than one counterpart. These cases can be specified by clicking on the empty boxes below the "Confidence" section. The user can also write a comment to record special characteristics or click on the "Clear counterparts" button to eliminate all displayed information and start classifying that MUSE source from scratch.

If the possible counterpart is not in the photometric catalogue, no white circle appears around the galaxy in the main HST image. However, the user may yet see a counterpart in the HST data. It is then possible to perform a forced photometry by clicking on the center of that possible galaxy. Once the user has clicked on the position of the main HST image where that counterpart is, the GUI measures the flux and coordinates of the object. In this case, the user needs to specify the case that he/she encountered (e.g. "Counterpart not in catalog"), leave a comment if he/she wishes and click "next" to save the information.

It is of course possible to revisit the already classified objects by clicking on "previous" until the user reaches the desired object. A more practical way to do this is to write the MUSE ID of the desired object in the empty box on the right of the "Jump to MUSE ID" button, click on the button and that object will be displayed. Note that to save or rewrite the information of an object, the user must click on "next" once a button/counterpart on the interface has been clicked. If nothing was clicked on the GUI, nothing will be saved/rewritten.

To exit the GUI, the user can press the red cross on the top right corner of the interface. To continue the classification where it was left, the user can click on the "Jump to next unclassified ID" button.

## A.2.1 Output data

The output file generated by QtCounterpart is a fits Table containing all the counterpart identification information that was displayed in the GUI before "next" was clicked. The table contains the following columns:

```
'ID': ID of the MUSE object
'UV_ID': photometric ID of the counterpart
'MUSE_RA': spectroscopic RA of the MUSE object (in deg)
'UV_RA': photometric RA of the counterpart (in deg)
'delta_RA': difference between MUSE_RA and UV_RA
'MUSE_DEC': spectroscopic DEC of the MUSE object (in deg)
'UV_DEC': photometric DEC of the counterpart (in deg)
'delta_DEC': difference between MUSE_DEC and UV_DEC
'Separation': angular separation in rad between the spectroscopic object
and the photometric location of the counterpart
'MUSE_lambda': spectroscopic wavelength of the MUSE object
'MUSE_z': spectroscopic redshift of the MUSE object
'UV_z': photometric redshift of the counterpart
'Photometry': flux or magnitude from photometric catalog
'Confidence': how sure are you of your counterpart (non-)selection?
'Comment': comment written during the selection, if any
'ra_noMatch': RA of the undetected counterpart in photometric catalogue,
in case 'Not in catalog' = 'Yes' and you have clicked somewhere on
the main HST image
'dec_noMatch': DEC of the undetected counterpart in photometric catalogue,
in case 'Not in catalog' = 'Yes' and you have clicked somewhere on
the main HST image
```



'Forced photometry': Forced photometry in case 'Not in catalog' = 'Yes' and you have clicked somewhere on the main HST image (units: erg/s/cm<sup>2</sup>/Angstrom)  
'More than one counterpart': 'Yes' if there was more than one counterpart and '-' if only one or none  
'No match': 'Yes' if there was no HST detection that matches the MUSE object and '-' if there is one/no counterpart  
'Not in catalog': 'Yes' if the counterpart is not in the photometric catalogue but you see a likely counterpart without a white circle around, and '-' for other cases e.g., there is one/no counterpart

## References

Herenz, E. C., & Wisotzki, L., (2017), A&A, 602, A111  
Kerutt, J., (2017), Astrophysics Source Code Library  
Urrutia, T., Wisotzki, L., Kerutt, J., et al., (2019), A&A, 624, 24